Magneto-optical spectroscopy and domain imaging of functional oxides

Blai Casals Montserrat

UNIVERSITAT AUTÒNOMA DE BARCELONA

DOCTORAL THESIS

Magneto-optical spectroscopy and domain imaging of functional oxides

---

Author:
Blai Casals Montserrat

Supervisor:
Gervasi Herranz Casabona

Tutor:
Javier Rodríguez Viejo

A thesis submitted in fulfillment of the requirements
for the degree of Doctor of Materials Science

in the

Laboratory of multifunctional thin films and complex structures
ICMAB-CSIC

June 21, 2017
Barcelona.

Gervasi Herranz Casabona, Tenured Scientist at the Institut de materials de Barcelona (ICMAB-CSIC) and Javier Rodríguez Viejo, Applied physics Professor at the Universitat Autònoma de Barcelona (UAB).

Certifiquen,

que el Blai Casals, llicenciat en física i màster en biofísica per la Universitat de Barcelona, ha desenvolupat sota la seva direcció la tesis titulada “Magnato-optic spectroscopy and domain imaging of functional oxides”, recollida en la present memòria per optar al títol de Doctor en Ciència de Materials.

I per a que consti, firmen el present certificat.

Dr. Gervasi Herranz Casabona Prof. Javier Rodríguez Viejo

“...there was an effect produced on the polarized ray... ”

Michael Faraday

“... Imagination is more important than knowledge... ”

Albert Einstein

Abstract

In this Thesis we have investigated the physical properties of different systems based on functional transition metal oxides. These materials show a large variety of properties –magnetism, ferroelectricity, superconductivity– that makes them interesting to explore novel devices beyond today's electronic and photonic technologies. The driving force of our study has been the understanding of the fundamental physical processes that explain a series of observed phenomena. In some cases, our interest has been to understand why a particular material shows an atypically large magneto-optical activity; in other cases, why and how ferroelastic domains move under electric fields; finally, we have turned our attention to surface acoustic waves and their interaction with magnetic materials. In spite of the disparity of materials and properties there is a common thread: our most important methodology to research these systems has been the use of light and, more specifically, the exploitation of magneto-optical spectroscopy and optical imaging. At the same time, efforts have been aimed at building, wherever possible, appropriate theoretical models that describe the experimental data.

In the following, a concise and brief account is given of the most relevant outcomes of the research described in this Thesis:

(i) We have determined the intrinsic contribution to the magneto-optical activity of polarons in manganites. Our study has revealed a large magneto-optical response in the visible, almost two orders of magnitude larger than the background response of the material and comparable to photonic- or plasmonic-mediated magneto-optical enhancement. Additionally, we have identified the photoinduced electronic transitions responsible for the intrinsic magneto-optical activity of self-trapped polarons. This finding opens new perspectives to explore other pathways to obtain large magneto-electric effects, using magneto-optics instead of magnetic properties.

(ii) We have analyzed the incorporation of Cerium into Yittrium Iron Garnet (YIG) and the consequences of this doping on the magnetic and electronic properties of YIG. Summarizing, our results show that Ce-doping triggers a selective charge transfer from Ce to the Fe tetrahedral sites in the YIG structure. This, in turn, causes a disruption of the electronic and magnetic properties of the parent compound, reducing the exchange coupling between the Ce and Fe magnetic moments and causing atypical magnetic behavior. Our findings represent an important step forward for the comprehension of the physical processes that determine the optical properties of YIG-based compounds. This specially relevant, taking into account that these materials are nowadays present in commercial devices in optical communication technologies.

(iii) We have used optical and magneto-optical imaging to analyze the spatial distributions of ferroelastic twin domains in $SrTiO_3$ crystals under the application of in-situ applied electric fields. Our work has enabled us to identify the sign of the anisotropy of the low-temperature dielectric behavior of $SrTiO_3$. Interestingly, the theoretical frame that we have developed to describe this anisotropy indicates the essential role of the emergence of an antiferroelectric displacement of the Ti ions that couples to polar and antiferrodistortive lattice modes. Our observations are very relevant for applications where understanding and controlling the distribution of all types of ferroelastic domains is essential for nanotechnology design.

(iv) Finally, we have used magneto-optical microscopy to access the magnetic properties of the individual piezoelectric/magnetic microstructured magnetoelectric devices. Specifically, we have studied the effects of surface acoustic waves (SAW), propagating on a piezoelectric ($LiNbO_3$), on the magnetic properties of microstructured Pt/Co/Pt squares with perpendicular magnetic anisotropy. Our results show that SAW can induce large changes in the magnetic coercive field, up to 80% of the initial value. By using a thermal proximity scanning probe we have shown that the changes in the magnetic properties are largely due to an intrinsic SAW induced heat dissipation.

Resum

En aquesta tesi s'han investigat les propietats físiques de diferents sistemes basats en òxids funcionals de metalls de transició. Aquests materials presenten una gran varietat de propietats -magnetisme, ferroelectricitat, superconductivitat- que els fan interessants per a ser explotats com a nous dispositius més enllà de les tecnologies electròniques i fotòniques d'avui dia. La força motriu del nostre estudi ha estat la comprensió dels processos físics fonamentals que expliquen una sèrie de fenòmens observats. En alguns casos, el nostre interès ha estat entendre perquè un determinat material mostra una gran activitat magneto-òptica atípica, i en altres casos, entendre com es mouen els dominis ferroelástics sota camps elèctrics. Finalment, hem concentrat la nostra atenció en les ones acústiques superficials i la seva interacció amb els materials magnètics. Tot i la diversitat dels materials i de les propietats estudiades, hi ha un tret en comú: la metodologia més important per investigar aquests sistemes ha estat l'ús de la llum i, més específicament, l'explotació de l'espectroscòpia magneto-òptica i la microscopía òptica. Alhora, els esforços s'han dirigit a la construcció, sempre que ha estat possible, dels models teòrics adequats que descriuen les dades experimentals.

A continuació, fem un recompte concís i breu dels resultats més rellevants de la investigació descrita a la tesi:

(i) La contribució intrínseca de polarons en manganites a l'activitat MO. En resum, el nostre estudi revela una resposta magneto-òptica gegant i inesperada de polarons auto-atrapats en el visible, que és gairebé dos ordres de magnitud major que la resposta de fons del material i comparable a millores de tipus plasmònic o fotòniques a l'activitat MO. A més, proporcionant un marc teòric, hem identificat les transicions electròniques fotoinduïdes responsables de l'activitat MO intrínseca dels polarons auto-atrapats. Aquesta troballa obre noves perspectives per explorar altres vies per obtenir grans efectes magnetoelèctrics, utilitzant la magneto-òptica en lloc de propietats magnètiques.

(ii) L'estudi de la incorporació de les terres rares en granats d'itri i ferro (YIG) i les conseqüències sobre les seves propietats magnètiques. Resumidament, els nostres resultats mostren que el dopatge de Ce provoca una transferència de càrrega selectiva des del ions de Ce als llocs tetraèdrics dels Fe en l'estructura del YIG. Això causa una pertorbació de les propietats electròniques i magnètiques del compost original i que redueix l'acoblament de canvi entre el Ce i els moments magnètics del Fe causant comportament magnètic atípic. Les nostres troballes representen un avanç important per a la comprensió dels processos físics que determinen les propietats òptiques dels compostos basats en YIG. Propietats especialment rellevants, tenint en compte que

aquests materials estan avui dia presents en els dispositius comercials en les tecnologies de comunicació òptica.

(iii) Hem utilitzat microscòpia òptica i magneto-òptica per analitzar la distribució espacial de domini de macla ferroelàstics en cristalls de $SrTiO_3$ sota camps elèctrics aplicats. El nostre treball ens ha permès identificar el senyal de l'anisotropia del comportament dielèctric de baixa temperatura de $SrTiO_3$. Curiosament, el marc teòric que hem desenvolupat per a descriure aquesta anisotropia indica el paper essencial de l'aparició de modes antiferroelèctrics dels ions de Ti que s'acoblen amb modes polars antiferrodistortive. Les nostres observacions són molt rellevants per a aplicacions en les quals és essencial la comprensió i el control de la distribució de tot tipus de resposta ferroelástica per al disseny nanotecnològic.

(iv) Finalment, hem utilitzat la microscòpia MO per accedir a les propietats magnètiques individuals de dispositius magnetoelèctrics de tipus piezoelèctric/magnètic microestructurats. Específicament, s'han estudiat els efectes de la propagació d'ones acústiques superficials (SAW) en un piezoelèctric ($LiNbO_3$) sobre les propietats magnètiques de microestructures de Pt/Co/Pt amb anisotropia magnètica perpendicular. Els nostres resultats mostren que les SAW poden induir grans canvis en el camp coercitiu magnètic, fins un 80% del valor inicial. Mitjançant l'ús d'una sonda tèrmica de proximitat i rastreig hem demostrat que els canvis en les propietats magnètiques són en gran part causa d'una dissipació de calor intrínseca de les SAW.

Acknowledgements

Firstly, I would like to express my deepest gratitude to my supervisor Dr. Gervasi Herranz for all his support, advice, fruitful discussions, meticulous suggestions, motivation and continuous guidance during all this period. Gràcies per la teva dedicació i paciència a formar-me com a científic.

I would also thank to Josep Fontcuberta for all the fruitful discussions we had, astute criticism and for his enthusiasm which never rest. My sincere gratitude to Florencio Sánchez for all his collaboration on the materials growth and his crucial scientific encouragement.

This thesis has been developed with several and valuable collaborations. I would like to acknowledge Profs. Javier Junquera and Pablo García Fernández for providing the fundamental support on the intrinsic optical polarization rotation of polarons, Prof. Sebastiaan van Dijken for his advise on the magnetic and ferroelastic domain imaging, fruitful discussions and for giving me the opportunity to work in the NanoSpin grup during my PhD stage, Prof. Max Stengel and Andrea Schiaffino for their theoretical analysis of the dielectric anisotropy behaviour on STO, Prof. Mariano Campoy Quiles for the spectroscopic ellipsometry and valuable discussions, Dr. Hari Babu Vassili for all his support on the synchrotron beamtimes and data analysis, Professor Julian Geshev for modeling the magnetic responses of YIG and CeYIG, Profs. Rudolf Gross, Stephan Geprägs and Matthias Opel for providing YIG samples and for helpful discussions, Dr. Ignasi Fina for sharing ideas and his support on the ferroelectric measurements, Andrés Gómes for his crucial help on SThM and scanning probes techniques, Dra. Lucia Aballe and Dr Michael Foerster for all their support on PEEM measurements at Alba synchrotron, Dr. Ferran Macià for all his advise on the SAW-induced effects, encouragement and guidance.

This thesis, has been supported by the Spanish government project FPI 2012 BES-2012-059023. I would also thank the COST TO-BE action for the short term scientific mission founding COST-STSM-MP1308-32429.

I would thank my lab colleagues, Rafael Cichelero (Cica), an indispensable experimental colleague, together with Gervasi, we have built a great team for great challenges. I want to thank Nahuel Statuto for his advise on the micromagnetic simulations and his friendship. I acknowledge all the people in the MULFOX group, specially Dr. David Pesquera, Dr. Diego Gutiérrez, Marina Espínola, Dr. Ondrej Vlasin, Dr. Mateusz Scigaj, Fanmao Liu, Mengdi Qian, Prof. Vassil Skumryev and Prof. Vladimir Laukhin. And all members of NanoSpin group in Aalto University, specially to Dra. Arianna Casiraghi, Diego López González, Sampo Hämäläinen, Sampo Inkinen and

Francisco Freire Fernandez.

Gràcies als companys de dinar i del ICMAB per fer el dia més humà, a la Laura López, al Bernat Mundet, al meu primer company en Carlos Escorihuela, al Bernat Bozzo, al Bernhard Dörling, al Gustau Catalan per les mil discusions, a la Ela, al Ashley, al James, al Roque, al Jaume Roqueta, a la Kumara, al Fabian, al Federico, al Alex, al Matteo, a l'Anna May, a l'Hugo, a la Coco, al Joan Esquius, al Carlos Frontera, a la Greta Radaelli, Al Pablo, a la Jackeline Narvaez, al Jose, a la Maria Milla, a la Mar Tristany que ha estat la millor companya de despatx, a la Regina Galceran, a la Jessica Nava, al Juan Carlos i l'Ana, al Ferran Vallès, al Jaume Gázquez i a totes aquelles que han compartit discussions i cafès.

Vull també mencionar el bon tracte i el suport de tot l'equip dels serveis cientificotècnics i de l'administració del ICMAB, especialment a la Pietat, gràcies per fer-ho tot més senzill i alegre.

El suport de totes les amigues i amics ha estat una peça clau, gràcies als del barri i als del Guinardó, als del Cau Can Baró, als d'Escoltes Catalans, i els d'arreu! També gràcies a la música i a l'acordió que m'omple l'esperit i les idees, al Manu i l'Heura que han fet de Morena una gran experiència. I els dinars del Roc i l'Ari que han fet més bonics els diumenges de tesi.

A la Raquel, sens dubte la coautora emocional d'aquesta tesi.

Finalment vull agraïr de tot cor a tota la meva familia Casals Ortuño Montserrat Boada, i dir que del Pere, el meu pare, i de l'Anna, la meva mare, han nascut les meves inquietuts. Gràcies.

Scientific output

LIST OF PUBLICATIONS

Scientific publications derived from the work depicted in this thesis:

- B. Casals, N. Statuto, R. Cichelero , A. Gómez , A. Hernández-Mínguez, J. M. Hernàndez, G. Herranz, F. Macià. *Directional heat dissipation generated by surface acoustic waves in Co/Pt/LiNbO3 structures*. Manuscript in preparation.
- B. Casals, A. Schiaffino, A. Casiraghi, S.J. Hämäläinen, D. López González, J. Fontcuberta, S. van Dijken, M. Stengel, G. Herranz. *In-situ imaging of electric field-induced ferroelastic domain motion in* $SrTiO_3$. Manuscript submitted.
- L. Vistoli, Wenbo Wang, Qiuxiang Zhu, B. Casals, A. Sander, R. Cichelero, A. Barthélémy, S. Fusil, G. Herranz, Weida Wu, V. Garcia and M. Bibes. *Giant topological Hall effect from magnetic skyrmion bubbles in correlated manganite thin films*. Manuscript submitted.
- H. B. Vasili, B. Casals, R. Cichelero, F. Macià, J. Geshev, P. Gargiani, M. Valvidares, J. Herrero-Martin, E. Pellegrin, J. Fontcuberta, G. Herranz. *Direct observation of multivalent states and* $4f \rightarrow 3d$ *charge transfer in Ce-doped yttrium iron garnet thin films*. Manuscript submitted.
- B. Casals, R. Cichelero, P. García Fernández, J. Junquera, D. Pesquera, M. Campoy-Quiles, I.C. Infante, F. Sánchez, J. Fontcuberta, G. Herranz. *Giant Optical Polarization Rotation Induced by Spin-Orbit Coupling in Polarons*. Physical Review Letters, 117 (2016)
- B. Casals, M. Espínola, R. Cichelero, S. Geprägs, M. Opel, R. Gross, G. Herranz, J. Fontcuberta. *Untangling the contributions of cerium and iron to the magnetism of Ce-doped yttrium iron garnet*. Applied Physics Letters, 108 (2016).
- O. Vlasin, B. Casals, N. Dix, D. Gutiérrez, F. Sánchez, G. Herranz. *Optical Imaging of Nonuniform Ferroelectricity and Strain at the Diffraction Limit*. Scientific Reports, 5, (2015).

LIST OF COMMUNICATIONS

The work in this thesis has been presented by the author (B. Casals) in several conferences and seminars:

- *Imaging of magnetoelectric coupling mediated by entangled ferroelastic domain and polar domain walls in non-polar materials*. **Oral presentation**. MMM2016 (New Orleans, USA, from 30th October to 4th November 2016).

- *Optical Polarization Rotation Induced by Spin-Orbit Coupling in Polarons*. **Oral presentation**. MMM2016 (New Orleans, USA, from 30th October to 4th November 2016).

- *Untangling the contributions of cerium and iron ions to the magnetism of Ce-doped yttrium iron garnet*. **Poster**. MMM2016 (New Orleans, USA, from 30th October to 4th November 2016).

- *Imaging of magnetoelectric coupling mediated by entangled ferroelastic domain and polar domain walls in non-polar materials*. **Oral presentation**. "TOWARDS OXIDE BASED ELECTRONICS" Cost to-be fall meeting 2016 (Ljubjana, Slovenia, 28-30th September 2016).

- *Optical polarization rotation induced by spin-orbit coupling in polarons*. **Oral presentation**. JEMS2016 (Glasgow, UK, 22-26th August 2016).

- *Untangling the contributions of cerium and iron ions to the magnetism of Ce-doped yttrium iron garnet*. **Poster**. JEMS2016 (Glasgow, UK, 22-26th August 2016).

- *In-situ Optical Imaging of Magnetoelectric Coupling*. **Oral presentation**. Nanoselect Annual Meeting 2016 (Sant Feliu de Guíxols, Spain, 8-10 July 2016).

- *Exploiting magneto-optics as a gateway to the magnetism of Ce-YIG fims grown on strongly paramagnetic garnet substrates*. **Oral presentation**. ICM2015 (Barcelona, Spain, 5-10th July 2015).

- *Imaging the electro-optic response of ferroelectrics at the diffraction limit*. **Poster**. ICM2015 (Barcelona, Spain, 5-10th July 2015).

- *Imaging the electro-optic response of ferroelectrics at the diffraction limit*. **Oral presentation**. EMRS Spring Meeting 2015 (Ille de France, France, 11-15th May 2015).

- *Exploiting magneto-optics as a gateway to the magnetism of Ce-YIG fims grown on strongly paramagnetic garnet substrates*. **Poster**. EMRS Spring Meeting 2015 (Ille de France, France, 11-15th May 2015).

- *Imaging Optical Responses of Magnetism and Ferroelectricity with Submicron Resolution*. **Oral presentation**. Nanoselect Annual Meeting 2014 (Sant Feliu de Guíxols, Spain, 25-27th July 2014).

- *Magnetopolarons in manganites: a magnetooptic study*. **Oral presentation**. Nanoselect Annual Meeting 2013 (Sant Feliu de Guíxols, Spain, 14-16th July 2013).

- *Magneto-polaron response at optical frequencies of* $La_{2/3}Ca_{1/3}MnO_3$ *thin films*. **Poster**. International School of Oxide Electronics, ISOE213. (Cargèse, Corsica, France, 2-14th September 2013).

Contents

List of Figures

List of Tables

List of Abbreviations

AFM	Antiferromagnetic
AFM	Atomic Force Microscopy
AFD	Antiferrodistortive
AFE	Antiferroelectric
CCD	Charge-coupled device
CMR	Colossal Magnetoresitance
CT	Cubic to Tetragonal transition
CeYIG	Cerium doped Yttrium Iron Garnet
DW	Domain Wall
FE	Ferroelastic
FM	Ferromagnetic
FMR	Ferromagnetic Resonance
IDT	Interdigitated Ttransducer
LMOKE	Longitudinal Magneto-Optical Kerr effect
ME	Magnetoelastic
MO	Magneto-Optic
MR	Magnetoreflectance
MOKE	Magneto-Optical Kerr effect
PEM	Photoelastic Modulator
PLD	Pulsed Laser Deposition
PMA	Perpendicular Magnetic Anisotropy
PMOKE	Polar Magneto-Optical Kerr effect
PMT	Photomultiplier tube
PUND	Positive Up Negative Down
rf	radiofrequency
RT	Room Temperature
SAW	Surface Acoustic Wave
SQUID	Superconducting Quantum Interference Devices
SThM	Scanning Thermal Microscopy
TMOKE	Transverse Magneto-Optical Kerr effect
XAS	X-ray Absorption Spectroscopy
XMCD	X-ray Magnetic Circular Dichroism
XRD	X-ray Diffraction
YIG	Yttrium Iron Garnet

List of Symbols

T	Temperature	K
T_c	Curie Temperature	K
f	Frequency	Hz
α	Gilbert damping	
r_{ij}	Fresnel coefficients of the reflection matrix	
J_n	First kind Bessel's function of order n	
S_{ii}	Amplitude of absorption coefficients	dB
S_{ij}	Amplitude of transmission coefficients	dB
θ	Kerr rotation	rad or deg
ϵ	Kerr ellipticity	rad or deg
δ_K	Transverse Kerr	
$\Re(\delta_K)$	Real transverse Kerr	
$\Im(\delta_K)$	Imaginary transverse Kerr	
λ	Wavelength	nm
λ_SAW	SAW wavelength	μm
H	Magnetic field	Oe
H_c	Coercive magnetic field	Oe
M	Magnetization	emu
M_r	Remanence magnetization	emu/cm^3
M_s	Magnetization at saturation	emu/cm^3
K_u	Uniaxial magnetic anisotropy	erg/cm^3
K_{me}	Magnetoelastic magnetic anisotropy	erg/cm^3
E	Electric field	V/m
E_c	Coercive electric field	V/m
P	Polarization	μC/cm^2
P_r	Remanent polarization	μC/cm^2
ε	Dielectric permittivity	F/m

A la humanitat, que per ella la ciència.

Chapter 1

Introduction

1.1 Brief overview of transition metal oxides

Transition metal oxides represent a vast family of materials comprising a broad scope of crystal structures. These range from simple binary oxides of MO composition - where M is the transition metal-, which generally possess a rock-salt structure, to dioxides, $M0_2$, which can display fluorite, rutile, or even more intricate structures. Beyond this, higher complexity can be found in many sesquioxides, with composition M_2O_3, which may possess the corundum structure. Most relevant for the context of this Thesis, are transition metals forming ternary oxides like perovskites, spinels, or garnets.

One of the hallmark features of these oxides is the rich variety of physical properties, closely related to the structure of the materials, which are very sensitive to any eventual phase transitions from one crystal structure to another. These properties - which encompass several phenomena, such as magnetism, piezoelectricity, ferroelectricity, superconductivity, birefringence, and many others- are very often signaled as the basis for the design of future functional devices, offering alternative pathways for the further development of today's electronic and photonic technologies [1, 2, 3]. One of the key futures of oxides is that, beyond the development based purely on device miniaturization and increase of computational speed, they afford the additional possibility of increasing the functionality of devices to keep up with Moore's law and the impressive development of information technologies over the past decades.

The underlying premise for the fascinating diversity of physical properties displayed by oxides is rooted in the role played by the outer electrons in d-shells of the transition metal ions. These d electrons can neither be described by a collective electron model (as in the case of s and p electrons) nor by a localized electron model (as in the case of f electrons which are tightly bound to the nuclei) [4]. The intermediate state of these electrons shows itself in terms of localized electron behavior in some oxides and collective electron behavior in some others; in a few instances, both kinds of d electrons can even exist simultaneously. Additionally, the bandwidth of the electronic states derived from the d-shells is much narrower than that s- or p- derived electrons bands. In consequence, electronic correlations are vigorously promoted in states derived from d-bands. Not surprisingly, many of transition metal oxides display magnetic ordering, including ferromagnetism, antiferromagnetism, ferrimagnetism or more exotic forms of magnetism based on noncollinear spiral, conical spin textures. Similarly, electron correlations in d-bands are behind the emergence of Mott or charge transfer insulators, a class of materials that should conduct electricity under conventional band theories, but are indeed insulators [5].

In this Thesis we have investigated the physical properties of different systems based on transition metal oxides. In most cases, the magnetic properties have been researched by the use of light and, more specifically, exploiting magneto-optical spectroscopy and optical imaging. Although magnetism is the common thread throughout our investigations, other not less relevant phenomena have been subject to study, including electron-lattice interactions, ferroelasticity or magnetoelastic interactions in complex piezoelectric/magnetic systems. In the following of this introductory chapter, this common thread is broken down into the different aforementioned aspects related to the different topics and materials that have been addressed in this Thesis.

1.2 Lattice distortions and self-trapped polarons in CMR manganites

In a solid, beyond the aforementioned interactions between electrons, the latter can also interact with the lattice -for instance, via the electron-phonon coupling-. In this context, an important phenomenon in transition metal oxides is the Jahn-Teller effect [6, 7], by which the symmetry and energy of the solid is reduced by a geometric distortion. The Jahn-Teller effect is typically observed among octahedral complexes -for instance, in oxides of the perovskite family- where the two axial bonds can be shorter or longer than those of the equatorial bonds. This is schematically depicted in figure 1.1, where the distortions of an octahedral unit are shown.

The Jahn–Teller theorem requires a spatially degenerate electronic ground state whose degeneracy, by reason of the geometrical distortion, is removed by reducing the overall energy of the system [9]. In the case of a perovskite oxide, the five d atomic orbitals are split into two degenerate sets by the octahedral oxygen coordination that surrounds the transition metal. The split orbital levels are then represented by the symmetry labels: the lower energy t_{2g} (d_{xz}, d_{yz}, d_{xy}) states and the e_g (d_{z^2} and $d_{x^2-y^2}$) levels that are higher in energy. When in a given crystal phase the solid possesses a degenerate electronic ground state -e.g., t_{2g} or e_g levels are degenerate-, it will distort by the Jahn-Teller effect to remove the degeneracy and form a lower energy -and by consequence, a lower symmetry- system. The octahedral complex will either elongate or compress the z ligand bonds as shown in the figure 1.1.

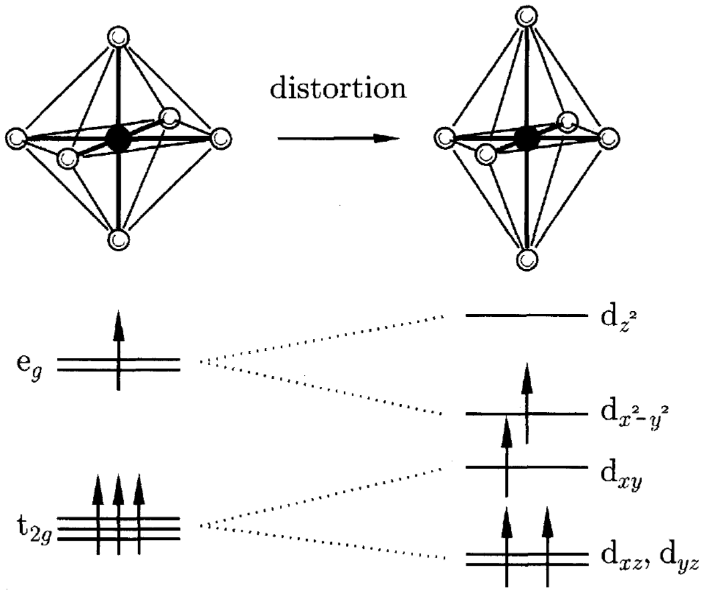

FIGURE 1.1: The Jahn-Teller effect for Mn^{3+} ($3d^4$). An octahedral complex (left) can distort (right), thus splitting the t2g and eg levels. Adapted from [8].

The concept of Jahn-Teller distortions is closely related to the emergence of polarons, especially when the coupling of electrons and the lattice is particularly strong. Since their first inception by Landau in 1933, polarons have grabbed the attention of many other physicists (including, notably, prominent scientists such as Feynman [10] or Rashba [11]). Since then, polarons have been shown to be a key ingredient to understand the physics of many materials, including high-Tc superconductors, colossal magnetoresistance (CMR) oxides or semiconductors [12, 13].

Precisely, the case presented by self-trapped polarons in colossal magnetoresistance manganites is described in Chapter 3. Manganite perovskites are compounds with $AMnO_3$ chemical composition, in which A is usually a lanthanide or a rare earth, and the physics of manganites is mainly derived from electrons in the e_g-levels. An important observation is that when an electron is localized in the e_g shell of an octahedral Mn complex the resulting degenerate state (see Fig. 3.3 of Chapter 3), triggers a geometrical instability in the form of the Jahn-Teller effect. As a consequence, the complex becomes elongated and electrons occupy preferentially orbitals with $3d_{3_{z^2}-r^2}$ symmetry. In the particular case of $La_{2/3}Ca_{1/3}MnO_3$ this distortion can be experimentally observed by EXAFS and is found to increase as the temperature approaches the magnetic transition [14]. Interestingly, when polarons are intensely bound to the lattice, the electronic states are intermixed with vibronic deformations, forming a new kind of physical entity, the small polaron, which can have physical properties and electronic band structure markedly different from those of the background solid. When electrons move around in a magnetic field, that motion generates a magneto-optical gyrotropic response, by which the polarization of light is rotated in proportion to the induced magnetization. In consequence, the emergence of self-trapped polarons in some compounds, such as the optimally doped ferromagnetic manganites, can give rise to the appearance of a distinctive magneto-optical response, different from the background response of the non-trapped free-like electrons. Our discovery of an unexpectedly large magneto-optical response intrinsic to self-trapped polarons in a CMR manganite is discussed in Chapter 3. In collaboration with P. García Fernández and J. Junquera (U. Cantabria) we have established a solid theoretical framework to understand the astonishingly large magneto-optical response induced by the self-trapped polarons. It has been found that the answer lies in the nontrivial interplay between different factors: (i) the spin-orbit coupling, which induces spin-mixed states that allow describing spin flips during the photoinduced polaron motion, (ii) the intersite Mn-Mn polaron hopping that allows electronic e_g-e_g transitions that are forbidden by parity, and (iii) the Jahn-Teller interaction that enhances the effect of the spin-orbit coupling.

The uncovering of a large polaron-induced gyrotropic response is intriguing for different reasons. Firstly, because an unsuspected mechanism for large gyrotropic effects comes to light. Secondly, the phenomenon is observed close to room temperature; one can then envision strategies to raise the effect to higher temperatures by engineering materials suitably. And, finally, strain modulation by piezoelectrics may lead to a large modulation of the magneto-optical activity by electric fields, thus opening novel avenues for magnetoelectric coupling beyond the conventional modulation of magnetization, which are so far unforeseen.

1.3 Magneto-optical responses in oxides: rare-earth doped iron garnets

Precisely, the large magneto-optical activity of some materials form nowadays the basis for crucial devices that integrate today's optical networks. More specifically, the communication of information along optical fibers requires the insertion of optical isolators, i.e., devices that enable the propagation of light along one direction, but forbid the propagation along the opposite direction. This ability is essential for the suppression of the damaging effects of backscattered light on the signal quality. Not surprisingly, optical isolators are today a mainstay of any communication technology based on light [15]. Most of the actual optical isolators are based on the magneto-optical Faraday effect: in this case, a slab of a magneto-optical material, mostly the $Y_3Fe_5O_{12}$ (YIG) garnet, is sandwiched between two crossed optical polarizers (figure 1.2). The polarization of the light traveling along YIG is rotated by the magneto-optical Faraday effect and is proportional to the optical path length along the YIG crystal. Since the magneto-optical effect is non-reciprocal, light is only enabled to propagate forwards, while backward propagation is blocked (figure 1.2).

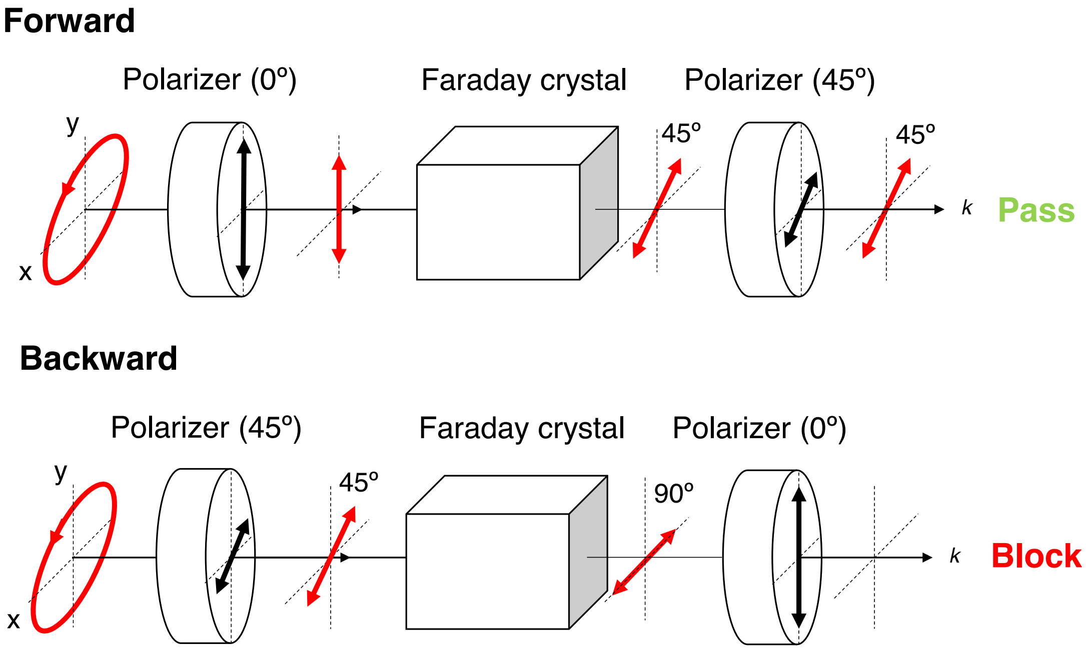

FIGURE 1.2: Optical isolator operation principle scheme.

Although YIG is the staple material for Faraday isolators, today's drive for new materials shifts the research towards other systems with even larger magneto-optical responses that, eventually, could be integrated in smaller photonic devices. In this line, a successful strategy to enhance significantly the magneto-optical response is to dope YIG with rare earths and, in particular, with Ce. Indeed, Ce-doping on yttrium sites yields a considerably enhanced near-infrared Faraday rotation and magneto-optical figure of merit [16, 17, 18, 19, 20]. With these interesting properties, Ce-YIG is promising for nonreciprocal photonic device applications, such as the abovementioned optical isolators and circulators. Broadly speaking, the larger magneto-optical response of Ce-doped YIG can be explained by the emergence of new optical transitions -absent in the parent undoped YIG compound- involving ions (Ce in this case) with large spin-orbit coupling. Yet, some fundamental physical mechanisms behind the Ce-induced optical transitions are still under debate. In particular, most works propose two types of electronic transitions: (i) intra-atomic orbital dipole transitions between the $4f$ and 5d states of Ce or (ii) interatomic dipole transitions between the $4f$-Ce and $3d$ states of Fe [21, 16, 22]. However, it is still unclear whether both transitions are equally relevant or if, on the contrary, one of them is predominant.

To investigate the impact of Ce-doping on the magnetism and electronic properties of the YIG parent compound, we undertook an ambitious experimental approach, combing magneto-optical and synchrotron x-ray spectroscopies. As described in Chapter 4, our work shows that doping YIG with Ce generates a disruption of the electronic and magnetic properties of the parent compound, which causes a reduction of the exchange coupling between the Ce and Fe magnetic moments. Our element- and site- specific soft x-ray spectroscopy measurements demonstrate that this disruption is caused by an electron charge transfer from $4f$-Ce states towards $3d$-Fe states. More importantly, we find that such charge transfer is found to occur only towards some of the iron sites in the YIG structure -namely, the iron ions that are located in tetrahedral sites in the YIG structure, while those at octahedral positions are left spare-. As a consequence of the perturbation of the ionic electronic states, the site-specific (Ce and Fe) sublattice magnetizations are disturbed in such a way that their respective magnetization hysteretic curves show atypical signatures, departing from the deviations from the conventional saturation-magnetization behavior. As described in Chapter 4, although we cannot anticipate what of the aforementioned Ce → Ce or Ce → Fe transitions is most relevant for the higher magneto-optical response of Ce-doped YIG, our study establishes a step forward in the comprehension of the fundamental physical processes caused by rare-earth doping in the YIG electronic and magnetic properties that, as aforementioned, is an indispensable knowledge to further optimize and tailor the optical properties of these important materials.

1.4 Low-temperature dielectric properties and ferroelastic domains in $SrTiO_3$

Noble Prize-winner Alex Müller once described strontium titanate as the “drosophila of solid state physics” [23, 24]. This assertion has a good reason, since $SrTiO_3$ is host to many intriguing condensed matter states, including the most dilute known superconductivity [25], incipient ferroelectricity suppressed by quantum fluctuations [26], or the emergence of two-dimensional electron gases (2DEGs) with very large Rashba spin-orbit fields [27, 28, 29, 30, 31, 32, 33]. All these phenomena occur below the cubic-to-tetragonal transition where $SrTiO_3$ undergoes antiferrodistortive (AFD) lattice distortions, whereby octahedral units of the perovskite structure are counter-rotated along different axes and ferroelastic twins emerge as a consequence of the lower symmetry (figure 1.3). It is well known that the formation of such twins has a strong impact on the transport properties of 2DEGs and on superconductivity [28, 34, 35, 25, 36, 37, 38], and, obviously, could play a key role in the dielectric properties, including the emergence of ferroelectricity. Nevertheless, surprisingly, the knowledge of the low-temperature dielectric properties of $SrTiO_3$ is rather partial. In particular, although it is known that the dielectric properties are anisotropic –as expected for a tetragonal symmetry– the relation of this anisotropy to the AFD rotation axis is still not clarified. This knowledge gap is particularly detrimental for the full comprehension of the physical properties of $SrTiO_3$ since, as mentioned above, a detailed understanding requires an accurate description of the ferroelastic twin distribution and its motion under electric fields.

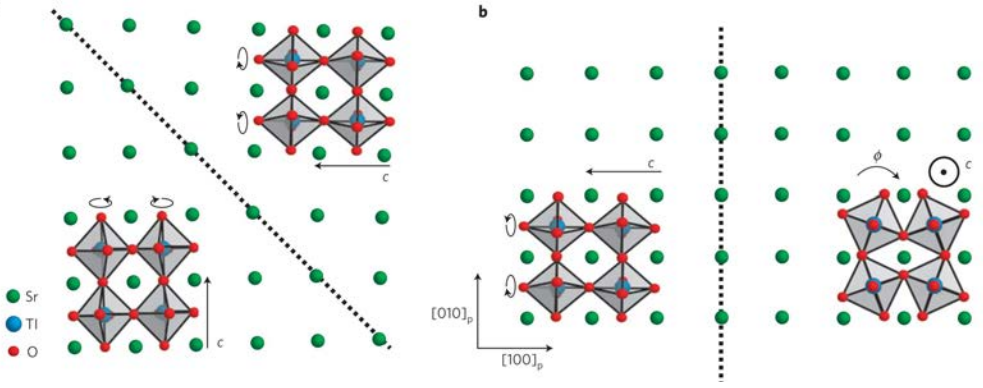

FIGURE 1.3: Schematic twin boundaries and domains in the SrTiO$_3$ crystal structure in the tetragonal phase. Extracted from [36].

In order to shed light on the dielectric properties of SrTiO$_3$, we have carried out a detailed analysis intended to visualize the evolution of the spatial distribution of ferroelastic domains under the action of in-situ applied electric fields. For that purpose, we have relied on the magneto-optical imaging of the domain pattern of magnetic thin films -Co$_{40}$Fe$_{40}$B$_{20}$ (CoFeB) in our case- grown on the surface of SrTiO$_3$ crystals. This approach is similar to the previously reported imprinting of ferroelastic domains into a magnetostrictive film on BaTiO$_3$ [39, 40, 41, 42, 43, 44, 45, 46, 47, 48], in which a strain transfer takes place from the ferroelastic twins, causing a modulation of the magnetic anisotropy of the magnetic overlayer via inverse magnetostriction. As discussed in Chapter 5, in an appropriate magnetic state configuration, it is possible to establish a biunivocal correspondence between the magnetic domains observed in CoFeB by magneto-optical imaging and the ferroelastic twin domains in SrTiO$_3$. Thus, magneto-optical microscopy is used in this case to image directly the changes in the space distributions of ferroelastic twins upon the application of electric fields. As shown in Chapter 5, our analysis has confirmed that the low-temperature dielectric properties of SrTiO$_3$ are anisotropic and, additionally, has revealed that the dielectric susceptibility is higher along the normal to the axis of the octahedral tilts in the AFD tetragonal phase.

Interestingly, the collaboration with Prof. M. Stengel (ICMAB-CSIC) has enabled the identification of the driving force of this anisotropic behavior. More specifically, an analysis based on first-principles and Landau theory, associates the observed anisotropy to the emergence of an antiferroelectric (AFE) lattice instability of the Ti ions that couples to polar and AFD lattice modes. Consequently, the results presented in Chapter 5 are all-important to understand the motion and distribution of ferroelastic twins in SrTiO$_3$ under electric fields.

Beyond this important conclusion, we have also studied how the electric field-induced changes of the ferroelastic twin distributions are related to macroscopic dielectric measurements. This is a relevant aspect of the physics of $SrTiO_3$. In general, there is a common acceptance that $SrTiO_3$ is a non-ferroelectric material; yet, ferroelectricity has been reported several times in this system. For instance, it has been claimed that ferroelectricity can be induced under strain [49, 50] or by doping with O^{18} isotopes [51]. Beyond this, a giant piezoelectric effect has been reported in the $SrTiO_3$ surface [52], and even nominally stoichiometric $SrTiO_3$ has been reported to be ferroelectric under large applied electric fields [26]. Moreover, it has been shown that the twin domain walls exhibit a polar character [53, 24, 54] and some works attribute this fact to the origin of the observed changes under electric field [55, 56].

Our magneto(optical) approach to the study of the ferroelastic domain structure of $SrTiO_3$ crystals has enabled an unprecedented analysis in connection with the macroscopic dielectric properties. More specifically, we have been able to track down the evolution in small regions (typically about a few tens of μm or even less) of ferroelastic twin distributions as a function of the electric field, as it is changed over a complete cycle. These efforts were aimed at identifying any ferroelectric-like features in the twin's reconfiguration under electric fields. Studying the optical images obtained over the entire sample area, we have identified different regions that were characterized by hosting ferroelastic domains with different orientations with respect to the surface and with respect to the applied fields. We have found that, while some areas do not show a significant redistribution of twins with fields, other regions over the sample do exhibit significant changes in the spatial distribution of the ferroelectric domains. Interestingly, we find that those regions displaying higher ferroelastic twin mobility are those that show at the same time ferroelectric-like features in the optical signal. This seems to point to a correlation between ferroelastic motion and redistribution and ferroelectric-like dielectric responses, a point that justifies further research to better settle this relationship.

1.5 Localized heating generated by pulsed surface acoustic waves

In the last section we have described how we imaged ferroelastic twins by magneto-optical imaging, exploiting the fact that the strain generated by the ferroelastic domains is transferred to the modulation of the magnetic anisotropy of the magnetic overlayer via inverse magnetostriction. This is a particular case of a magnetoelastic interaction taking place across the interface between two systems. Yet, this topic is of a much broader scientific and technological interest and is indeed a very active field of research. More specifically, over the recent years, there has been a high interest to find mechanisms to control the magnetization of nanodevices alternative to the application of magnetic fields, which usually requires the use of electrical currents to generate the magnetic fields, with consequent increase of power consumption [57, 58]. In this line, the possibility to control a nanomagnet with an electric current via the spin-transfer torque effect or with an electric field through the magnetoelectric coupling has inspired a considerable amount of technological concepts. Particularly, magnetoelectric materials such as artificial or intrinsic multiferroics are particularly promising [59, 60, 61, 62, 63, 64, 65, 66, 67, 68]. There are two essential different mechanisms by which an electric field can exert a control of the magnetic state of multiferroic system, involving either electronically driven interface coupling [69, 70] or via strain-mediated mechanisms, involving the converse piezoelectric effect and magneto-elastic interaction.

Following this kind of magnetoelectric systems mediated by strain, we have explored new scenarios with the purpose to control dynamically the magnetic states. Along this line, as described in Chapter 6, we have considered the case where the strain is generated by the propagation of surface acoustic waves (SAW) [71]. Indeed, SAW devices that operate at high GHz frequencies are of prime interest for applications in communications applications [72]. This proposition is reinforced by recent studies that indicate that magnetic states can be dynamically changed at the SAW frequencies (MHz) [73, 74, 75]. In the work presented in Chapter 6, we describe our research on the effects that SAWs generate on magnetic devices consisting in multilayers exhibiting perpendicular magnetic anisotropy (PMA). Our choice of PMA magnetic devices is motivated by the fact that these materials are considered advantageous for their high-capacity and high density for nanomagnetic devices, such as STT-MRAMs memories [76, 77, 78]. Bearing this in mind, we selected to grow Pt/Co/Pt thin films with PMA on the surface of ferroelectric $LiNbO_3$ substrates. The use of $LiNbO_3$ is justified by its extensive use in the telecoms market, e.g. in mobile telephones and optical modulators, and it is indeed the material of choice for the manufacture of surface acoustic wave devices. As discussed in Chapter 6, the operating frequency of SAW devices is proportional to the substrate's acoustic wave velocity and inversely proportional to the spatial periodicity of the interdigital transducers (IDTs); the fabrication of GHz frequency devices thus requires the fabrication of IDTs with periods in the micron range.

In our research, we have used polar magneto-optical microscopy to access the magnetic properties of the individual Co/Pt microstructured devices, and to analyze the effects that SAW propagation has on the magnetization reversal process of these devices. Interestingly, we observed that SAW propagation can alter some magnetic properties and, in particular, the coercive field. Although certainly SAWs can induce spin precession effects on the magnetic overlayer, thus causing an alteration of the magnetic state, our detailed study suggests instead a prominent role of the propagation of heat associated to SAWs and to subsequent increase of temperatures that they carry with them.

A key aspect of our investigation has been the use of space- and time-resolved scanning thermal microscopy to analyze the propagation and spatial distribution of the heat generated by SAWs on the surface of $LiNbO_3$ crystals. Our study has revealed that the heat generated by SAWs is strongly directional and causes local temperature increases up to 10 K and above. We have tested the effects of heat dissipation in the Co/Pt structures induced by SAW pulses, showing that SAWs can be exploited to generate fast and local heating, which can be used to alter the magnetic properties of the devices. All in all, our work shows that beyond the control of magnetic states by strain, our approach provides interesting perspectives to control magnetic nanodevices using heat dissipation induced by SAWs.

1.6 Epilogue

Over the previous sections, the different topics covered in this Thesis have been briefly overviewed. In the next Chapter, before plunging into the detailed explanation of the research activities and outcomes, a description will be given of the experimental methodologies that have been exploited in this Thesis.

Chapter 2

Experimental Section

> *"I was led some time ago to think it very likely, that if a beam of plane-polarized light were reflected under proper conditions from the surface of intensely magnetized iron, it would have its plane of polarization turned through a sensible angle in the process of reflection."*
>
> John Kerr, Phil. Mag. 3 (1877) p.321

When polarized light interacts with a magnetic material, its polarization state can be modified as a function of the magnetization giving rise to the so-called magneto-optical effects (MO). The most relevant MO responses are the Faraday effect, in which the change of polarization state of the light occurs through the light transmitted (figure 2.1) and the Kerr effect (MOKE), in which the effects are caused in the reflected light (figure 2.1) [79].

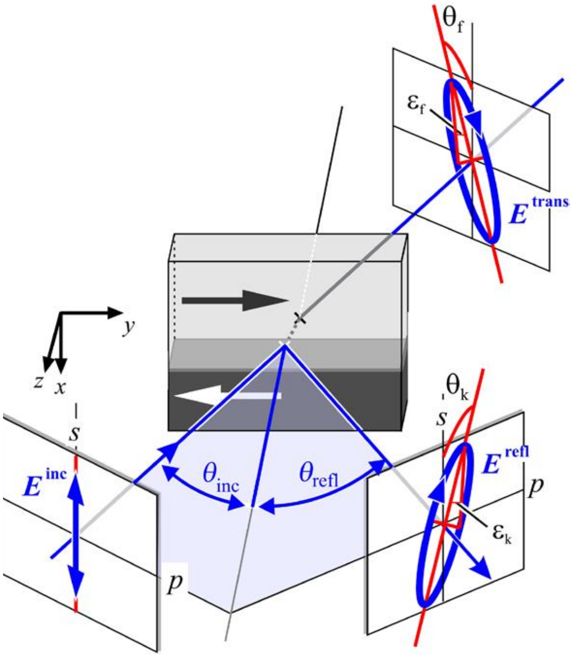

FIGURE 2.1: Magneto-optical effects scheme. Polarized light has changed its polarization state after being reflected or transmitted through a magnetic material. Extracted from [80].

For instance, in the case of MOKE, when s-polarized light is reflected from a magnetic material also p-polarized wave appears on the reflection, thus, the reflected light exhibits an elliptical polarization (figure 2.1). The changes on the polarization state can be depicted as a rotation of the polarization plane (Kerr rotation θ_K) and as a change of the polarization ellipticity (ellipticity ϵ_K). Analogously, the same angular magnitudes are defined for the Faraday effect.

Magneto-optics (MO) can be exploited in two different ways. On the one hand, the ability of magnetic materials to change the polarization of light is useful for sensing and optical telecommunications. That is why efforts are put on finding materials to enhance the magneto-optical activity. In the present thesis we have explored two ways into this field:

- The intrinsic contribution of polarons in manganites to the MO activity.

- The study of rare-earth incorporation into Yittrium Iron Garnet (YIG) and the consequences on its magnetic properties.

On the other hand, MO can be used as a probe for magnetism. We have used this capability to understand the role of strain-mediated responses (ferroelastic twin domains and surface acoustic waves) in the magnetic properties of thin films.

In the this Chapter, we describe the experimental strategies used in the present thesis to measure the MO activity of a magnetic sample and to resolve via imaging its magnetic domain configuration. In addition, the main techniques used to grow the studied materials are explained.

2.1 Magneto-optical spectroscopy

The MO spectroscopy is a technique that study the MO effects as a function of the photon energy. In the following, we will describe the physical origin of MO effects.

2.1.1 Magneto-optical effects

The optical properties of a material are originated from the interaction between light and matter. In particular, the electric field of the light exerts a force to the free and bound electrons in the solid. In a first approximation, this interaction between electrons and light can be described by a classical model, in which electrons are considered as classical oscillators. Using this picture, one can assume that the displacement of electrons generated by the electromagnetic waves creates dipoles in the material. How these dipoles are created is governed by the dielectric permittivity ϵ of the material that is a complex magnitude. Figure 2.2 shows schematically a typical spectral response of the dielectric permittivity. The resonances in the spectra are associated to the different vibrational modes of the material structure which, at optical frequencies, are coupled to electronic vibrational modes.

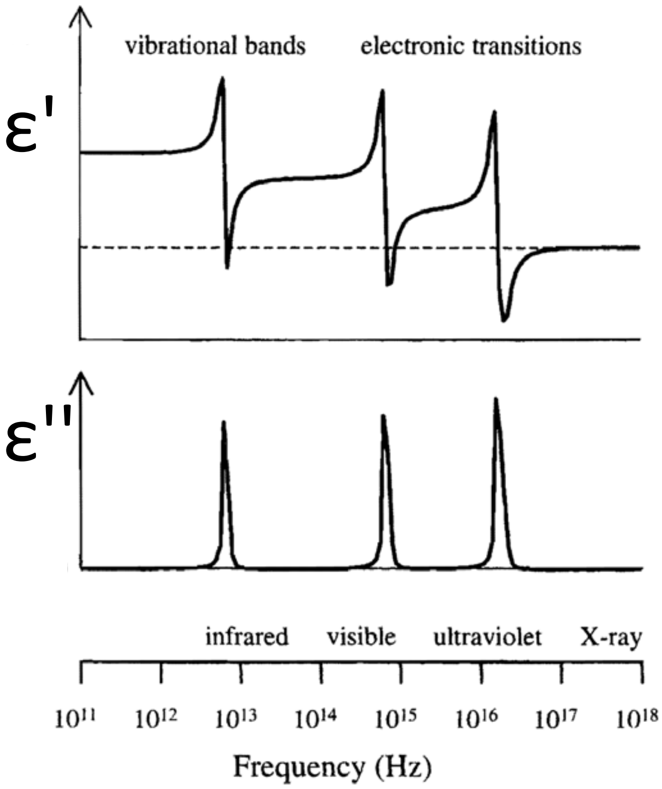

FIGURE 2.2: Schematics of the spectral response of the dielectric permittivity. Adapted from [81].

Two main contributions related to light interaction with bound and free electrons are necessary to model the permittivity response:

- A Lorentz term that describes the electronic transitions between two energy levels induced by the absorption of a photon (figure 2.3 a): $\epsilon = \frac{A}{\omega^2 - \omega_0^2 + i\gamma\omega}$; where A is the probability of the absorption, ω is the photon energy, ω_0 the energy between the levels and γ the sharpness of the absorption related to the lifetime of the electronic states.

- A Drude term that describes the absorption of photons by free electrons ($\omega_0 = 0$, figure 2.3 b).

Under an applied magnetic field, the permittivity will be affected by the Lorentz force acting on the electronic motion. Therefore, the propagation of electromagnetic waves (governed by the permittivity) will be changed.

Considering this simple model we can write the Maxwell's equations to describe the electromagnetic wave propagation in a magnetic material. We obtain the general form for the permittivity tensor ϵ_{ij}, that for a magnetized material with negligible

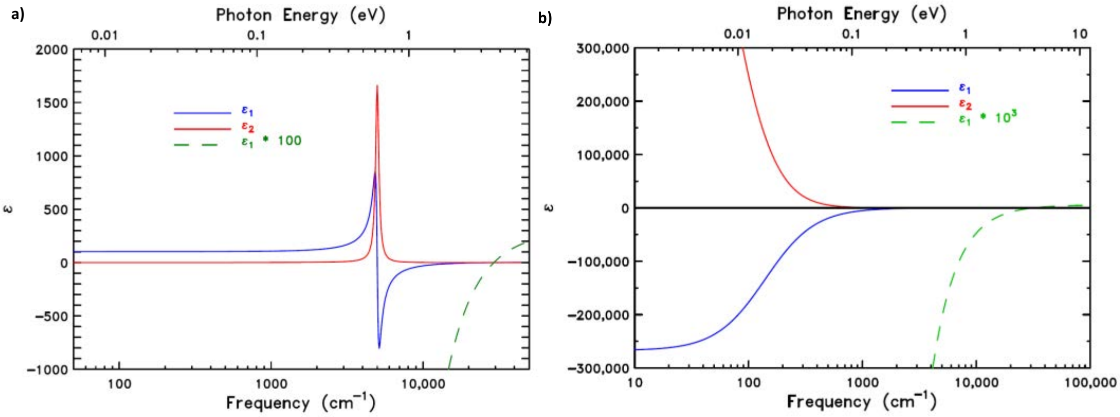

FIGURE 2.3: Real ϵ_1 and imaginary ϵ_2 permittivity response of (a) the Lorentz term and (b) the Drude term. Extracted from [82].

losses can be written as following:

$$\widehat{\epsilon}_{ij} = \begin{pmatrix} \epsilon'_{xx} & \epsilon'_{xy} + ig''_z & \epsilon'_{xz} - ig''_y \\ \epsilon'_{xy} - ig''_z & \epsilon'_{yy} & \epsilon'_{yz} + ig''_x \\ \epsilon'_{xz} + ig''_y & \epsilon'_{yz} - ig''_x & \epsilon'_{zz} \end{pmatrix} \tag{2.1}$$

where $g_x\prime\prime$, $g_y\prime\prime$ and $g_z\prime\prime$ are the gyration components, which are odd as a function of the magnetic field ($g''_i(H) = -g''_i(-H)$) and $\epsilon_{ij}\prime$ is the real permittivity components, which are even as a function of the field. In general, this dielectric tensor can be decomposed into symmetric and antisymmetric parts. The normal modes of the symmetric tensor are linearly polarized light which does not give rise to MO effects. The off-diagonal components (antisymmetric parts) produce the difference in the refractive indexes between the two circularly polarized modes originating the MO effects. In general $\widehat{\epsilon}_{ij}$ can be expanded in terms of the magnetization components:

$$\widehat{\epsilon}_{ij} = \epsilon^0_{ij} + K_{ijk}M_k + G_{ijkl}M_kM_l + ... \tag{2.2}$$

where ϵ^0_{ij} are the components at zero magnetization, K_{ijk} the third rank magneto-optical tensor that describes the linear dependence on the magnetization and the G_{ijkl} is the fourth rank tensor describing the quadratic dependence on the magnetization. Usually, the measured MO signal has a linear dependence on the magnetization because linear terms K_{ijk} use to be larger than the quadratic ones G_{ijkl}.

It is known that the MO response is strongly dependent on the material and, for a given material, on the wavelength. This is not surprising, since the photon absorption at a given material depends on the electronic transitions. The largest contribution to the absorption is given by the so-called electric-dipole approximation allowing electric-dipole transitions that comply with selection rules [79]. The most relevant energy scales to the analysis of the light induced electronic transitions is described briefly in the following. In the first place, spin-orbit interaction originates the energy splitting that allow different electronic transitions for left and circular polarized light and thus, creating a difference in absorption for both polarizations. However, the Heisenberg exchange and Zeeman interaction are needed to generate a difference in absorption between spin up and down or under a magnetic field. In the figure 2.4 a simple transition diagram is shown with the aforementioned energy splittings giving rise to a difference in the spectrum between spin up and down.

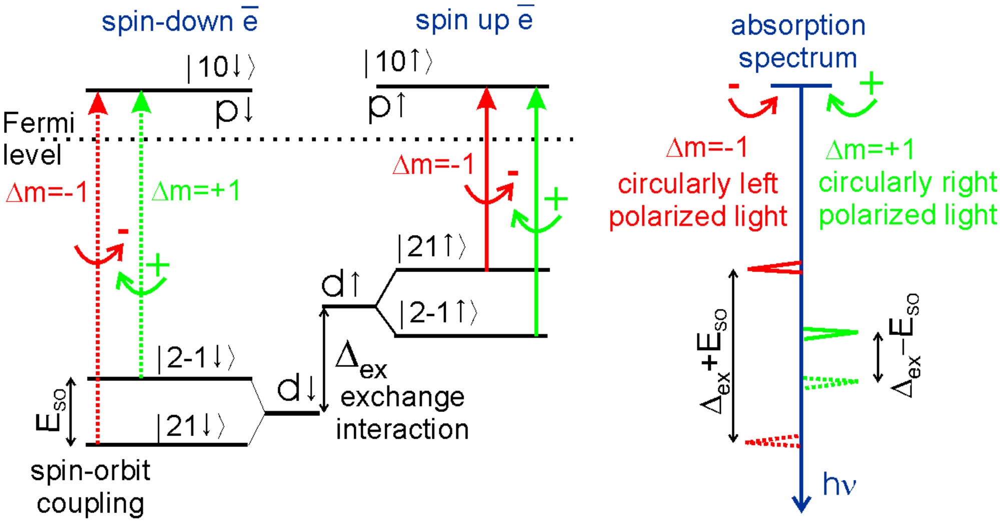

FIGURE 2.4: Transitions scheme for MOKE. The spin-orbit coupling and the exchange interaction are the origin of the main energy splitting that give rise to a different absorption for left and right circularly polarized light. Courtesy of Dr. Jaroslav Hamrle.

All materials, even those without any magnetic order, can display MO effects, but the specific MO response per unit of optical path is very weak, unless the material has a magnetic order with net magnetization. MO effects, generally observed by changes in the polarization state of light, can be measured in different optical configurations. One particular case is when light is transmitted through a sample; in this case we talk about the Faraday effect when the wavevector of light is parallel to the magnetization ($\kappa \parallel H$) or the Voigt or Cotton-Mouton effect if they are normal to each other ($\kappa \perp H$). On the other hand, when the magneto-optical effects are measured by measuring the changes in the reflected light we talk about magneto-optical Kerr effects (MOKE). Usually, MOKE is very convenient to study ferromagnets because most of them are metals, hence, almost all the light is reflected making very difficult to measure MO effects in transmission. In the following, we give a more detailed description of MOKE.

2.1.2 Magneto-optical Kerr effect (MOKE)

In reflection, the polarization state is defined respect to the plane of incidence of the light. With this reference, two orthogonal linearly polarized states can be taken as the basis to define the polarization of light, whose components are: $s-$polarized, which is the component perpendicular to the plane of incidence and $p-$polarized, with the component contained in the plane of incidence. The components of an arbitrary polarized light are (E_s^i, E_p^i) for incident light and (E_s^r, E_p^r) for the reflection in the (s,p) basis. Thus, all the optical effects in reflection can be modeled by the Jones matrix formalism with the reflection matrix:

$$R = \begin{pmatrix} r_{ss} & r_{ps} \\ r_{sp} & r_{pp} \end{pmatrix} \tag{2.3}$$

Where $r_{ss} = \frac{E_s^r}{E_s^i}$ and $r_{pp} = \frac{E_p^r}{E_p^i}$ describe the intensity and phase changes for a certain polarization. The off-diagonal terms $r_{sp} = \frac{E_s^r}{E_p^i}$ and $r_{ps} = \frac{E_p^r}{E_s^i}$ describe the ratio of the polarization conversion from s to p and from p to s respectively and quantify the MO response of a material. Therefore, for a small angles, the complex Kerr angle $\theta + i\epsilon$ for s and p polarized light is defined as:

$$\begin{aligned} \theta_s + i\epsilon_s &= \frac{r_{sp}}{r_{ss}} \\ \theta_p + i\epsilon_p &= -\frac{r_{ps}}{r_{pp}} \end{aligned} \tag{2.4}$$

Three main geometries are distinguished with respect to the angle between the plane of incidence and the magnetic field (or magnetization). These geometries are called: polar, longitudinal and transverse (figure 2.5).

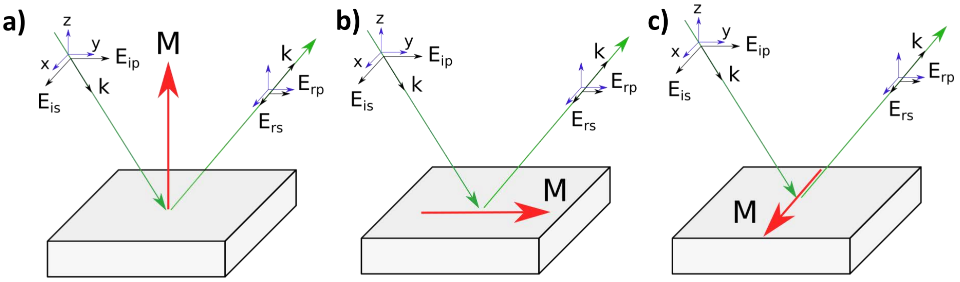

FIGURE 2.5: MOKE geometrical configurations, a) Polar, b) Longitudinal and c) Transverse.

In the polar configuration the complex Kerr angle is sensitive to the out of plane magnetization component. Generally, near normal incidence is needed to avoid any in-plane projection of the propagation vector k giving also sensitivity to the in-plane components. For the longitudinal configuration, an angle of incidence is needed to give sensitivity to the in-plane magnetization components. In the case of transverse configuration, there is no projection of k on the magnetization. This case is sensitive to the in-plane component but, unlike the previous configurations that measure the complex Kerr angle, a change of p-polarized light intensity is measured in the transverse configuration. Therefore, in this case, the observable is a change of the r_{pp} coefficient (Δr_{pp}).

2.1.3 Experimental approach for MOKE measurements

The Kerr angles are usually in the order of $\sim$mrad. For this small signal amplitudes, the sensitivity of light detectors and the responses of optical elements become very important. In order to decrease the signal-to-noise ratio, modulation techniques are required for a clear improvement of the Kerr detection [83]. In the case of magneto-optics, three magnitudes can be modulated: magnetic field, light intensity and light polarization (phase modulation). The most successful technique in terms of Kerr resolution is the phase modulation of the light. One of the important arguments is that the phase of light can be modulated at higher frequencies than magnetic field or light intensity using for example a conventional optical chopper. Another advantage is that both real θ and imaginary ϵ Kerr angles can be measured independently. For these previous reasons, our selected experimental method has been the phase modulation.

In order to realize phase modulation, a photo-elastic modulator (PEM) device is needed. The PEM is composed by a birefringent slab of quartz coupled to a piezoelectric that via strain, introduces a retardation phase between the two orthogonal light components respect to the optical axis of the PEM's birefringent crystal. The retardation is modulated between $+\varphi$ and $-\varphi$ at 50 kHz. As an example, if the retardation is $\varphi = \pi/2$, the light after the PEM will change its polarization state between left circular polarized to right circular polarized through all the intermediate elliptical and linear states (figure 2.6).

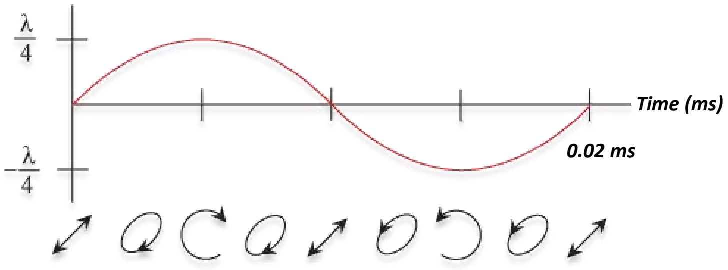

FIGURE 2.6: Polarization state of the light modulated by the PEM for 0.5λ retardation. Adapted from Hind's Instruments ©.

PEM can be modeled using the Jones matrix formalism as following where $\varphi = \varphi_0 \sin(\omega t)$ and φ_0 is the maximum retardation:

$$PEM = \begin{pmatrix} e^{i\frac{\varphi}{2}} & 0 \\ 0 & e^{-i\frac{\varphi}{2}} \end{pmatrix} \tag{2.5}$$

In the following, with the help of the Jones matrix formalism, we will describe the details of the experimental instrumentation needed to measure the MOKE effects in the three aforementioned optical configurations, namely, polar (PMOKE), transverse (TMOKE) and longitudinal (LMOKE).

Polar Magneto-optical Kerr effect (PMOKE)

The experimental setup to measure PMOKE is shown in the figure 2.7. Other optical arrangements can be considered but always guaranteeing near normal incidence and out of plane magnetic field. In our case, monochromatic light is generated using a Xenon lamp and a monochromator. The monochromatic light is polarized at $P = 45^{o}$ respect to the PEM's optical axis in order to have equal orthogonal components before being modulated by the PEM. Up to this point, all these optical elements will have the same configuration for all the Kerr geometries. In this setup, a beam splitter and a mirror are needed to give an accurate normal incidence parallel to the applied magnetic field. The reflected light is detected using an analyzer (polarizer) and a photomultiplier tube (PMT). Although part of the light intensity is lost through the beam splitter and the mirror can also introduce non desired signals [84], these detrimental effects can be corrected properly and signals down to $\sim$ μrad can be resolved.

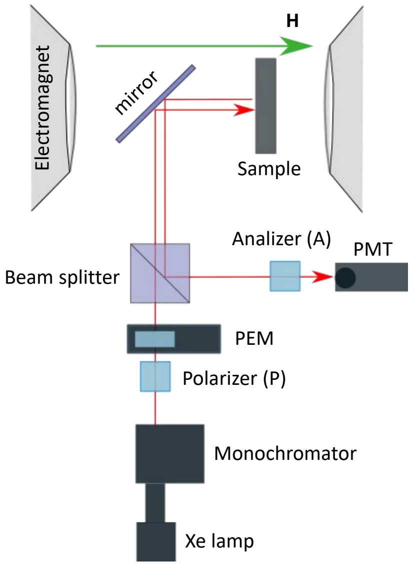

FIGURE 2.7: PMOKE configuration scheme.

The detected signal in the PMT can be calculated using Jones matrix formalism The simplest system can be modeled taking into account the Polarizer (P), the PEM, the sample (reflection matrix) and the analyzer (A). The reflection matrix has been rewritten substituting 2.4 into 2.3. Thus, the polarization state of the reflected light (E_x^r, E_y^r) (before the analyzer) is given by:

$$\begin{pmatrix} E_x^r \\ E_y^r \end{pmatrix} = \begin{pmatrix} 1 & -r_{pp}(\theta_p + i\epsilon_p) \\ r_{ss}(\theta_s + i\epsilon_s) & 1 \end{pmatrix} \begin{pmatrix} e^{i\varphi/2} & 0 \\ 0 & e^{-i\varphi/2} \end{pmatrix} \begin{pmatrix} \cos(P) \\ \sin(P) \end{pmatrix} \tag{2.6}$$

where P is the angle of the polarizer set at 45°. The intensity at the detector is given by conjugate product of the Jones matrix $J_{xy} = (E_x^r, E_y^r)$:

$$I_{s,p} = J_{xy} J_{xy}^* \tag{2.7}$$

Multiplying the matrix, the intensity (without analyzer) can be decomposed as the sum of the s and p components $I_{sp} = I_s + I_p$. Experimentally, both components can be measured individually setting the analyzer at $A = 0^\text{o}$ for I_s and $A = 90^\text{o}$ for I_p:

$$I_s = \frac{1}{2} |r_{ss}|^2 [1 + 2\theta_s \cos(\varphi) + 2\epsilon_s \sin(\varphi)] + I_s(\theta_s^2, \epsilon_s^2) \tag{2.8}$$

$$I_p = \frac{1}{2} |r_{pp}|^2 [1 - 2\theta_p \cos(\varphi) + 2\epsilon_p \sin(\varphi)] + I_p(\theta_p^2, \epsilon_p^2) \tag{2.9}$$

Where $I_s(\theta_s^2, \epsilon_s^2)$ and $I_p(\theta_p^2, \epsilon_p^2)$ are neglected quadratic Kerr terms. Using the Jacob expansion by the first kind Bessel functions J_n:

$$\begin{aligned} \sin(\varphi_0 \sin(\omega t)) &= 2 \sum_{n=1}^{\infty} J_{2n-1}(\varphi_0) \sin[(2n-1)\omega t] \\ &\approx 2J_1(\varphi_0)\sin(\omega t) + 2J_3(\varphi_0)\sin(3\omega t) + \dots \end{aligned} \tag{2.10}$$

$$\begin{aligned} \cos(\varphi_0 \sin(\omega t)) &= J_0(\varphi_0) + 2 \sum_{n=1}^{\infty} J_{2n}(\varphi_0) \cos[(2n)\omega t] \\ &\approx J_0(\varphi_0) + 2J_2(\varphi_0)\cos(2\omega t) + \dots \end{aligned} \tag{2.11}$$

We can rewrite the equation in terms of ω and 2ω (neglecting the 3th harmonic) as following:

$$\begin{aligned} I_s &= \frac{1}{2} r_{ss}^2 + J_0(\varphi_0) r_{ss}^2 \theta_s + 2J_1(\varphi_0) r_{ss}^2 \epsilon_s \sin(\omega t) + 2J_2(\varphi_0) r_{ss}^2 \theta_s \cos(2\omega t) \\ I_p &= \frac{1}{2} r_{pp}^2 - J_0(\varphi_0) r_{pp}^2 \theta_p + 2J_1(\varphi_0) r_{pp}^2 \epsilon_p \sin(\omega t) - 2J_2(\varphi_0) r_{pp}^2 \theta_p \cos(2\omega t) \end{aligned} \tag{2.12}$$

The modulated terms ω and 2ω can be measured independently using a lock-in amplifier that gives the root mean square (RMS) value of the amplitude. Then, the measured amplitude will be normalized by the non-modulated term that can be measured by a dc voltmeter. However, the non-modulated term depends also on the Kerr rotation $\theta_{s,p}$ unless $J_0(\varphi_0) = 0$ [85]. The first kind zero order Bessel's function is zero at $\varphi_0 = 2.405$

rad, corresponding to a retardation of 0.383λ. Thus, the polarization as a function of time after the PEM settled at 0.383λ is schematically represented in the figure 2.8.

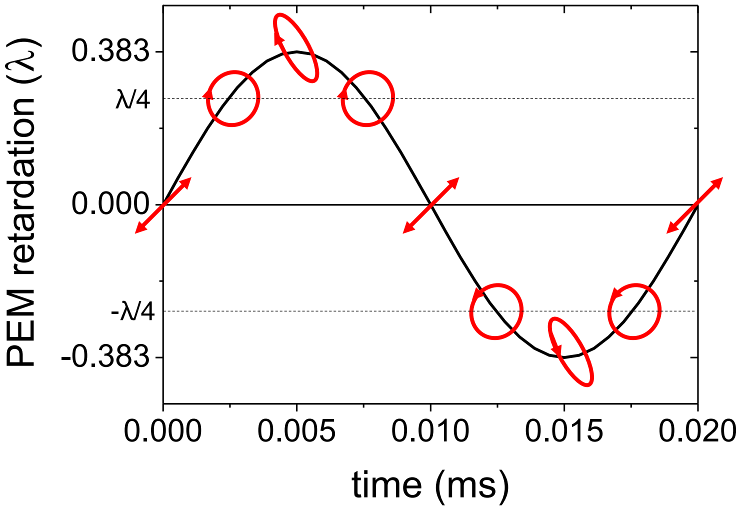

FIGURE 2.8: Polarization state of the light modulated by the PEM for 0.383λ retardation as a function of time.

In order to give a graphical view of these equations, we simulated the intensity I_p of the system 2.6 given by the expression 2.7 changing the Kerr ellipticity from -1 to +1 mrad and keeping the rotation constant at 1 mrad and oppositely. The intensity as a function of the time for the Kerr ellipticity and rotation variation is plotted in the figure 2.9 a) and b) respectively. Applying the Fourier transform, notice that only the odd (1st, 3rd) harmonic changes when changing the ellipticity (figure c) 2.9) and only even harmonic (2nd, 4th) changes when the rotation changes (figure d) 2.9). This is a graphical proof that the rotation θ and the ellipticity ϵ can be measured from the 1st and 2nd harmonics in the lock-in detection.

We consider I_ω and $I_{2\omega}$ as the terms modulated by $\sin(\omega)$ and $\cos(2\omega)$ respectively and I_{dc} are the non-modulated terms. Thus, the Kerr rotation and ellipticity are given by:

$$\begin{aligned} \epsilon_s &= \frac{1}{4kJ_1(\varphi_0)}\frac{I_{\omega,s}}{I_{dc,s}}, \quad \epsilon_p = \frac{1}{4kJ_1(\varphi_0)}\frac{I_{\omega,p}}{I_{dc,p}} \\ \theta_s &= \frac{1}{4kJ_2(\varphi_0)}\frac{I_{2\omega,s}}{I_{dc,s}}, \quad \theta_p = -\frac{1}{4kJ_2(\varphi_0)}\frac{I_{2\omega,p}}{I_{dc,p}} \end{aligned} \tag{2.13}$$

Where k is an added calibration constant which is obtained experimentally by changing the smallest possible angle in the analyzer (typically > 5 μrad) and measuring the respective change of intensity, therefore, the constant has units of rad^{-1}.

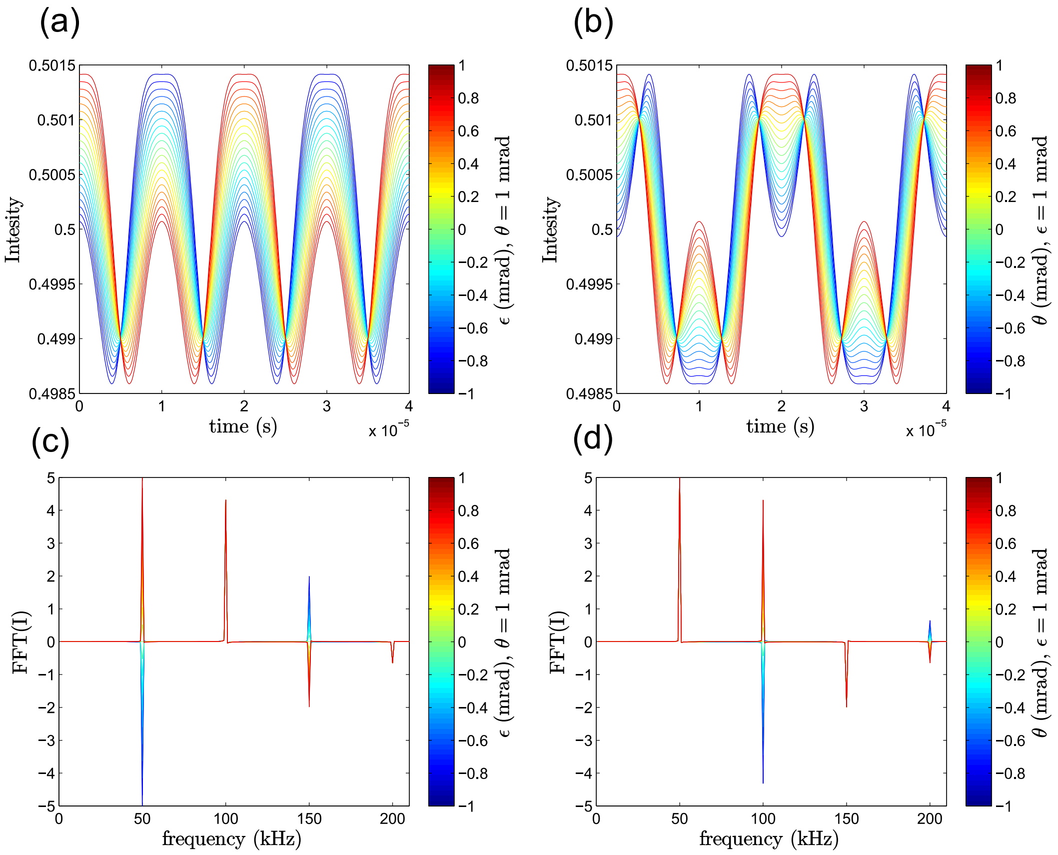

FIGURE 2.9: (a) and (b) show the light intensity measured by the PMT when varying the ellipticity and keeping constant the rotation and oppositely. (c) and (d) show the fast Fourier transform of (a) and (b) respectively. Notice that even harmonics exhibit changes for a pure change of ellipticity and odd harmonics changes for a pure change of rotation.

Transverse Magneto-optical Kerr effect (TMOKE)

The complex Kerr effect is defined as the change of the coefficient r_{pp} under a magnetic field, thus $\Delta r_{pp}(M) = r_{pp}(M) - r_{pp}(0)$. The real and imaginary part are related to small perturbations of the ellipsometric angles ψ and Δ. Taking into account the complex reflectance ratio $\frac{r_{pp}}{r_{pp}} = \tan(\psi)\exp(i\Delta)$ and assuming by symmetry reasons that r_{ss} does not change under magnetic field, the complex transverse Kerr can be written as [86]:

$$\frac{\Delta r_{pp}(M)}{r_{pp}} = \frac{2}{\tan(2\psi)}\delta\psi + i\delta\Delta \tag{2.14}$$

The usual experimental setup [86] is shown in the figure 2.10 where the magnetic field is applied in the plane of the sample and perpendicular to the plane of incidence of the light. The system can be solved using Jones matrix formalism as previous configurations but now adding a quarter wave-plate as a compensator set to $\pm 45^{\circ}$. Following

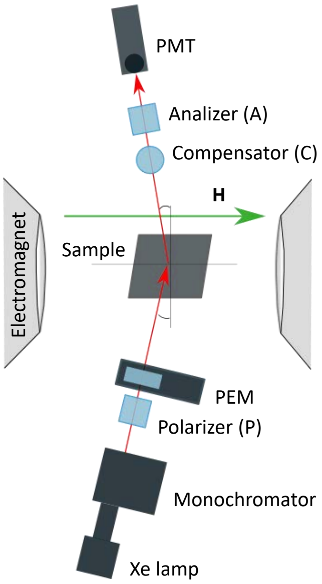

FIGURE 2.10: TMOKE configuration scheme.

similar steps than previously, the intensity measured at the PMT is given by [86]:

$$\frac{I_\omega}{I_0} = (\pm)_C(\pm)_A \sin(2\psi)\Im(\frac{\Delta r_{pp}}{r_{pp}}) + \sin(2\psi)(\theta_s - \theta_p)\sin(\Delta) - (\epsilon_s + \epsilon_p)\cos(\Delta)$$
$$\frac{I_{2\omega}}{I_0} = (\pm)_C(\pm)_P(\pm)_A \sin(2\psi)\Re(\frac{\Delta r_{pp}}{r_{pp}}) + (\mp)_P \sin(2\psi)(\theta_s + \theta_p)\cos(\Delta) + (\epsilon_s - \epsilon_p)\sin(\Delta) \tag{2.15}$$

Where $\Re(\frac{\Delta r_{pp}}{r_{pp}})$ and $\Im(\frac{\Delta r_{pp}}{r_{pp}})$ are the real and imaginary parts of the transverse effect. In order to measure purely the transverse effect, two angles of the analyzer are needed for a fixed angle of the compensator and the polarizer [110, 86].

Longitudinal Magneto-optical Kerr effect (LMOKE)

In the longitudinal configuration an angle of incidence is needed to probe the in-plane magnetization. The plane of incidence of the light contains the applied magnetic field. The figure 2.11 shows the experimental configuration. It is modeled as previously giving rise to the Kerr rotation and ellipticity expressions 2.13. Usually this configuration is used to resolve the angular dependence of the in-plane magnetization.

2.2 Magneto-optical imaging

Magneto-optical imaging exploits the MO activity of the materials to map their magnetization over the space. This technique is useful to resolve the magnetic domain structure and its dependence with applied magnetic fields. There are two main kind of Kerr effect microscopes:

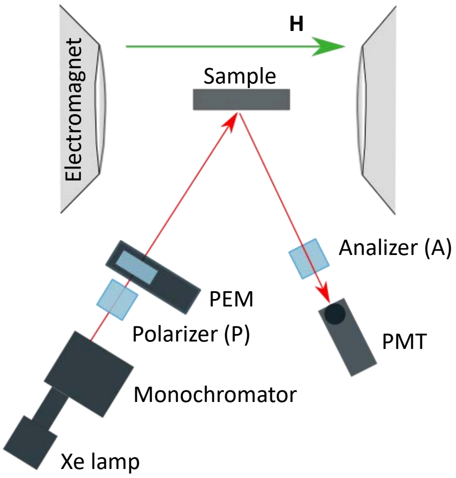

FIGURE 2.11: LMOKE configuration scheme.

- Polarized optical microscopy. The structure of the microscope is mainly a confocal optical microscope but with a polarizer after the light source and an analyzer before the CCD camera (see figure 2.12).
- Scanning optical polarized microscopy [87]: The light is focused at the diffraction limit and scans the sample's surface using a piezoelectric system. Phase modulation techniques can be used in this setup.

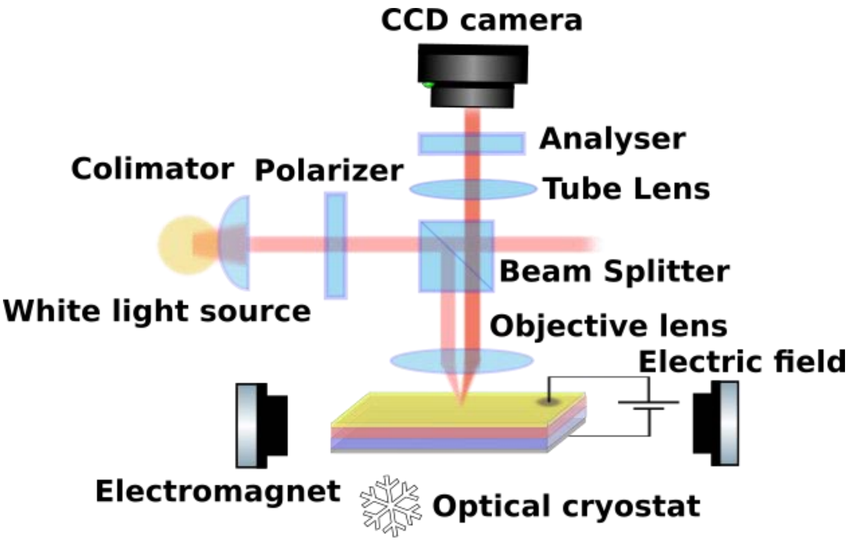

FIGURE 2.12: Experimental setup scheme of a Kerr microscope.

Usually the most common setup is the polarized optical microscopy because the image acquisition times are faster than the scanning one. However, phase modulation techniques can not be implemented unless each pixel of the camera has a lock-in amplifier. Therefore, the scanning setup can give more sensitivity and resolution. In order to increase the sensitivity in the CCD camera setup, in general, a background is generated at the magnetic saturation state (where no domains are present). Hence, the magnetic domain pattern can be modified each time that a new background is needed. We have compared both imaging techniques in our lab by mapping out the MO response of a sample with perpendicular magnetic anisotropy (PMA). More specifically, the test sample was a $(\mathrm{Pt/Co})_{n=15}$ multilayer, in which the MO response was measured in PMOKE configuration (because of its PMA). Figure 2.13 shows the magnetic domain pattern of the $(\mathrm{Pt/Co})_{n=15}$ multilayer measured at remanence using the two approaches outlined above, a CCD camera (2.13 a) and scanning with PEM (2.13 b) where the inset show the out of plane contrast convention. The image (b) takes several minutes to be acquired due to the integration time in the lock-in amplifier limited by the modulation frequency of the PEM.

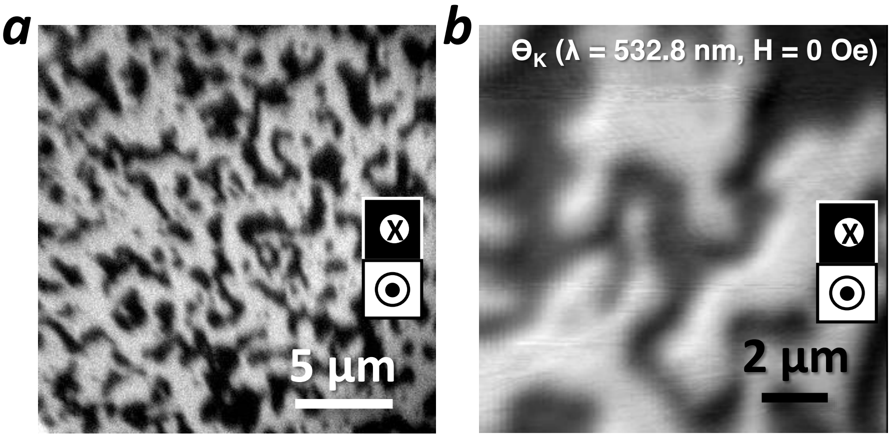

FIGURE 2.13: Out-of-plane magnetic domains of $(\mathrm{Pt/Co})_{n=15}$ multilayer measured by a polarized light microscope (a) and by scanning polarized microscope (b) in the PMOKE configuration.

Different strategies are used to maximize the MO contrast [80]:

- Köhler illumination is used for an homogeneous illumination of the field of view.
- White light is commonly used for imaging, in order to maximize the total MO effects in the case of a polarized light microscope. By contrast, monochromatic light is a requirement for phase modulation techniques.
- The analyzer position. The maximum contrast is reached near the extinction condition, meaning that the polarizer and analyzer are almost crossed.
- The angle of incidence (for longitudinal and transverse-like). The larger angle, the larger contrast but it is limited by the numerical aperture of the objective.
- The camera system is also important, since it can limit the resolution and it has a significant contribution on the signal-to-noise ratio. Typically the MO suitable CCD have a bit depth of 12-16 bit, a maximum quantum efficiency above 70% and a cooler system for the sensor chip.

- Digital image processing is a key point for improving the contrast and suppress background effects. Usually, a background image taken at the saturation state of the material is subtracted from the as-taken images in order to enhance the MO contrast.

2.2.1 Geometric configurations in the optical illumination for imaging

In order to resolve the magnetic domain structure and its dependence on the applied magnetic field, it is convenient to map out the MO response using more than one optical configuration to obtain the magnetization projections along different orientations. In general, all the possible configurations, i.e., polar, longitudinal and transverse-like are needed for that purpose. Figure 2.14 shows the domain configuration and its contrast depending on the effective plane of incidence. The alignment of the light source on the rear aperture plane of the objective defines the effective plane of incidence. To do so, a mobile Köhler illumination has been mounted on the experimental setup (shown in the figure 2.15). Polar configuration (figure 2.14 a) is sensitive to the out of plane magnetization component and the light source is placed in the middle of the objective aperture reaching normal incidence. Longitudinal (figure 2.14 b) and transverse-like (figure 2.14 c) configurations are sensitive to the longitudinal and transverse components of the magnetization. In both configurations the plane of incidence is created placing the light source in one side of the objective plane. In this section, transverse configuration is called transverse-like to differentiate from TMOKE because it measures a change of Δr_{pp} and transverse-like imaging configuration measures the transverse component of the magnetization. In Both cases the plane of incidence of light is perpendicular to the applied magnetic field.

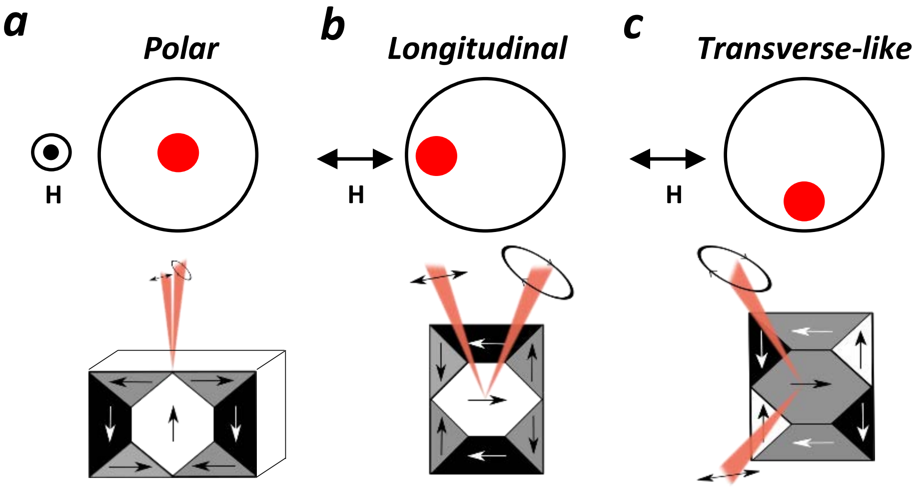

FIGURE 2.14: Kerr microscopy configuration vs domains contrast, (a) Polar, (b) Longitudinal, (c) Transverse.

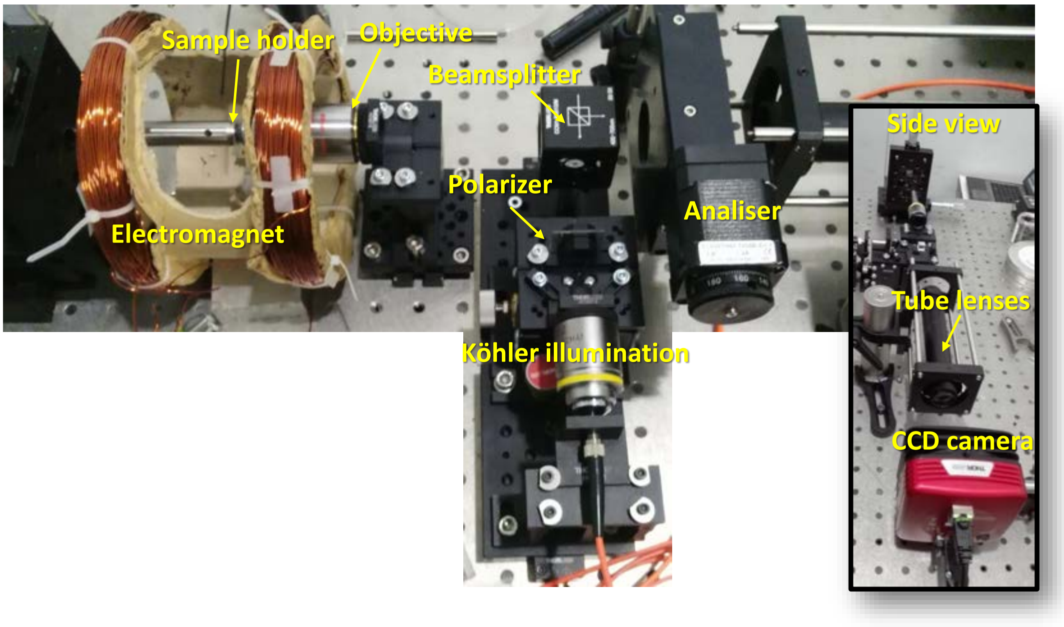

FIGURE 2.15: Experimental setup of a lab-made Kerr microscope. A mobile stage has been mounted on the Köhler illumination in order to create an effective plane of incidence.

2.3 X-ray magnetic circular dichroism (XMCD)

Analogous to magnetic circular dichroism (MCD) due to magneto-optical effects, XMCD is the difference in absorption between left and right circular polarized x-ray light. The magnetic response in the x-ray region of the spectra becomes very relevant for a fundamental understanding of the materials properties. Since photons in the x-ray region are more energetic than in the visible, deeper electronic levels (from the core electrons) can be excited. Generally, the initial and final states of these transitions are pure atomic states, that gives the element specificity and gives information of the valence state, the spin moment and orbital moment. Synchrotron light source is needed in order to generate light with enough energy to excite M, L, and K edges, typically in the 80-4000 eV range. These core level transitions are illustrated in the figure 2.16 (a) for the case of $2p$-$3d$ excitation of Fe as an example of $3d$ transition metals [88, 89]. The Fe $2p$ level is split, due to the spin-orbit interaction, into a more bound $(l + s)$ $2p_{3/2}$ and a less bound $(l - s)$ $2p_{1/2}$ state excitation. The $2p_{3/2}$ $(2p_{1/2})$ transition is also called L_3 (L_2) edge respectively. Opposite spin polarization of the edges gives more absorption of positive helicity for spin down and vice versa. The related change in the absorption called X-ray absorption spectroscopy (XAS) is shown in the figure 2.16 (b) for left and right circular polarized light (black and red curves). Thus, the XMCD (figure 2.16 c) is the difference between both absorptions. Notice that XMCD gives information of the magnetization state, for instance, no XMCD signal can be observed for a demagnetized state or for an antiferromagnet. Taking into account the XMCD sum rules the orbital m_o and spin moment m_s can be derived [90, 91]. Similarly to the Kerr effects, the angle of incidence of the x-ray beam gives the optimal signals when is aligned to the magnetic moment.

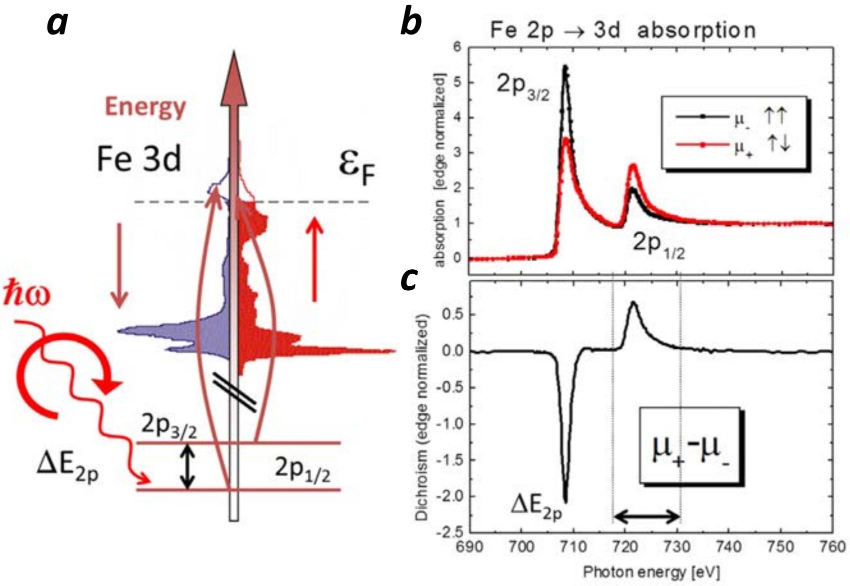

FIGURE 2.16: XMCD for Fe, (a) $2p$-$3d$ excitation scheme, (b) XAS for left and right circular polarized light (black and red curves), (c) XMCD. Extracted from [92].

2.4 Growth techniques: PLD and Sputtering

Thin films are made by depositing atoms onto a substrate. Their properties depends on different features such as composition (stoichiometry), structure, thickness and strain state. In order to reach the desired properties, accurate growth methods are needed. Even though same material can be grown with different techniques, generally each technique has specific advantages and disadvantages making it unique and appropriate for certain objectives [93]. In this thesis, magnetic materials, specifically, magnetic oxides and ferromagnetic metals are on the main focus. Common techniques to grow such materials are pulsed laser deposition (PLD) and magnetron sputtering (rf, dc). These physical growth methods allow easily to change the growing conditions and the deposited thickness with very high accuracy. In order to give a general view of how these techniques works, we describe it briefly:

PLD is a vapor deposition technique [93], that uses high-power pulsed laser radiation to vaporize the material of the target. Since most nonmetallic materials have strong absorption in the ultraviolet spectral range, the used beam is a gas excimer of KrF with $\lambda = 248$ nm. The absorbed energy is converted into thermal, chemical, and mechanical energy, causing electronic excitation of the target atoms, ablation of the surface and plasma formation. The vapor form a plume above the target and its contents are propelled to the substrate where they condense and form a film. Usually, gases, such as N_2 or O_2 are introduced in the deposition chamber in order to maintain the desired stoichiometry. An sketch of the PLD system is shown in the figure 2.17. PLD technique has been used in this thesis for the growth of $La_{2/3}Ca_{1/3}MnO_3$ (chapter 3), $Y_3Fe_5O_{12}$ and $CeY_2Fe_5O_{12}$ (chapter 4) thin films.

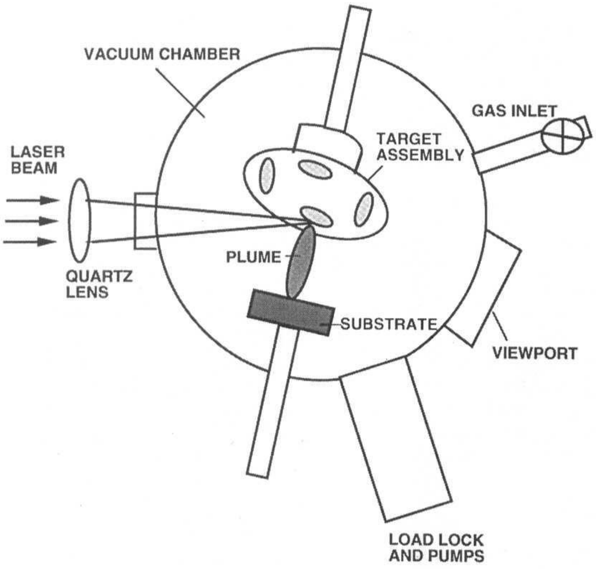

FIGURE 2.17: PLD setup scheme. Extracted from [93].

Magnetron sputtering is also a vapor deposition technique [93] but instead of a laser radiation, it uses Ar plasma to eject material from the target. An electric field is applied between the target and the substrate, a small amount of argon gas is introduced to the deposition chamber. The electric field ionize the argon atoms, accelerating them toward the negatively charged target. The resulting collision leads to the ejection of atoms and electrons from the target. Part of the ejected atoms are deposited on the substrate, building up the film. The emitted electrons are confined close to the surface by a magnetic field generated by an array of magnets beneath the target. This confinement increases the ionization rate of argon atoms and therefore increases the deposition rate. Magnetron sputtering is a conventional technique to grow metallic thin films. In the present thesis it has been used for the growth of $Co_{40}Fe_{40}B_{20}$, ultrathin Co/Pt thin films (chapter 5). However, it can be also used to grow insulator materials, for that purpose, a radio frequency source is needed in order to avoid charging effects on the target and on the substrate. This rf technique has been used for the growth of $La_{2/3}Ca_{1/3}MnO_3$ thin films (chapter 3).

The samples used in this thesis have been grown on the thin films scientific service at ICMAB in collaboration with Professor Florencio Sánchez. Thin films of $Co_{40}Fe_{40}B_{20}$

have been grown in collaboration with Prof. Sebastiaan van Dijken (Nanospin group) in Aalto University, Finland.

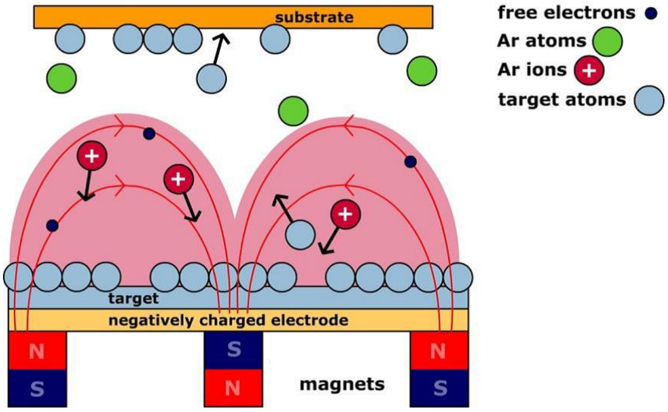

FIGURE 2.18: Magnetron sputtering working principle. Extracted from ©polifab, Politecnico di Milano.

2.5 Dielectric/Polarization characterization

Ferroelectricity is a phenomenon that takes place in materials that present the capability to display switchable spontaneous polarization. This switchable polarization is concomitant to the presence of ferroelectric domains with opposite sign which exhibit a hysteretic behaviour under electric field (figure 2.19 a). First, saturation polarization (P_s) is achieved after applying a large electric field. After zeroing the external field, the polarization decreases to the remanence (P_r), or remanent polarization. The electric field required to change the polarization sign is called the electric coercive field (E_c).

The most suitable method to measure the ferroelectric hysteresis is the I(V) characterization, which provide an abrupt current peak where the ferroelectric switching (switching between P^+ and P^- at coercive field) occurs, and allows to easily disclose the extrinsic ferroelectric effects. A typical I(V) loop for a ferroelectric is shown in the figure 2.19 (b). In order to obtain the polarization derived from the I(V) response, first, charge is obtained integrating the current through the time. Thus, modeling the measured dielectric material as plano-parallel capacitor with known geometry (area A, and thickness d), the polarization and electric field can be obtained by computing the charge per unit surface ($P = \frac{1}{A} \int I(t)dt$), and the electric field is obtained by dividing the applied voltage (V) by the thickness of the measured sample ($E = V/d$). We should stress that the polarization response can be affected by non-remanent polarization extrinsic to the measured ferroelectric material, such as, parasitic resistances or linear capacitances. In the following we describe an additional experimental method that suppresses all these non-desired effects.

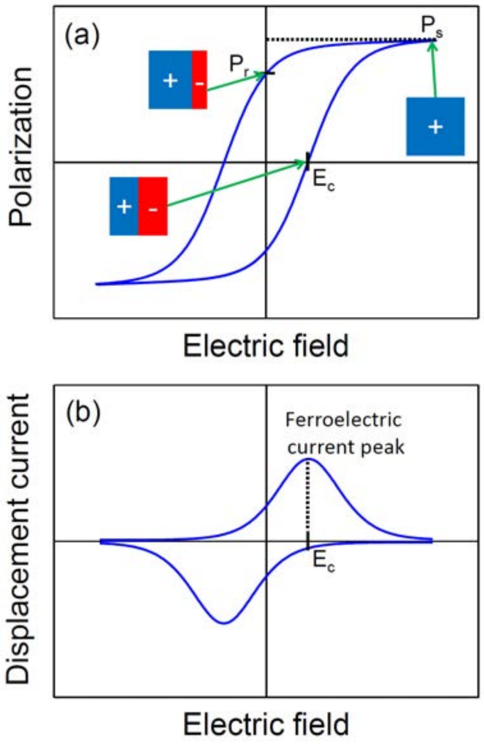

FIGURE 2.19: (a) P(E) loop for a standard ferroelectric. Ferroelectric domain configuration at different points of the ferroelectric loop is sketched. (b) I(V) loop measurement for an standard ferroelectric. Extracted from [94].

Positive-Up-Negative-Down (PUND) technique which is a well-known method to obtain reliable values for remanent polarization [95]. In the used PUND measurement five voltage pulses are applied to the sample. The first is negative and pre-polarizes the sample to a negative polar state. The second and the third pulses are positive: the second (P) polarizes the sample and therefore the corresponding current contains the ferroelectric and non-ferroelectric contributions, while current during the third (U) pulse only contains the non-ferroelectric contributions; therefore, their subtraction allows to obtain, in principle, only the ferroelectric contribution. The same applies for the fourth (N) and fifth pulses (D), for the negative state, so that the current loop $I_{PUND}(V)$ is obtained from $I_P - I_U$ for the positive voltages and from $I_N - I_D$ for the negative voltages. Consequently, PUND current only contains the switchable ferroelectric contribution and all the other contributions are excluded.

In Chapter 5, P(E) loops have been performed on $SrTiO_3$ crystals with the electric field applied out of the plane by using a TFAnalyser2000 (Aix-ACCT Systems GmbH. Co.). For that purpose, the top and bottom surface of the measured dielectric must be metallic contacts.

Chapter 3

Magneto-optical activity intrinsic to polarons

3.1 Introduction

The MO activity of a material is conditioned by the balance of different energy scales, related mainly to Zeeman splitting, spin-orbit coupling and exchange interactions [79, 89]. In consequence, the MO responses are intrinsically associated with the features of the electronic properties and band structure of solids and, therefore, any changes on them will strongly affect the MO response of a material. A canonical example is given by yttrium iron garnets (YIG), where the doping with rare earth ions induces the emergence of new optical transitions -absent in the parent undoped YIG compound- involving ions with large spin-orbit coupling. The appearance of these new optical transitions is at the origin of the enhanced magneto-optical response of doped YIG [96, 16]. Regarding this topic, in this Thesis we have considered the case of Ce-doped YIG, which is discussed in Chapter 4.

Inspired by the aforementioned observations, we turned our attention to polarons, which is the subject of the present Chapter. Polarons, first conceived by Landau [97], are quasiparticles formed by electrons that are bound to lattice deformations. Their physics is underpinned by electron-phonon interactions, which dominate transport in semiconductors, many poor metals, and organics [98]. Since their inception, polarons have been shown to be a key ingredient to understand the physics of many materials, including high-Tc superconductors, colossal magnetoresistance (CMR) oxides or semiconductors [12, 98]. When polarons are intensely bound to the lattice, the electronic states are inextricably interwoven with vibronic deformations, forming a new kind of physical entity, the small polaron, which can have physical properties markedly different from those of the background solid. In particular, because of these properties, it is expected that the electronic band structure is locally deformed by the presence of polarons. In view of this and the expected strong impact of the electron band structure on the optical properties, it is reasonable to presume the existence of a magneto-optical response intrinsic to polarons, different from the background magneto-optical response of the material.

In this Chapter we present our experimental approach to this problem and the results and interpretation of the experimental data. Our research has been focused to the $La_{2/3}Ca_{1/3}MnO_3$ manganite which, as discussed below, is a convenient material to investigate the magneto-optical response of polarons. Briefly, our study reveals an unexpected giant magneto-optical response of self-trapped polarons in the visible, which is almost two orders of magnitude larger than the background response of the material. The crux of the matter is the fortunate coincidence of a large coupling of electrons to phonons -mediated by Jahn-Teller interactions- together with strong spin-orbit interactions, all that in a ferromagnetic system. Such a favorable state of things occurs in optimally doped manganites, such as $La_{2/3}Ca_{1/3}MnO_3$, since in the colossal magnetoresistance (CMR) materials the electrons are prone to deform the lattice, particularly around the ferromagnetic transition and, thus, the transport is dominated by small polarons. Another crucial ingredient is the spin associated with the polaron photoconductivity, since we argue that the unexpected large magneto-optical response arises only when the spin is reversed during the polaron motion. In the next section we describe the basic concepts involved in the polaron photoconductivity.

3.1.1 Polaron photoconductivity

In the small polaron limit -which is commonly accepted to be valid for CMR manganites-the polaron binding energy $E_b/2$ is larger than the half-bandwidth, i.e., $\lambda = (2E_b/w) > 1$. In this situation, the coupling to the lattice is so strong that electronic states are heavily dressed by phonons and electrons are self-trapped, forming the so-called small Holstein polarons [99, 100, 101]. In the latter, the transport rather than diffusive proceeds by thermally activated hopping. Interestingly, thermal agitation or phonons are not the only ways to prompt polaron hopping; light provides an additional pathway, thus generating a polaron photoconductivity. In particular, the absorption of photons may deliver the required energy to jump between sites, i.e., approximately $E_b/2$ or half the polaron binding energy. In the presence of a magnetic field breaking time-reversal symmetry, the conductivity tensor acquires asymmetric nondiagonal terms, thus generating gyrotropic responses associated with the photoconductivity [102]; as a consequence, light with different circularly polarized states is absorbed differently, inducing rotation and ellipticity in the polarization of light [98, 103, 79, 89]. Coherent with this picture, magneto-optical absorption measurements in the THz range have revealed signatures of polaron contribution to the measured signal in a number of semiconductors [12, 98, 103]. So far, however, there has been no reported contribution of polarons to the magneto-optical response at optical frequencies. This contrasts with the fact that the interaction of small polarons with the lattice implies vibronic states with energy scales close to the eV, so that magneto-gyrotropic responses are expected in the optical range [102].

Bearing on mind these considerations, we undertook the investigation of the magneto-optical activity of polarons in optimally doped ferromagnetic manganites of composition $RE_{1-x}A_xMnO_3$ ($x \approx 0.3$), where RE is a rare earth and A an alkaline element (figure 3.1). As described in the next section, in these systems the formation of self-trapped polarons occurs in a particular range of temperatures and can be tuned by an external magnetic field, providing an excellent platform to investigate the specific magneto-optical response of polarons.

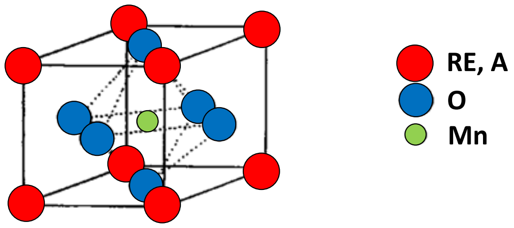

FIGURE 3.1: $RE_{1-x}A_xMnO_3$ ($x \approx 0.3$) cubic perovskite structure. Adapted from [104].

3.2 $La_{2/3}Ca_{1/3}MnO_3$: an ideal material to probe the MO properties of polarons

As described in the following, colossal magnetoresistance (CMR) manganites provide an ideal playground to study polaronic effects. Indeed, the physics of polarons is a key ingredient to explain the CMR phenomenon, defined as the resistivity change under magnetic field. In the case of $La_{2/3}Ca_{1/3}MnO_3$ (LCMO), the metal-insulator transition is tuned under magnetic fields around the Curie temperature (figure 3.2). This effect is related to the electronic conductivity in strongly electron-correlated and electron-lattice-coupled systems such as the LCMO manganite. The electronic structure of the LCMO is explained in the following.

The crystal field induced by the oxygen ions in the perovskite structure splits the 3d levels of the Mn^{3+}-site into a low energy triplet (t_{2g}) and a high energy doublet (e_g) giving to the Mn^{3+} site the electronic configuration of $t_{2g}^3 e_g^1$. The t_{2g} electrons are always localized due to the more stabilization of the crystal field energy and the lower hybridization with the oxygen $2p$ states. The e_g electrons are the charge carriers that become localized forming self-trapped polarons when the hopping interaction gets smaller (around T_c). This localization has two reasons: one is the electron correlation, similar to the t_{2g} electrons. The other is the Jahn-Teller (J-T) distortion formation, coupling the e_g electrons with oxygen displacements that deform the octahedral coordination surrounding the Mn ions (3.3 a). A large part of the polaron binding energy E_b can be identified with the Jahn-Teller energy E_{JT} arising from strong electron-phonon interactions. The Jahn-Teller coupling breaks the degeneracy of the

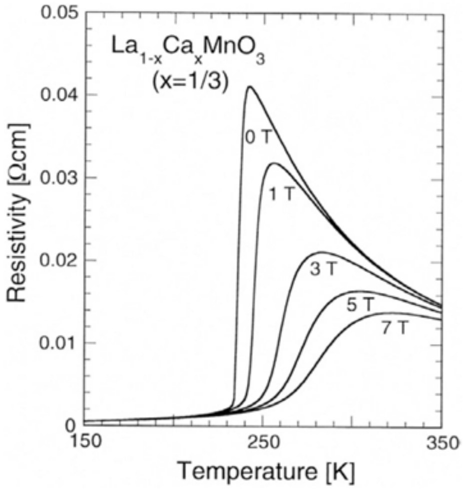

FIGURE 3.2: CMR behaviour for $La_{2/3}Ca_{1/3}MnO_3$ single crystal at different applied magnetic fields (1-7 T). Extracted from [105].

e_g orbital into $3z^2 - r^2$ and $x^2 - y^2$ orbitals by deforming the MnO_6 octahedra (figure 3.3 a), generally an apical deformation of the oxygen position when coupled to the $3z^2 - r^2$ occupied orbital or in-plane when coupled to the $x^2 - y^2$ occupied orbital. Due to the Hund's-rule exchange energy, the inter-site hopping of the e_g electrons between the neighbouring Mn sites preserves the spin orientation. The system becomes ferromagnetic due to the so-called double-exchange mechanism which is the transfer of an electron from the Mn^{3+} to the oxygen and from the oxygen to the neighbouring Mn^{4+} preserving its spin (figure 3.3 b). The effective hopping depends on the relative angle between the neighbouring spins and therefore, on the ferromagnetic exchange interaction. Hence, fully spin polarization of the conduction band is expected at the ferromagnetic metallic phase. Around the critical temperature, the spin alignment decreases, and therefore, the hopping reduces. Thus, the e_g electrons becomes self-trapped forming magnetic small polarons. Under the presence of a magnetic field aligning the spins, the double-exchange mechanism hopping is favored and the small polarons are suppressed. These changes on the electronic conductivity give rise to a colossal change in the measured resistance (CMR).

The coupling of electrons in e_g states to phonon modes can stabilize J-T polarons. Specifically, the electron-phonon coupling strength λ_{e-p} depends on the ratio between the energy cost of the J-T-driven lattice distortion and the electronic bandwidth $\lambda_{e-p} \sim \frac{2E_{JT}}{w}$ [106]. A way to enhance the strength of λ_{e-p} is to decrease the Mn-O-Mn bond angle [107] (figure 3.4 a) by reducing the size of the $Re_{1-x}A_x$ ions. In previous studies [108], the polaron effects on the optical response has been studied as a function of λ_{e-p} by changing the $Re_{1-x}A_x$ cations. Figure 3.4 (b) shows schematically the J-T interaction strength and the Curie temperatures (Tc) for different compounds extracted from reference [108]. Notice that the J-T strength increases giving larger CMR response when

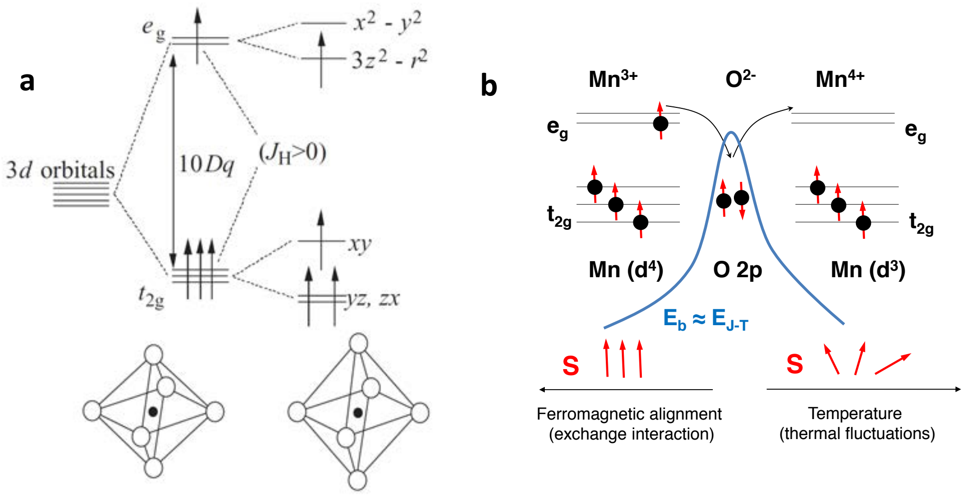

FIGURE 3.3: 3d orbitals in Mn^{3+}. Extracted from [105]. (b) Double exchange mechanism scheme.

Tc is lower [109]. In the present work, we have chosen LCMO because is the compound with bigger J-T strength for a Tc closer to room temperature.

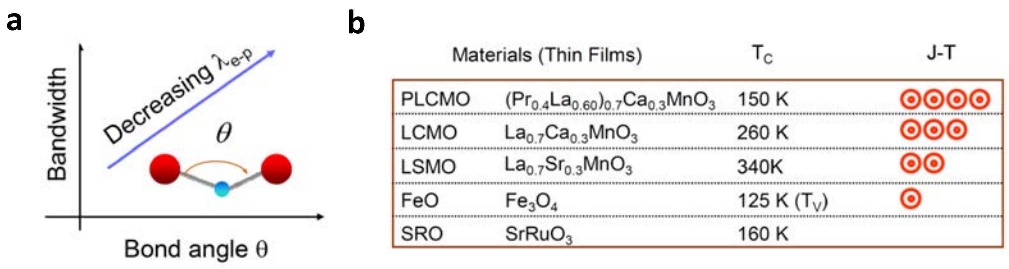

Materials (Thin Films)		Tc	J-T
PLCMO	$(Pr_{0.4}La_{0.60})_{0.7}Ca_{0.3}MnO_3$	150 K	◉◉◉◉
LCMO	$La_{0.7}Ca_{0.3}MnO_3$	260 K	◉◉◉
LSMO	$La_{0.7}Sr_{0.3}MnO_3$	340K	◉◉
FeO	Fe_3O_4	125 K (T_V)	◉
SRO	$SrRuO_3$	160 K	

FIGURE 3.4: (a) Mn-O-Mn bond angle as a function of the bandwidth. The electron-phonon coupling λ_{e-p} decreases for larger bond angles and larger bandwidth. (b) Table of transition temperatures for the oxides . Dotted circles under the J-T column symbolize graphically the strength of the J-T interaction in each compound. Adapted from [108].

3.3 Magneto-optical activity intrinsic to small polarons

3.3.1 Optical responses in CMR manganites

The optical response of polarons can be observed by the magnetoreflectance effect (MR), largely studied in CMR manganites [108, 110, 111, 112, 113]. The observation of the MR is a consequence of the formation or polarons and their suppression under magnetic fields. More specifically, in the absence of any magnetic field, self-trapped polarons emerge close to the ferromagnetic transition. If the energy of a photon is comparable to the inter-site hopping energy, it will be absorbed (figure 3.5 a). Under a magnetic field favoring again the double-exchange mechanism, polarons are reduced because the field favors the alignment of the spins of the Mn ions in neighboring sites, thus increasing the bandwidth and weakening the J-T interaction. Under these circumstances the e_g orbitals become degenerate and therefore, the photon-induced inter-site hopping cannot take place (figure 3.5 b). As a consequence, the optical reflectance is substantially modulated by the change of polaron photoconductivity induced by magnetic field, giving rise to MR. We stress that MR is a non-gyrotropic effect because it only entails a change in the intensity of light, without mixing its polarization components (figure 3.6 a). In other words, the MR phenomenon does not change the polarization of light. Due to its temperature cusp-like response around Tc (figure 3.6 b), the MR can be identified as the optical counterpart of CMR.

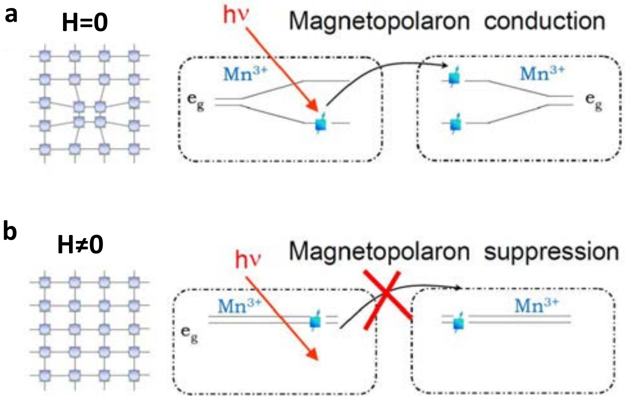

FIGURE 3.5: (a) Polaron photon-induced inter-site hopping in the absence of magnetic field. (b) Under magnetic field, polarons are suppressed and e_g orbitals become degenerate canceling the photon-induced inter-site hopping. Adapted from [108].

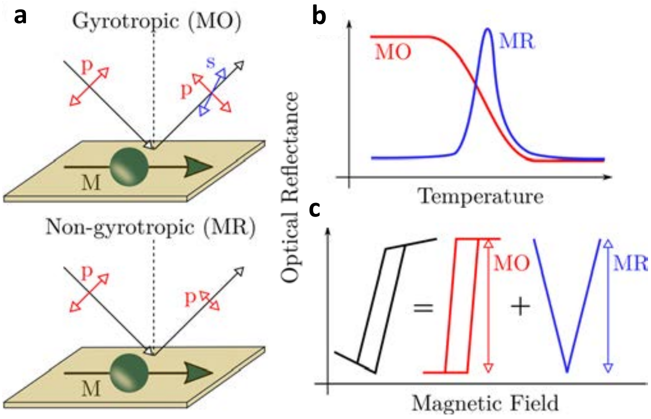

FIGURE 3.6: Schematic depiction of (a) gyrotropic (MO) effects (up) and non-gyrotropic (MR) effects (down) on the light polarization in CMR manganites. (b) Temperature dependence of MO (red) and MR (blue) effects. (c) Hysteresis measured signal (black) is decomposed into odd- (MO) and even-parity (MR).

Transverse MOKE (TMOKE), is the most suitable approach to measure the MR signal of polarons because, as discussed in Chapter 2, it measures the change of reflectance under magnetic fields. In the TMOKE signal, the MR (non-gyrotropic) is mixed with the intrinsic MO activity of the manganite. Contrary to the magnetoreflectance, the MO activity does change the polarization of light, i.e., is a gyrotropic effect. Since the MO activity depends on the sign of the magnetic field (H) while the MR does not, we can distinguish the MR and MO taking into account the parity of each effect as a function of the magnetic field (figure 3.6 c). The decomposition into odd-parity and even-parity components of the TMOKE signal has been done according to the expressions 3.1 where I is the measured signal and H is the applied magnetic field. Odd-parity and even-parity correspond to the MO and MR responses respectively.

$$I_{odd} = \frac{I(H) - I(-H)}{2}, \quad I_{even} = \frac{I(H) + I(-H)}{2} \tag{3.1}$$

3.3.2 Magneto-optical spectroscopy in LCMO

In this section we describe the analysis of the contribution of polarons to the optical properties of LCMO films. To illustrate this issue, we focus on data measured in a film with thickness of 80 nm grown by rf magnetron sputtering on (110)-oriented $SrTiO_3$ single crystals. As previously mentioned, TMOKE is a convenient configuration to explore the optical responses of manganites because it measures both MR and MO effects. Specifically, it probes the relative change of p-polarization intensity δ_K (chapter 2). In order to simplify, we will focus our analysis on the imaginary part of the TMOKE signal $\Im(\delta_K)$. Firstly, the general behavior of the temperature dependence of the TMOKE signal is summarized in the following. Figure 3.7 shows three hysteresis loops measured at $\lambda = 400$ nm and extracted at T=230 K (T<Tc), T=260 K (T=Tc) and at T=286 K (T>Tc), in which data in black represents the as-measured signal and in red and blue the MO and MR components, respectively, computed applying the parity relations from the expressions 3.1. As can be appreciated, the response below Tc is almost governed by MO, while near Tc the raw loop is strongly distorted by the large MR contribution as it is expected from the changes of optical conductivity induced by the suppression of self-trapped polarons with fields [108, 110, 111, 112, 113]. Finally, above the ferromagnetic transition, both MR and MO signals vanish.

Now, we will analyze the wavelength dependence of the polaron signatures measuring hysteresis loops as a function of the temperature across the visible spectra. For that purpose, the wavelength response is evaluated by tracking the amplitude of the MO ($\Im(\delta_K)_{MO}$) and MR ($\Im(\delta_K)_{MR}$) hysteresis defined as the change between maximum and zero magnetic field (expressions 3.2).

$$\begin{aligned} \Delta\Im(\delta_K)_{MO} &= \Im(\delta_K)_{MO}[H = 12\,\text{kOe}] - \Im(\delta_K)_{MO}[H = 0\,\text{kOe}] \\ \Delta\Im(\delta_K)_{MR} &= \Im(\delta_K)_{MR}[H = 12\,\text{kOe}] - \Im(\delta_K)_{MR}[H = 0\,\text{kOe}] \end{aligned} \tag{3.2}$$

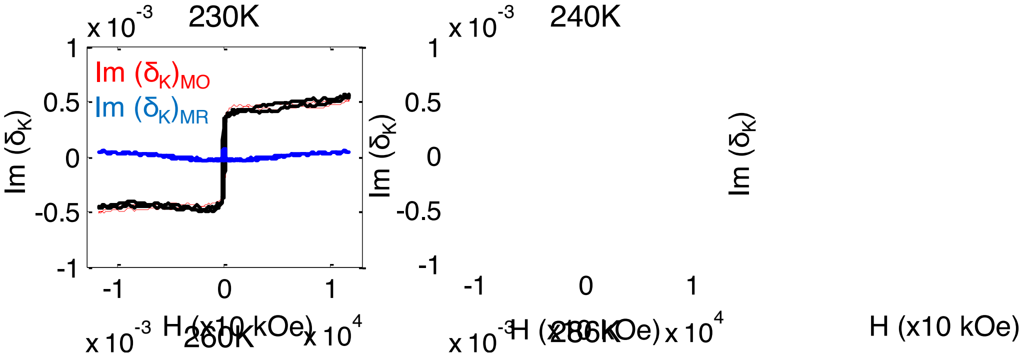

FIGURE 3.7: TMOKE as measured signals increasing the temperature. At the lower temperatures the TMOKE signal is mainly odd. Close to the Tc the even contribution becomes larger. Both odd and even contributions vanish after Tc.

To illustrate this analysis, we discuss the particular case of the spectroscopic measurements done near the Curie temperature T=260 K (figure 3.8 a).Focusing first on the magnetoreflectance, we see in figure 3.8 (a) (upper panel) that MR spectroscopic response almost vanishes around 530 nm dividing the visible spectra in two regions where the MO response is enlarged below 550 nm and almost constant above 550 nm. These two regions in the MR spectrum plausibly indicate that two broad electronic transitions are excited by photons, corresponding to transitions occurring below (blue region) and above (red region) 550 nm (2.3 eV). Indeed, variable angle spectroscopic ellipsometry corroborates this view, as shown in figure 3.8 (b), the imaginary part of the dielectric function (ϵ_2) can be also described by two transitions. The involvement of these two broad transitions also seems to be reflected in the spectral dependence of the MO response shown in the lower panel of figure 3.8 (a). We call the two spectral regions defined by these two transitions as SP as (spin-preserved) and SF (spin-flip) for reasons that will be discussed later in this section.

In order to study the evolution of these two regions as a function of the temperature, we have measured one hysteresis loop per each temperature around Tc (from 230 K to 290 K) and at two different wavelengths representing the SF (400 nm) and SP (700 nm) regions respectively. If we draw our attention first to the MO signal measured at $\lambda = 700$ nm (see figure 3.9 a), we see that its temperature dependence reproduces the temperature dependence of the magnetization of the LCMO film. This is what is expected for a conventional MO response which, generally, is proportional to the magnetization. In particular, the data displayed in figure 3.9 (a) show the ferromagnetic transition occurring at Tc ~260 K. Now, if we turn our attention to the temperature dependence of the MO response measured at shorter wavelength $\lambda = 475$ nm, we observe that close to the Tc there is an anomaly that consists of a bump around the ferromagnetic transition (signaled by an arrow in figure 3.9 b), indicating that the MO signal is enhanced around the Curie temperature. Interestingly, we observe that the

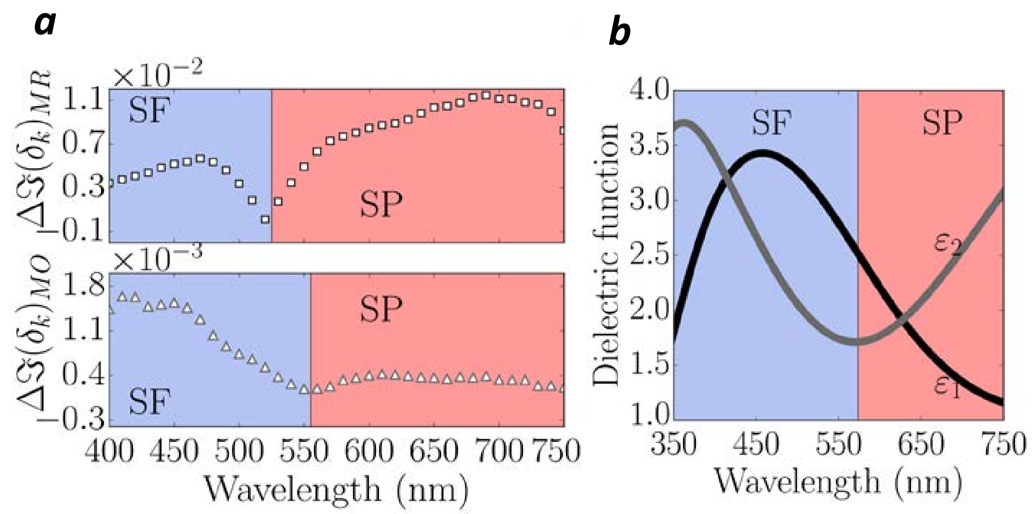

FIGURE 3.8: (a) TMOKE hysteresis decomposition into odd (MO) and even (MR) at T=260 K and $\lambda = 475$ nm. (b) MO and MR spectral response at T=260 K. (c) Dielectric function measured by variable angle spectroscopic ellipsometry.

appearance of the anomalous bump around Tc is concomitant with the emergence of the cusp-like MR response at those temperatures (upper panel of figure 3.9 b) and, therefore, related with the emergence of self-trapped polarons. In order to have a better understanding of the relation between the anomalous MO signal and the presence of self-trapped polarons, we have carried out a detailed spectroscopic study in order to characterize with accuracy these anomalous distortions. For that purpose, the MO and MR signals have been measured systematically across many values of the temperature and wavelength. The results of this exhaustive analysis are shown in figure 3.10 and, as discussed in the following, reveal again the emergence of an anomalously large MO signal around Tc at the range of short wavelengths ($\lambda < 500$ nm). In particular, figure 3.10 (a) shows the MO amplitude $\Im(\delta_K)_{MO}$ as a function of the temperature for different wavelengths normalized to the MO amplitude at 230 K. The areas shaded under the bumps correspond to the difference between the curves measured at different wavelengths and that measured at $\lambda = 700$ nm. These shaded areas are used to estimate the enhancement of the MO signal that is shown in the mappings of figure 3.10 (c). Having this information, the MO and MR amplitudes are mapped as a function of wavelength and temperature. In particular, the MR response is mapped out in figure 3.10 (b), and shows two prominent areas around Tc where the intensity is particularly large, indicating the presence of self-trapped polarons. These regions are in agreement with the spectral response previously analyzed (figure 3.8 b), in which there were signatures of two different electronic transitions in the optical response. However, unexpectedly, the MO enhancement, shows only one prominent peak at shorter wavelength and around Tc. Put in other words, the data can be interpreted as if two kinds of self-trapped polarons could be excited at two different wavelengths (two peaks in the MR mapping of figure 3.10 b), but only one of these polarons is able to enhance the MO signal.

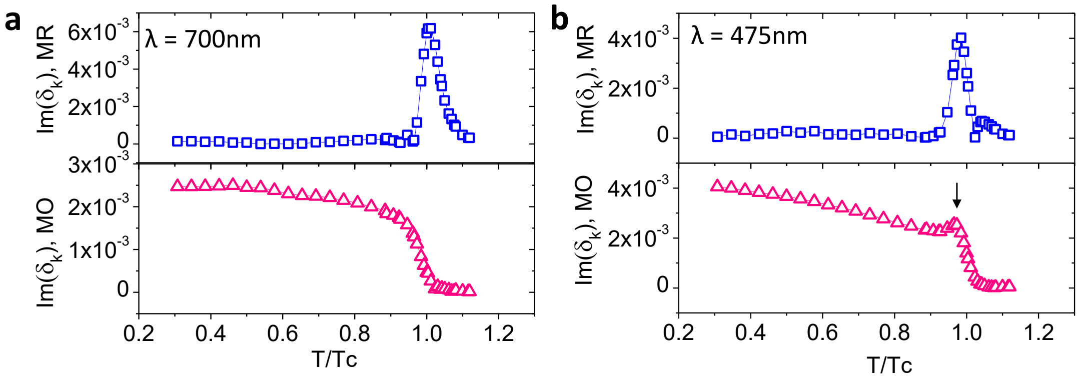

FIGURE 3.9: TMOKE transition at $\lambda = 475$ nm (a) and $\lambda = 700$ nm (b). The temperature axis is normalized by Tc=260 K.

The emergence of a MO enhancement is visible in the temperature dependence of the TMOKE signal shown in figure 3.10 (a). Subsequently, we have investigated if in other optical arrangements the MO increase could be even larger. For that purpose, we measured the Kerr ellipticity in Polar MOKE geometry, because in this configuration the MO effects are usually larger. The ellipticity (ϵ) of the polarized light as a function of temperature at three wavelengths (402, 632, 700 nm) is shown in the figure 3.11 (a). As expected, a remarkable enhancement of the ellipticity at $\lambda = 402$ nm occurs around the Curie temperature. This enhancement vanishes while increasing the wavelength. Thus, just a tiny bump is seen at $\lambda = 632$ nm and no visible enhancement is observed at $\lambda = 700$ nm as it is expected from the TMOKE previous experiments. The inset of 3.11 (a) shows the as-measured hysteresis loops for three temperatures representing the regions below Tc (246 K), close to Tc (258 K) and just after Tc (272 K). Notice that the hysteresis loop at 258 K has larger amplitude than the loop at 246 K due to the MO enhancement.

In addition, we have studied the magnetic field dependence of the polaronic enhancement. More specifically, figure 3.11 (b) shows the ellipticity as a function of the temperature normalized by the ellipticity measured at 230 K. The data displayed in figure 3.11 (b) shows that the enhancement becomes more prominent when the field is reduced. As discussed in the following, this fact can be explained by the suppression of self-trapped polarons by magnetic fields. More specifically, one would expect that more polarons survive at lower fields as they are suppressed by magnetic field; hence, the relative increase of MO is expected to become larger as the applied field is reduced. In order to quantify the MO enhancement as a function of the applied magnetic field and temperature, we have plotted the ratio between the ellipticity measured at $\lambda = 402$ nm and 700 nm ($\epsilon(402\text{ nm})/\epsilon(700\text{ nm})$) where there is any MO enhancing

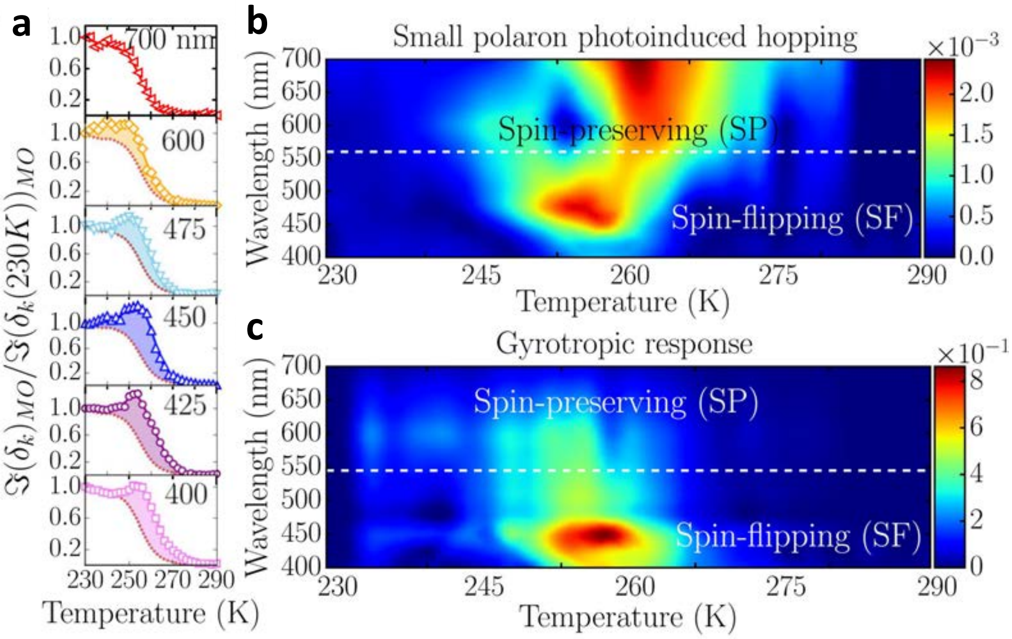

FIGURE 3.10: (a) MO ferromagnetic-paramagnetic transition at λ = 700, 600, 475, 450, 425, 400 nm. A bump appears near around the transition at shorter wavelength (b) MR spectral response as a function of the temperature. Two regions can be distinguished. (c) MO enhancement, mapped taking the area under the bump shaded in (a). A single peak appears at shorter wavelength around Tc.

(figure 3.11 c). This analysis shows an enhancement up to 60-fold for low applied magnetic field and it reduces up to 30-fold at the maximum applied field (12 kOe).

The fact that the MO enhancement is strongly modulated by magnetic fields (see data in figure 3.11 a) suggests that the shape of the hysteresis loops should be largely distorted in the vicinity of the transition for wavelengths were the action of polarons modify the MO response. Indeed, the experimental data corroborate these expectations. We have plotted in figure 3.12 the ellipticity curves measured at 402 nm (where polarons enhance the gyrotropic response) and at 632 nm (where polarons are inactive for that matter). At T = 230 K, we are far enough from the Curie temperature Tc, so that polarons have little effect on the magneto-optical signal; on the contrary, at T= 260 K and 264 K and at short wavelengths polarons exert a strong effect on the gyrotropic response. In the main panels of figure 3.12 we display the as-measured values, while in the insets we show the loops normalized by the ellipticity at 12 kOe. In a conventional system, even though the magnitude of the magneto-optical signal depends on the wavelength, it is always proportional to the magnetization. Therefore, if we normalize to the unity all the hysteresis curves measured at the same temperature they should superimpose to each other. At T = 230 K, where the effect of polarons is expected to be residual, we see in the inset of figure 3.12 (a) that the normalized loops measured at 402 mn and 632 nm have indeed a rather similar shape, although a small

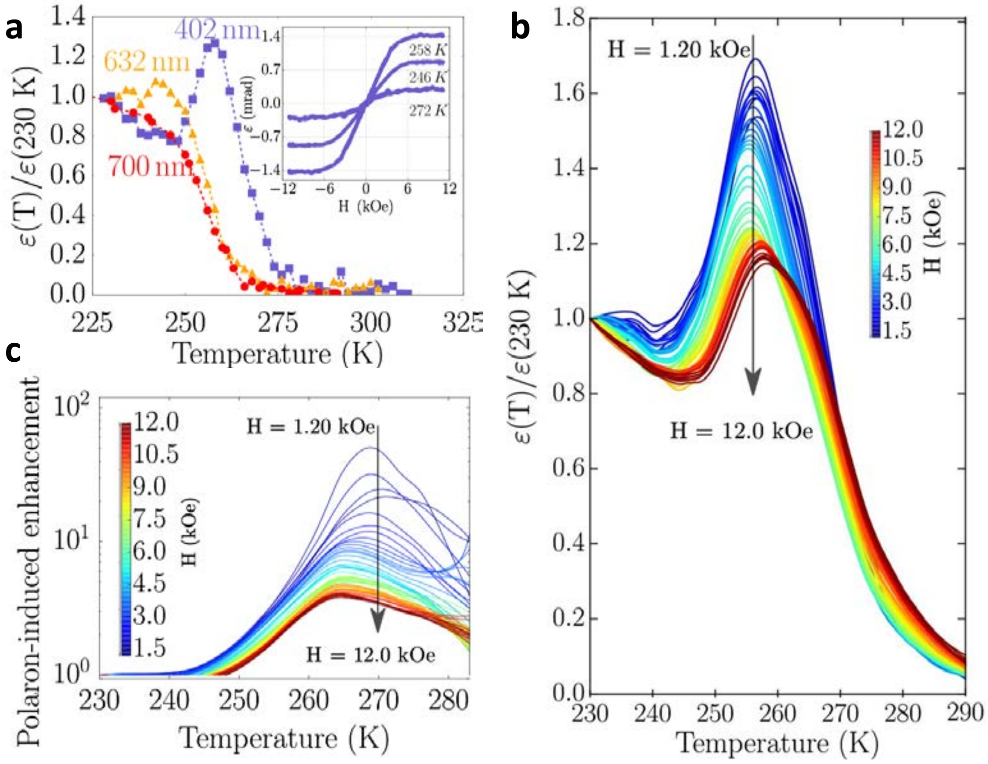

FIGURE 3.11: (a) Normalized PMOKE ellipticity as a function of the temperature at $\lambda = 402$ nm, 632 nm, 700 nm. Inset: raw hysteresis loops measured at $\lambda = 402$ nm at T=246 K, T=258 K and T=272 K. (b) Normalized PMOKE ellipticity transition as a function of the magnetic field at $\lambda = 402$ nm. The bump increases for lower values of magnetic field. MO enhancement as a function of the temperature and magnetic field. A 60-fold enhancement is observed at the Tc at low magnetic field.

change in shape may be due to some remaining slight effect of polarons. However, the shape of the normalized loops measured at 402 nm and 632 nm is manifestly changed at temperatures just next to Tc (T=260 K, 264 K) (3.12 a, b). As aforementioned, this is at odds with what is expected for a conventional magnetic system and is attributable directly to the influence of polarons, which enhance strongly the magneto-optical activity measured at 402 nm, especially at low fields. As a consequence, the shape of the loops measured at short wavelengths change their shape significantly with respect to those measured at longer wavelengths. We note further that the gyrotropic enhancement is so strikingly conspicuous that the magneto-optical signal measured at longer wavelengths (632 nm) is reduced by more than one half as the temperature goes from T=230 K to T=264 K, whereas the signal measured at shorter wavelengths (402 nm) barely changes its value at the selected three temperatures. Again, this is at variance with what is expected in a conventional material, where the magneto-optical signal measured at both wavelengths should be reduced by the same amount.

In the previous paragraphs we have described all the evidence that support to a direct relationship between the observed large MO enhancement at shorter wavelengths

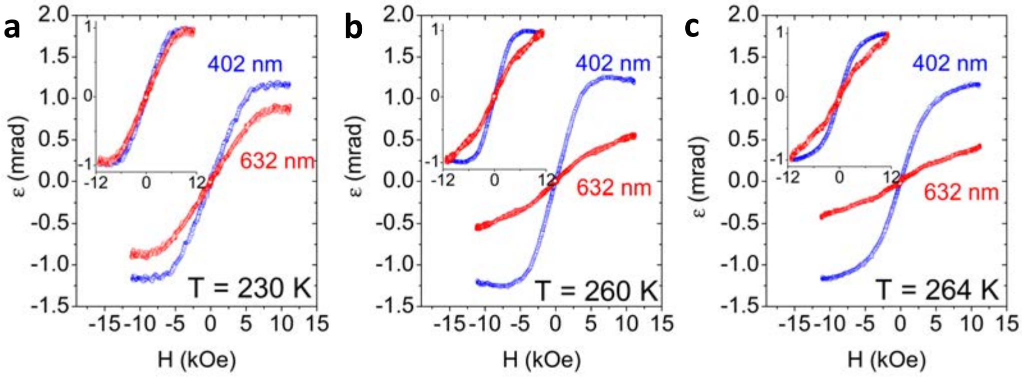

FIGURE 3.12: PMOKE ellipticity loops at: (a) T=230 K <Tc, (b) T=260 K ~Tc and (c) T=260 K >Tc for $\lambda = 402$ nm and 700 nm. The inset show the loops normalized by the signal at 12 kOe.

in the visible (up to 60-fold increase with respect to the baseline MO signal at low applied magnetic field) and the emergence of self-trapped polarons around Tc. In order to better understand these relationship, we need to give a more detailed discussion of the spectroscopic measurements of the MR and MO responses shown in figures 3.8 and 3.10. We remind that the data shown in those figures indicate the involvement of two different electronic transitions excited by photons of different wavelengths. The discussion in terms of two optical transitions are indeed consistent with a large number of spectroscopy studies in CMR manganites showing two main bands extending around $E_{ph} \sim 1 - 2$ eV and $E_{ph} \sim 3 - 5$ eV, respectively [114, 115, 116, 117, 118, 119]. Such spectral features have received different interpretations in terms of either intrasite [115, 117] or intersite transitions between e_g states for bands at $E_{ph} \sim 1 - 2$ eV as well as intra-atomic charge transfer excitations for optical bands at $E_{ph} \sim 4 - 4.5$ eV [119]. We make a special mention here of the interpretation put forward by Quijada et al. [114], who claimed the polaronic character of the observed spectral features [114, 117]. The authors of those works assigned the lower-energy bands at $E_{ph} \sim 2$ eV to intersite $e_g - e_g$ photoinduced transitions of small polarons that hop between neighbouring Mn sites without changing their spin, while optical bands at $E_{ph} \sim 3$ eV were assigned to intersite $e_g - e_g$ transitions in which the spin state is changed [114]. In view of this, we have defined two spectral regions distinguished in the figures 3.8 (b, c) and in 3.10 (b, c) as a function of photon wavelengths at which the spin is either preserved (SP) or flipped (SF) during the photoinduced transitions of small polarons (see figure 3.13). We, then, reach the conclusion that the MO enhancement only occurs when the photoconducitivity is associated with the motion self-trapped polarons that reverse their spin during the hopping between two neighboring sites. On the contrary, motion of self-trapped polarons in which the spin is preserved do not induce any MO enhancement. In order to understand why SF photoinduced transitions increase the MO activity around Tc, we have developed a theoretical model in collaboration with Profs. Javier Junquera and Pablo García Fernández (Universidad de Cantabria), which is described in the following.

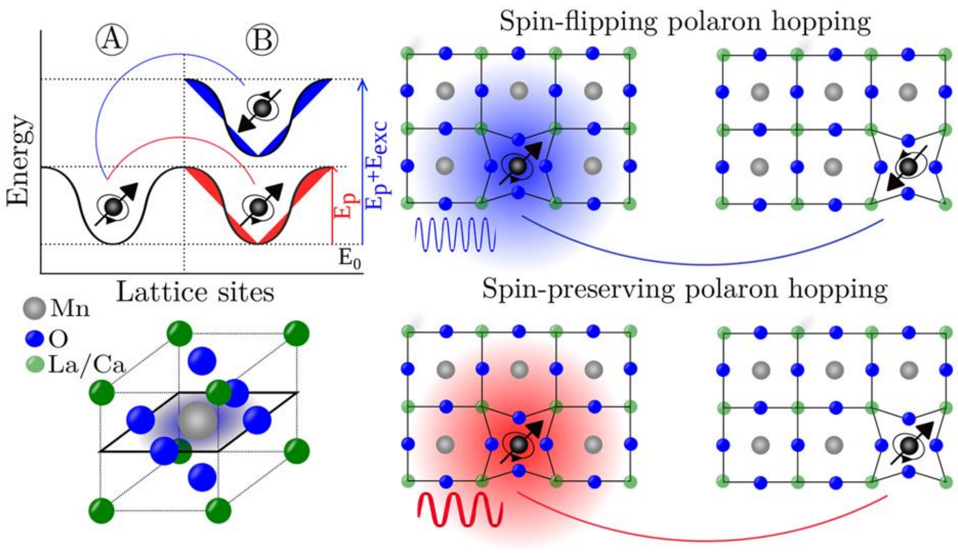

FIGURE 3.13: Spin-flipping (blue) and spin-preserving (red) photoinduced polaron hopping. Electrons in e_g states of Mn^{3+} jump into an empty state of a neighbouring Mn^{4+} site, with their spin unchanged. Contrarily, spins are flipped in transitions induced by higher energy photons in region SF.

3.4 Theoretical model to understand the intrinsic MO response of polarons

In the metallic and ferromagnetic state of La$_{2/3}$Ca$_{1/3}$MnO$_3$ e_g electrons have relatively large mean free paths before they are scattered. As the temperature is raised towards the magnetic transition this length is reduced due to the higher probability of finding a Mn site with opposite spin that acts as a scattering site. As soon as the transition temperature is reached, the optical activity drops abruptly since the eg electrons are essentially localized in a single Mn ion and intrasite $d-d$ transitions are forbidden by parity. In order to understand qualitatively the origin of the magneto-optical properties close to the ferromagnetic-paramagnetic transition in La$_{2/3}$Ca$_{1/3}$MnO$_3$ we will consider a model in which an electron is moving in the conduction band of this perovskite, which has a strong Mn(e_g) character, and has to hop into a Mn^{IV} ion with an empty eg shell (figure 3.14 a). An important fact to take into account is that when an electron is localized in the e_g shell of an octahedral Mn complex the resulting degenerate state (figure 3.14 b), triggers a geometrical instability in the form of the Jahn-Teller effect. As a consequence, the complex becomes elongated and electrons occupy preferentially orbitals with $3d_{3z^2-r^2}$ symmetry. In La$_{2/3}$Ca$_{1/3}$MnO$_3$ this distortion can be experimentally observed by EXAFS and is found to increase as the temperature approaches the magnetic transition [14]. This can be understood in terms of the interactions that cause the Jahn-Teller effect, which are proportional to the occupation of each complex and are thus enhanced by electron localization. This effect allows the electrons to self-trap and form polarons. In larger bandwidth perovskites like La$_{2/3}$Ca$_{1/3}$MnO$_3$ the localization is much smaller and electron self-trapping is impeded.

3.4.1 Mechanism of the photoinduced hopping

To understand how the polaron moves between complexes we will take a two-site model where the electron is initially localized in the mainly $3d_{3z^2-r^2}$ orbital ($|z_1^2\rangle$) of one manganese ion with nominal charge $+3(\text{Mn}^{\text{III}})$ and moves towards a contiguous Mn^{IV} that presents an empty e_g shell. First, we will establish that the most probable mechanism for this hopping mechanism involves the direct charge transfer from $|z_1^2\rangle$ to the mainly $3d_{3z^2-r^2}$ orbital in the second center ($|z_2^2\rangle$). To do so, we will consider the movement of an electron in a generic two-center tight-binding model where each site has a coupling to local vibrations Q_i. The energy of this system is:

$$E = \frac{1}{2}KQ_1^2 + \frac{1}{2}KQ_2^2 + \epsilon_1 \tag{3.3}$$

where K is the local force constant associated to the distortions and ϵ_1 is the energy of the electron, obtained as the lowest eigenvalue of the Hamiltonian matrix. In order to build this matrix we will consider that the electronic state on each site can be described by a single Wannier function. Defining V as the linear electron-lattice coupling constant (equivalent to the Jahn-Teller linear coupling in systems with degenerate electronic levels) and γ as the tight-binding constant associated to the interaction between the two Wannier functions, we obtain the following interaction matrix:

$$h = \begin{pmatrix} -VQ_1 & \gamma \\ \gamma & -VQ_2 \end{pmatrix} \tag{3.4}$$

Using equation 3.3 we can now calculate the polaron's binding energy,

$$E_b \approx \frac{V^2}{2K} \tag{3.5}$$

and the adiabatic barrier for the charge transfer of the electron from site 1 to site 2 at first order in γ:

$$B \approx \frac{V^2}{4K} - |\gamma| + \cdots \tag{3.6}$$

Hence, we see that the barrier reduces as the interaction γ becomes larger. We can now determine the smallest barrier for polaron hopping by using standard Koster-Slater constants to find the largest hopping constant between the ($|z_1^2\rangle$) orbitals and the d-orbitals of the surrounding Mn ions. As already anticipated, the result is that the most probable hop is to the mainly $3d_{3z^2-r^2}$ orbitals of the complexes along the z-direction.

While we developed this simple model for a generic non-degenerate case, its extension to the two Jahn-Teller sites necessary for its application in the manganites

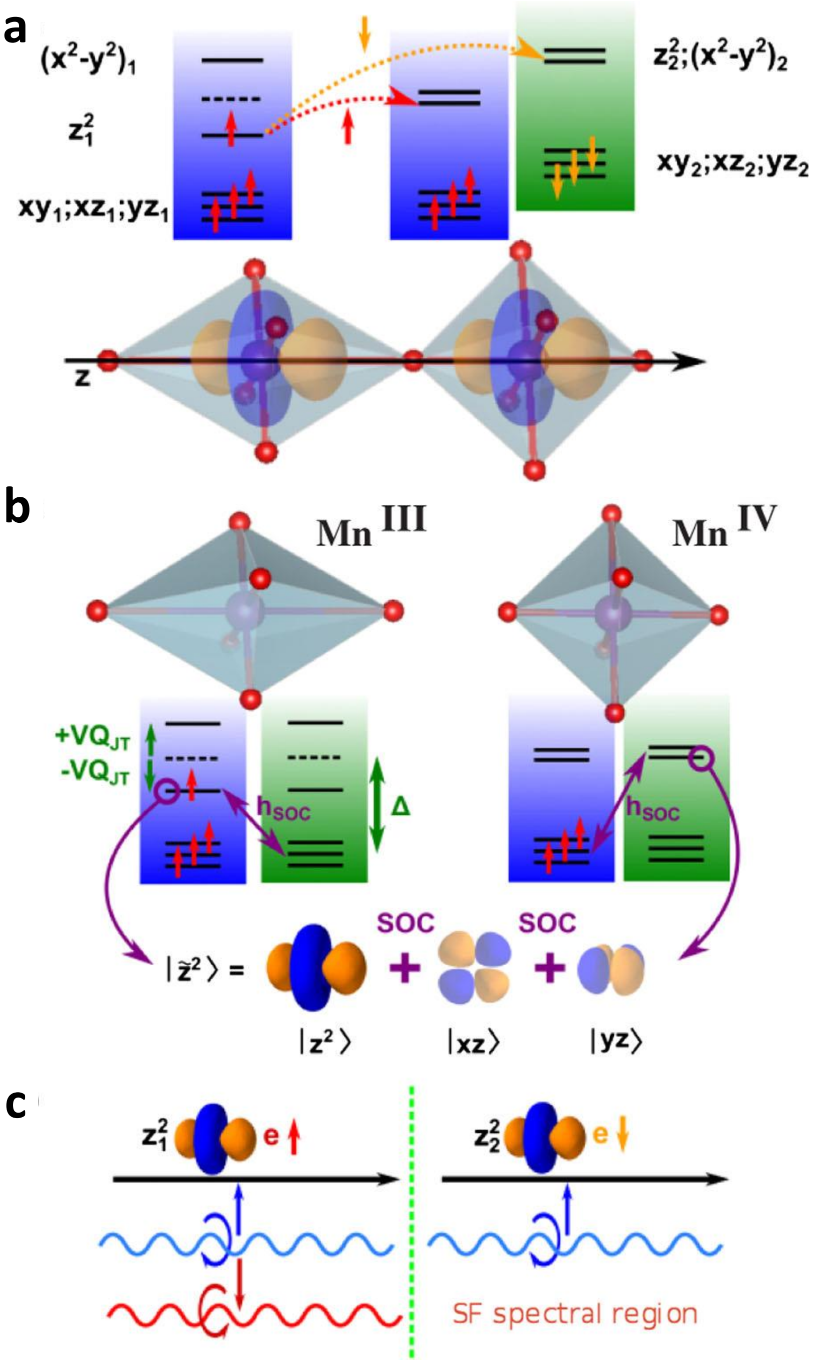

FIGURE 3.14: (a) Scheme of the main process describing the polaron hopping around Tc. A spin-up self-trapped electron moves from the z^2 orbital in an elongated $\mathrm{Mn^{III}O_6}$ complex into the z^2 orbital of a $\mathrm{Mn^{IV}O_6}$ complex that can have the same spin-up (blue box) or spin-down (green box) (b) Local d levels in $\mathrm{Mn^{III}}$ and $\mathrm{Mn^{IV}}$ complex where the effect of the Jahn-Teller distortion (Q_{JT}), is seen, effectively reducing the energy spacing between the z^2 levels and those of xz and yz states in tetragonal symmetry. This distortion helps the mixing of occupied and unoccupied levels due to the spin-orbit coupling (shown in purple). (c) Electrons with a particular spin polarization can only absorb circular polarized light that rotates in a specific direction to invert the spin upon hopping.

follows the same pattern where the binding energy can be directly identified with the Jahn-Teller energy (this is an approximation given that other vibrational modes like the octahedral breathing and rotation modes also participate in the stabilization of the polaron).

3.4.2 Optical activity associated to the photoinduced polaron hopping

It is well known that due to the even character of the 3d-levels of an octahedral complex, $d-d$ transitions in a single transition site are forbidden by parity. However, in the two-site model a new dipole-allowed transition is opened. In particular, if we consider that the electron is initially spin-up ($S = \uparrow$) we find that the only non-zero transition dipole matrix element is $\langle z_1^2, S|z|z_2^2, S\rangle$ associated to the spin-conserving transfer of the electron from the mainly $3d_{3z^2-r^2}$ orbital in one center to the other. Thus it is clear that, at this level of theory, no magneto-optical effect can be found associated to polaron hopping.

In order to find these effects we will include the effect of the spin-orbit coupling between the mainly $3d_{3z^2-r^2}$ levels with other d-levels in the same site. We take the usual expression for the one-site spinorbit operator,

$$\widehat{h}_{SOC} = \zeta(r)\overrightarrow{l}\overrightarrow{s} \tag{3.7}$$

where $\zeta(r)$ is the radial part of the spin-orbit interaction and $\overrightarrow{l}$ and $\overrightarrow{s}$ are the orbital and spin angular momentum operators. Given that the $|z_1^2\rangle$ state has zero orbital angular momentum – it has the same symmetry as the Y_2^0 spherical harmonic – it can only couple to functions with ±1 orbital angular momentum, i.e. $|xz\rangle$ and $|yz\rangle$, through the $\widehat{l}_x$ and $\widehat{l}_y$ operators. Given that the spin-orbit coupling interaction is represented here as a one-electron operator, the energy of the system can only become lower when occupied and unoccupied orbitals are mixed (figure 3.14 b). We find that, at first perturbation order, the initial state with the electron spin-up is corrected to

$$|\widetilde{z}_1^2 \uparrow\rangle \approx |z_1^2 \uparrow\rangle + \frac{\sqrt{3}}{2}\frac{\zeta}{\Delta - VQ_{JT}}(|xz_1 \downarrow\rangle + i|yz_1 \downarrow\rangle) + \cdots \tag{3.8}$$

while the corresponding spin-down case is corrected to

$$|\widetilde{z}_1^2 \downarrow\rangle \approx |z_1^2 \downarrow\rangle + \frac{\sqrt{3}}{2}\frac{\zeta}{\Delta - VQ_{JT}}(|xz_1 \uparrow\rangle + i|yz_1 \uparrow\rangle) + \cdots \tag{3.9}$$

It is important to note that the second term in equations 3.8 and 3.9 corresponds to functions with well-defined orbital angular momentum ($l_z = \pm 1$ for equations 3.8 and 3.9, respectively), so the above equations can be rephrased into

$$|\widetilde{z}_1^2 \uparrow\rangle \approx |z_1^2 \uparrow\rangle + \frac{\sqrt{6}}{2}\frac{\zeta}{\Delta - VQ_{JT}}|l_{+1} \downarrow\rangle + \cdots \tag{3.10}$$

$$|\tilde{z}_1^2 \downarrow\rangle \approx |z_1^2 \downarrow\rangle + \frac{\sqrt{6}}{2} \frac{\zeta}{\Delta - VQ_{JT}} |l_{-1} \uparrow\rangle + \cdots \tag{3.11}$$

The well-defined angular momenta in the spin-orbit-corrected states of Equations 3.10 and 3.11 influence decisively on the sensitivity of the states with spin-up and spin-down to absorbing right and left-handed circularly polarized light.

For the second site, which initially contains the $\mathrm{Mn^{IV}}$ ion with the empty e_g shell, we find that the first-order spin-orbit correction to the orbital receiving the electron is null both when the global spin of the ion is up,

$$|\tilde{z}_2^2 \uparrow\rangle = |z_2^2 \uparrow\rangle \tag{3.12}$$

$$|\tilde{z}_2^2 \downarrow\rangle = |z_2^2 \downarrow\rangle \tag{3.13}$$

In the above equations 3.8 to 3.11, ζ is the covalency-corrected spin-orbit coupling constant of Mn, Δ is the so-called $10Dq$ crystal splitting for the $\mathrm{Mn^{III}}$ ion, V is the linear Jahn-Teller coupling constant and Q_{JT} is the Jahn-Teller distortion (an illustration of the meaning of these magnitudes can be found in the figure 3.14).

Now we can consider the optical properties associated to two photoinduced hopping processes denoted in the previous section as spin-preserving (SP) and spin-flipping (SF). We are going to study each situation considering that the initial electron is spin-polarized up or down to find the differences in interaction with polarized light. In the case of SP, the spin is conserved during the charge transfer so that,

$$Mn^{III}(\uparrow) + Mn^{IV}(\uparrow) \rightarrow Mn^{IV}(\uparrow) + Mn^{III}(\uparrow) \tag{3.14}$$

$$Mn^{III}(\downarrow) + Mn^{IV}(\downarrow) \rightarrow Mn^{IV}(\downarrow) + Mn^{III}(\downarrow) \tag{3.15}$$

In spectral region SF the spin is reversed so the two processes to consider are:

$$Mn^{III}(\uparrow) + Mn^{IV}(\downarrow) \rightarrow Mn^{IV}(\uparrow) + Mn^{III}(\downarrow) \tag{3.16}$$

$$Mn^{III}(\downarrow) + Mn^{IV}(\uparrow) \rightarrow Mn^{IV}(\downarrow) + Mn^{III}(\uparrow) \tag{3.17}$$

To qualitatively estimate the optical activity we will use Fermi's Golden rule that says that the transition probability is proportional to the squared modulus of the transition matrix element. We will consider here the radiation-electron interaction Hamiltonian of the form,

$$\widehat{h}_E = -\overrightarrow{E}(t)\overrightarrow{r} \tag{3.18}$$

Thus, we need to evaluate the corresponding dipole transition matrix elements, $\langle \tilde{z}_1^2, S_1 | \overrightarrow{r} | \tilde{z}_2^2, S_2 \rangle$, for each case (SP or SF) and starting with spin-up or spin-down.

For the case SP and using equations 3.8-3.9 and 3.10-3.11 we find that the only non-null matrix elements are,

$$\langle \widetilde{z}_1^2, \uparrow |z| \widetilde{z}_2^2, \uparrow\rangle = \langle \widetilde{z}_1^2, \downarrow |z| \widetilde{z}_2^2, \downarrow\rangle = \langle z_1^2|z|z_2^2\rangle \tag{3.19}$$

while for case SF we get that the non-null elements are,

$$\langle \widetilde{z}_1^2 \uparrow |x| \widetilde{z}_2^2 \downarrow\rangle \approx \frac{\sqrt{3}}{2}\frac{\zeta}{\Delta - VQ_{JT}}\langle xz_1|x|z_2^2\rangle \tag{3.20}$$

$$\langle \widetilde{z}_1^2 \uparrow |y| \widetilde{z}_2^2 \downarrow\rangle \approx -i\frac{\sqrt{3}}{2}\frac{\zeta}{\Delta - VQ_{JT}}\langle yz_1|y|z_2^2\rangle \tag{3.21}$$

$$\langle \widetilde{z}_1^2 \downarrow |x| \widetilde{z}_2^2 \uparrow\rangle \approx \frac{\sqrt{3}}{2}\frac{\zeta}{\Delta - VQ_{JT}}\langle xz_1|x|z_2^2\rangle \tag{3.22}$$

$$\langle \widetilde{z}_1^2 \downarrow |y| \widetilde{z}_2^2 \uparrow\rangle \approx i\frac{\sqrt{3}}{2}\frac{\zeta}{\Delta - VQ_{JT}}\langle yz_1|y|z_2^2\rangle \tag{3.23}$$

where (x, y, z) designate the projections of the vector $\overrightarrow{r}$ along the three directions in space. We will now consider an experiment in polar configuration (the main magnetic axis is along direction z) with light propagating also along z and a polarization described by a phase factor φ between the electric field components along the directions x and y.

Let us focus first on case SP (spin-conserving electron transfer). Given that no electric field component is along z, equation 3.19 tells us that we would not expect any optical activity along this direction. However, the matrix element $\langle z_1^2|y|z_2^2\rangle$ is equal to $\langle x_1^2|x|x_2^2\rangle$ and $\langle y_1^2|y|y_2^2\rangle$, which are their equivalents along the x and y directions. Note that $|x_i^2\rangle$ and $|y_i^2\rangle$ represent, respectively, $3d_{3x^2-r^2}$ and $3d_{3y^2-r^2}$ orbitals. Thus, the transition probability for case SP (processes described by equations 3.12 and 3.12) are:

$$\rho_{SP}^{\uparrow\uparrow} \propto \frac{1}{3}|\langle \widetilde{x}_1^2 \uparrow |x| \widetilde{x}_2^2 \uparrow\rangle|^2 + \frac{1}{3}|\langle \widetilde{y}_1^2 \uparrow |y| \widetilde{y}_2^2 \uparrow\rangle|^2 = \frac{2}{3}|\langle z_1^2|z|z_2^2\rangle|^2 \tag{3.24}$$

$$\rho_{SP}^{\downarrow\downarrow} \propto \frac{1}{3}|\langle \widetilde{x}_1^2 \downarrow |x| \widetilde{x}_2^2 \downarrow\rangle|^2 + \frac{1}{3}|\langle \widetilde{y}_1^2 \downarrow |y| \widetilde{y}_2^2 \downarrow\rangle|^2 = \frac{2}{3}|\langle z_1^2|z|z_2^2\rangle|^2 \tag{3.25}$$

Thus, we see that for the SP case -independently of the magnetic polarization of the sample- the optical signal is insensitive to the polarization of light, i.e. the transitions in spectral region SP do not present magneto-optical activity.

Operating in a similar fashion for the spin-flip processes (case SF) described in Equations 3.16 and 3.17 we get,

$$\rho_{SP}^{\uparrow\downarrow} \propto |\langle \widetilde{z}_1^2 \uparrow |\overrightarrow{r}| \widetilde{z}_2^2 \downarrow\rangle|^2 = 3(\frac{\zeta}{\Delta - VQ_{JT}})^2|\langle xz_1|x|z_2^2\rangle|^2(1+\sin(\varphi)) \tag{3.26}$$

$$\rho_{SP}^{\downarrow\uparrow} \propto |\langle \widetilde{z}_1^2 \downarrow | \overrightarrow{r} | \widetilde{z}_2^2 \uparrow \rangle|^2 = 3(\frac{\zeta}{\Delta - VQ_{JT}})^2 |\langle xz_1|x|z_2^2\rangle|^2 (1 - \sin(\varphi)) \tag{3.27}$$

where we plainly see that systems with starting spin-up or spin-down electrons interact with polarized light in a clearly different way. In particular, we observe that each case (either equation 3.26 or 3.27 is sensitive, respectively, to just one circularly polarized state (either $\varphi = +\frac{\pi}{2}$ or $\varphi = -\frac{\pi}{2}$) and is completely insensitive to the other. Thus, we can conclude that equations 3.23 and 3.24 describe the magneto-optical effect associated to the polaron hopping in the spectral region SF (when the spin is reversed during the transition).

Looking at equations 3.10 and 3.11 we can easily understand why these transitions are sensitive to polarized light. In our set-up for the polaron movement, we have an initial angular momentum $J_z = 1/2$ and an axial symmetry. Thus, processes must conserve this total angular momentum and simple spin-reversal is forbidden as it alters this quantity. However, under polarized light the necessary orbital angular momentum can be gained through the radiation, yielding the magneto-optical effects associated to spectral region SF (figure 3.14 c).

Moreover, using equations 3.26 and 3.27 we can now understand the enhancement of the gyrotropic activity as the system gets closer to the transition temperature. As previously remarked, the average Jahn-Teller distortion Q_{JT} gets larger as the temperature rises towards Tc. This means that as electrons get more localized approaching the magnetic transition the denominator in equations 3.26-3.27 gets smaller and the transition probability increases. Thus, the electron-lattice coupling in these systems (perovskites) plays an important role enhancing the effect of the spin-orbit coupling.

3.5 Influence of the structure quality on the polaronic response

Finally, we have explored the influence of the structure quality on the intrinsic MO effect of polarons by measuring LCMO films with different thickness and with distinct $SrTiO_3$ substrate orientations. This idea has been motivated by previous studies [120, 121] where the structural features have been studied as a function of the thickness and the substrate orientation. These features plays a role on the cationic disorder having an impact on the transport properties of manganites [14], hence, we expect a direct impact on the polaronic response of LCMO. To test this idea, $La_{2/3}Ca_{1/3}MnO_3$ thin films were grown by rf sputtering on (110) and (001)-oriented $SrTiO_3$ single crystals. During the deposition, the substrate was held at a temperature of 800 ºC and a pressure of 330 mTorr, with an O_2/Ar pressure ratio of 1/4. After growth, the samples were annealed in-situ at 800 ºC for 1h in an O_2 atmosphere at 350 Torr.

We have measured the MO effects with PMOKE configuration at $\lambda = 402$ nm around the ferromagnetic transition on three different samples: (110)- and (001)-oriented

93 nm thick samples and (110)-oriented 17 nm sample. As shown in the figure 3.15 (a), only the 93 nm thick sample (110)-oriented $SrTiO_3$ shows a MO enhancement similar in nature to the 80 nm thickness sample on (110)-oriented $SrTIO_3$ (results presented in the section 3.3). However, the MO transition for the 93 nm thick sample on (001)-oriented $SrTiO_3$ shows a much broader and less pronounced enhancement than in the (110)-oriented sample (figure 3.15 a). In addition to the 93 nm-thick film, we have also measured the MO transition of a 17 nm thick (110)-oriented sample. The temperature dependence of the MO signal indicates that there is also some sort of MO enhancement around Tc, although the peak around the transition temperature is still broader and smaller than in the case of the 93 nm-thick sample. In order to correlate the MO enhancement observed in these films with the emergence of self-trapped polarons, the MR response has been measured in a TMOKE configuration at $\lambda = 475$ nm. These results of these measurements are shown in figure 3.15 (b), where the data of the 80 nm-thick (110)-oriented thin film analyzed in previous sections is also included. The data in figure 3.15 (b) show that the highest and narrower MR peak is observed for the sample of 93 nm on $SrTiO_3$ (110), while a weaker and broader MR peak is measured for the 93 nm-thick 001 oriented film. Finally, the thinnest sample (17 nm) on (110) substrate shows only a small and much broader MR response (figure 3.15 b). Summing up, the data displayed in figure 3.15 shows that in order to have a clear well-defined and large MO enhancement, the emergence of self-trapped polarons –revealed by the measurement of the MR response– has to be restricted to a very narrow range of temperatures around Tc. If, for whatever the reason, the emergence of self-trapped is distributed across a wide range of temperatures –as the MR data show– for the case of the (001)-oriented 93 nm and 17 nm-thick samples, see figure 3.15 (b), then the MO enhancement is much less pronounced. As discussed next, the temperature dependence of the distribution of self-trapped polarons is presumably strongly dependent on the structural properties of the thin films.

The strong sensitivity of the optical properties on the structural features may be explained in terms of cationic disorder. For instance, previous studies describes how LCMO grows on $SrTiO_3$ [120, 121]. Due to the mismatch between the cell parameter of LCMO and $SrTiO_3$, different mechanisms of relaxation takes place depending on the LCMO thickness, the substrate orientation and affecting the cationic ordering. General features can be summarized: cell parameters of LCMO films grown on (001) $SrTiO_3$ are closer to cell parameters of $SrTiO_3$ bulk than LCMO films on (110) $SrTiO_3$ and becomes more pronounced lowering the thickness. Another important observation is the appearance of a Mn^{4+} peak in the NMR spectra measured at temperatures below the ferromagnetic transition in the (001) samples indicating the presence of ferromagnetic insulating phase with localized charges. This phase is absent in the (110) films [120]. This Mn^{4+} peak depends on the thickness, decreasing for large thickness. This behaviour is a consequence of a mechanism for cell-parameter matching that uses cation migration for elastic strain accommodation, due to the larger ionic size of La^{3+}

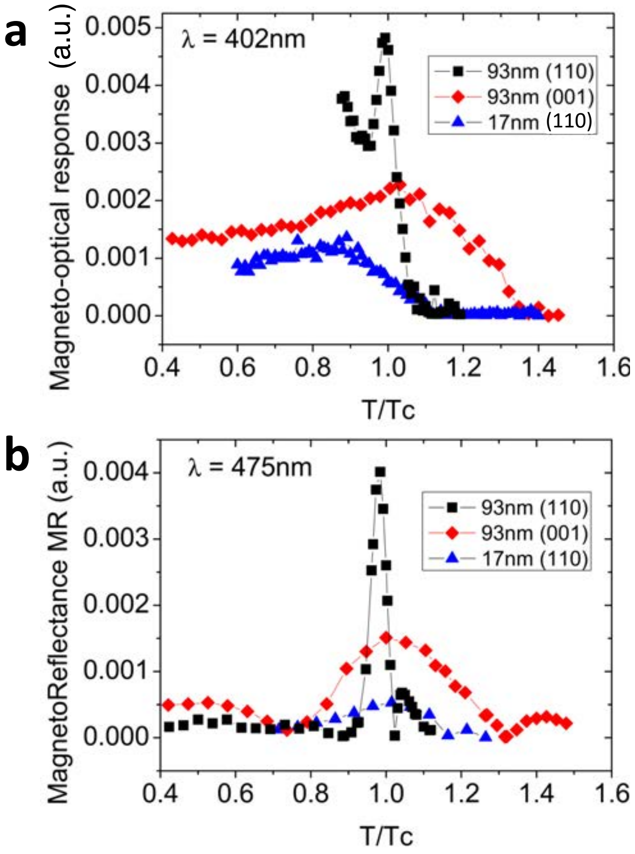

FIGURE 3.15: (a) MO response measured with PMOKE at $\lambda = 402$ nm of a 93 nm (black squares) and 17 nm (blue triangles) thick LCMO samples on (110) $SrTiO_3$ and 93nm thick LCMO sample on (001) $SrTiO_3$ (red rhombus). (b) MR response measured with TMOKE at $\lambda = 475$nm.

than Ca^{2+}, an enrichment of La^{3+} is found close the $SrTiO_3$ interface [121]. Therefore, two relaxation mechanisms are present on (001) and (110) films giving rise to small differences in the functional properties of these films [120, 121]. Our observation fits on this view. The MO and MR responses of thinnest sample on (110) are similar to the 93 nm sample on (001) because the transition is broader as the thickness decreases and due to the different relaxation mechanisms for (001) and (110).

Birefly, the MO enhancement intrinsic to polarons described in the present chapter has been only observed for samples around 80nm on (110)-oriented $SrTiO_3$ with a sharp metal insulator transition. The effects of the MO enhancement are strongly reduced and more difficult to observe when the thickness of LCMO films is decreased or when the growth proceeds on (001)-oriented substrates, where structural relaxation mechanisms can, as discussed above, lead to important changes in the cationic spatial distribution across the sample. We can conclude, then, that the distribution of self-trapped polarons around the transition temperature is extremely critical to observe the phenomenon. Therefore, a sharp ferromagnetic transition –with a narrow distribution of self-trapped polarons, particularly peaked around the transition– is required to observe the giant gyrotropic enhancement.

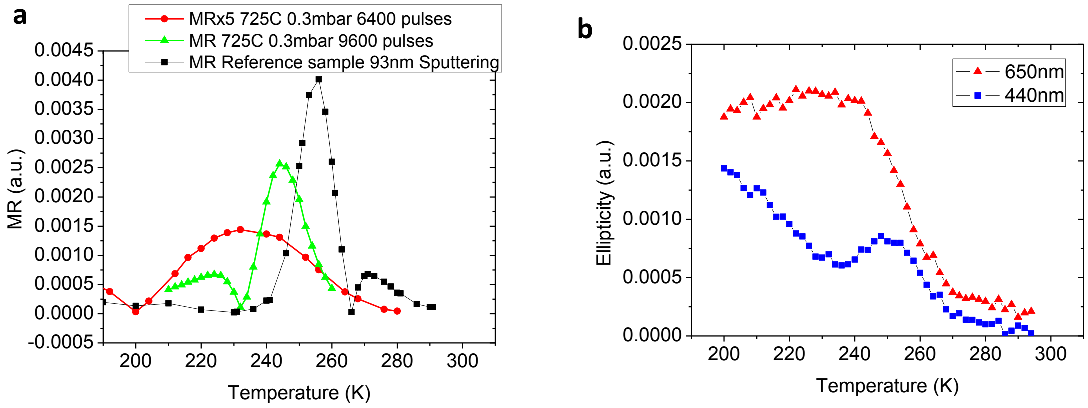

FIGURE 3.16: (a) MR response of thin films grown by PLD (725 ºC, 0.3 mbar PO_2) for 6400 pulses (red circles, signal multiplied by 5) and 9600 pulses (green triangles). As a comparing reference, the MR response of the 93 nm sample grown by sputtering is plotted (black squares). (b) MO response of the 9600 pulses sample measured with PMOKE. A typical transition is shown at $\lambda = 650$ nm (blue squares). However, a peak in the ellipticity appears at $\lambda = 440$ nm (red triangles).

In order to corroborate this view, we have grown new films on $SrTiO_3$ (110) with a different growth technique (PLD) changing the growing conditions as a function of the feedback of the optical measurements trying to reach the narrowest MR peak. First we have adjusted the growth parameters in order to get reasonable values of magnetization and a Curie temperature close to 260 K. After reaching these growth conditions (700 ºC, 0.3 mbar P_{O_2}) we have played as a function of the thickness varying the number of pulses, guessing that a similar relaxation process than the previous growth using magnetron sputtering occurs also by PLD. In the figure 3.16 (a) show the MR response of two samples grown by PLD using the same growth conditions but increasing the thickness, the sample with 9600 (90 nm aprox.) pulses show a narrow MR peak and notice that, as it is expected, the sample of 6400 pulses (60nm aprox) show a broader MR peak with much lower response. Therefore it seems than the previous view can also explain this behaviour. In the same figure is plotted the MR peak of the 93 nm sample grown by sputtering as a reference. Any visible peak appear in the MO activity measured using TMOKE in both samples. However, measuring around the transition by PMOKE, a peak appears in the MO activity at $\lambda = 440$ nm in the thickest sample. In order to check if this peak have the same polaronic origin, as described previously, we have measured the same temperature range at $\lambda = 650$ nm and as it is expected, the MO peak has completely vanished (figure 3.16 b). Comparing this response to the sample of similar thickness grown by sputtering, even though there is a peak in the MO activity, this enhancement is now much lower. However, similar thickness dependence is observed suggesting a similar relaxation mechanism than the samples grown by sputtering, playing also a role on the cationic ordering and modifying the polarons formation around the curie temperature. We can conclude that, to observe a clear peak on the MO activity, a narrow MR peak is needed, indicating that the polaron's formation is narrowly around the Tc. Further characterization is needed to improve our knowledge of how to maximize the intrinsic contribution of polarons in LCMO manganites.

3.6 Conclusions and perspectives

As a conclusion, our finding reveals an unreported physical mechanism for enhanced gyrotropic responses. Interestingly, the observed polaron-induced enhancement is comparable in magnitude with the gyrotropic increase observed in magnetic media coupled to plasmons, where the magneto-optical activity is enhanced by more than one order of magnitude for wavelengths that are correlated to the excitation of propagating or localized surface plasmons [122]. Yet, the latter represent extrinsic routes for the magneto-optical enhancement, which require the gyrotropic media to be suitably nanostructured to couple the magneto-optical effects to either photonic band edges [123, 124], or to plasmon resonances [125, 126]. In contrast, here we show that there is another mechanism, which is intrinsic to the material by which self-trapped polarons can increase remarkably the magneto-optical response. The case of polarons is particularly interesting, since they are ubiquitously inherent to many strongly correlated electronic systems. One can, therefore, imagine that the exploitation of polarons may be also instrumental to achieve large gyrotropic responses in other materials. This opens up enticing perspectives. On the one hand, because the phenomenon has been observed in the vicinity of room temperature and rising the effect to higher temperatures may be envisioned by materials engineering, e.g., by partial substitution of Ca by Sr or Ba [127, 128], which are known to increase the Curie temperature in manganites. On the other hand, polarons may be rather sensitive to strains, so that their emergence might be adjusted eventually by electric fields through the piezoelectric effect. If successful, the latter prospect might enable a very large modulation of the magneto-optic activity by electric fields, thus opening novel avenues for magnetoelectric coupling beyond the conventional modulation of magnetization. This last possibility is very appealing. However, as discussed in Section 3.5 the structural quality, which ultimately determines the distribution of self-trapped polarons in the system, is a very important aspect to have a large MO enhancement. In this sense, growing LCMO films on piezoelectric substrates with the high structural quality required to have the appropriate distribution of self-trapped polarons is not an easy task and poses an interesting and challenging problem of materials engineering.

Chapter 4

Cation-specific contributions to the magnetism of Ce-doped YIG

4.1 Introduction

In the previous chapter we have shown an enhancement of the MO activity in LCMO films due to changes in its electronic structure caused by the emergence of small polarons. In the present chapter we describe our research in material in which the MO enhancement is due to the effects of chemical doping on the electronic band structure. Specifically, we have studied the effects of doping Yttrium Iron Garnet (YIG), with a rare-earth ion, Ce in this case, on the MO response and the magnetization.

YIG is an insulator ferrimagnet with remarkable small Gilbert damping parameters and for these reason YIG becomes an appropriate material for magnonics [129], spintronics [130, 131], and spin caloritronics [132, 133, 134]. Moreover, because of its transparency and its large MO activity specially in near IR, it has been used in non-reciprocal devices for optical communications [135, 136, 20, 19, 137, 138, 139]. The incorporation of rare-earth elements into YIG can give rise to an enhancement of its MO activity [140, 17, 16, 141, 96] which is highly desirable for these applications. This enhancement has been interpreted to arise by the emergence of two new types of electronic transitions: (i) intra-atomic orbital dipole transitions between the $4f$ and $5d$ states of Ce and (ii) interatomic dipole transitions between the $4f$-Ce and $3d$ states of Fe [21, 16, 22]. It is unclear, though, whether both transitions are involved or if one of them is prevailing over the other. Bearing this in mind, and with the purpose to understand the impact of Ce doping on the magnetic and electronic properties [16, 22], we have undertaken an extensive study combining different experimental methodologies. A first step towards this direction has aimed at untangling the individual contributions of Ce and Fe ions to the magnetism of Ce-YIG samples. For that purpose, we have first performed a magneto-optical spectroscopic study of CeYIG samples. As a result of this study, we have found that, especially for some range of frequencies, the measured hysteretic magneto-optical loops are anomalous. We have interpreted this anomaly as arising from two different MO hysteretic contributions coming from the Ce and Fe sublattices. To understand better the plausibly different magnetic behavior of the Ce and Fe ions, we exploited element-specific techniques (XAS and XMCD) to have access to the electronic structure of the Ce/Fe cations and their specific contributions to the magnetism of doped YIG. Summarizing, our results show that Ce-doping triggers a selective charge transfer from Ce to the Fe tetrahedral sites in the YIG structure. This, in turn, causes a disruption of the electronic and magnetic properties of the parent compound, reducing the exchange coupling between the Ce and Fe magnetic moments and causing atypical magnetic behaviour.

Our study establishes a step forward in the comprehension of the fundamental physical processes caused by Ce doping in the electronic and magnetic properties of the YIG parent compound. This knowledge can be eventually used to further optimize and tailor the optical properties of these important materials.

4.2 Material preparation and characterization

YIG has a $Y_3{}^c[Fe_2]^a[Fe_3]^dO_{12}$ composition with a complex cubic structure (space group $O_h^{10} - Ia\overline{3}d$). As shown in figure 4.1, the non-magnetic Y^{3+} ions occupy dodecahedral (c) sites while the Fe^{3+} ions occupy both tetrahedral (d) and octahedral (a) sites in the oxygen polyhedron structure. The ferrimagnetism arises from the antiferromagnetic coupling between the two Fe^{3+} cations in a-sites and the three Fe^{3+} in d-sites creating an uncompensated magnetic moment. The origin of this coupling comes from the superexchange interaction via the O^{2-} anions.

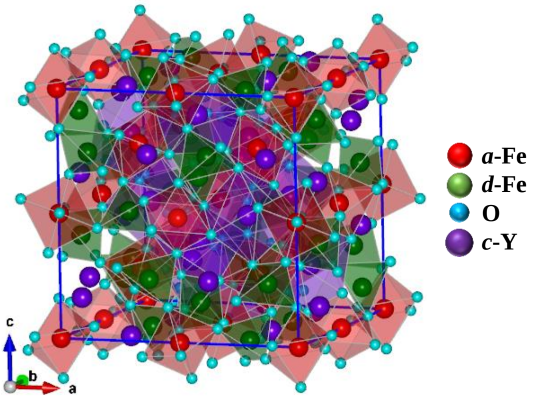

FIGURE 4.1: Schematic diagram of the YIG crystal structure.

4.2.1 Growth and structural characterization

Due to YIG's complex structure, the substrate can play a critical role on the crystal quality and its properties. For the deposition of Ce-YIG and YIG thin films, we used (001)- and (111)-oriented gadolinium gallium garnet (GGG) crystals with a thickness of $\sim 500\ \mu$m, which are frequently used for the growth of high-quality YIG films [142] due to the small lattice mismatch (0.057%). The samples were grown in oxygen atmosphere by PLD using an excimer laser at 10 Hz. The Ce-YIG films of composition $CeY_2Fe_5O_{12}$ and thicknesses $t \approx 54$ nm (for the (001)-oriented Ce-YIG) and $t \approx 56$ nm (the (111)- oriented Ce-YIG) were grown at 880 ºC in an oxygen partial pressure of 0.3 mbar, whereas the (111)-oriented YIG films of composition $Y_3Fe_5O_{12}$ and thickness $t \approx 200$ nm were deposited at 550 ºC and 0.2 5mbar.

After the growth, we have checked the structural parameters by X-ray diffraction (XRD) analysis done in the Bragg-Brentano geometry using the Cu-Kα radiation. The $\theta - 2\theta$ XRD scan of the Ce-YIG/GGG(001) film shows a Ce-YIG(004) reflection as a pre-peak feature to the strongest GGG(004) reflection that arise from the substrate (figure 4.2 a). In addition, the XRD pattern did not reveal any additional peak indicating other grown phases such as CeO_2. Apart from the (004)-reflection, the GGG substrate shows a small (006)-reflection possibly due to non-perfect atomic ordering of the substrate [142]. In order to have a more detailed information, we have performed $\theta - 2\theta$ XRD scans of Ce-YIG(001) and Ce-YIG(111) films, respectively, collected around their main respective peaks (Figures 4.2 b and c). Even though the peak reflections of the films cannot be clearly resolved, we could observe the Laue oscillations testifying the high quality of the films.

4.2.2 Spin dynamics

To obtain information on the spin dynamics of Ce-YIG films we performed FMR experiments where the absorbed signal was recorded while the applied magnetic field was swept and the microwave frequency was fixed at certain values. In figure 4.3 (a) we plot representative curves of the amplitude of transmission coefficients (S_{12}) as a function of the magnetic field for different frequencies (5, 11 and 17.5 GHz) on both (001)- and (111)-oriented Ce-YIG thin films. These curves were fitted using the Lorentz equation:

$$S_{12}(H) \propto \frac{(\Delta H)^2}{(H_{FMR} - H)^2 - (\Delta H)^2} \tag{4.1}$$

where H_{FMR} is the magnetic field under the resonance condition, and ΔH is the half linewidth. Figure 4.3 (b) shows the parameter ΔH extracted from the fittings as a function of the excitation frequencies. We thus determine the Gilbert damping by fitting the data (straight lines) using the following equation:

$$\Delta H = \Delta H_0 + \frac{2\pi}{\gamma} \alpha f \tag{4.2}$$

where γ is the gyromagnetic ratio ($\gamma/(2\pi) = 27$ GHz/T), α is the Gilbert damping, and ΔH_0 is the inhomogeneous damping of the films. We have obtained a good estimation of the Gilbert damping values of $\alpha = 0.025$ and $\alpha = 0.035$ for (001)- and (111)-orientations, respectively. In fact, the above values are very close to those reported previously for Ce-YIG thin films [142]. The slightly larger damping of the (111)-oriented

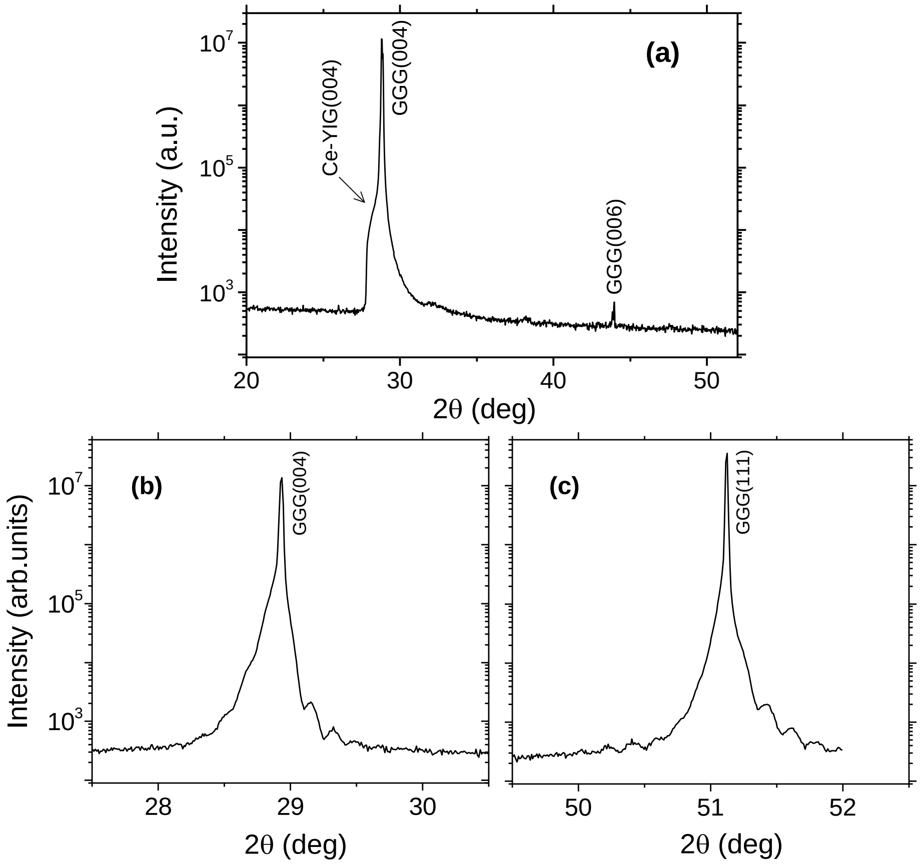

FIGURE 4.2: XRD pattern of Ce-YIG thin film grown on GGG(001) substrate.This scan shows a Ce-YIG(004) reflection as a shoulder to the strong GGG(004) reflection from the substrate. XRD scans of (b) Ce-YIG(001) (c) Ce-YIG(111) films show the Laue oscillations, which indicates the films are in good epitaxy.

film might be related to some induced magnetic anisotropy induced during growth. As discussed by Kehlberger et al. [142], this observation is supported by the different strain states of the (111)- and (001)-oriented films, plausibly leading to a magnetoelastic contribution to the magnetic anisotropy.

We also notice that the damping values of Ce-YIG films are considerably larger than those usually reported for undoped YIG films, which are in the order of 10^{-4} [142]. As discussed previously by other authors [142], this reduction of about two orders of magnitude can be explained from various contributions, such as lattice dilation and different environments of the Fe cations due to the Ce-doping. These observations are also in agreement with the values that we obtain for the inhomogeneous damping, since our analysis yields values around $\Delta H_0 \approx 5\,\mathrm{mT}$, which are considerably larger than in undoped YIG films (< 0.5 mT) [142]. We stress, however, that despite the higher damping values in Ce-YIG films, the damping parameters are comparable to most of the metallic ferromagnetic systems [143, 144].

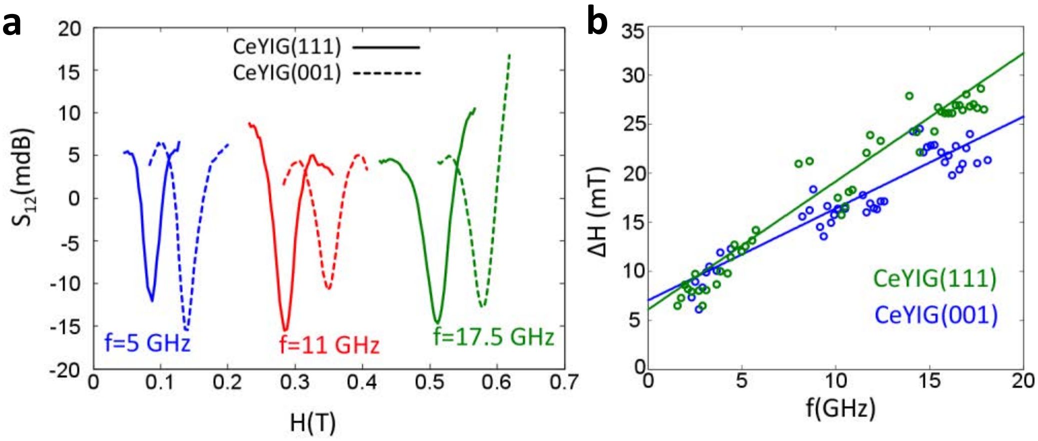

FIGURE 4.3: Gilbert damping of FMR response in Ce-YIG thin films. (a) FMR spectra of the (001) and (111)- oriented Ce-YIG films for the frequencies: f= 5, 11, and 17.5 GHz. (b) The FMR peak linewidths as a function of the resonance frequencies. Straight lines are the best fits based on equation 4.2.

4.2.3 Magnetic characterization

Finally, magnetic characterization has been done using SQUID magnetometer at room temperature. A strong paramagnetic signal from the GGG substrate is superposed to the hysteresis response of the CeYIG film, as illustrated by the measurement of (001)-oriented sample (figure 4.4) for the magnetic field applied in-plane. The inset shows a zoom taken at low magnetic field where an hysteresis behavior can be appreciated. The magnetization can be estimated at remanence, where the magnetic contribution of the substrate is zero. Thus, our films show smaller magnetization at remanence (75-100 emu/cm^3) than bulk (140 emu/cm^3) and also smaller than films reported in [142] at saturation (152±8 emu/cm^3). Usually, in order to disentangle the response of the film from the paramagnetic signal of the substrate a mathematical treatment is needed. For instance, subtracting a slope fitted on the measured signal at magnetic fields higher than the saturation of the film. However, this method can introduce artifacts to the shape of the hysteresis and information of the an eventual saturation slope intrinsic of the film could be lost. To overcome these difficulties, we have used Kerr MO spectroscopy which is known to be more sensitive to the film magnetization. In the next section, we show a wavelength-selective method able to measure purely the film signal without needing a post data processing.

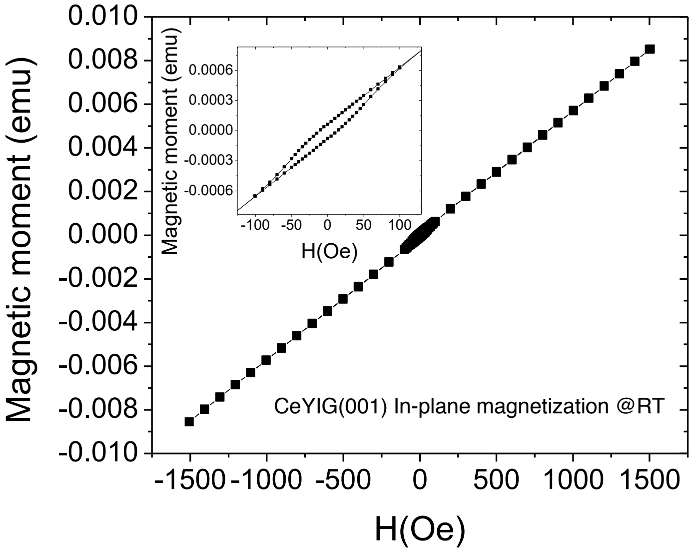

FIGURE 4.4: Magnetic characterization of CeYIG/GGG(001). A paramagnetic signal from the GGG substrate is superimposed to the ferromagnetic response of the film. Inset shows a zoom between -100 and 100 Oe where the ferromagnetic signal of the film can be observed.

4.3 MO spectroscopy of undoped and Ce-doped YIG

Taking advantage of the wavelength selectivity of the MO spectroscopy, we have explored the consequences of doping YIG with Ce to the MO activity. However, as previously shown on the magnetization measurements, a strong paramagnetic signal coming from the GGG substrate also affects the MO signal. In order to solve this issue, a strategy has been developed to cancel the substrate contribution. First of all, we measured the polar Kerr rotation (θ) and ellipticity (ϵ) of the (001)- and (111)-oriented GGG crystals. The $\theta(\lambda)$ and $\epsilon(\lambda)$ spectra for both orientations measured at a magnetic field $H \approx 17.5$ kOe turned out to exhibit similar wavelength dependence (figures 4.5 a and b). While the Kerr rotation preserved the sign for all wavelengths, the ellipticity reversed sign twice, with two particular frequencies at which the ellipticity vanished, namely, $\lambda_1 \approx 450$ nm and $\lambda_2 \approx 550$ nm (figures 4.5 a and b). This is readily seen in the ellipticity loops measured at different wavelengths around λ_1 (figure 4.5 c). At wavelengths below λ_1, the ellipticity exhibits a linear dependence with the field having a positive slope. In contrast, at wavelengths above λ_1, the slope reverses sign (figure 4.5 c), indicating that the ellipticity decreases on increasing the field. Just in the vicinity of λ_1, the ellipticity is vanishingly small for any value of the magnetic field. The same figure shows the ellipticity data of GGG corresponding to wavelengths around λ_2.

The selection of wavelengths λ_1 and λ_2 at which the ellipticity of GGG vanishes has been used as the sweet spot to probe the properties of YIG and Ce-YIG films, as it allows to virtually cancel the paramagnetic contribution from GGG leaving that of

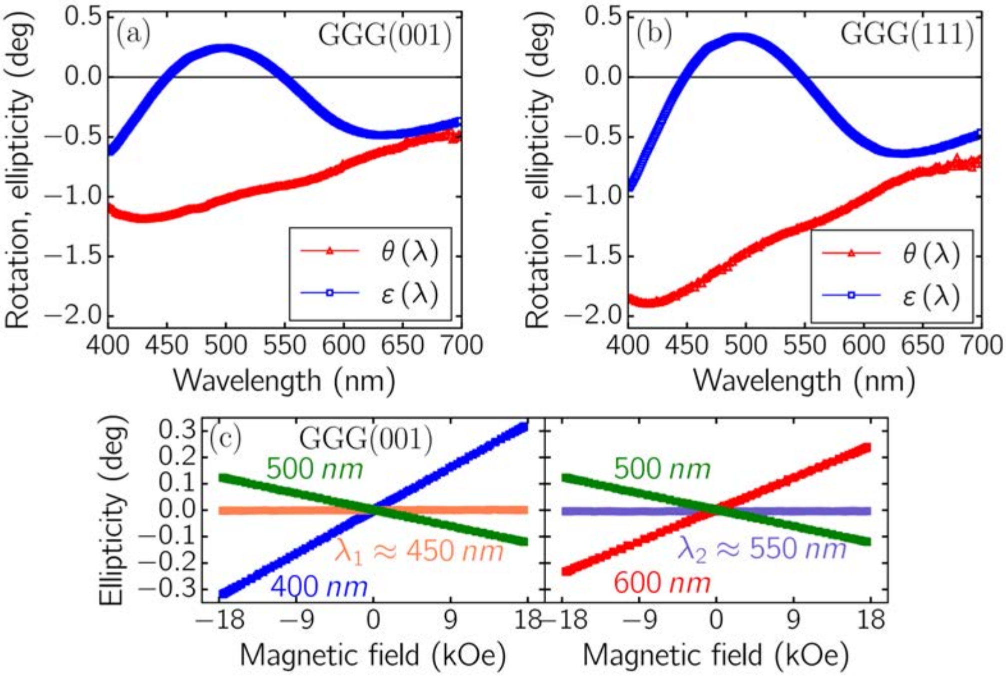

FIGURE 4.5: Spectra of the Kerr rotation $\theta(\lambda)$ and ellipticity $\epsilon(\lambda)$ of a (001)-oriented GGG crystal (a) and (111)-oriented GGG crystal (b), measured at a field $H \approx 17.5$ kOe. (c) The ellipticity of the (111)-oriented GGG crystal measured at different wavelengths is plotted as a function of the magnetic field. The wavelengths λ_1 and λ_2 at which the ellipticity of GGG vanishes are identified from this data.

CeYIG accessible. For instance, figures 4.6 (a) and (b) display, respectively, the ellipticity of the (001) oriented Ce-YIG film around λ_1 and λ_2. In both cases, we observed loops that exhibited a positive or negative slope at the highest fields, revealing the contribution of the GGG crystal at wavelengths shorter or longer than λ_1 or λ_2. Interestingly, figures 4.6 (a) and (b) show that for wavelengths in the vicinity of λ_1 and λ_2, the slope of the hysteresis loops at high fields is the smallest; since these are precisely the wavelengths at which the substrate contribution vanishes, we can therefore infer that the ellipticity intrinsic to the Ce-YIG films nearly saturates. Additionally, the hysteresis curves shown in figure 4.6 (c) also indicate that the magnetization increases faster along the $\langle 111 \rangle$ direction, in agreement with previous studies reporting on the magnetic anisotropy of YIG [145].

The previous discussion gives unambiguous evidence that the measurement of ellipticity enables the access to the intrinsic magnetic properties of YIG and Ce-YIG films grown on GGG. We have taken this vantage point to scrutinize their gyrotropic response, with an emphasis on untangling any eventual individual contribution from cerium and iron to the magneto-optical activity. A useful insight is provided by the analysis of the spectral dependence of the shape of the hysteresis loops. In the case

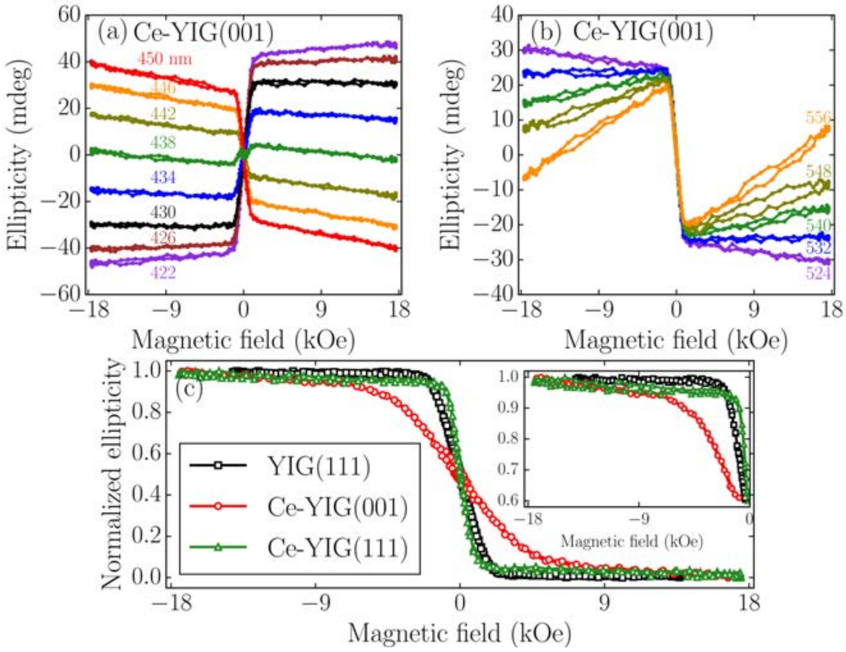

FIGURE 4.6: Ellipticity loops of the (001)-oriented Ce-YIG measured in the vicinity of (a) $\lambda_1 \approx 450$ nm and of (b) $\lambda_2 \approx 550$ nm. (c) Ellipticity curves of the (001)- and (111)-oriented Ce-YIG as well as the undoped (111)-oriented YIG, measured at $\lambda_1 \approx 450$ nm. The inset shows a zoomed in region of the loops around the highest applied fields.

analyzed here, the ϵ-loops of the Ce-YIG films display an unusual shape when measured at wavelengths in the vicinity of $\lambda = 440$ nm, exhibiting a wavy magnetic field dependence in the central part of the loops (figures 4.7 a and b). As seen in the insets of figures 4.7 (a) and (b), this atypical behavior disappears gradually as soon as the wavelength moves away from $\lambda = 440$ nm, at which point the loops progressively recover the usual shape.

We address now the origin of such anomalous loops. Extracted from the SQUID measurements (shown in the previous section), the magnetization of the Ce-YIG films analyzed in this study turned out to be substantially smaller (75–100 emu/cm^3) than values reported elsewhere [142] and bulk (140 emu/cm^3). We may speculate whether the existence of some defects, particularly antiphase boundaries, which could cause the magnetization drop, could partly explain the abovementioned atypical shape of loops. Yet, the fact that this phenomenon is only observed for an extremely narrow range of wavelengths (see below) is a clear indication that alternative scenarios have to be envisioned to explain the emergence of anomalous loops. In this sense, the most plausible explanation for the unusual hysteresis is that it arises from the superposition of two independent ellipticity loops with opposite signs. The two-contribution scenario goes a long way towards explaining the observed complex loop behavior and was indeed originally proposed by other authors to explain similar anomalies in the Faraday hysteresis loops of the bismuth-doped garnets [146].

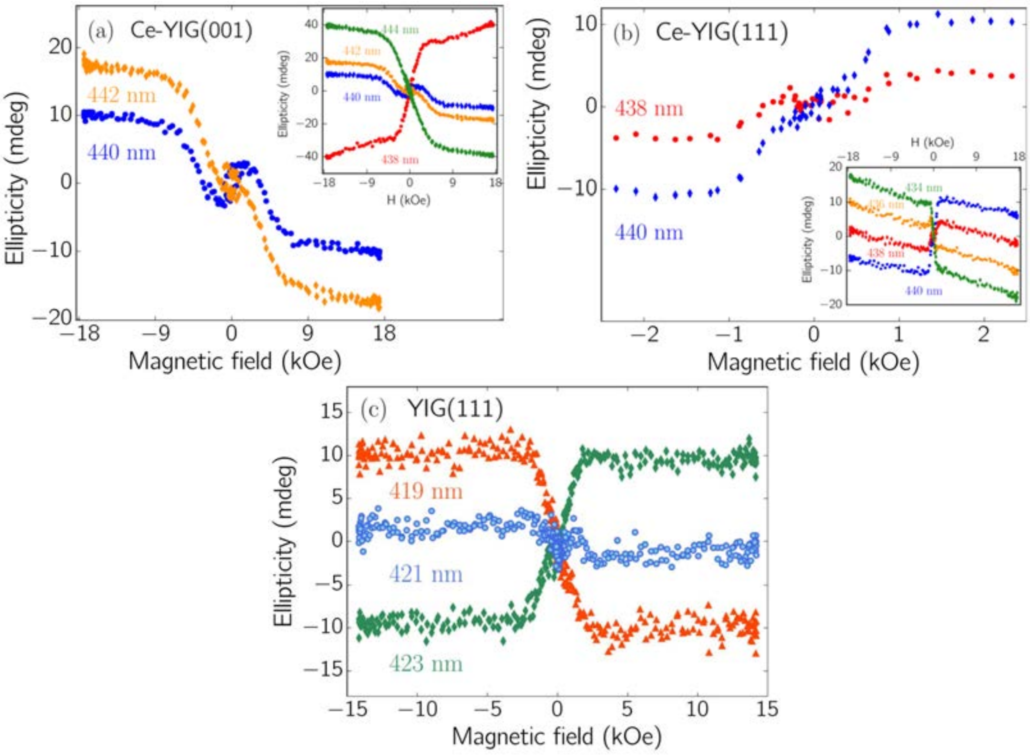

FIGURE 4.7: Panels (a) and (b) show the ellipticity loops of (001)- and (111)- oriented Ce-YIG films, respectively. The displayed curves were measured at wavelengths for which they exhibited an anomalous dependence on the magnetic field. These critical wavelengths were close to the point where the ellipticity curves reverse sign (see the insets). In contrast, undoped (111)- oriented YIG did not show any atypical hysteresis curve at any wavelength, see panel (c).

Different hypothesis can be put forward to explain the emergence of two distinct hysteresis contributions. One first possibility is that Fe at tetrahedral and octahedral coordination sites contribute differently to the ellipticity [146]. Another option is that one of the two contributions is linked to the iron sites-whatever in tetrahedral or octahedral coordination- while the other is related to cerium in dodecahedral sites. To discern which scenario is at play, we have analyzed the spectral response of the undoped YIG. As revealed from inspection of figure 4.7 (c), the ellipticity loops of YIG display a conventional shape for all wavelengths, including those straddling the wavelengths at which the ellipticity reverses sign. We conclude, therefore, that the atypical loops observed in doped YIG are related to the presence of Ce on the system.

To gain insights into this issue, we fitted the experimental hysteresis curves to the expression:

$$\epsilon_{fit} = A_1 erf\left(\frac{H - H_{C_1}}{H_{S_1}}\right) + A_2 erf\left(\frac{H - H_{C_2}}{H_{S_2}}\right) + A_3 H \tag{4.3}$$

where H_{C_1}, H_{C_2} and H_{S_1}, H_{S_2} are the coercive and saturation fields of the two contributing loops named Hyst1 and Hyst2, respectively, H is the magnetic field, and A_1, A_2, and A_3 are the weights of the different terms to the simulated ellipticity ϵ_{fit}. Equation 4.3 uses the fact that hysteresis loops may be approximated by error functions or hyperbolic tangents [146, 147]. This approximation is sufficient because our main purpose is to disentangle quantitatively the two contributions. For our simulations, we have chosen to feed the abovementioned parameters into the error function:

$$erf(x) = \frac{2}{\sqrt{\pi}} \int_0^x \exp(-t^2)dt \tag{4.4}$$

The first two terms of equation 4.3 take account of the two hysteresis curves contributing to the ellipticity, while the last term is plausibly related to the residual ellipticity of the GGG substrates when the gyrotropic response is measured for wavelengths slightly off λ_1 or λ_2, so that the contribution from GGG is not strictly null. In the analysis, a least-squares method was used to approximate the Hyst1 and Hyst2 curves to the experimental data. For the quality assessment, the correlation coefficient was used, defined as:

$$r^2 = \frac{\sigma_{\epsilon\lambda}}{\sigma_{\epsilon\epsilon} \times \sigma_{\lambda\lambda}} \tag{4.5}$$

where $\sigma_{\epsilon\lambda} = \sum_i(\epsilon_i - \bar{\epsilon})(\lambda_i - \bar{\lambda})$, $\sigma_{\epsilon\epsilon} = \sum_i(\epsilon_i - \bar{\epsilon})^2$, and $\sigma_{\lambda\lambda} = \sum_i(\lambda_i - \bar{\lambda})^2$ are the sum of squared values for the set of (ϵ, λ) data points about their respective means. Figure 4.8 (a) shows the particular case of the ellipticity measured at $\lambda = 440$ nm. Interestingly, we observe that the Hyst1 and Hyst2 loops shown in figure 4.8 (a) display different saturation and coercive fields. To evaluate the accuracy of these values, we ran a large set of simulations in which particular values of H_{C_1} and H_{C_2} were imposed in the fittings, while the saturation fields H_{S_1} and H_{S_2} were left free to adjust. The (H_{C_1}, H_{C_2}) and (H_{S_1}, H_{S_2}) parameter datasets were extracted from the fittings with a margin of error $< 5\%$ with a confidence interval of 95%. Figure 4.8 (b) shows the correlation coefficient r^2 mapped as function of values in the (H_{C_1}, H_{C_2}) dataset. We see that the highest-quality fittings were obtained for values $H_{C_1} \approx 310$ Oe and $H_{C_2} \approx 150$ Oe. Outside this region, the values of r^2 were significantly smaller (figure 4.8 b), indicating that solutions other than those mentioned above were unlikely. At values of (H_{C_1}, H_{C_2}) where r^2 is the highest, the anisotropy fields are $H_{S_1} \approx 5850$ Oe and $H_{S_2} \approx 2150$ Oe, respectively. In consequence, the analytical study discussed here is consistent with two hysteresis contributions with slightly different dependence on the applied magnetic field.

The previous analysis can be applied over the all measured spectra, however, it is only within an extremely narrow window of wavelengths that the two contributing loops combine with opposite signs, yielding the anomalous hysteresis shown in figure 4.8. Therefore, it is just inside this limited spectral region that one can reliably deconvolve the two contributions from the as-measured signals. This is illustrated by the

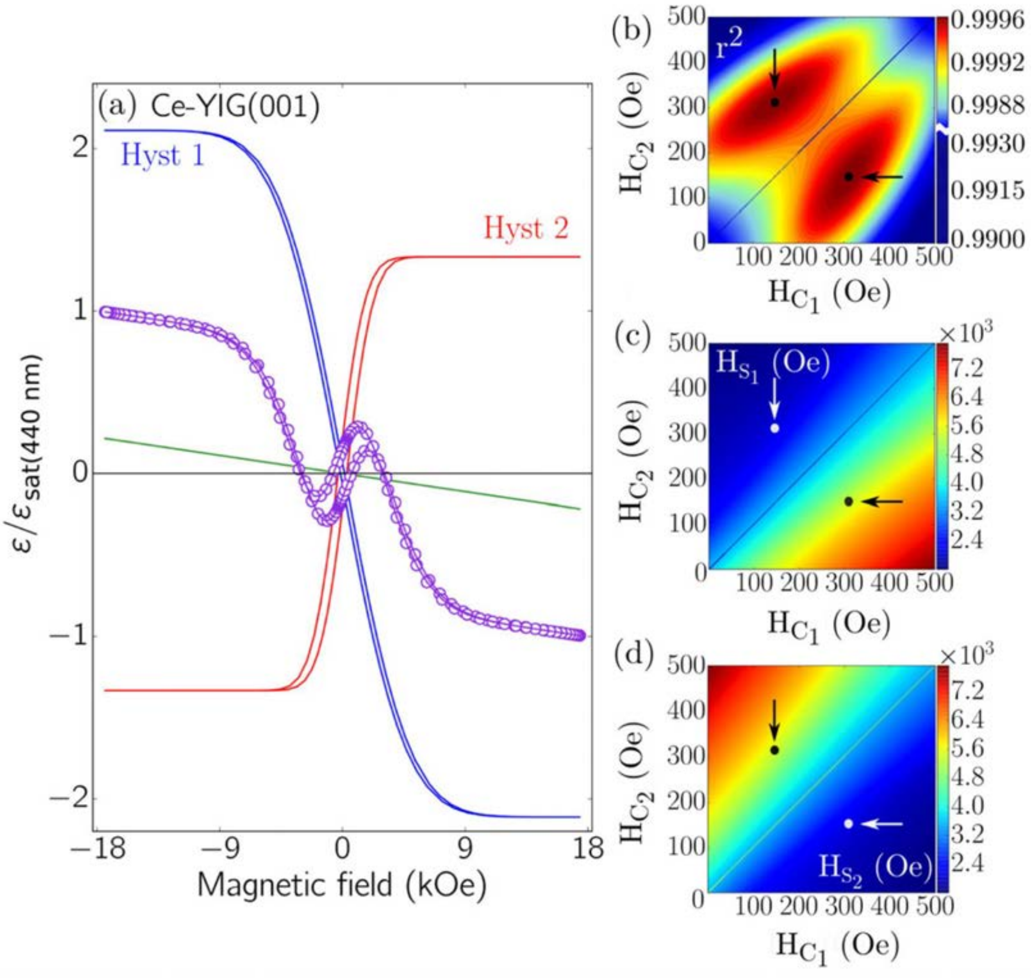

FIGURE 4.8: (a) The ellipticity loop of the (001)-oriented Ce-YIG measured at λ =440 nm (purple) is broken down into the sub-loop components Hyst1 (blue) and Hyst2 (red). For that purpose, fittings to equation 4.3 were used. The plot also includes a residual linear dependence on the magnetic field (green). (b) The correlation coefficient r^2 of the least-squares fitting is mapped against the values of the coercive fields H_{C_1} and H_{C_2} of the simulated Hyst1 and Hyst2 sub-loops. The points at which r^2 is maximum are indicated by small circles in this chart. (c) and (d) map the values of the saturation fields H_{S_1} and H_{S_2} obtained from fittings to equation 4.3; each point of these maps was calculated after fixing in the simulations the values of the coercive fields H_{C_1} and H_{C_2} while H_{S_1} and H_{S_2} were left free to adjust. Small circles in (c) and (d) are at the same location as the maximum value r^2 in (b). The colored vertical bars in panels (c) and (d) refer, respectively, to the magnitude of H_{S_1}, H_{S_2}, given in units of Oe.

analysis of the ϵ loops of the (111)-oriented Ce-YIG film in the range $\lambda \approx 438 - 443$ nm, see figure 4.9. At $\lambda = 438$ nm (figure 4.9 a), one of the contributing loops –Hyst2– is almost zero; the corresponding hysteresis curve displays a conventional loop, bereft of any anomalous shape. In contrast, at $\lambda = 441$ nm (figure 4.9 b), Hyst1 and Hyst2 are finite with opposite signs, and their sum shows the anomalous shape. The magnitudes of Hyst1 and Hyst2 are plotted as a function of wavelength in figure 4.9 (c). Within the interval $\lambda \approx 438 - 443$ nm, the as-measured ϵ-curves can be decomposed into the Hyst1 and Hyst2 loops, thus accessing the individual contributions to the magnetic and gyrotropic response of the Ce-doped YIG. Outside this spectral region, both contributing loops have the same sign and the mathematical decomposition becomes extremely difficult. Therefore, the differential spectral evolution of the gyrotropic response of each cation sublattice can be used as the optimal condition to access each individual contribution to the magnetism of doped YIG.

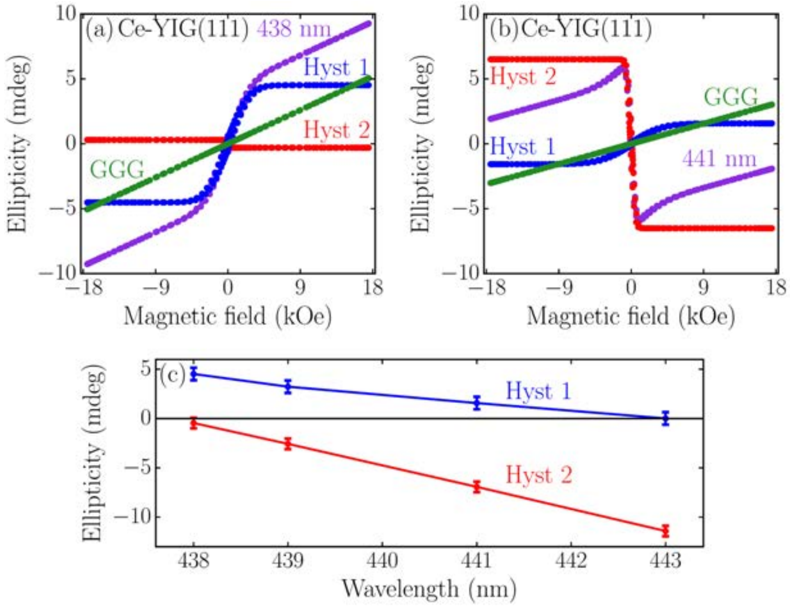

FIGURE 4.9: Plots of the as-measured ellipticity loops of the (111)-oriented Ce-YIG film, measured at (a) λ =438 nm and (b) λ =441 nm, respectively. The figures include the simulated Hyst1 and Hyst2 loops. The magnitudes of Hyst1 and Hyst2 are plotted in (c) as a function of wavelength within the range of λ =438-443 nm. Within this narrow spectral range, the Hyst1 and Hyst2 loops have opposite sign, yielding the anomalous loop shapes displayed in panel (b). The atypical complex dependence of the ellipticity measured in the range of λ =438-443 nm allows a reliable decomposition of the as-measured data into the contributing Hyst1 and Hyst2 loops, enabling the access to the magnetic and optical properties of each ion sublattice.

Briefly, our extensive magneto-optical spectroscopy study reveals that doping YIG with Ce causes the appearance of anomalous MO hysteresis loops, which we attribute to the contributions from different sublattices to global MO signal. Even though the presence of Ce is unambiguously the responsible of these anomalous shape of the hysteresis loops, element-specific techniques, such as XAS and XMCD, are needed to probe the individual magnetic contributions of each ion. Along this line, we anticipate that XAS and XMCD experiments indeed confirm that the doping with Ce induce important changes in the magnetic and electronic properties of YIG that are the ultimate cause of the observed anomalous MO loops and provide important clues to understand the impact of Ce doping on both the electronic and magnetic properties of Ce-YIG system. For instance, our results reveal a charge transfer Ce$^{3+}(4f^1)$+Fe$^{3+}(3d^5) \rightarrow$ Ce$^{4+}(4f^0)$ + Fe$^{2+}(3d^6)$ taking place specifically at the tetrahedral d-sites of Fe, which causes a partial reduction of Fe^{3+} into Fe$^{2+}(3d^6)$. We demonstrate that the ensuing electronic changes alter the exchange coupling constant (J$_{d/a}$) between Fe ions at d- and a-sites. We complete our study with analytic simulations, which consistently explain the Ce and Fe sublattice magnetizations in terms of the reduction of J$_{d/a}$, basically driven by the Ce doping. In the following, we give a detailed description of the experiments and analyses that drive us to reach such conclusions.

4.4 X-ray magnetic circular dichroism

XAS and XMCD measurements (chapter 2) were performed in total electron yield mode at room temperature at the BOREAS beamline of ALBA Synchrotron light source[1] [148]. For Ce, the spectra were taken at the M$_{4,5}$ absorption edges, while for Fe the spectra were recorded at the L$_{2,3}$ absorption edges. XMCD spectra were obtained by taking a difference between the XAS of right (σ^+) and left (σ^+) circularly polarized light. In the XMCD measurements, the samples were magnetized by applying a magnetic field (H) of 2 T along the out-of-plane direction of the films and parallel to the beam. For XMCD data analysis, we have calculated model XMCD spectra using the CTM4XAS 5.5 program which is based on crystal field multiplet calculations including the Slater integrals, crystal field parameters (crystal symmetry, 10Dq, and magnetic energy) and spin-orbit coupling [149]. Site-specific magnetization (M) vs H curves were measured by selecting the photon energies at the XMCD peaks of Fe ions at a-sites, Fe ions at d-sites and Ce ions at the c-sites at the corresponding photon energies. To obtain the above XMCD hysteresis cycles, H was varied between -2 and +2 T, and the polarization of light was successively switched from left- to right-handed circularly polarized light.

4.4.1 Valence states of Ce and Fe: evidence of charge transfer

Firstly, the valence state of Ce were assessed by Ce-M$_{4,5}$ XAS spectra of the (001)- and (111)-oriented Ce-YIG thin films, respectively (figure 4.10 a and b). After normalizing the raw XAS signal with the gold mesh signal, the spectra were further renormalized to unity at the post-edge (912 eV) of the M$_4$ peak. We first draw the attention to the fine structure in the Ce-M$_{4,5}$ spectra, which arises from the multiplet structure of the final

---

[1] I am thankful to Dr. Hari Babu Vasili for his support on the data analysis and for the simulations of the XAS and XMCD spectra.

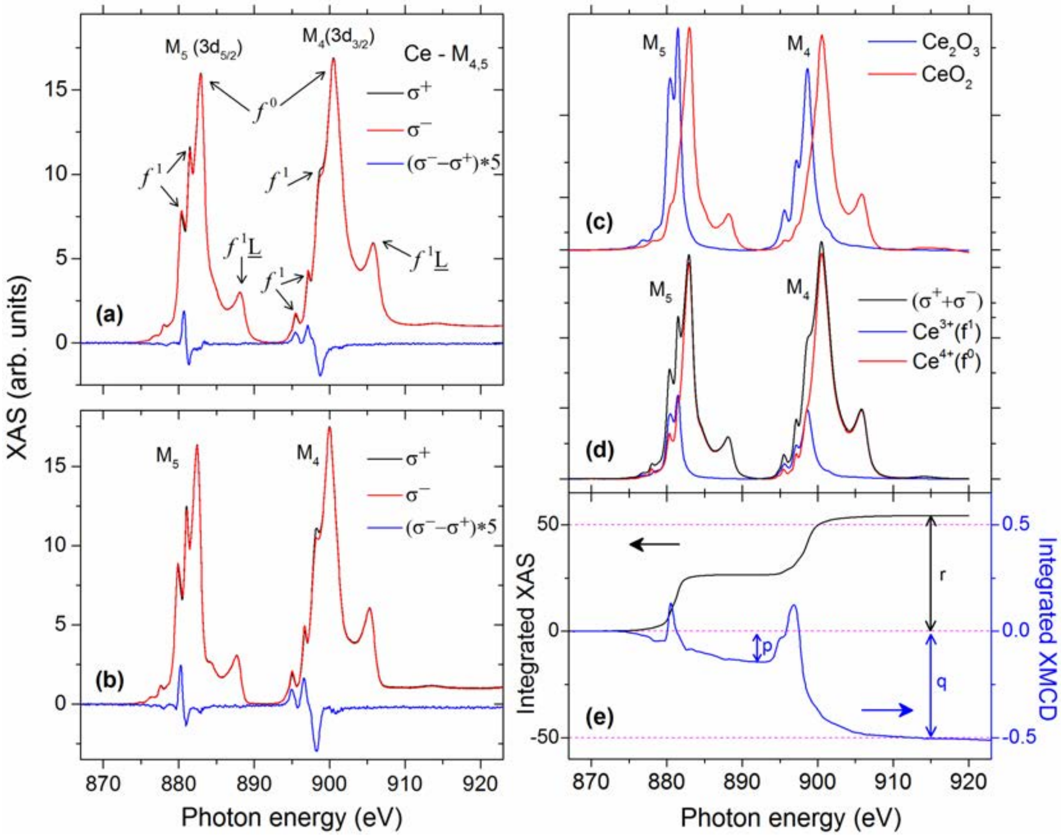

FIGURE 4.10: Ce-$M_{4,5}$ XAS and XMCD of (a) Ce-YIG(001) (b) Ce-YIG(111) thin films at 300 K. The spectral features of mixed Ce^{3+} (f^1) and Ce^{4+} (f^0, f^1L) ground state contributions are well understood from the experimental Ce-$M_{4,5}$ XAS data extracted from reference [150], given in (c). The XMCD ($\sigma^- - \sigma^+$) in panels (a) and (b) arises mainly from the Ce^{3+} contribution. (d) The Ce^{3+} XAS was separated out by fitting the experimental data to the extracted data. Panel (e) shows integration of the Ce^{3+} XAS and XMCD spectra. Read the text for a detailed sum-rule analysis.

states of the Ce^{3+} ($4f^1$) and Ce^{4+} ($4f^0$) ground state configurations. Different spectral signatures can be observed in the XAS spectra, i.e., contributions from Ce^{3+} (f^1), Ce^{4+} (f^0) and Ce^{4+} (f^1L) states as shown in figure 4.10 (a). These signatures enable the identification of the Ce valence states, clearly visible in the experimental XAS data of pure Ce_2O_3 (Ce^{3+}) and CeO_2 (Ce^{4+}) as extracted from [150] (figure 4.10 c). In consequence, we have used these data to quantify the relative amount of Ce^{3+} and Ce^{4+} in our Ce-YIG(001) and Ce-YIG(111) films. Total XAS spectra ($\sigma^+ + \sigma^-$) of the Ce-$M_{4,5}$ recorded from our samples were then fitted to the reference spectra shown in figure 4.10 (c). Such a fitting of the total XAS is shown in figure 4.10 (d) for the Ce-YIG(001) film. From the comparison of spectral weights -shown in figure 4.10 (d) -we could estimate that the fraction of Ce^{3+} is approximately 30%, while the remaining Ce cations are in the Ce^{4+} state.

On the other hand, to unveil the valence states of iron, we analyzed the pre-peak

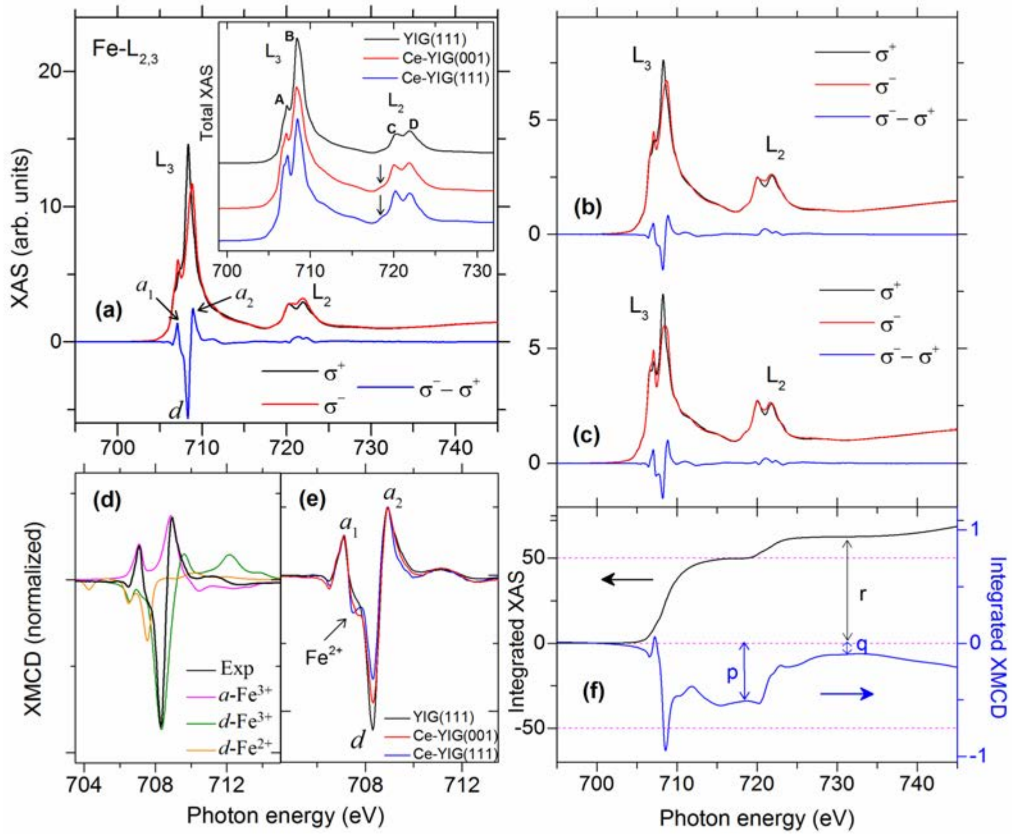

FIGURE 4.11: Fe-$L_{2,3}$ XAS and XMCD of (a) YIG(111), (b) Ce-YIG(001) and (c) Ce-YIG(111) thin films at 300 K. Total XAS ($\sigma^+ + \sigma^-$) in the inset (a) reveals that the YIG film has only Fe^{3+} while the Ce-YIG films exhibit an additional Fe^{2+} contribution. The A/B peak ratio along with the growing L_2 pre-edge feature (shown by arrows) hints at the presence of Fe^{2+} in the films. Panel (d) shows the calculated XMCD spectra for a-Fe^{3+}, d-Fe^{3+}, and d-Fe^{2+} contributions. From this, it appears that the Fe-L_3 XMCD of YIG film has two positive peaks for a-sites and a large negative peak for d-sites. Panel (e) shows a growing extra XMCD peak (shown by arrow) that confirms the Fe^{2+} in the Ce-YIG films. Panel (f) shows the integration of Fe-XAS and XMCD spectra of YIG film. Please refer to the text for the sum-rule analysis.

structure of the L_3-edge (A and B peaks) and the double-peak structure (C and D peaks) of the L_2-edge in the total Fe-$L_{2,3}$ XAS spectra of the Ce-YIG films as well as undoped YIG film (inset of figure 4.11 a). These multiplet analyses could be used as a proxy to determine the valence state of Fe. The $L_{2,3}$-edge spectral features observed in our undoped YIG film (figure 4.11 a) are those typical of Fe^{3+} -similar to, e.g., $\gamma-Fe_2O_3$ structure [151], -in which the A/B peak ratio is ~ 0.46. On the contrary, as seen in figure 4.11 (b) and (c), the Ce-YIG films display significantly higher A/B ratio, ~ 0.62 and ~ 0.70 for (001) and (111)-oriented films, respectively. Therefore, the evolution of the A/B ratio with Ce doping indicates the emergence of a Fe^{2+} oxidation state [151, 152]. This observation is further confirmed by the growing pre-edge Fe-L_2 feature (indicated by arrows in the XAS inset of figure 4.11 a) which is often regarded as the presence of Fe^{2+} in the system [151, 152]. Therefore, the analysis of our XAS spectra shows that doping YIG with Ce induces the concurrent emergence of Fe^{2+} and Ce^{4+} valence states, which gives evidence for a charge transfer from Ce to Fe. Indeed, Ce^{4+} states have been reported for other Ce oxide structures and their origin has been attributed to the hybridization between Ce $4f$ and neighboring O $2p$ or transition metal $3d$ bands [153, 154]. From first-principles calculations reported on Ce-YIG system, it has been known that the charge transfer takes place from Ce($4d$) to Fe($3d$) states at d-(tetrahedral) sites [21]. In the following, we show that this prediction is confirmed by the analysis of our XMCD spectra and further supported by our multiplet XMCD calculations.

The XMCD ($\sigma^- - \sigma^+$) spectrum of the undoped YIG film shows two positive peaks caused by Fe^{3+} ions at octahedral a-sites and one large negative peak for tetrahedral d-sites (labeled as a_1, a_2 and d in figures 4.11 a and e). We have simulated these XMCD spectra (using CTM4XAS 5.5) by ligand field multiplet (LFM) calculations on a-Fe^{3+} and d-Fe^{3+} sites which are in very good agreement with the above experimental spectra (see figure 4.11 d). This observation confirms that Fe ions in the undoped YIG film are all in a Fe^{3+} state. However, the XMCD of Ce-YIG films, normalized to both a-site peaks, show a prominent extra peak at energy (707.5 eV) below the d-site feature (see figure 4.11 e). This extra peak, which can also be reproduced by our multiplet calculations, is a direct evidence of the aforementioned presence of Fe^{2+} ions, specifically at d-sites in the Ce-doped YIG films. Further indication of specific charge transfer to d-sites can be inferred from changes in the ratio between the d- and a-site peak intensities of the Fe-L_3 XMCD spectra. In particular, the intensities of a_1 and a_2 peaks remain unchanged in the normalized XMCD (figure 4.11 e) which rules out any charge transfer to the a-sites. On the contrary, our XMCD results confirm that the charge transfer occurs to the tetrahedral d-(Fe^{2+}) sites, since the calculated intensity ratio between the d-peak (708.3 eV) and the a_2-peak (708.9 eV) is smaller in Ce-YIG films than for the undoped YIG film.

4.4.2 Specific magnetic contributions from Ce and Fe

To investigate the impact of Ce-doping on the YIG magnetic properties, we have evaluated the magnetic moments of Ce and Fe ions in the Ce-YIG films as well as the Fe moments in the undoped YIG film. Concerning Ce, our XMCD spectra reveal that the magnetism arises mainly from the localized $4f^1$ electrons (Ce^{3+}) while the $4f^0$ (Ce^{4+}) ground state shows a considerably smaller dichroic effect and the $4f\ ^1L$ ground state exhibits no contribution to the magnetism, as seen in figures 4.10 (a) and (b). Consequently, to evaluate the magnetic moment of Ce we have separated out the Ce^{3+} contribution from the total XAS spectra by fitting the Ce^{3+} and Ce^{4+} XAS data of figure 4.10 (c). The spin (m_s) and orbital (m_l) components of atomic magnetic moments per YIG and Ce-YIG formula unit were obtained by applying the sum rules to the integrated intensities of total XAS and XMCD spectra [155, 156, 157]. The results of the analysis are summarized in Table I. For the sum rules, the electric dipole transitions of an ion are considered from a spin-orbit-split core level to the shell-resolved operators of the valence electrons. The sum rule equations for Fe-$L_{2,3}$ ($2p \rightarrow 3d$) and Ce-$M_{4,5}$ ($3d \rightarrow 4f$) absorption edges are given, respectively, by:

$$\begin{aligned} 2\langle S_z\rangle + 7\langle T_z\rangle &= \frac{6p-4q}{r}N_h, \\ \langle L_z\rangle &= \frac{4q}{3r}N_h, \end{aligned} \tag{4.6}$$

for $2p \rightarrow 3d$ dipole transitions and by:

$$\begin{aligned} 2\langle S_z\rangle + 6\langle T_z\rangle &= \frac{5p-3q}{r}N_h, \\ \langle L_z\rangle &= \frac{2q}{r}N_h, \end{aligned} \tag{4.7}$$

for $3d \rightarrow 4f$ transitions. In equations 4.6 and 4.7, r is referring to the integrated value of the total XAS (after subtracting the step-function) at L_2 or M_4 post edge as shown in figures 4.11 (f) and 4.10 (e), respectively. The p and q are referred to the integrated values of the XMCD at L_3 (M_5) and L_2 (M_4) post edges, respectively (see figures 4.11 f and 4.10 e). The $\langle L_z\rangle$, $\langle S_z\rangle$, and $\langle T_z\rangle$ are the expectation values with respect to the z component of the orbital angular momentum, the spin angular momentum, and the magnetic dipole operator of the $3d(4f)$ shell for $L_{2,3}(M_{4,5})$ edges, respectively. The N_h is the number of holes taken as 4.7 for the $3d^5$ [158] and 13 for $4f^1$ shell in the calculations. Using the above equations, one can estimate the orbital and spin magnetic moments as $m_l = -\langle L_z\rangle\mu_B$ and $m_s = -2\langle S_z\rangle\mu_B$, respectively. The derived moments of the YIG and Ce-YIG films are listed in table 4.1.

Sample	**Edge**	$2\langle S_z\rangle + n\langle T_z\rangle$ /f.u. (μ_B)	$2\langle S_z\rangle$ /f.u. (μ_B)	$2\langle L_z\rangle$ /f.u. (μ_B)	m_{tot} /f.u. (μ_B)	$\lvert\frac{\langle Lz\rangle}{2\langle Sz\rangle}\rvert$
Ce-YIG(001)	Ce-M	-0.191	-0.033	0.243	0.052	7.379
	Fe-L	1.461	1.461	0.050	1.511	0.034
					1.563	
Ce-YIG(111)	Ce-M	-0.214	-0.037	0.280	0.066	7.589
	Fe-L	1.320	1.320	0.045	1.365	0.034
					1.431	
YIG(111)	Fe-L	2.558	2.558	0.017	**2.575**	0.006

TABLE 4.1: Effective spin $2\langle S_z\rangle + n\langle T_z\rangle$ and orbital $\langle L_z\rangle$ magnetic moments of the YIG and Ce-YIG films per YIG and Ce-YIG formula unit calculated using the XMCD sum rules on Ce-M and Fe-L absorption edges. Here, $n = 6$ for Ce-M edges and $n = 7$ for Fe-L edges. The m_s of Ce and tetrahedral Fe ions are coupled antiferromagnetically with Ce carrying a very small m_s value as compared to Fe. The m_{tot} is defined as the total effective spin and orbital magnetic moments. The Ce-YIG films exhibit a smaller m_{tot} than the undoped YIG film.

A few comments about the evaluation of the magnetic moments are relevant. In the first place, corrections to the spin sum rules were taken into account for the Fe^{3+} values given in table 4.1, as it is well known that strong deviations are caused by core-valence exchange interactions in the transition-metal ions [159]. Additionally, the values of $\langle S_z \rangle$ for Fe^{3+} were determined by assuming that $\langle T_z \rangle$ is negligible due to the cubic symmetry of the d-orbitals. However, the assumption of negligible $\langle T_z \rangle$ does not hold for rare-earth ions like Ce, because of the localized and aspherical $4f$ electron charge densities. For these ions, the magnitude of $\langle T_z \rangle$ is indeed comparable to that of $\langle S_z \rangle$ and the former cannot be determined directly. In order to have an estimation of the spin-only component of the Ce magnetic moment, we assumed that the $\langle T_z \rangle$ is scaled with $\langle S_z \rangle$ -as demonstrated in reference [160]. The ratio $\langle T_z \rangle / \langle S_z \rangle = 8/5$ for Ce^{3+} was then calculated using the theoretical expectation values for $\langle T_z \rangle$ and $\langle S_z \rangle$ from the Hund's rule states given in reference [161]. Using the above ratio, we have extracted the $2\langle S_z \rangle$ values from the $2\langle S_z \rangle + 6\langle T_z \rangle$ of the Ce-M edges (see table 4.1). The consistency of these assumptions is shown by noting that for Ce^{3+} ($4f^1$) ($S = 1/2$, $L = 3$) we should expect $m_l/m_s = [L(L+1)/2S(S+1)] = 8$. Our experimental values of $|m_l/m_s|$ are indeed close to 8, confirming the abovementioned assumptions. Furthermore, the moments in table 4.1 reveal that the m_s of Fe and Ce are antiparallel to each other (see the negative (positive) signs for the m_s of Ce(Fe) in table 4.1). We note also that the Y_{3+} ions exhibit almost negligible magnetic moments (<0.01 μ_B) and, therefore, they were not considered for evaluating the m_{tot} values. Note that, the m_{tot} of YIG film (2.57 μ_B) is reduced from being 5 μ_B (Fe^{3+} free ion moment) for the YIG structure. This reduction is understood from the fact that the YIG magnetization decreases monotonically with the increasing temperature below Tc [162].

From table 4.1 we see also that the Ce-doped YIG films exhibit significantly smaller m_{tot} values than the undoped YIG film, indicating that Ce-doping affects the magnetization of the Fe sublattice. In principle, this is expected from the fact that the Ce-doping induces a charge transfer on the Fe sites, so that Fe^{2+} valence states emerge, thereby causing a reduction in the nominal Fe(d) spin magnetic moment from $S = 5/2$ to $S = 4/2$. Additionally, this also produces concomitant changes in the antiferromagnetic coupling between the a(Fe)- and d(Fe)- sites. To gain a valuable insight into this antiferromagnetic exchange coupling, we have studied the site-specific magnetic contributions of d-Fe, a-Fe, and c-Ce and their evolution with magnetic field. For that purpose, we exploited the site-dependent XMCD magnetization curves of the undoped YIG as well as the Ce-doped YIG films (figure 4.12). For a better visualization, the curves in figure 4.12 (a) are shown only in the positive field range, and were obtained by selecting the XMCD peak energies at d-sites (708.2 eV) and a-sites (708.9 eV). Drawing first our attention to the undoped YIG film in figure 4.12 (a), we see that the measured Fe-L_3 XMCD signal saturates at $H = 200$ mT. However, the Fe-L_3 XMCD magnetization curves of (001) and (111)-oriented films of Ce-doped YIG show deviations from the conventional saturation-magnetization behavior at $H = 500$ mT (figure 4.12 b) and $H = 200$ mT (figure 4.12 c), respectively. More precisely, in contrast to the undoped YIG film -where the magnetization, once saturated, remains constant (figure 4.12 a)- the hysteresis curves of Ce-YIG films exhibit a small magnetization overshoot at the fields indicated above. These atypical magnetization curves are reminiscent of those that we obtained previously in our magneto-optical spectroscopy experiments, for instance, the anomalous hysteresis measured at $\lambda = 441$ nm shown in figure 4.9 (b). In the MO section we have interpreted this anomalous behaviour as two different hysteresis contributions, nevertheless, in XMCD we have learned that the Fe loops are indeed themselves anomalous.

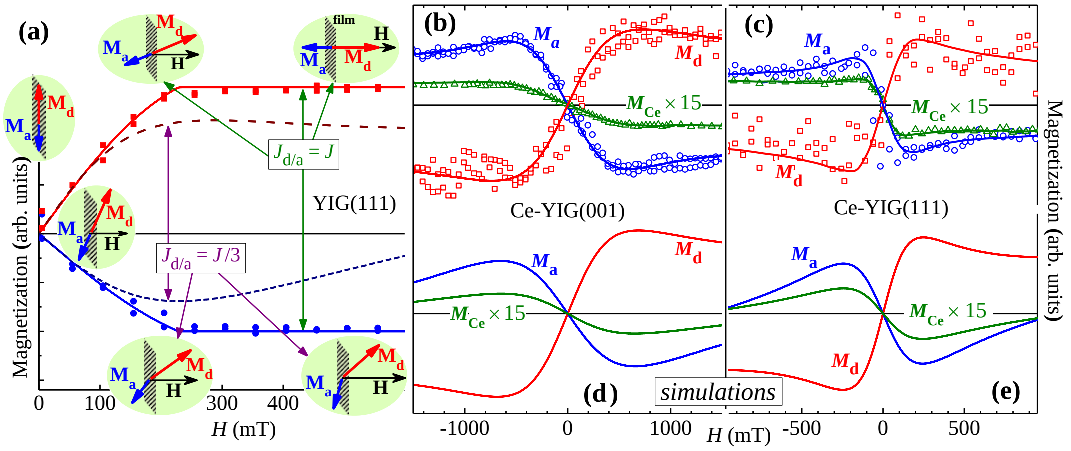

FIGURE 4.12: (a) Out-of-plane XMCD (symbols) and model (solid lines) magnetization curves of d- and a-sites of YIG(111) film given in the upper and lower side of the panel, respectively. For the sake of clarity, only the positive field range is plotted. The evolution of magnetizations in the d- and a-sites (M_d and M_a, respectively) is given for the M_d/M_a antiparallel coupling ($J_{d/a}$) in two cases: (i) J (top sketches) for YIG film and (ii) $J/3$ (bottom sketches) for the Ce-YIG films. The solid lines in the XMCD hysteresis data of (b) Ce-YIG(001) and (c) Ce-YIG(111) films are given for a guided view. Panels (d) and (e) represent the simulated magnetization loops for (001) and (111)-oriented Ce-doped YIG films, respectively.

4.5 Phenomenological interpretation of the anomalous magnetizations of Fe and Ce

In order to find an explanation for this apparently unconventional behavior, the XMCD loops were interpreted through numerical simulations performed using a phenomenological model in collaboration with Professor Julian Geshev from the Instituto de Física, Universidade Federal do Rio Grande do Sul, Brazil. The model incorporates as inputs the normalized values of the XMCD loops, in which the Fe spins of d-sites ($\mathbf{M}_d$) are antiferromagnetically coupled (via superexchange) to those at a-sites ($\mathbf{M}_a$) as well as to the Ce^{3+} spins in the c-sites ($\mathbf{M}_{Ce}$). We assumed that the magnetic energy density

(E) for $\mathbf{H}$ applied along the out-of-plane direction to the film surface is given by

$$E = \sum_{i}^{d,a} K_i^{eff} \left(\frac{\mathbf{M}_i \cdot \mathbf{n}}{M_i} \right)^2 - \sum_{i}^{d,a,Ce} \mathbf{H} \cdot \mathbf{M}_i + \sum_{i \neq j}^{d,a,Ce} J_{i/j} \left(\frac{\mathbf{M}_i \cdot \mathbf{M}_j}{M_i M_j} \right) \tag{4.8}$$

The first term in equation 4.8 represents the in-plane magnetic anisotropies of $\mathbf{M}_d$ and $\mathbf{M}_a$. The effective anisotropy constants K_d^{eff} and K_a^{eff} result from the shape and any other anisotropy contributions and the unit vector $\mathbf{n}$ gives the out-of-plane direction. The second term adds the Zeeman energies of all magnetic contributions, whereas the last term takes account of all the effective coupling energies parameterized by the $J_{i/j}$ constants. Since the Ce^{3+} ions have small magnetic moments (table 4.1), we have assumed that the Ce^{3+} anisotropy is negligible. The values of the magnetizations of each sublattice at any value of $\mathbf{H}$ are obtained by minimizing E with respect to the equilibrium states of $\mathbf{M}_d$, $\mathbf{M}_a$ and $\mathbf{M}_{Ce}$. More details on the energy minimization procedure employed here can be found in references [163, 164] and the references therein.

Sample	$H_d = H_a = 2K_d^{eff}/M_d$ (kA/m)	$J_{d/a}$ (MJ/m^3)	$J_{Ce/d}$	$J_{Ce/a}$
Ce-YIG(001)	58	4.20	0.10	-0.10
Ce-YIG(111)	19	1.70	0.07	-0.07

TABLE 4.2: Fitting parameters of the magnetization hysteresis loops according to equation 4.8.

The results of fitting our model to the experimental data are shown in figures 4.12 (a), (d), and (e). In the case of the undoped YIG film, the $\mathbf{M}$ vs $\mathbf{H}$ curves obtained from the model show a linear slope (positive for d-sites, negative for a-sites) up to about 200mT and then they saturate for higher magnetic fields, matching perfectly to the experimental data (symbols in figure 4.12 a). Configurations of $\mathbf{M}_d$ and $\mathbf{M}_a$ are schematically represented in the four top-most ellipse-shaped sketches in figure 4.12 (a). In this case, the evolution of $\mathbf{M}_d$ and $\mathbf{M}_a$ with $\mathbf{H}$ is precisely what one would expect for antiparallel-coupled $\mathbf{M}_d/\mathbf{M}_a$ magnetizations with uniaxial anisotropy, provided that $\mathbf{H}$ is not sufficiently large to overcome the exchange coupling field. In these simulations, the antiparallel $\mathbf{M}_d/\mathbf{M}_a$ coupling, denoted by $J_{d/a}$ in equation 4.8, is $J_{d/a} = J$ (see figure 4.12 a, solid lines). When we apply $\mathbf{H}$ perpendicular to the film plane, the magnetization vectors of both sublattices rotate coherently in the magnetization reversal process, as shown by the schematic arrows of the upper sketches in figure 4.12 (a). At higher fields, $\mathbf{M}_d$ is aligned parallel to $\mathbf{H}$ while $\mathbf{M}_a$ points to the opposite direction.

However, as described above, the $M_d(H)$ and $M_a(H)$ curves of the Fe ions for Ce-doped YIG films have an unusual change of the slope that causes the overshoot of the magnetization revealed in the XMCD loops displayed in figure 4.12 (b) and (c). Given that the contribution of $\mathbf{M}_{Ce}$ to the total moment is very small, we made the reasonable assumption that the unusual slope is solely attributed to the decrease of the antiparallel M_d/M_a coupling caused by the presence of Ce. To proof that a reduction of $J_{d/a}$ can explain the change of slope, we have simulated a fictitious YIG sample by calculating a pair of curves by using $J_{d/a} = J/3$ as the value for the exchange coupling (figure 4.12 a), i.e., reducing $J_{d/a}$ to one third of the value used to simulate the experimental data of the undoped YIG film. As seen in the solid lines of figure 4.12 (a), after reducing the value of $J_{d/a}$ the shape of the respective simulated curves reproduces very well the atypical shape of the Fe-XMCD loops of Ce-doped samples. Using this idea, the XMCD loops of Ce-YIG films (see figures 4.12 b-c) were also modeled according to equation 4.8 and the resulting parameters are displayed in table 4.2. Note that the undoped YIG sample could fit to any value $J_{d/a} > 0.48\,\mathrm{MJ/m^3}$ for matching the experimental XMCD loop. Therefore, our assumption is that the value of $J_{d/a}$ for the YIG film is significantly larger than those for (001)- and (111)-oriented Ce-YIG films which, according to the fittings, have the values of $J_{d/a} = 4.20\,\mathrm{MJ/m^3}$ and $1.70\,\mathrm{MJ/m^3}$, respectively.

The effects of the reduced exchange coupling on the sublattice magnetization loops can be understood intuitively as indicated in the two sketches depicted at the bottom of figure 4.12 (a). For small values of H, the a- and d-site magnetization components are practically perfectly antiparallel, as observed for the undoped YIG. However, at higher fields, the competition between the Zeeman and the exchange coupling energies leads to dissimilar rotations of $\mathbf{M}_d$ and $\mathbf{M}_a$, as depicted in the bottom sketches of figure 4.12 (a). Focusing on the d-sublattice, the evolution of $\mathbf{M}_d$ for weak $J_{d/a}$ coupling can be described by an energy term $-\mathbf{M}_d \cdot \mathbf{H}_d^{eff}$, where the effective field is given by $\mathbf{H}_d^{eff} = \mathbf{H} + k|\mathbf{M}_a|$, being $k = J_{d/a}/(M_d M_a)$. As H increases, $\mathbf{M}_a$ - which is antiparallel to $\mathbf{M}_d$ - starts to rotate towards H. As a result, the projection of $\mathbf{M}_a$ along H decreases with the increase of H, so that the value of H_d^{eff} may actually decrease, thus inducing a decrease of the projection of $\mathbf{M}_d$ along the H-direction at high enough fields, as observed in the unusual XMCD loops of the Ce-YIG films (see figure 4.12 a). A similar analysis can be done by interchanging the roles of $\mathbf{M}_a$ and $\mathbf{M}_d$. We therefore conclude that the observed decreasing high-field slopes of the XMCD loops obtained from Fe a-sites and d-sites are due to a weakening of the exchange coupling $J_{d/a}$ driven by charge transfer processed triggered by doping YIG with Ce.

4.5.1 Microscopic interpretation of the anomalous magnetizations of Ce and Fe

We discuss in the following the microscopic mechanisms that may lead to the reduction of the exchange coupling in the Ce-doped YIG films. In magnetic insulators, it is well-known that the exchange interaction is predominantly defined by the so-called superexchange interaction, which is due to the overlap of the electronic orbitals from the magnetic cations via intermediate ligands. Starting from the undoped YIG system, the FeO_6 octahedra are corner-linked to the neighboring FeO_4 tetrahedral sites via the

O ligands, with all the Fe $3d$ orbitals being half-occupied in a high-spin configuration, which results in a quenching of the orbital moment (see 4.1 for undoped YIG case).

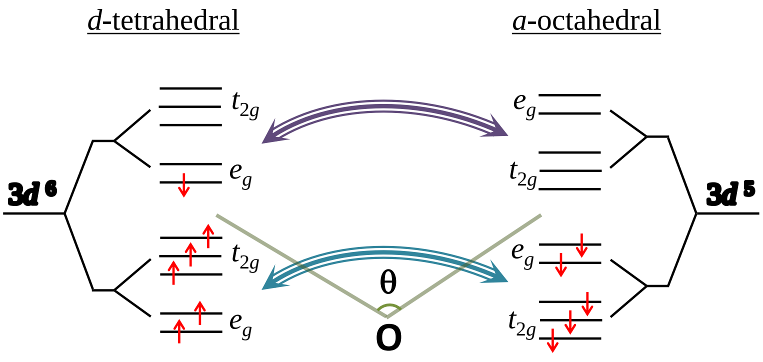

FIGURE 4.13: Schematic diagram of the energy levels at Fe($3d^6$)-O-Fe($3d^5$) superexchange coupling. Where θ is the angle between the d-Fe and a-Fe sites. The $d^5 - d^5$ coupling is a strong antiferromagnetic while the spin-down electron of d^6 weakens the coupling by freely moving to empty spin-up states of d^5 orbitals.

In YIG, the Fe(d)-O-Fe(a) bond angle θ between these two crystallographically inequivalent Fe sites is about ~ 126 degrees [165], and their magnetic coupling is mostly accomplished by the superexchange interaction via the $2p$ orbitals of the common O ligand atom. According to the Goodenough-Kanamori-Anderson (GKA) rules [166], $3d^5 - 3d^5$ superexchange interactions via 180 degree bond angle would stipulate an antiferromagnetic (AFM) coupling. As in YIG the metal-oxygen-metal bond angle connecting tetrahedral and octahedral sites is ~ 126 degree [165], the AFM interaction, although weaker than for 180 degrees, shall produce an antiparallel coupling of Fe^{3+}(d)-Fe^{3+}(a), which thus gives rise to the observed ferrimagnetic arrangement of tetrahedral and octahedral sublattices.

Now, turning to the case of Ce-doped YIG, our experimental data point to a charge transfer promoted from Ce to Fe, which can cause a double occupancy to one of the two e_g levels at the Fe^{2+}($3d^6$) ions on the tetrahedral d-sites. In this scenario, the additional electron coming from the charge transfer will occupy available spin-down states of the low-lying e_g orbitals of either $d_{x^2-y^2}$ or d_{z^2} symmetry of $3d^6(e_g^{1\downarrow})$ (see figure 4.13). Therefore the strength of the newly established $3d^6(t_{2g}^{3\uparrow}e_g^{2\uparrow}e_g^{1\downarrow}) - O - 3d^5(t_{2g}^{3\uparrow}e_g^{2\uparrow})$ interaction must be modified. Due to the fact that for a Fe-O-Fe bonds differing from 180 or 90 degrees, the contribution of different $3d$ orbitals to the bond become somehow mixed, in practice the GKA rules cannot be simply used to predict the strength of the new interaction. However most likely the contribution from the transferred $3d^6(e_g^{1\downarrow})$ electron shall reduce the strength of the AF coupling and the magnitude of net exchange constant, $J_{d/a}$, arising from the superexchange $\mathrm{Fe}^{2+/3+}(d) \leftrightarrow \mathrm{Fe}^{3+}(a)$ interaction (see the sketch in figure 4.13). In other words, charge doping at Fe ions arising from Ce^{4+} substitution explains the reduction of the $J_{d/a}$ exchange coupling constant.

4.6 Conclusions and perspectives

To sum up, XAS and XMCD experiments were used to probe site-specific sublattice contributions to the magnetism of Ce-doped YIG and to and have a direct observation on the valence states of Ce and Fe ions. Our experimental results were consistent with the emergence of a charge transfer from $\mathrm{Ce}^{3+}(4f^1) + \mathrm{Fe}^{3+}(3d^5) \rightarrow \mathrm{Ce}^{4+}(4f^0) + \mathrm{Fe}^{2+}(3d^6)$ into the tetrahedral d-sites of Fe driven by the Ce-doping into YIG. As a result, a large fraction of Ce^{4+} ions appears and, on the other hand, the charge transfer also induces as well as a partial reduction of Fe^{3+} into $\mathrm{Fe}^{2+}(3d^6)$, which causes a reduction of the overall magnetic moment. Furthermore, the value of the exchange coupling constant ($J_{d/a}$) between Fe ions at d-(tetrahedral) and a-(octahedral) sites is reduced which also entails a reduction of the magnetic coupling between both sublattices. This produces visible features in the magnetization process, noticeable at low magnetic fields. The last observation is responsible for the occurrence of atypical XMCD magnetization curves for the Fe ions, caused by an overshoot of the magnetization and a subsequent reduction of the Fe-sublattice magnetization with increased applied magnetic fields. The atypical signatures observed for the site-specific magnetic contributions in doped YIG may prove relevant for a better understanding of the magneto-optical properties of these compounds.

At this point, it is worth to stress that it may be surprising, at first sight, that Ce-doping can cause an enhancement of the MO signal of YIG, in spite of causing a degradation of the magnetic properties -e.g., reduction of exchange coupling and magnetic moment-. However, we should bear in mind that, although linear magneto-optical effects are proportional to the magnetization, the constant of proportionality depends decisively on the details of the electronic band structure and the allowed optical transitions. In the case of Ce-YIG, the charge transfer from Ce to Fe plays a crucial role to understand the enhanced magneto-optical response in the Ce-YIG as the response can be explained by the emergence of new optical transitions -absent in the parent undoped YIG- involving ions (Ce in this case) with large spin-orbit coupling.

Finally, we should stress that beyond the relevance for the understanding of the optical properties of doped YIG, our findings can be also important for other applications in which, e.g., spin waves are exploited. In this case, site-specific doping may reveal itself as an important toolkit for engineering the dynamic magnetic properties based on the demanding of potential applications.

Chapter 5

In-situ imaging of electric field-induced ferroelastic domain motion in $SrTiO_3$

5.1 Introduction

In the previous chapters, we have studied enhancement effects on the magneto-optical properties via polarons on $La_{2/3}Ca_{1/3}MnO_3$ or by the incorporation of a rare-earth, such as Ce, into YIG. In the present chapter, magneto-optics will be used as a tool to probe magnetism and to resolve magnetic domain patterns. Specifically, we used magneto-optics to analyze the spatial distributions of ferroelastic twins domain in $SrTiO_3$ crystals under the application of in-situ applied electric fields. These ferroelastic twins appear below the cubic to tetragonal transition of $SrTiO_3$ (~ 105 K).

At room temperature, bulk $SrTiO_3$ crystallizes in the cubic perovskite structure with space group $Pm\bar{3}m$ [167]. Yet, at a temperature of $T \sim 105$ K, $SrTiO_3$ crystals undergo a transition to a tetragonal phase ($I4/mcm$ space group) with a small distortion $c/a \approx 1.0005$ (figure 5.1) [168, 169] involving an antiferrodistortive (AFD) lattice mode, with counter-rotations of neighboring TiO_6 octahedra along the [001] axis. As a consequence, the unit cell volume changes from a^3 to $\sqrt{2}a \times \sqrt{2}a \times c$ [170] and three types of orientational domains appear, causing the emergence of ferroelastic domains [171, 172]. The effect of tetragonality can be observed directly by measuring the anisotropy of the dielectric constant [173] or the birefringence [174]. Additionally, electronic phenomena in $SrTiO_3$, viz., superconductivity [25] or two-dimensional electron gases at the surface or interface with polar oxides [28, 34, 35] may be strongly influenced by the emergence of the tetragonal asymmetry and ferroelastic twins [36, 37, 38].

Interestingly, ferroelectric signatures have been related to ferroelastic motion [24, 54, 26, 50] and interpreted as arising from polar domain walls [24, 53, 55]. Ferroelastic strains also couple across the interface between $SrTiO_3$ crystals and ferromagnetic materials, altering their magnetic domain structure with electric fields via magnetoelastic coupling [56]. In all these phenomena it is crucial to understand the spatial

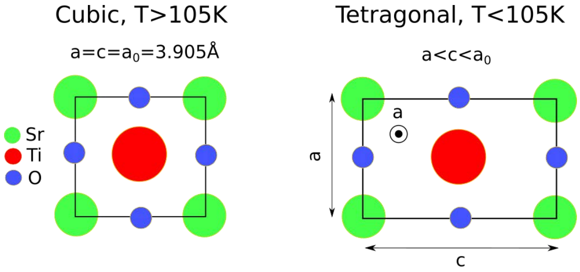

FIGURE 5.1: Scheme of unit cell of $SrTiO_3$ for cubic phase at $T > 105$ K and tetragonal phase at $T < 105$ K

distribution of ferroelastic domains, so that our attention has been focused on how the twins moves under electric field. In previous studies, the presence of ferroelastic twins has been revealed indirectly by using magneto-optical imaging [175] or directly by high-resolution x-ray diffraction [176]. However, it was not until the advent of two-dimensional electron systems in $SrTiO_3$-based structures that the topic took up a new turn. More specifically, researchers started paying attention to the in-situ evolution of ferroelastic twins with applied fields and its impact on the electric properties of oxide interfaces. Along this line, electrostatic and optical imaging were used to visualize directly the connection between ferroelastic domain configuration and transport along these interfaces [177, 37]: it was found that the conductivity is particularly enhanced along narrow paths, presumably along domain walls [36]. Incidentally, these works have demonstrated unquestionably that ferroelastic twins are endowed with significant motion as soon as electric fields are applied across $SrTiO_3$ crystals [177]. Yet, in spite of these notable advances, important aspects of the interaction of ferroelastic domains with electric fields remain unaddressed. This is particularly relevant for the understanding of the electric field-induced responses discussed above [24, 54, 26, 50, 56, 55, 36], which requires a detailed knowledge of the low temperature dielectric properties of $SrTiO_3$. In this respect, it is known that the dielectric behaviour at low temperature of $SrTiO_3$ is anisotropic, as expected from the tetragonal symmetry [173]. In this chapter we demonstrate that the dielectric anisotropy is such that the dielectric susceptibility is higher along the normal to the axis of the octahedral tilts in the AFD phase. This observation is a very relevant for applications where understanding and controlling the distribution of all types of ferroelastic twin domains is essential for nanotechnology design.

5.2 Imaging the electric field response of the FE twins in $SrTiO_3$: optical reflectance.

In order to shed light on the spatial distribution of twins we used confocal optical microscopy for imaging the optical reflectance produced by topography changes on the SrTiO$_3$ surface. As we will see in the following, some twins corrugate the surface and therefore, its movement under electric field can be mapped out by a change in the optical reflectance image. Figure 5.2 shows schematically the two types of ferroelastic twin domains that in the tetragonal phase may emerge on the surface of a (001)-oriented SrTiO$_3$ crystal. On the one hand, we have $\{a\}$ and $\{c\}$ domains, in which the elongated axes are in-plane and out-of-plane, respectively. Neighboring $\{a\}$ and $\{c\}$ domains are denoted by $\{a, c\}$. On the other hand, $\{a_1\}$ and $\{a_2\}$ domains denote $\{a\}$ domains having the elongated axis along orthogonal directions within the plane. If appearing contiguous, these regions are denoted by $\{a_1, a_2\}$. Over $\{a, c\}$ domains the surface is corrugated, so that these domains can be viewed as striped contrast in optical microscopy. In contrast, the topography over $\{a_1, a_2\}$ domains is flat, and they cannot be detected by these means. This is clearly seen in figure 5.3 (a), where stripes imaged at $T = 8$ K along the in-plane [100] and [010] directions reveals the areas with $\{a, c\}$ domains running along the [010] direction, while $\{a_1, a_2\}$ domains remain unnoticed. We will see below that $\{a_1, a_2\}$ domains can be instead visualized with the help of magneto-optical imaging, by exploiting magnetoelastic coupling with a magnetic overlayer. In order to elucidate the sign of the dielectric anisotropy, we designed the contact geometry to apply electric field out-of-the-plane, along the [001] direction (see figure 5.2 b).

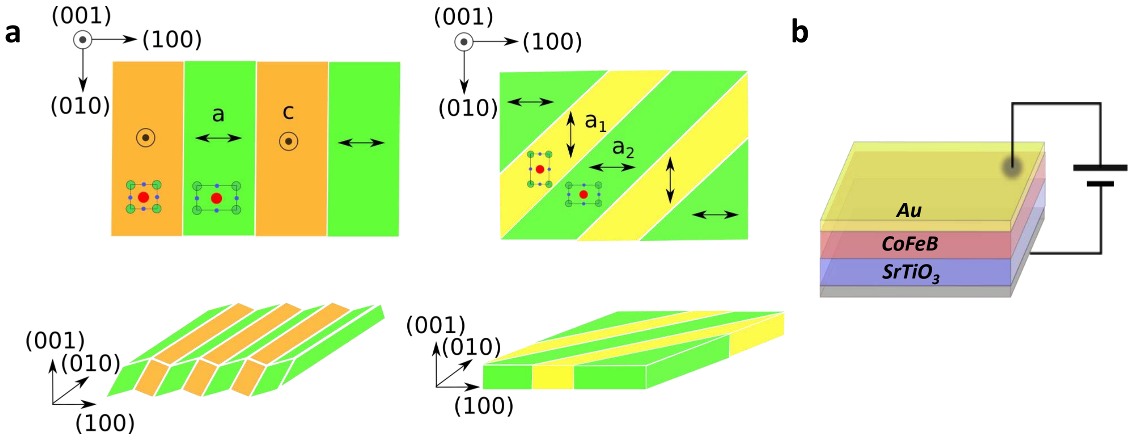

FIGURE 5.2: (a) Schematic representation of the ferroelastic twins in SrTiO$_3$ in the tetragonal symmetry. (b) Scheme of the applied electric field configuration in the sample.

We first discuss the optical reflectance images recorded below the ferroelastic transition in the absence of any electric field shown in figure 5.3 (a). In these images, we see that there are regions covered with a striped contrast along the in-plane [010] and [100] directions corresponding to $\{a, c\}$ domains, which corrugate the crystal surface. Away from these areas, there is no contrast; the most reasonable assumption is that these regions correspond to flat $\{a_1, a_2\}$ domains which cannot be detected by reflectance, as confirmed below by magneto-optical imaging. After application of a voltage, we see that the striped areas recede substantially, indicating that $\{a, c\}$ domains are suppressed by electric fields (figure 5.3 b). This observation is still clearer by inspection of the images ($I_{V=0} - I_{V\pm200}$) obtained by the subtraction of the images recorded at $V = 0$ and $V = \pm200$ V to obtain the zones over the surface where $\{a, c\}$ domains have been suppressed by the electric fields (figure 5.3 c). Consequently, we conclude that upon application of top-to-bottom electric fields $\{a, c\}$ domains are largely suppressed, whereas $\{a_1, a_2\}$ domains expand at the expense of the former.

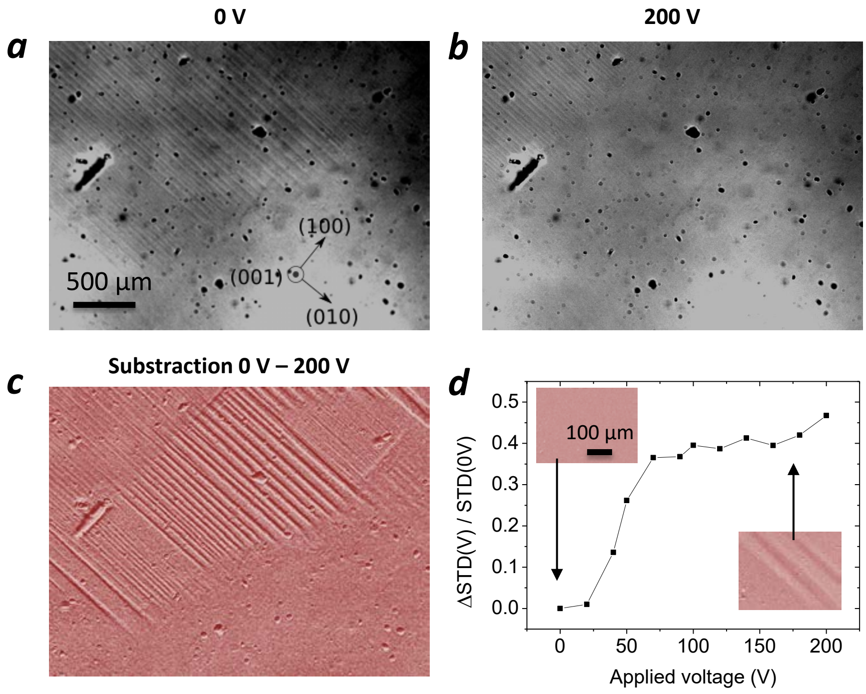

FIGURE 5.3: Panels (a) and (b) show, respectively, optical reflectance images measured at $T = 8$ K and $V = 0$ V and $V = +200$ V. In-plane crystal directions are indicated in panel (a). At zero-field, stripes along [010] indicate the presence of $\{a, c\}$ domains. After applying a voltage $V = +200$ V, the $\{a, c\}$ domains recede. The image of panel (c) is composed by the subtraction of the images taken at $V = 0$ V and $V = +200$V and, therefore, the large striped central area indicates the region were $\{a, c\}$ domains have been suppressed by fields. The data shown in panel (d) is calculated from the standard mean deviation (STD) of the intensities recorded in all pixels; this data demonstrates that the effect of applied fields is only visible for voltages above $V >\sim +25$ V ($E \sim 0.5$ kV/cm).

To know the minimum electric fields needed to observe these changes, we plotted in figure 5.3 (d) the parameter defined by $\overline{I_{STD}} = I_{STD(V)}/I_{STD(V=0)} - 1$, where $I_{STD}(V)$ denotes the standard deviation of the contrast map intensities as a function of the applied voltages defined as $I_{STD} = \sqrt{\frac{1}{N}\sum_1^N (p_i - \overline{p})}$, where p_i are the intensities detected at every pixel in the image, $\overline{p}$ is the averaged value $\overline{p} = \frac{1}{N}\sum_1^N p_i$ and N is the number of pixels. What we observe in figure 5.3 (d) is that $\overline{I_{STD}}$ is noticeably different from zero only at applied voltages $V >\sim +25$ V ($E \sim 0.5$ kV/cm). Thus, at $T = 8$ K, changes in ferroelastic twins are induced for fields above this value and saturate as the fields approach $V = +100$ V ($E \sim 2$ kV/cm).

5.3 Imaging the electric field response of the FE twins in $SrTiO_3$: MO imaging.

The images shown in figure 5.3 allow the direct visualization of $\{a, c\}$ domains, but not of $\{a_1, a_2\}$ domains. This difficulty can be overcome by performing magneto-optical imaging, which measures the changes on the polarization state of the light over space instead of topography. For that purpose, $Co_{40}Fe_{40}B_{20}$ (CoFeB) has been grown on $SrTiO_3$, as a ferromagnetic thin film with large magnetostriction coefficient and large MO activity, thus, its magnetic domain pattern is expected to reveal the ferroelastic twin structure via magnetoelastic coupling. The same approach has been used to reveal the imprinting of ferroelectric domains into a magnetostrictive film on $BaTiO_3$ [39, 40, 41, 42, 43, 44, 45, 46, 47, 48]. In this case, the strain transfer from the ferroelastic twins causes a modulation of the magnetic anisotropy via inverse magnetostriction. The validity of this approach is demonstrated in figure 5.4, which shows a longitudinal Kerr image at remanence where we have mapped out the in-plane orientation of the magnetization, thus identifying the areas where $\{a, c\}$ and $\{a_1, a_2\}$ domains emerged.

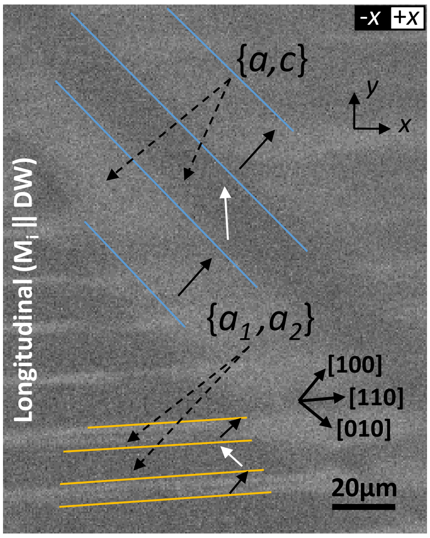

FIGURE 5.4: (a) Remanence longitudinal Kerr image sensitive to the [110] magnetization direction where $\{a, c\}$ and $\{a_1, a_2\}$ domains are present. The arrows indicates the in-plane orientation of the magnetization.

The visualization of both kinds of ferroelastic twins by magneto-optical imaging can be understood in terms of the imprint that the underlying ferroelastic twins impart on the magnetic domain structure of the overlying film. The strain $\epsilon = dl/l$ that the film suffers due to the substrate is computed by the the relative change of its cell parameters between the cubic and tetragonal phase $\Delta a/a_0$, $\Delta c/a_0$. Using the values for the lattice parameters of $SrTiO_3$ reported at 10 K [178], the $SrTiO_3$ cell for a and c domain and the strain suffered by the CoFeB film at each direction have been depicted in the figure 5.5. Thus, c-domains impose strains $\epsilon_x = \epsilon_y \approx -0.06\%$ and $\epsilon_z \approx +0.09\%$, while the values for a domains are $\epsilon_x \approx +0.09\%$ and $\epsilon_y = \epsilon_z \approx -0.06\%$. In turn, these strains generate a magnetoelastic response in CoFeB, defined by the anisotropy constant [179, 180]:

$$K_{me} = \frac{3}{2}\lambda\sigma, \tag{5.1}$$

where λ is the magnetostrictive constant $\lambda \approx 3 \cdot 10^{-5}$ [181], and σ the stress, which can be estimated taking into account a strain-stress relationship. Assuming that the film does not influence the crystal, the Hooke's law for a free-standing thin (quasi-2D) film in the linear elastic regime can be used:

$$\sigma = \frac{\epsilon E}{1-\nu^2}, \tag{5.2}$$

where ν is the Poisson's ratio $\nu \approx 0.3$ and E the Young's modulus $E \approx 1.6{\cdot}10^{12}$ dyn/cm^2 (values for metal alloys such as permalloy). For the particular case of an a domain and assuming literature values [180] for the elastic coefficients, the stress in the three directions are $\sigma_x = 158.2$ MPa and $\sigma_y = \sigma_z = 105.5$ MPa giving the largest magnetoelastic anisotropy $K_{me} \approx 4.7 \cdot 10^4$ erg/cm^3 in the x direction.

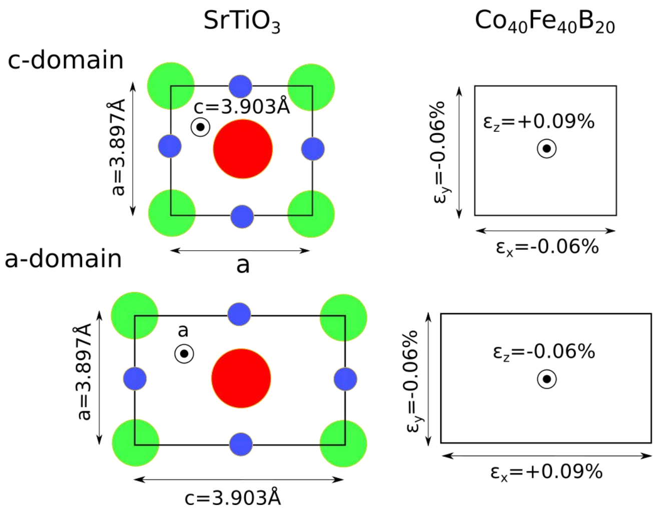

FIGURE 5.5: Scheme of $SrTiO_3$ tetragonal cell at 10K for $\{a, c\}$ twin domain's projection (left) and the strain suffered by the CoFeB film (right) due to the change of cell parameters. In the case of c-domain, the largest strain is 0.09% at z direction competing with the shape anisotropy. Analogously, for an a-domain the strain is in x direction.

In order to know if the magnitude of $SrTiO_3$ induced magnetoelastic anisotropy is large enough for driving the domain pattern of CoFeB, it has been compared to the growth induced anisotropy of our films. The CoFeB thin film has been grown at 175 °C with a dc magnetron sputtering on SrTiO$_3$. Even though at this growth temperature one should expect an amorphous texture of the film giving an in-plane isotropic magnetic response, our film presents a growth induced anisotropy due to the magnetron's magnetic field present during the growth. In order to asses this anisotropy, the longitudinal magneto-optical hysteresis response has been measured at different angles (0, 45, 90 and 135 deg) at room temperature (figure 5.6). The angular plot of the ratio between remanence and saturation of the longitudinal Kerr signal M_r/M_s, indicates an uniaxial anisotropy constant of $K_u = 8 \cdot 10^3$ erg/cm^3. Hence, the magnetoelastic anisotropy constant K_{me} imposed by ferroelastic twins at 10 K on CoFeB is much bigger than the growth induced anisotropy ($K_{me} = 4.7 \cdot 10^4$ erg/cm^3 $> K_u = 8 \cdot 10^3$ erg/cm^3) and, therefore, we should expect magnetoelastic effects reflecting the ferroelastic twins on the magnetic film. In consequence, the magnetic domain pattern in CoFeB is essentially determined by the underlying ferroelastic twin structure of the of the SrTiO$_3$ substrate. However, the magnetoelastic anisotropy has been estimated at 10 K and the transferred strain from the ferroelastic twins to the film decreases with the temperature [178]. Therefore, we have estimated the critical stress σ_c for that the both magnetic anisotropies are comparable $K_u/K_{me} \sim 1$. Obtaining a critical stress of $\sigma_c = 26.6$ MPa which indicates that effectively the cubic to tetragonal transition could be observed on the magnetic domain pattern few degrees below T$\sim$105 K. Similar discussions can be developed for a c domain, in this case, the largest strain is in the out-of-plane direction, perpendicular to the shape anisotropy that is bigger than the magnetoelastic anisotropy (pointing out-of-plane) because we know from Kerr imaging that the all magnetization is in-plane. Therefore, the magnetization on a c-domain will follow the growth induced anisotropy as in the cubic phase.

Using the extracted values from both magnetoelastic and growth induced anisotropies described above, we can obtain a qualitative view of the magnetic domain structure by carrying out micromagnetic simulations using the MuMax3 code [182] (see appendix A for more details). In the following we show that the direction of the initial magnetization has a strong influence on the magnetic domain pattern of CoFeB. We describe two cases, i.e.m the initial magnetization is all pointing perpendicular ($M_i \perp DW$) or parallel ($M_i \parallel DW$) to the $\{a_1, a_2\}$ twin domain walls. For the save of simplicity, in the following we will focus our attention specially on $\{a_1, a_2\}$ domains.

In the case where the initial saturation magnetization is perpendicular to the twin domain walls ($M_i \perp DW$), the micromagnetic simulations predict that a head-to-tail striped domain pattern is formed at the remanent, as shown in figure 5.7 (a). This result is confirmed by experimental transverse-like and longitudinal Kerr images corresponding to the in-plane x (transverse-like) and y (longitudinal) projections shown in figures 5.7 (b) and 5.7 (c), respectively. The insets in the experimental Kerr images represents the projections of the micromagnetics simulations. Note, therefore, that for

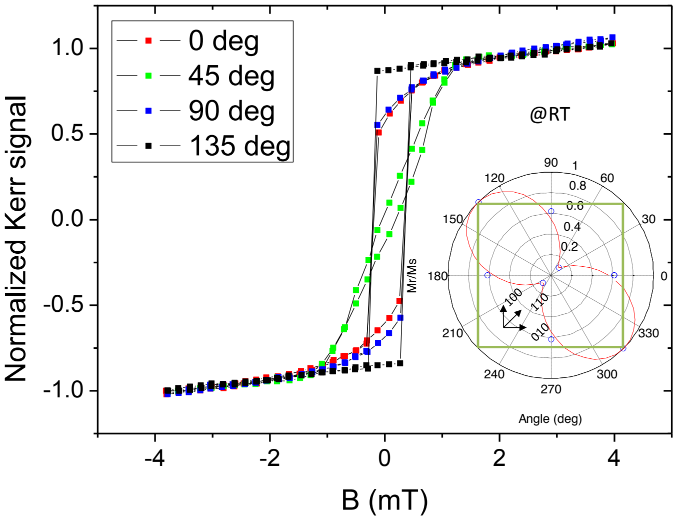

FIGURE 5.6: Normalized longitudinal Kerr signals measured at room temperature and at different angles, respect to the [100] direction. Inset shows the ratio between saturation and remanence ker signals (M_r/M_s) as function of the angle. The polar plot indicates an uniaxial growth induced anisotropy in the [-110] direction (the green square indicates the edges of the sample).

$M_i \perp DW$ there is a biunivocal correspondence between ferroelastic twins and magnetic domains. In the other hand, when the initial saturation magnetization is parallel to the twins domain walls ($M_i \parallel DW$), the micromagnetic simulations predict head-to-tail regions pointing in oppositely directions as shown in the figure 5.7 (d). This mechanism seems to be a more favorable than head-to-head pattern to minimize the magnetostatic energy [48]. This pattern is, as previously, confirmed by experiments, which show contiguous head-to-tail magnetic domains in which the y-component of the magnetization points along opposite directions (figures 5.7 e, f). Therefore, for $M_i \parallel DW$, there is not a biunivocal correspondence between the ferroelastic twins and magnetic domains, since several magnetic domains can forms within a single twin.

We see, therefore, that these micromagnetic simulations can reproduce the striped magnetic domain pattern that $\{a_1, a_2\}$ ferroelastic twins impose on the magnetic domain structure (figure 5.7). Since for the initial magnetization normal to the $\{a_1, a_2\}$ twin domain walls there is a biunivocal correspondence between the twins and the magnetic domain pattern (figure 5.7 b), we have used transverse-like Kerr imaging in this configuration to image the ferroelastic twins.

In order to double-check that the observed magnetic domain pattern are originated from ferroelastic twins, we took a transverse-like Kerr remanence at different increasing temperatures from 8 K to 110 K (above the cubic to tetragonal transition). As shown in figure 5.8, the domain pattern of CoFeB reflecting the $\{a_1, a_2\}$ twins starts to vanish at 80 K and disappears completely at 100 K, slightly before the 105 K transition

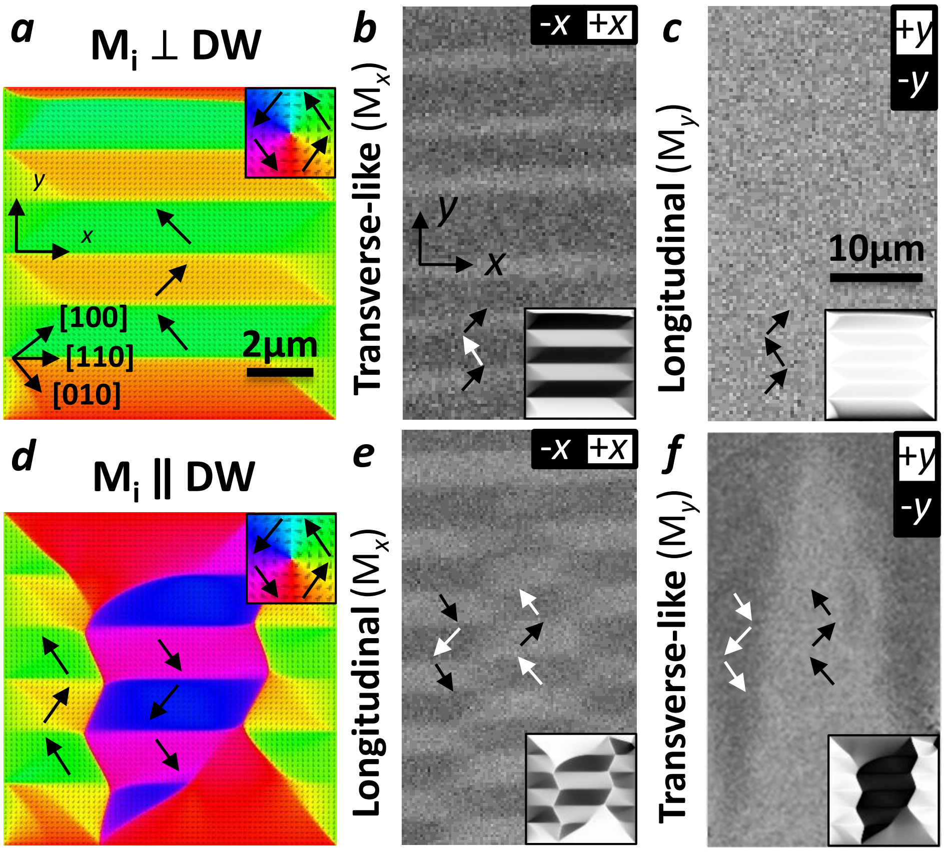

FIGURE 5.7: (a) Micromagnetic simulation of the remanent state for the initial magnetization perpendicular to the $\{a_1, a_2\}$ twin domain walls. The inset show the magnetization direction color-code. (b) Transverse-like and (c) longitudinal Kerr remanence image for $M_i \perp DW$ (d) Micromagnetic simulation of the remanent state for $M_i \parallel DW$. (e) Longitudinal Kerr and (f) Transverse-like Kerr remanence image for $M_i \parallel DW$. The insets of (b), (c), (e) and (f) show the x and$y$ magnetization projections (M_x, M_y) of the micromagnetic simulations respectively. The arrows indicate the magnetization orientation.

temperature. This little discrepancy could be understood as the competition between magnetic growth induced anisotropy and magnetoelastic anisotropy, as previously estimated by the critical stress. Thus, the magnetic domain pattern reveals clearly the ferroelastic twins.

Bearing in mind these observations, we used magneto-optical imaging to track the evolution of ferroelastic twins with electric fields. For instance, figure 5.9 (a) displays the images recorded over a large area (~ 0.15 mm^2) at a voltage cycle of V=0, 200, 0, -200, 0 V respectively. In these images the spatial distribution of magnetic domains reveals the presence of both $\{a, c\}$ (running along [010], [100] directions) and $\{a_1, a_2\}$ (along [110]) twins. We see also that the application of out-of-plane electric fields (Figure 5.2 b) causes an expansion of $\{a_1, a_2\}$ twins at the expense of $\{a, c\}$ domains, in agreement with the images taken from optical reflectance microscopy (figure 5.3). This

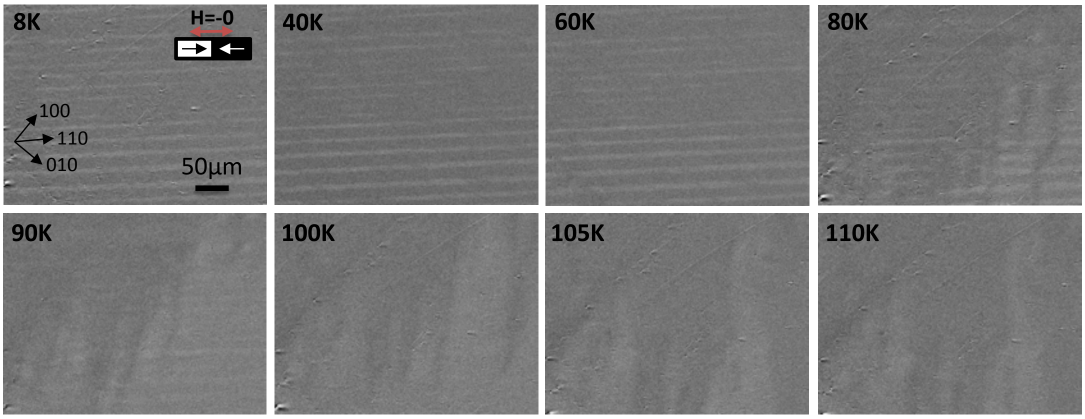

FIGURE 5.8: Kerr transverse-like images taken at different increasing temperatures. Magnetic domain pattern reflects the $\{a_1, a_2\}$ ferroelastic twins that vanishes slightly before the transition temperature (105 K).

electric-field driven expansion of $\{a_1, a_2\}$ twins can be even better visualized by presenting the subtraction optical images ($I^{subs}_{V_n} = I_{V_n} - I_{V_{n-1}}$), as shown in figure 5.9 (c).

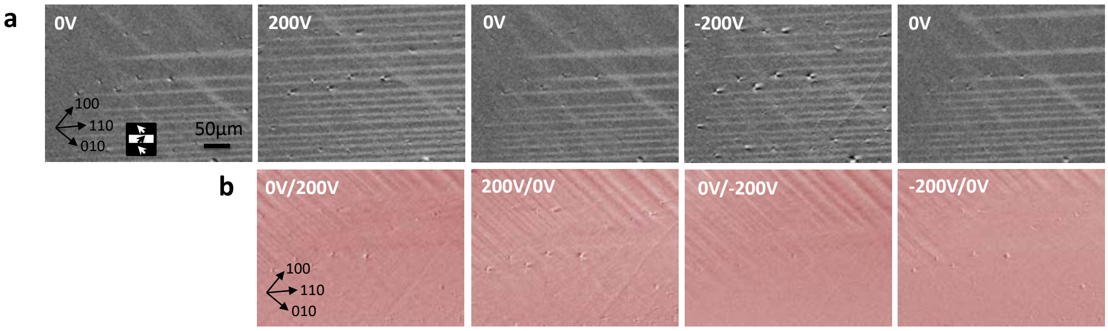

FIGURE 5.9: (a) Transverse-like Kerr remanence images at a voltage cycle of V=0, 200, 0, -200, 0 V respectively. (b) Changes on the twin structure are shown with subtracting optical images before and after change the applied voltage step $I^{subs}_{n} = I_{V_n} - I_{V_{n-1}}$.

Taking advantage of this methodology, we investigated the effects of temperature on the distribution of ferroelastic twins, which, at the end gave us additional information on the dielectric anisotropy. For that purpose, we consider the images shown in figure 5.10 (a), which display data recorded in the transverse-like configuration at T = 8K. These images are created by plotting a selected profile perpendicular to the $\{a_1, a_2\}$ twins from the corresponding Kerr image at each magnetic field [48]. Thus, the same figure 5.10 indicates the appearance/suppression of twins and possibles changes on the magnetization reversal process in CoFeB under electric field. Notice that more magnetic field is needed to saturate completely the film in the x direction. At zero-field a large fraction of the analysed area reveals the presence of $\{a_1, a_2\}$ domains. After the application of a voltage V = +200 V, the fraction of $\{a_1, a_2\}$ twins increases vigorously. The effect at this field is almost saturated, since the image

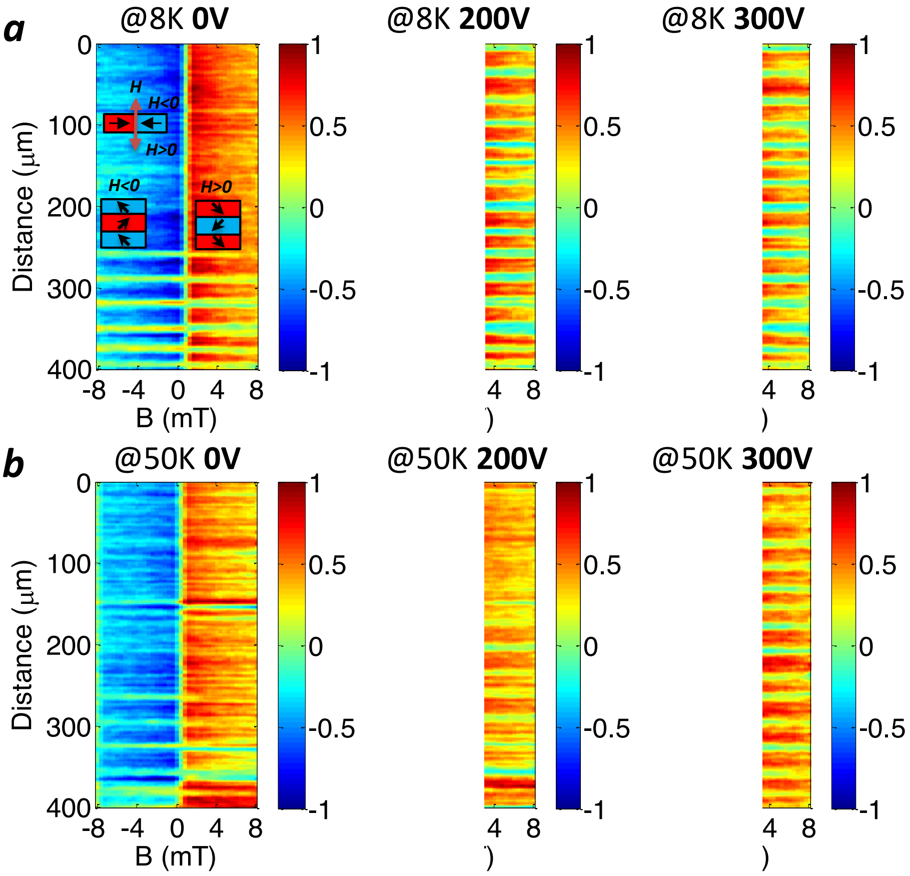

FIGURE 5.10: (a) Profiles of the optical signal obtained at a temperature T = 8 K at different voltage. The profiles run along the [1-10] direction on images that were recorded at different voltages in the transverse configuration. The horizontal axes indicate the applied magnetic field and the arrows in the left panel indicate the magnetization orientation in each domain. The vertical bars encode the values of the measured Kerr optical signals. (b) The same images as in panels (a) were measured at T = 50 K.

recorded at a higher voltage, V = +300 V, is very similar (figure 5.10 a). This observation is compatible with the plot shown in figure 5.3 (d), which shows that the effects of electric field at the lowest temperatures saturate when the voltages approach V = +200 V. However, when the temperature raises, higher electric fields are needed to change the distribution of ferroelastic twins. This is shown in figure 5.10 (b), which shows images recorded at T= 50 K. At V = +200 V $\{a_1, a_2\}$ twins expand, but the effect, contrary to T = 8 K, is not saturated: higher voltages (V = +300 V) are needed to expand further $\{a_1, a_2\}$ domains. Therefore, as temperature increases towards the transition, the electric-field motion of ferroelastic twins becomes harder. A possible reason for this behavior could be that the dielectric permittivity strongly decreases as a function of temperature [26]. Apart from that, we have observed that the magnetic reversal process of the CoFeB as a function of the electric field remains unchanged indicating that the effect inside a single twin are, at least, not enough to modify remarkably the magnetoelastic anisotropy.

Summing up, the application of an out-of-plane electric field expands $\{a_1, a_2\}$ twins -i.e., domains with both elongated axes in the plane- at the expense of $\{a, c\}$ twins. This hints at an anisotropic dielectric behaviour of $SrTiO_3$ with a higher susceptibility along the normal to the axis of the octahedral tilts in the AFD tetragonal phase.

5.4 Interpretation and modelling the results

In the following we will discuss the origin of the observed dielectric anisotropy. In order to understand the physical mechanisms responsible for the inferred dielectric anisotropy we initiated a collaboration with Prof. Massimiliano Stengel (Materials simulation and theory group at ICMAB-CSIC). His team undertook a first-principle analysis combined with Landau theory that we describe briefly in the following. For that purpose, the analysis proposed by Prof. Stengel and coworkers considered the energy expansion in the neighborhood of the parent cubic phase, so that

$$\begin{aligned} E = {} & \frac{C_{\alpha\beta}}{2}\varepsilon_\alpha\varepsilon_\beta + \frac{A}{2}|\phi|^2 + B|\phi|^4 - R_{ii\alpha}\phi_i^2\varepsilon_\alpha + \frac{\chi_0^{-1}}{2}|P|^2 - Q_{iijj}\phi_i^2P_j^2 - e_{ii\alpha}P_i^2\varepsilon_\alpha \\ & + \frac{\beta}{2}|u^{Ti}|^i + N\epsilon_{ijk}P_iu_j^{Ti}\phi_k. \end{aligned} \tag{5.3}$$

The first term in equation 5.3 describes the elastic energy ($C_{\alpha\beta}$ is the elastic tensor). The following two terms (A and B) define the double-well potential associated to octahedral tilts (ϕ_k). The fourth term describes the "rotostriction" coupling, responsible for the tetragonal deformation related to oxygen tilts. The next term is the harmonic energy associated with the soft polar mode (χ_0^{-1} is the inverse of its contribution to the dielectric susceptibility). The sixth and seventh terms include the Q_{iijj} and $e_{ii\alpha}$ tensors that describe the biquadratic coupling between the polar mode and oxygen tilts as well as electrostriction, respectively. Finally, the last two terms of equation 5.3 incorporate a new coupling mechanism associated with an antiferroelectric mode of the Ti atoms, (u_j^{Ti}) (see the schematic lattice representation in figure 5.11). In the tetragonal phase, the u_j^{Ti} mode strongly couples to the polarization and tilts via a trilinear term (N is a scalar and ϵ_{ijk} is the antisymmetric Levi-Civita tensor). We shall see in the following that this trilinear coupling is the key ingredient to account for the observed dielectric anisotropy.

With this in mind, we studied the inverse dielectric constant ϵ^{-1}, which is defined as

$$4\pi\epsilon^{-1} = \frac{d^2E}{dP_i^2} \sim \chi_0^{-1}(T) - 2\sum_k \widetilde{Q}_{kkii}\phi_k^2(T), \tag{5.4}$$

where $\widetilde{Q}_{kkii}$ is an effective biquadratic coupling tensor that includes the contribution of strain and the antiferroelectric mode. It can be demonstrated that this tensor can be written as

$$\widetilde{Q}_{kkii} = Q_{kkii} + e_{kk\alpha} C^{-1}_{\alpha\beta} R_{ii\beta} + \frac{T^2}{2\beta}(1-\delta_{ik}). \tag{5.5}$$

In equation 5.4, the term $\chi_0^{-1}(T)$ reproduces the experimental Curie-Weiss behaviour of the inverse dielectric susceptibility and $\phi_k^2(T)$ accounts for the temperature dependence of the octahedral tilts. Given the cubic symmetry and the nature of the spontaneous distortion, only two components of Q_{iikk} are relevant to our study, namely, the longitudinal Q_{1111} and transverse Q_{1122} components.

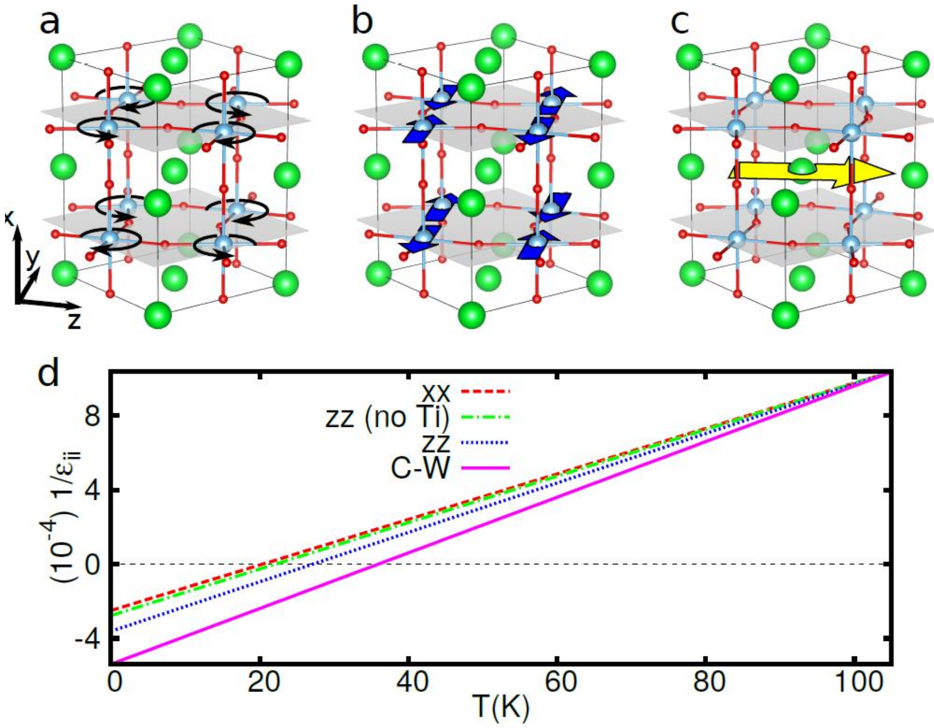

FIGURE 5.11: Panels (a)-(c) show schematically the three modes that are coupled by the tri-linear term in equation 5.3: (a) the AFD mode along the x axis, (b) the AFE mode of the Ti atoms along the z axis and (c) the polar mode along the y direction. The yellow arrow in (c) indicates the direction of the polar mode; in practice it is composed by the displacement, of a different amount, of all the atoms along the y direction. (d) Inverse dielectric constant, ϵ_{ii}^{-1}, as function of temperature. The pink dashed line is the Curie-Weiss law fitted by experimental data at high temperature, and represents the expected behaviour if the crystal remained in the cubic high-symmetry structure (i.e. neglecting the primary and secondary effects of the tilts). The red and the blue lines are the calculated values for ϵ_{xx}^{-1} (out-of-plane) and ϵ_{zz}^{-1} (in-plane), respectively. For comparison, we also show (green dashed line) the hypothetical behaviour of ϵ_{zz}^{-1} if we suppressed the trilinear coupling to the antiferroelectric-Ti mode.

Now we are in position to determine the specific contributions of strain, tilts and the antiferroelectric mode to the dielectric behaviour of $SrTiO_3$. For that purpose, all coefficients in equation 5.3 were calculated following the strategy outlined in reference [183], employing density functional perturbation theory (DFPT), and using the local-density approximation (LDA) and norm conserving pseudopotentials. As a first step, only the two first terms in equation 5.5 were considered, i.e., excluding the antiferroelectric mode. In these conditions, we found that the values for the longitudinal and transverse components of Q_{kkii} and $Q^{(e)}_{kkii} = e_{kk\alpha} C^{-1}_{\alpha\beta} R_{ii\beta}$ are similar ($\widetilde{Q}_{1111} = Q_{1111} + Q^{(e)}_{1111} = -0.113$, $\widetilde{Q}_{1122} = Q_{1122} + Q^{(e)}_{1122} = -0.103$, see table 5.1) and, thus, the calculated dielectric constant is nearly isotropic. Although such values soften the component dielectric normal to the octahedral tilt axis, seemingly the inferred anisotropy is too weak to describe the observed field-induced ferroelastic twin distributions.

$kkii$	Q_{kkii}	$Q^{(e)}_{kkii}$	$Q^{(Ti)}_{kkii}$
1111	-0.208	+0.095	-
1122	-0.031	0.072	0.033

TABLE 5.1: Values calculated for the coefficients Q_{kkii}, $Q^{(e)}_{kkii}$, $Q^{(Ti)}_{kkii}$ defined in the text. Ha/bohr units are used.

It turns out that the antiferroelectric u^{Ti}_j mode is the crucial ingredient to explain a stronger softening of the transverse $\widetilde{Q}_{1122}$ component. In this line, it is important to note that $Q^{Ti}_{ik} = \frac{T^2}{2\beta}(1 - \delta_{ik})$ in equation 5.5 is positive by construction and only affects the transverse $\widetilde{Q}_{1122}$ component, so that the net result is that Q^{Ti}_{ik} leads to a softening of the components of the dielectric tensor that are normal to the AFD tilt axis. Indeed, the calculated value is $Q^{Ti}_{ik} = 0.033$, so that now $\widetilde{Q}_{1122} = Q_{1122} + Q^{(e)}_{1122} + Q^{(Ti)}_{1122} = -0.070$, which is significantly smaller than $Q_{1111} = -0.113$ (see table 5.1). Therefore, the incorporation of the u^{Ti}_j mode is indispensable to obtain a strong dielectric anisotropy, compatible with the observed twin distributions. The key role of u^{Ti}_j is further underlined by the calculations of the out-of-plane ϵ^{-1}_{xx} and in-plane ϵ^{-1}_{zz} components of the inverse dielectric constant. We find that unless the trilinear coupling to the antiferroelectric-Ti mode is included, the dielectric constant is nearly isotropic, as seen in figure 5.11 (d). We stress that our conclusions on the dielectric anisotropy are in good agreement with the available experimental literature [184, 185], and is consistent with earlier theoretical studies [186].

We, therefore, reach the important conclusion that the observed dielectric anisotropy, i.e., a higher dielectric anisotropy perpendicular to the AFD tilt axis, is originated by the emergence, below T∼105 K, of an AFE lattice mode that couples with polar and AFD tilt modes.

5.5 Ferroelastic twins and dielectric responses in $SrTiO_3$

We have seen before how the distribution of the ferroelastic twins changes with electric fields. Now we will relate these changes with macroscopic dielectric measurements. In this context, it is relevant to stress that commonly $SrTiO_3$ is considered to be a non ferroelectric material. However, it is also known that ferroelectricity can be induced under strain [49, 50] or by doping with O^{18} isotopes [51]. Additionally, several reports exist on the observation of ferroelectric behavior on $SrTiO_3$ even for nominally stoichiometric $SrTiO_3$, under large electric fields or mechanical stress [187, 26, 188] and even a giant piezoelectric effect has been reported in the $SrTiO_3$ surface [52]. Moreover, it has been shown that the twin domain walls exhibit a polar character [53, 24, 54] and some works attribute this fact to the origin of the observed changes under electric fields [55, 56]. Yet, other works purpose that ferroelectric states can be induced by non-stoichiometric polar nanoregions [188, 50] in absence of any external stress. In view of all these observations, we have measured the electric field responses of $SrTiO_3$ crystals, and correlated the dielectric measurement with the field-induced spatial redistributions of ferroelastic twins observed by optical imaging.

To explore this issue, a ferroelectric test system (Radiant Technologies Inc.) has been used in order to measure the displacement currents. A triangular voltage cycle at 20 Hz has been used in our measurements. Figure 5.12 (a) shows the current measured by cycling the voltage at different temperatures from 6.5 K to 140 K. Below ~ 50 K, two current displacement peaks appear (indicated by arrows), similar to the typical ferroelectric I(V) behaviour. These peaks appear around 10 V (0.2 kV/cm) and 100 V (2 kV/cm), these field asymmetry could be related to an imprint caused by the different material of top (Au/CoFeB) and bottom electrodes (Ag). Integrating the current over time (50 ms per voltage cycle) and dividing by the contact area (5x5 mm), the polarization (P) can be plotted as a function of the applied voltage. An hysteretic behaviour below ~ 50 K can be appreciated in the figure 5.12 (b). Moreover, a linear response with voltage is observed for all measured temperatures, and from the slope of these responses the relative permittivity can be extracted, which in our samples varies from $\epsilon_r \sim 5400$ at 10 K to $\epsilon_r \sim 1200$ at 110 K in agreement with previous studies [187]. A similar procedure has been done to measure the polarization at different maximum applied fields. For instance, figure 5.12 (c) shows hysteresis loops at 6.5 K, where minor loops (non-saturated loops) can be observed at lower applied voltages as a typical ferroelectric behaviour for applied fields lower than the coercive field. Having both, temperature and voltage hysteresis dependence, we have mapped out the negative remanent polarization as a function of temperature and voltage $P_{r^-}(V, T)$ (figure 5.12 d). As can be appreciated, the remanent polarization increases for large applied voltages and decreases dramatically above ~ 50 K defining a region from which can be derived that high voltages (> 180 V) and low temperatures (< 40 K) are required for a ferroelectric-like behaviour on $SrTiO_3$. Our conclusion is in agreement with previous works that show that ferroelectric-like behavior can be induced in $SrTiO_3$ in a range of temperatures and electric fields very similar to those reported here [187].

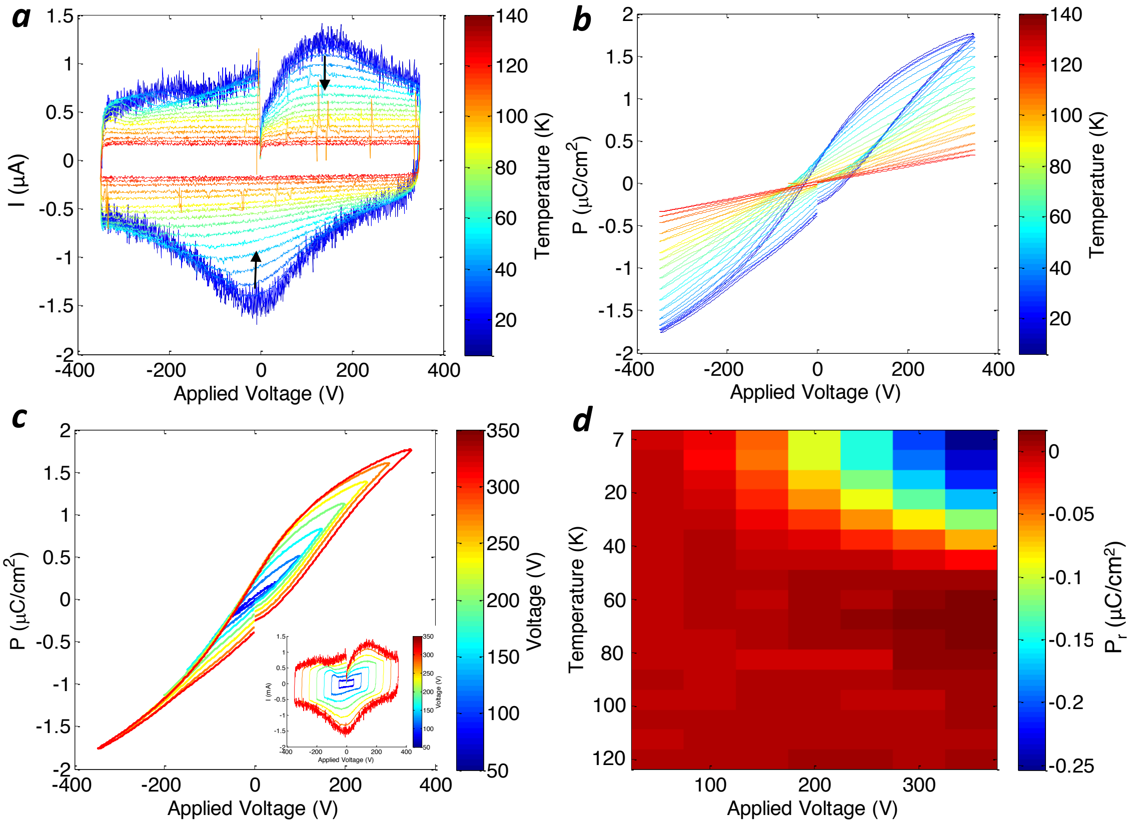

FIGURE 5.12: (a) Current as a function of cycled voltage (50 ms per cycle) at different temperatures. (b) Polarization extracted from (a) at different temperatures. (c) Polarization as a function of different maximum applied voltages at 6.5 K. (d) Mapping of the negative remanent polarization as a function of temperature and applied voltage.

Alternatively, we have measured the dielectric properties using PUND method, which has the advantages of only measuring the intrinsic/remanent polarization of the system. In the previous measurements, the polarization response can be affected by non-remanent polarization extrinsic to $SrTiO_3$, such as, parasitic resistances or linear capacitances. These non-desired contributions can be removed by measuring two opposite voltage cycles after pre-polarizing the crystal with a voltage pulse with the same sign than the starting cycle. Thus, after the pre-polarizing pulse, only non-remanent effects i.e., not relate to displacement currents coming from switching the electric polarization, can be measured and, therefore, by subtracting both cycles, these effects can be eliminated giving only the intrinsic polarization hysteresis loop. This method is called PUND remembering the measurement sequence, Positive Up, Negative Down. In the figure 5.13 (a) are plotted PUND loops at different temperatures.

Notice that now the hysteresis do not exhibit a linear behaviour with the voltage. Similar than previously, the largest remanent polarization $\sim 0.2\mu$ C/cm^2 is measured at 6.5 K and it decreases abruptly below ~ 40 K (figure 5.13 b). Our results are in agreement with other previous studies reporting a ferroelectric-like behaviour on SrTiO$_3$ crystals [188, 187].

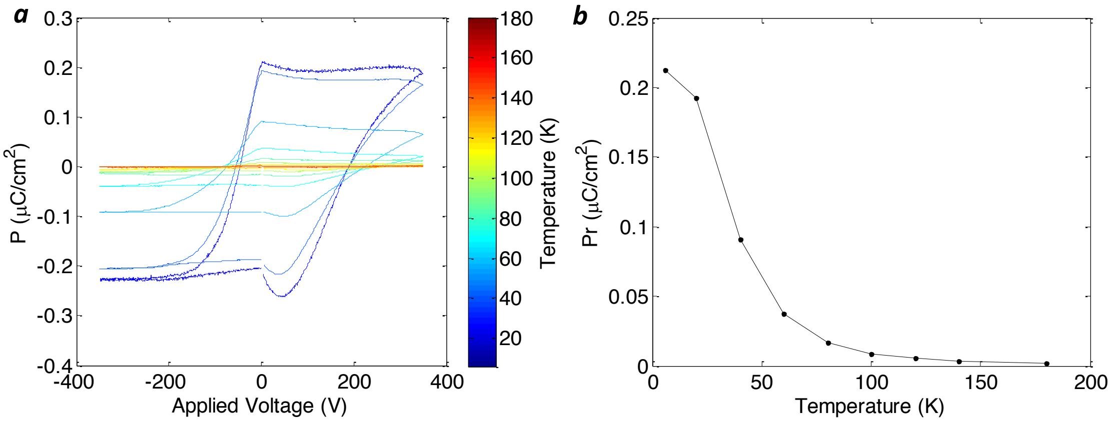

FIGURE 5.13: (a) Polarization as a function of applied voltage measured using PUND method at different temperatures. (b) Remanent polarization extracted from (a) as a function of temperature.

At this point, our efforts has been focused on the imaging, trying to identify any ferroelectric-like features in the twin's reconfiguration under electric field, which could somehow relate to the aforementioned observed ferroelectric-like dielectric behaviour. To do so, we have used, as previously, optical reflectance imaging to track the changes on the surface topography. Studying the effects over entire sample area, we have identified three main different regions. Region (i) contains only $\{a_1, a_2\}$ twins, for that reason, no changes are visible in reflectance. Region (ii) represents the majority part of the surface and contains $\{a, c\}$ twins that under electric field are suppressed while $\{a_1, a_2\}$ expands. The last region (iii) presents $\{a, c\}$ twins that seems to be changed under field but not suppressed as in (ii), this region corresponds to the non-suppressed twins at 200 V in the optical image shown in figure 5.3 (b). These regions are schematically depicted in the figure 5.14 (a) corresponding to optical image subtraction between 0 V and 200 V. An area of 50x500 μm containing all defined regions has been selected (black square in the figure5.14 a). Using a similar method than in section 5.2, the standard deviation of each row on the selected area has been tracked from each respective subtraction image ($I(V) - I(V = 0)$) as a function of the applied field at 6.5 K (figure 5.14 b). The electric field response of the topography changes (represented as the standard deviation) can be classified into the same previously defined regions. In the region (i) there is no visible effect, as it is expected because, according to our previous acquired knowledge, no changes can be appreciated on $\{a_1, a_2\}$ twins under field. In the interface between region (i) and (ii) the response is completely symmetric and reversible, indicating that same changes occurs for positive and negative field. Inside region (ii) the signal is reversible but very asymmetric, more changes occurs for positive field. Finally, in the region (iii) the response starts to develop an hysteretic behaviour. Although the observation of this hysteretic behaviour is not a direct signature of ferroelectricity, the identification of specific regions in which two remanent topography states are observed may provide important clues to understand the $SrTiO_3$ ferroelectric-like signatures in the dielectric characterization. An example of this observation is provided in the following.

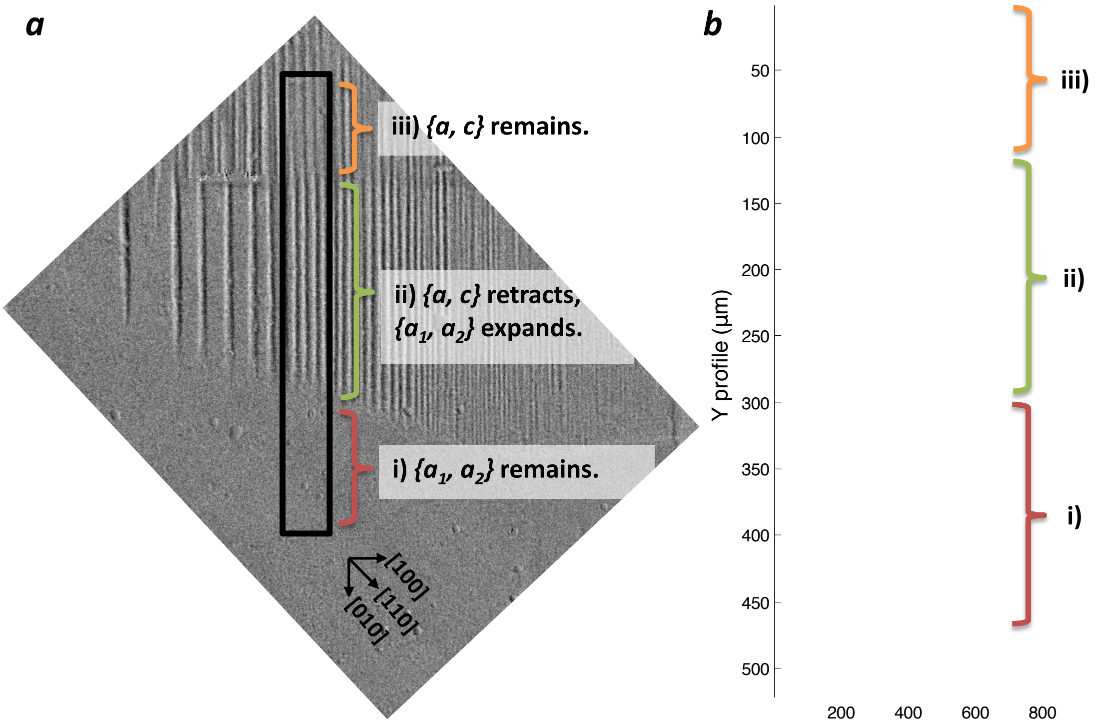

FIGURE 5.14: (a) Subtraction image from optical microscopy images at 0 V and 200 V ($I(200V) - I(0)$) at 6.5 K. Three main regions (i, ii, iii) are defined respect its response under electric field. The black box defines a selected representative area. (b) Standard deviation extracted row-to-row from the selected area at each subtracting image ($I(V) - I(V = 0)$). The response can be classified mainly into the previously defined regions.

In this line, the experiments described previously seem to indicate an important role of the changes in the ferroelastic twin distribution to understand the ferroelectric-like signatures in the dielectric measurements. In order to investigate more in detail this issue, we analyzed the evolution of ferroelastic twins in three different $SrTiO_3$ crystals in which the relative amount of $\{a, c\}$ and $\{a_1, a_2\}$ domains changed significantly. This is seen in the insets of figure 5.15, which show the subtraction optical images, using the same procedure as the one used to obtain the images shown in figures

5.3 (c) or 5.9 (b). Therefore, these optical images indicate the regions were $\{a, c\}$ domains have been suppressed by the electric fields. For instance, the leftmost image in figure 5.15 corresponds to a sample in which only a small area was affected by electric fields, in other words, the initial distribution of $\{a, c\}$ domains was restricted to a small region on the sample. On the other hand, the rightmost optical image in figure 5.15 corresponds to a sample in which $\{a, c\}$ domains were converted into $\{a_1, a_2\}$ domains in a very large fraction of the sample. Finally, the middle optical image shows an intermediate case. To do a more quantitative analysis, we defined the ratio between the integrated area where ferroelastic domains were changed by electric fields relative to the total area of the sample. Using this definition, the leftmost image in figure 5.15 corresponds to a ratio of about 0.3, while the middle and rightmost images correspond, respectively, to ratios of 0.5 and 0.9. Subsequently, we compared the values of these ratios to the polarization hysteresis loops obtained via dielectric characterization. As shown in figure 5.15, we observed that the remanent polarization increases with the area of the aforementioned ratio. In other words, the experimental data shown in figure 5.15 seems to indicate that those regions displaying higher ferroelastic twin mobility are those that show at the same time more pronounced ferroelectric-like features in the dielectric response (i.e., a higher remanent polarization). Therefore, the data presented in figure 5.15 points apparently to a correlation between ferroelastic motion and ferroelectric-like dielectric responses. In spite of the observed correlation, it is fair to say that we are still far from understanding the precise origin of the hysteretic dielectric response of $SrTiO_3$ crystals. In particular, as pointed out at the introduction of this Chapter, the origin of the suspected ferroelectricity may be within the domains or, alternatively, in the domain walls. Along this line, it is interesting to note that relatively small mechanical stresses can generate ferroelectric behaviour in $SrTiO_3$ [187, 26, 188, 50]. This is an important point to consider, as residual stresses in ferroelastic domain structures might provide the mechanical stress required to generate the ferroelectric behavior. On the other hand, as explained in the introduction, many works point to a polarity inside the ferroelastic domain walls [53, 24, 54, 50, 55], which, again, could be also at the origin of a ferroelectric behavior. In any case, the origin of the peculiar ferroelectric signature in the dielectric response of $SrTiO_3$ is still an open question that undoubtedly deserves more attention in the future.

5.6 Conclusions and perspectives

Combining optical reflectance and MO imaging, we have identified how the ferroelastic twins reorganize under an electric field applied in the [001] direction. From these experiments, we have confirmed that the low-temperature dielectric properties of $SrTiO_3$ are anisotropic and, additionally, that the dielectric susceptibility is higher along the normal to the axis of the octahedral tilts in the AFD tetragonal phase. Interestingly, we have uncovered that the driving force of this anisotropic behavior is related to the emergence of an antiferroelectric (AFE) displacement of the Ti ions that

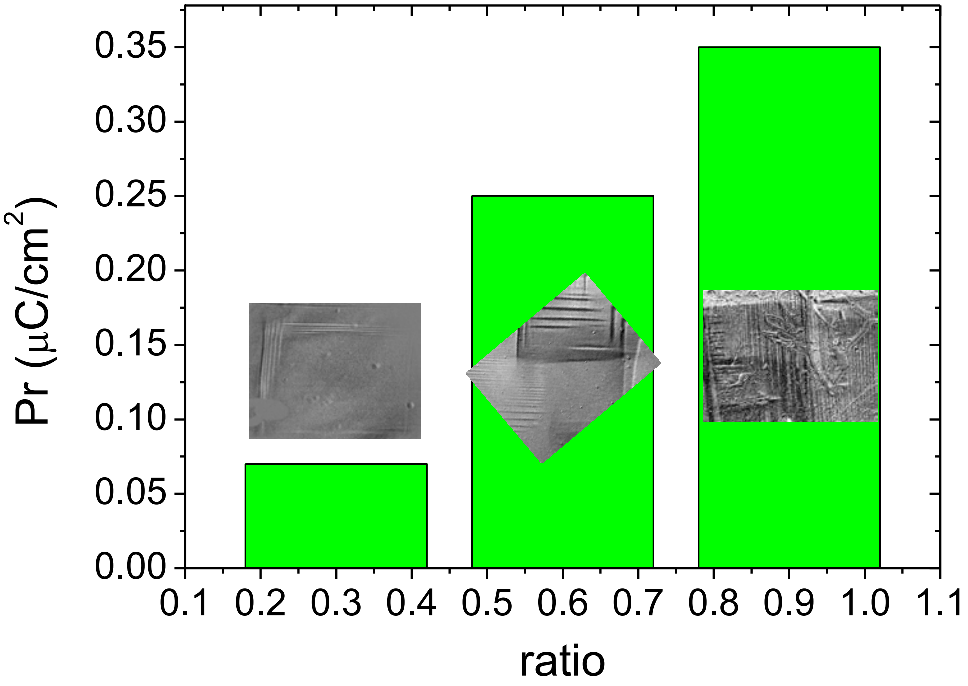

FIGURE 5.15: Remanent polarization as a function of the twin's reconfiguration area quantified as the ratio between the changed area at 200 V and the total area. Insets show similar area of the subtracting image (200 V-0 V) at 10 K of each sample.

couples to polar and AFD lattice modes.

Beyond this important conclusion, we have also studied how the electric field-induced changes of the ferroelastic twin distributions are related to macroscopic dielectric measurements. Our magneto(optical) approach to the study of the ferroelastic domain structure has revealed that the spatial redistribution of the twins depends strongly on the orientational character of the ferroelastic domains. Interestingly, we find that those regions displaying higher ferroelastic twin mobility are those that show at the same time more pronounced ferroelectric-like features in the dielectric measurements. This seems to point to a correlation between ferroelastic motion and redistribution and ferroelectric-like dielectric responses, a point that justifies further research to better settle this relationship. In particular, an important point is to elucidate whether the ferroelectric-like response comes from within the domains or in the domain walls. To investigate this issue, future experiments may be directed at exploiting optical birefringence imaging under field to probe electro-optical effects and the possible ferroelectricity inside ferroelastic domains in $SrTiO_3$. Alternatively, other experimental approaches with atomic-scale resolution -e.g., transimission electron microscopy- may be important to reveal if signatures of electric polarization may be present inside the domain walls.

Chapter 6

Directional heat dissipation generated by surface acoustic waves in Co/Pt/$LiNbO_3$ heterostructures

6.1 Introduction

In this chapter, the magneto-optics is used to probe the properties of magnetic microstructures coupled to a piezoelectric material. The interest of these heterostructures comes from the advantages of controlling the magnetic states with electric fields. In this line, in the previous chapter, we presented a magnetoelectric system composed by a ferromagnetic film grown on top of $SrTiO_3$, where the magnetoelectric coupling was governed by the magnetoelastic effects between the ferroelastic twins of the substrate and the film's magnetization. In that case, we saw that the electric field modifies the ferroelastic twin structure of $SrTiO_3$ and therefore, alters the strain-induced magnetoelastic anisotropy, changing the magnetic domain pattern of the magnetic overlayer. Following the approach of controlling magnetization states with electric fields through magnetoelastic coupling, we have explored new scenarios that allow a dynamic control of the magnetic states. Surface acoustic waves (SAW) are propagating strain waves that can be generated through oscillating electric fields at the surface of piezoelectric material [71] and may be exploited to modulate the properties of adjacent magnetic layers. Indeed, recent studies have demonstrated that magnetic states can be dynamically changed at the SAW frequencies (MHz) [73]. Moreover, SAWs have been used for detecting ferromagnetic resonances [74] and for spin pumping [75]. In the present work, we explore the SAW effects on films with perpendicular magnetic anisotropy (PMA) which are advantageous for high-capacity and high-density STT-MRAMs [76, 77, 78]. For this purpose, Pt/Co/Pt ultrathin films with PMA have been grown and patterned into microstructures on $LiNbO_3$ substrates. Because the out-of-plane projection of the magnetization, we used polar magneto-optical microscopy to access the magnetic properties of the individual microstructures and study the effects of SAWs on the magnetization reversal process.

In this Chapter we observe how the effect of SAW change the coercive fields in the magnetic microstructures. We propose that the main mechanism for the observed changes of the coercive fields is the generation of a highly directional heat created by SAWs.

6.1.1 Generation and characterization of SAW

SAWs are generated by applying an oscillating electric field at microwave frequencies on interdigitated (IDT) structured contacts of Al grown by sputtering on top of the piezoelectric 128º Y-cut LiNbO$_3$ (figure 6.1). When an oscillating electric field is applied to the IDT it causes a periodic displacement of the piezoelectric surface, also creating a surface potential wave. When the applied frequency matches the resonance condition a SAW is generated and propagates out of the IDT and on the piezoelectric material. The resonance frequency is determined by the Rayleigh wave velocity (v_R) by:

$$f_0 = \frac{v_\mathrm{R}}{\lambda_\mathrm{SAW}} = \frac{v_\mathrm{R}}{2d} \tag{6.1}$$

where d is the distance between consecutive +/- interdigit contacts. Therefore, all frequencies generate a propagating SAW on the system; only the resonance frequency and its harmonics. In order to characterize the generated SAWs, two identical IDTs grown one in front to the other are needed. Measuring the rf power absorption applied to IDT$_1$ (S_{11}) with a network analyzer, the resonance frequencies can be identified (figure 6.2 a). However, intrinsic absorptions of the IDT, for instance, acting as an antenna, could also appear in the absorption spectra. Hence, S_{11} does not characterize the propagating SAW power generated by the IDT$_1$.

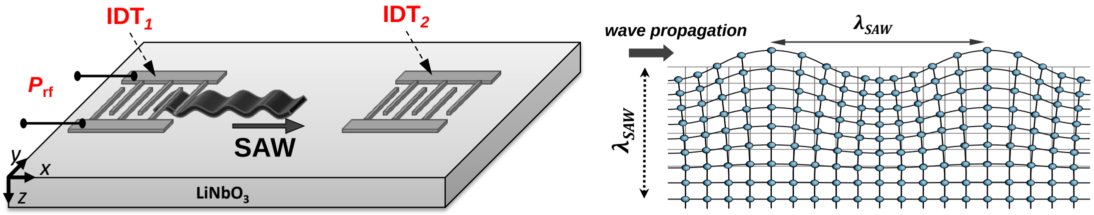

FIGURE 6.1: In the left, scheme of SAW generation with interdigitated (IDT) contacts on LiNbO$_3$. The rf power (P_{rf}) is applied on IDT$_1$ and its transmittance is measured on IDT$_2$. In the right hand side, scheme of propagating SAW with wavelength λ_SAW.

Measuring the transmitted electric signal (S_{21}) applied on IDT$_1$ on the symmetric IDT$_2$, the efficiency to convert microwave into SAW of the IDT$_1$ is characterized. Figure 6.2 (b) shows the S_{21} spectra, where it can be appreciated that the transmission magnitude at the harmonics has not a direct correlation with the $S_1 1$ absorption spectra (figure 6.2 a). Therefore, for a same applied power on the IDT$_1$, SAW propagation power is different as a function of the harmonic. Since not all absorbed power in the

IDT$_1$ is converted to SAW, we will use both S_{11} and S_{21} magnitudes to discuss the origin of SAW's heat dissipation.

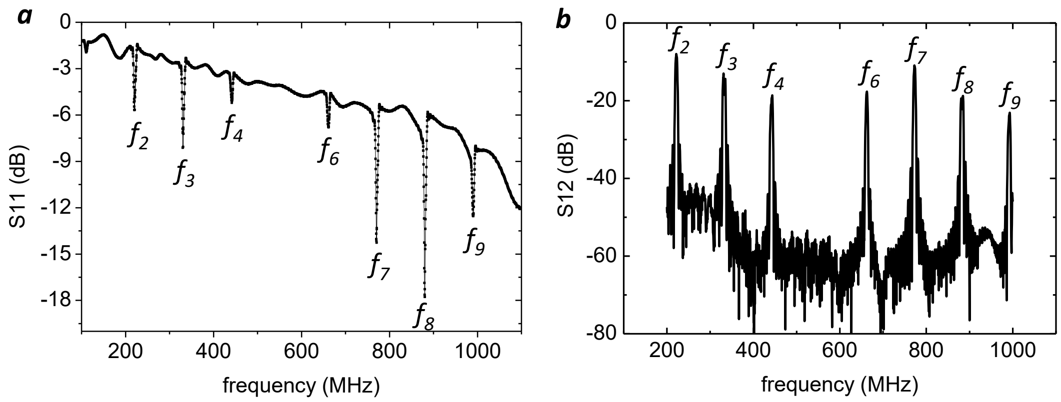

FIGURE 6.2: (a) S_{11}, absorption spectra of IDT$_1$. (b) S_{21}, transmitted power from IDT$_1$ to IDT$_2$ via SAW.

6.1.2 Co/Pt microsctructured thin films with PMA

Pt/Co/Pt has been chosen as the magnetic system coupled to SAWs for two main reasons: first, because it is well known that PMA can be induced for certain thicknesses of cobalt due to the spin-orbit coupling between the interfaces of Pt/Co/Pt [189, 190, 191]. Second, because cobalt has a large magneto-optical activity [192, 193, 79], thus, facilitating its magnetic characterization by Kerr microscopy. For these reasons, we have grown Pt/Co/Pt structures by dc magnetron sputtering varying the Co thickness and keeping it fixed for both Pt capping (1.5 nm) and bottom (6 nm) layers. Thus, an accurate control of the Co thickness is needed and therefore, low growing rates of 0.2 Å/s are used (see appendix B). The values of Co thicknesses have been determined on continuous films grown on Si substrates. Figure 6.3 shows polar Kerr rotation hysteresis loops of thin films done at room-temperature (RT) and at $\lambda = 475$ nm for different Co thickness (0.6, 0.8, 1, 1.2 and 2 nm). Below 2 nm Co thickness, squared loops are measured, indicating that at remanence, all the magnetization is pointing out of the plane. From the polar Kerr measurements we notice that for the 2 nm-thick Co the hysteresis does not show PMA as it is expected for larger thickness of Co in the Pt/Co/Pt systems [189, 194]. For our measurements coupled to SAW, we have chosen the thinner Co system with PMA, because due to its low coercive field, it becomes more susceptible to external anisotropy variations. Then, microstructured (Pt(6 nm)/Co(0.6 nm)/Pt(1.5 nm)) made by optical lithography have been grown, with different shapes and sizes (4-80 μm) on top of the SAW device (see figure 6.3). At this point, polar Kerr microscopy is needed to access its individual magnetic properties. Even though all microstructures have been grown simultaneously, variations on the coercive field are observed between them. For instance, figure 6.4 shows a polar Kerr image of four squares (10x10 μm) taken near its negative coercive field. As can be

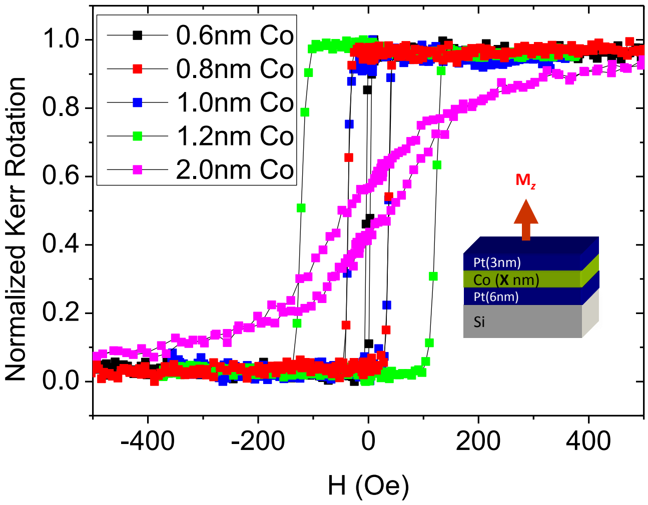

FIGURE 6.3: Normalized polar Kerr hysteresis for different Co thickness (from 0.6 to 2 nm) measured at RT and at $\lambda = 475$ nm.

appreciated, some of them have already reversed its magnetization, one is reversing it and the last one has still magnetization in the positive remanence state. These variations between identical microstructures, could be related to lithography imperfections.

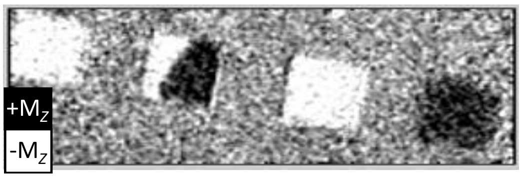

FIGURE 6.4: Variations on the coercive field between microstructures can be seen in this polar Kerr images taken near Hc of four squares (10x10 μm) simultaneously.

6.2 SAW effects on PMA Co/Pt microstructures

We have taken Polar Kerr images as a function of magnetic field in the Pt/Co/Pt squares of 40x40 μm. Figure 6.5 shows a hysteresis loop extracted by plotting the mean value of the Kerr image at each magnetic field (see insets figure 6.5). SAW effects on the magnetization has been studied on different structures obtaining similar results. Thus, to illustrate the effects of SAW on the magnetism, we have chosen a particular microstructure (40x40 μm square) that is discussed in the following.

Firstly, we have studied the SAW effects on the magnetization reversal process keeping the SAW frequency at 331 MHz (f_3, see S_{21} spectra in figure 6.2 b) and varying the applied power from 12 to 25 dBm in the input rf source. A clear reduction

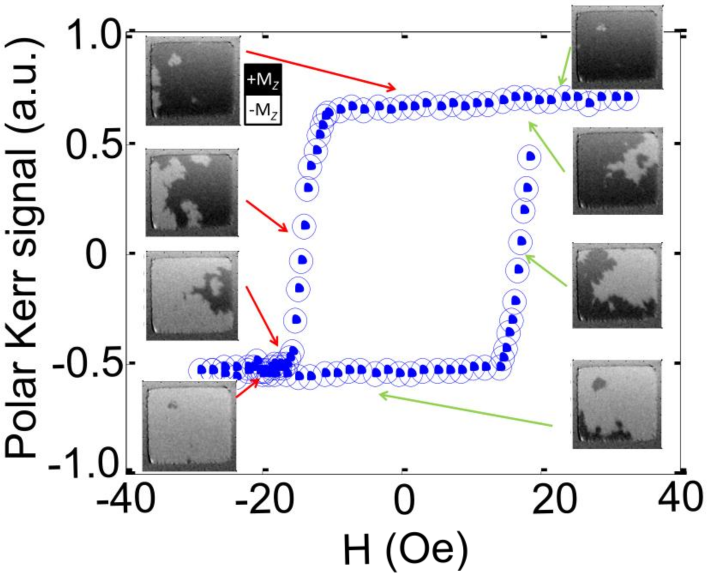

FIGURE 6.5: Polar Kerr hysteresis loop extracted by computing the mean value of the polar Kerr image at each magnetic field from a 40x40 μm Pt/Co/Pt square on LiNbO$_3$. The insets show polar Kerr images illustrating the domain pattern at different increasing (green arrows) and decreasing (red arrows) fields.

of coercive field is observed (6.6 a) when the power supplied by the rf source is increased. In order to understand better the decrease of the coercive field, we plot the relative change of coercive field ($\Delta H_c/H_c$) as a function of the SAW power (P_{SAW}) in the figure 6.6 (b). A large reduction, up to $\sim 40\%$ of coercive field change, is found at the highest applied power (25 dBm).

These experiments relate the power delivered to generate the SAWs with the decrease of H_c. Regarding this observation, two main scenarios may be proposed: In the first one, SAWs destabilize the magnetic equilibrium state near H_c via the coupling between the SAWs induced oscillating magnetoelastic anisotropy and the spin precession (see appendix C) as experimentally shown in the reference [195]. In the second scenario, SAWs modifies the Pt/Co/Pt anisotropy by transferring heat to the system. In order to understand better which of these scenarios is at play, we have prepared an experiment, in which two MO loops have been measured at two SAW frequencies keeping the applied power at 25 dBm (depicted in figure 6.7 a). The two measurements done at the resonance frequencies of 331 MHz (f_3) and 773 MHz (f_7) show changes in the coercive field of $\sim 40\%$ and $\sim 80\%$ respectively (figure 6.7 b). Taking into account that the difference between f_3 and f_7 is around 3 dB in the S_{21} spectra - *i.e.* the amplitude of SAW at f_7 is twice that for f_3 -, the difference on the effects at these frequencies (f_3 and f_7) can be explained by the power transferred to the SAWs. At this point, both scenarios, namely SAW-induced magnetic coupling and heat transfer generated by SAWs could explain these results. However, we have measured a $\sim 3\%$ of change in the coercive field at 360 MHz (out-of-resonance frequency), where there

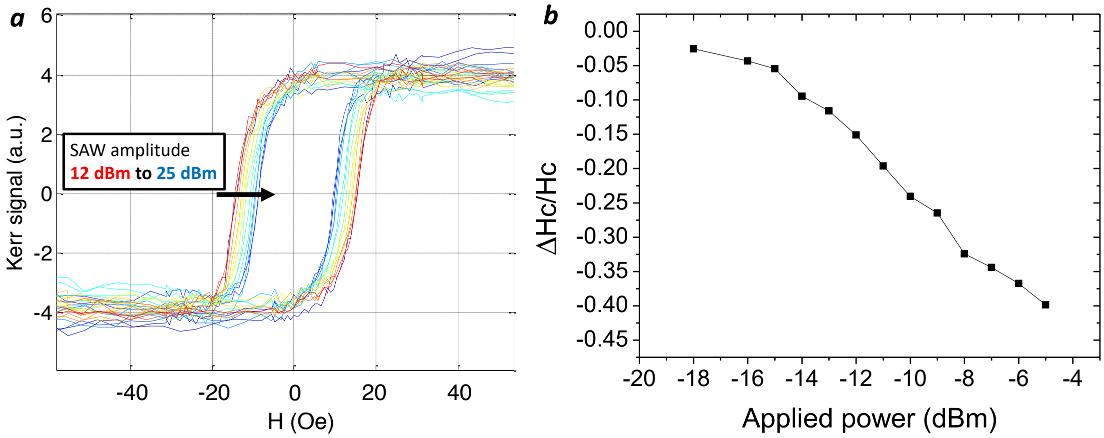

FIGURE 6.6: (a) Polar Kerr hysteresis loops at different SAW applied powers (from 12 to 25 dBm) at 331 MHz. (b) Relative change of the coercive field as a function of P_{SAW}.

is no SAW propagating on the $LiNbO_3$ (figure 6.7 b). This variation suggests that the heating from the IDT might be playing a role.

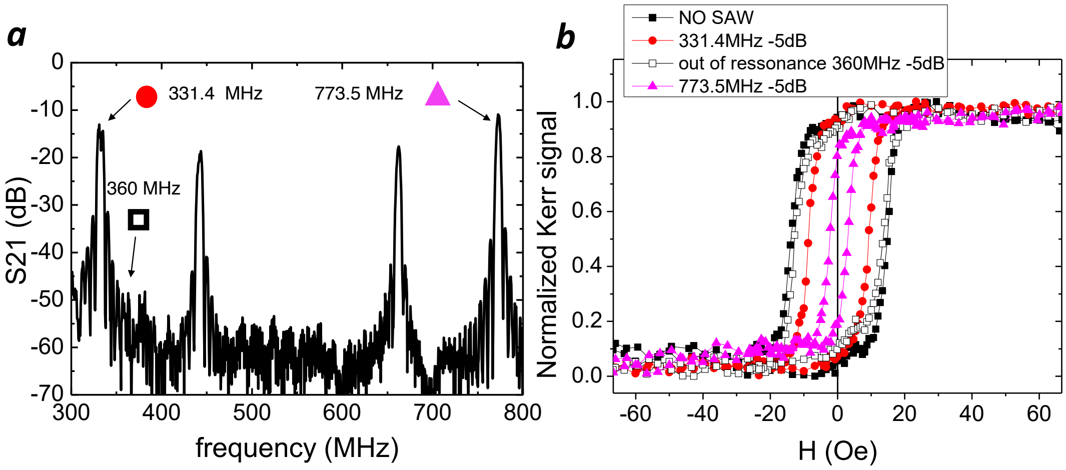

FIGURE 6.7: (a) S_{21} spectra where the measured frequencies are indicated. (b) Polar Hysteresis loops without SAW (black squares), at 331 MHz (red circles), at 773 MHz (magenta triangles) and at 360 MHz out-of-resonance frequency (open squares).

As a summary, our results show an assisted magnetization reversal process caused by SAW on Pt/Co/Pt microstructures with PMA on $LiNbO_3$. However, the mechanism responsible of SAW effects is unclear at this point. The reason for this uncertainty is that a small reduction of the coercive field has been found even at out-of-resonance frequency where the SAWs do not propagate. This observation may hint to some heat generated by the creation of SAWs, which is larger in resonance conditions, but still may be present out-of-resonance. To clarify the origin of the SAW-induced changes, a first step is to study the temperature dependence of the coercive field. For that purpose, polar hysteresis loops have been extracted at different temperatures of the system using a Peltier cell. Figure 6.8 show the coercive field as a function of the temperature change with respect to room temperature (RT). Even though, cobalt has its Curie temperature higher than RT (Tc=1400 K), from temperature-dependent measurements of the MO loops we see large variations of the coercive field, plausibly due to a strong reduction of Tc by the ultrathin thickness of the Co layer. Our results are in agreement with previous studies on PMA Pt/Co/Pt systems where strong temperature-dependent changes in the magnetization have been observed [196, 197]. Therefore, the magnetic properties of the analyzed Pt/Co/Pt microstructures are very sensitive to temperature variations around RT. A proof of this is that almost all the Kerr signal is lost at 9 K above RT. Hence, the MO experiments under SAWs together with temperature-dependent H_c measurements, seem to indicate that the observed changes of H_c under SAW are compatible with heat generated by SAWs. To investigate these issues in more detail, we used scanning probe microscopy (SThM) to map out the heat generated by SAWs as described in the next section.

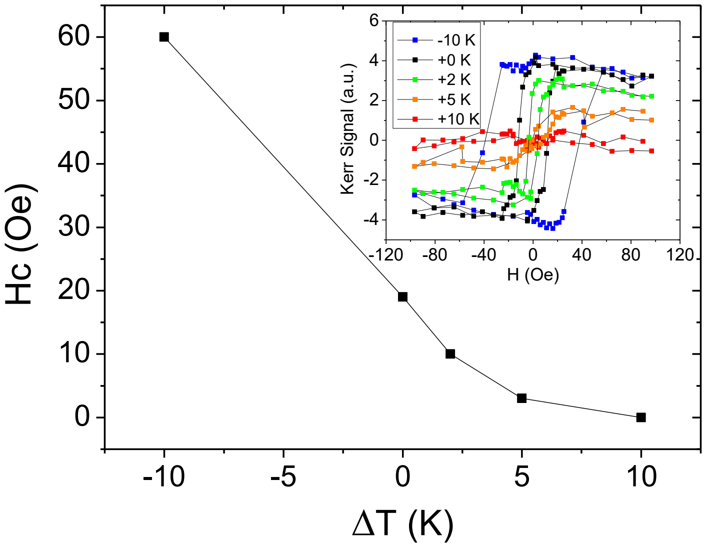

FIGURE 6.8: Polar hysteresis loops has been extracted at different temperatures of the system using a Peltier cell. The coercive field is plotted as a function of the temperature change respect to RT (ΔT).

6.3 SAW induced heat probed by Scanning thermal Microscopy

In order to check if thermal effects are the responsible mechanism for the observed reduction of coercive field in magnetic structures caused by SAWs, an experimental method to asses the SAW-induced temperature increase is needed. Since, SAW are surface propagating waves at the hundreds of MHz with a penetration depth of $\sim \lambda_{\mathrm{SAW}}$ (figure 6.1), a local and fast temperature probe is required. Notice that thermocouples bigger than $\sim \lambda_{\mathrm{SAW}}$ and with poor surface contact can not give a reliable information, specially on time-resolved measurements. To overcome these difficulties, we have used Scanning Thermal Microscopy (SThM) that measures the resistance change of a nanometric Pt AFM tip to map out the changes of temperature over space [198]. Moreover, in these experiments the distance from the surface of the Pt tip can be controlled with high accuracy. The resistance of the Pt tip (R_{TIP}) is measured using the standard Wheatstone bridge (see appendix C). In order to increase the signal to noise ratio and avoid possible couplings between the tip and the applied electric field (microwaves) on the IDT. The voltage on the bridge has been modulated by an ac signal (V_{ac}) and then filtered by a lock-in amplifier. The scheme of used SThM setup is shown in figure 6.9 (a). The change of resistance is converted to temperature by calibrating the setup using a Peltier cell and a thermocouple.

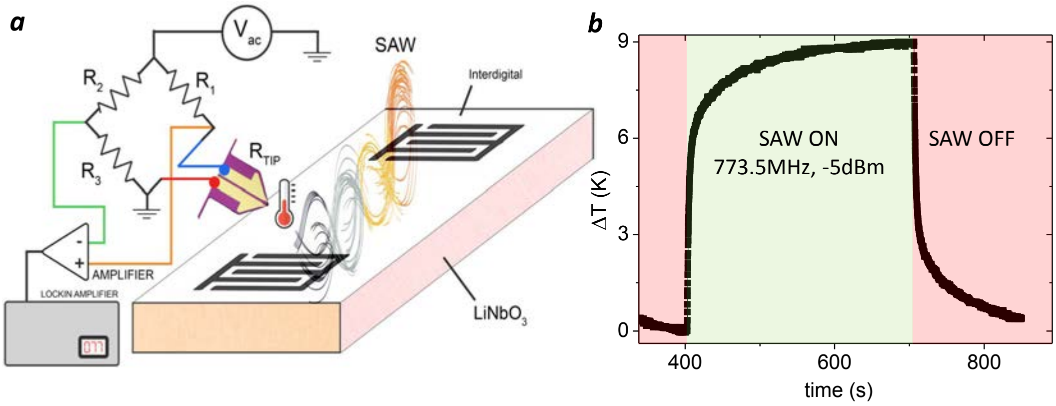

FIGURE 6.9: (a) SThM experimental setup. (b) Change of temperature respect to RT (ΔT) as a function of time. Green panel indicates SAW switched on at 773 MHz at 25 dBm during 300 s and red panel SAW off.

We have measured the temperature with the tip in contact with the surface and at 2 mm in front of the acoustic path, defined as the region between IDT$_1$ and IDT$_2$. In these experiments, typically an increase of temperature can be observed in all resonance frequencies. For instance, the largest increment of 9 K has been found at 773 MHz (25 dBm) as shown in figure 6.9 (b). When turning off the applied field on the IDT, the system's temperature relaxes to RT (figure 6.9 b). At this point, thermal effects cannot be disentangled from the origin of the assisted magnetization reversal process observed in our Pt/Co/Pt microstructures under the effect of SAWs propagation. Nevertheless, taking into account that not all the power absorbed in the IDT$_1$ is converted to SAWs and that the IDT absorbs power even at out-of-resonance frequencies, a new question appears. More specifically, we want to understand whether these thermal effects are originated from Joule heating induced by absorbed power on the IDT or there is an additional contribution intrinsic to the SAW propagation. To answer this question, we have designed an experiment to distinguish the origin of possible heat sources consisting on measuring the temperature increment near before

(f_{o1}), in (f_r) and near above (f_{o2}) a resonance IDT frequency. In figures 6.10 (a) and (b) these three frequencies are depicted on S_{11} and at S_{21} respectively at around 773 MHz. Its correspondent temperature increments are shown in figure 6.10 (c) where it can be appreciated that the out-of-resonance frequencies f_{o1} and f_{o2} cause lower temperature increments than at resonance f_r. In order to quantify the amount of temperature induced by SAWs, we have defined two parameters, namely, the temperature increment at resonance $\Delta T(f_r)$ and the difference between the mean value of both out-of-resonance increment and the one at resonance $\Delta T(f_r - f_o)$.

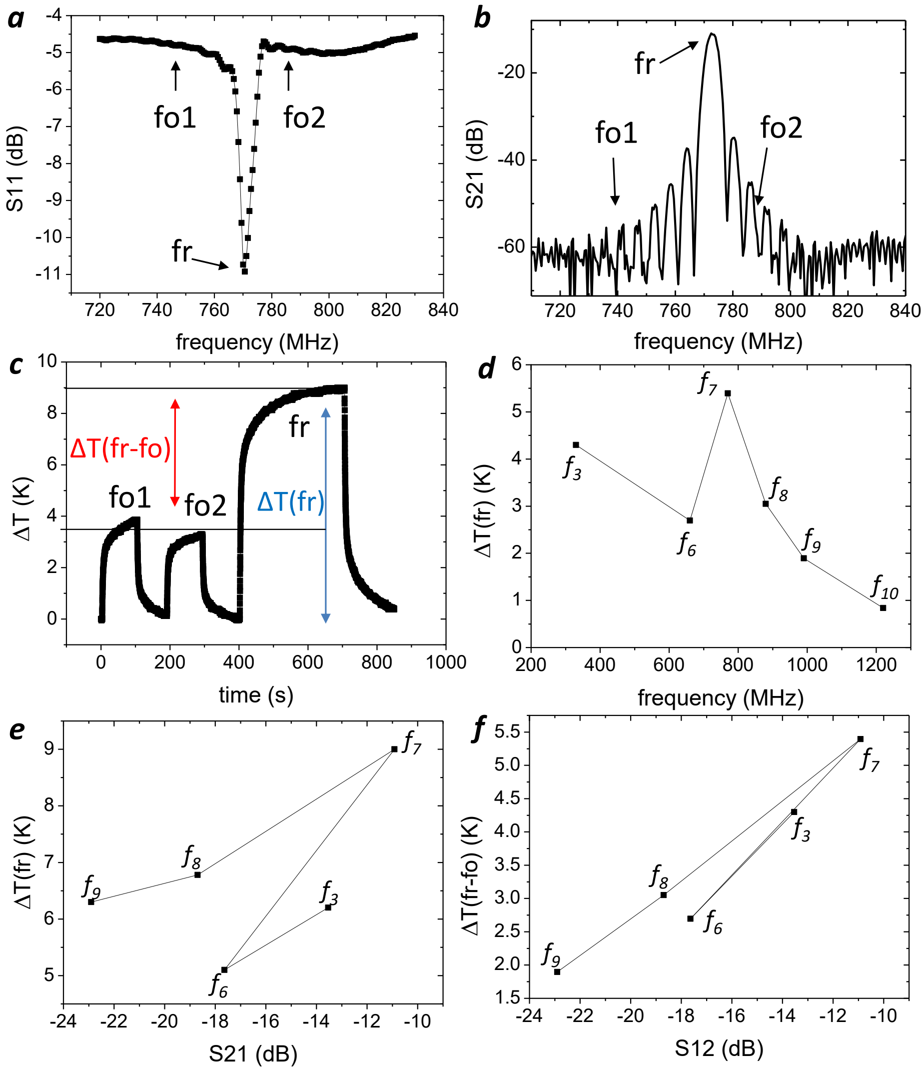

FIGURE 6.10: (a) and (b) S_{11} and S_{21} respectively where the frequencies, near before (f_{o1}), in (f_r) and near above (f_{o2}) are indicated. (c) Change of temperature measured at f_{o1}, f_{o2} and f_r consecutively. $\Delta T(f_r - f_o)$ has been defined as the change between mean change out-of-resonance and in resonance. (d) $\Delta T(f_r - f_o)$ as a function of the SAW resonance frequencies. (e) Temperature changes $\Delta T(f_r)$ at resonance as a function of each S_{21} power (transmitted powers due to SAW). (f) $\Delta T(f_r - f_o)$ as a function of each S_{21} power at resonance.

Repeating the same procedure around different SAW harmonics (figures 6.2), for the same applied power (25 dBm), allows us to discuss the origin of these temperature increments. Plotting $\Delta T(f_r - f_o)$ (figure 6.10 d) and $\Delta T(f_r)$ (not shown) as a function of each respective frequency, no direct relation can be found because, as it is expected, each SAW harmonic has different transmission power (S_21) (see figure 6.2). On the other hand, if $\Delta T(f_r)$ were only originated by SAW intrinsic effects, $\Delta T(f_r)$ should scale with the correspondent S_{21} power of each harmonic. However, it does not (figure 6.10 e), indicating that this increment is affected by an additional source, plausibly coming from the IDT power absorption. Finally, a clear relation has been found by plotting $\Delta T(f_r - f_o)$ as a function of each S_{21} power (figure 6.10 f). This relation shows that an intrinsic heating effect of SAWs is needed to explain the measured temperature increment at resonance and also that its magnitude depends on the SAWs power. As a conclusion, our results suggest two contributions to the SAW induced heating, one coming from the absorbed power on the IDT (Joule effect) and another that is intrinsic to SAWs propagating on LiNbO$_3$. The first contribution, related to the ohmic losses in the IDT (Joule effect), is responsible for the increase of temperature out-of-resonance $\Delta T(f_r) - \Delta T(f_r - f_o)$, while the one intrinsic to SAW is responsible to $\Delta T(f_r - f_o)$.

If two different processes contribute to the SAW-induced heating, different time responses between both heat sources might be expected. To investigate this idea, instead of a continuous SAW excitation, we prepared experiments in which pulsed SAWs where generated at different resonance frequencies and applied powers. Figure 6.11 (a) shows the temperature response of a 50 ms SAW pulse at 773 MHz (f_7), where a fast increase of 0.5 K was measured. After the pulse, the temperature decays rapidly down to 0.25 K and then slowly reduces to RT. In order to analyze this decaying behaviour, the time evolution of ΔT shown in figure 6.11 (a) has been fitted using an exponential function with two decay times ($\Delta T = \Delta T_1 \exp(-t/t_1) + \Delta T_2 \exp(-t/t_2)$). Analogous experiments have been carried out for all SAW resonance frequencies, obtaining similar fast ($t_1 \sim 30$ ms) and slow ($t_2 \sim 1050$ ms) characteristic times (inset figure 6.11 a). Taking into account that SAWs propagate around 3000 m/s (at the sound speed of LiNbO$_3$), the slower characteristic time can be associated to the IDT heat source and the faster one to SAW's intrinsic heat dissipation. Therefore, using short enough SAW pulses (~ 50 ms), both sources can be distinguished. For instance, near resonance where the IDT produces similar heating but the SAWs power decreases, the faster peak reduces and decays visibly before the IDT heat diffusion peak (see figure 6.11 b). This also indicates that at 50 ms pulses, almost all the measured heating is produced by SAWs. Then, the dependence on the transmitted power spectra (S_{21}) has been checked measuring pulses around each resonance harmonic. Figure 6.11 (c) show the change of temperature for a sweep of frequencies at the same interval than figure 6.11 (d), as can be observed, the shape of created by the highest temperature increment each pulse reproduces the S_{21} spectra. The amplitude of pulsed temperature at resonance, as it is expected, scales as a function of each correspondent S_{21} power

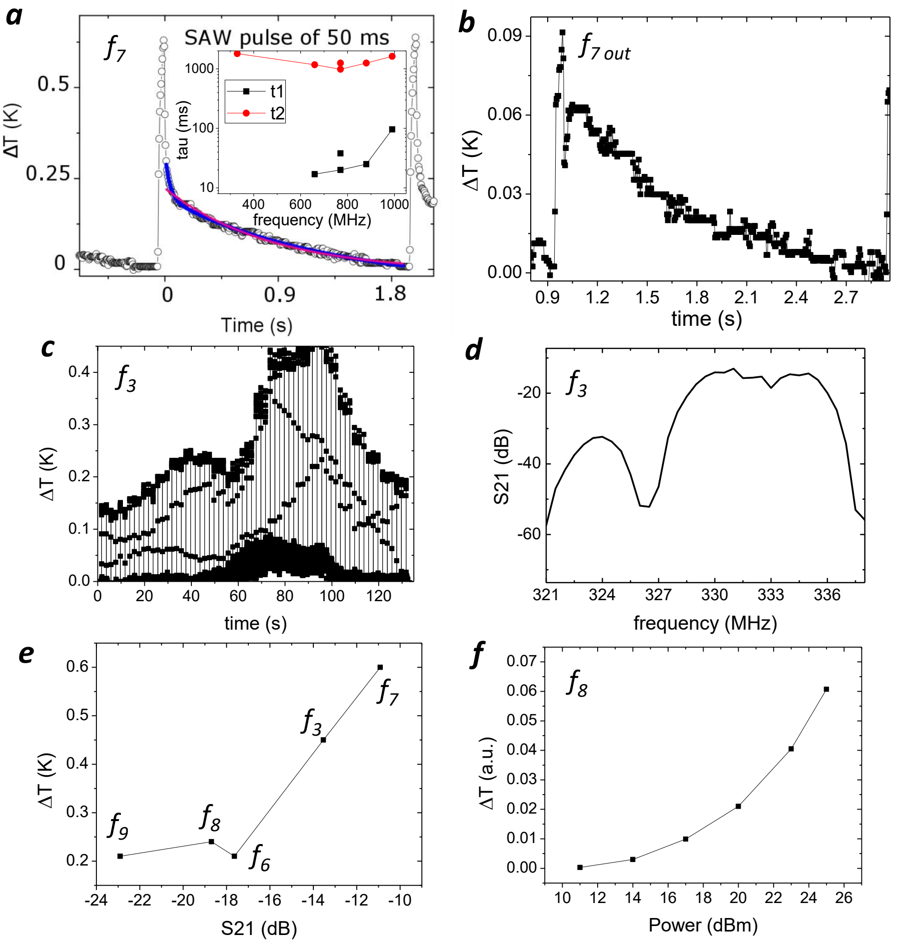

FIGURE 6.11: (a) Temperature increment for a 50 ms SAW pulse at f_7 and at 25 dBm. The inset show two fitted characteristic times on the decay at all the measured harmonics. (b) Same pulse than (a) but at nearly out-of-resonance. (c) Temperature increment for a sweep of pulses around f_7 with the same interval than (d). (d) S_{21} in the interval of (c). (e) Change of temperature of pulses with same power at different harmonics as a function of its S_{21} power. (f) Temperature change of a pulse at f_8 as a function of applied power.

(figure 6.11 e). We have seen, that the intrinsic SAW heating depends on the SAW S_{21} power, in order to characterize its power relation, pulses at constant frequency (f_8) varying the applied power has been measured. The exponential relation shown in figure 6.11 (f) is compatible with 6.11 (e).

Finally, we have explored the SAW heating effects over the space. Since, SAW are propagating waves generated by the IDT, typically are localized on the IDT pathway [199]. Hence, intrinsic SAW effects should vanish moving out its pathway along the perpendicular direction. SAW directionality has been measured by placing the SThM in the middle and 2 mm away from the pathway defined by the IDT shape. In the figure 6.12 is shown that the temperature increment has been reduced dramatically out of the SAW's pathway. This result reconfirms the hypothesis of intrinsic heating SAW effects.

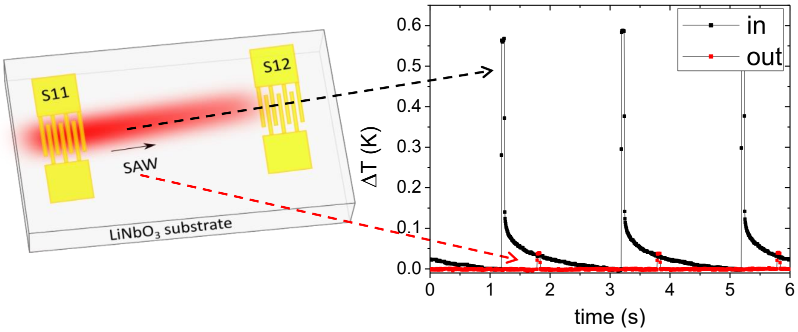

FIGURE 6.12: Directional heating SAW effects. Temperature change in the middle of the SAW's pathway (black pulses) and 2 mm away in its perpendicular direction (red pulses).

In order to check the SAWs directionality, we have measured stroboscopically the piezoelectric field created by the SAWs in a photoemission electron microscopy (PEEM) at Alba synchrotron (CIRCE beamline [200]). Details of the stroboscopic measurements can be found in reference [73] and in Appendix D. Figure 6.13 shows three images of the SAWs piezoelectric voltage taken at three different sample positions (0, 175, 335 μm) respect to the acoustic pathway. As can be appreciated, the SAWs amplitude vanishes critically after the acoustic pathway. This observation reinforces the previous SThM measurements in which a directional SAW induced heat has been observed.

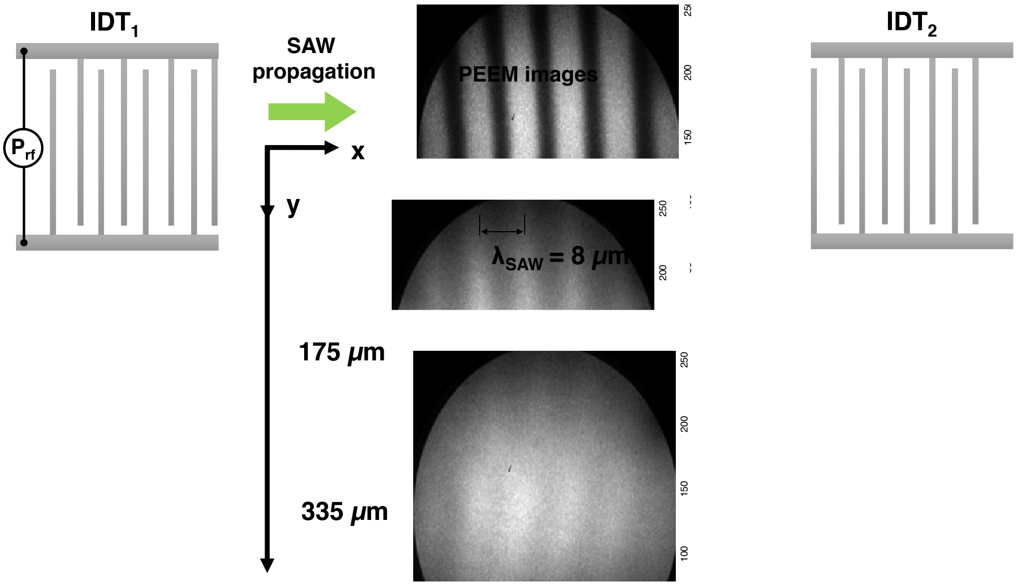

FIGURE 6.13: Stroboscopic PEEM images have been taken at different positions respect to the center of the acoustic path (area between the IDTs). The contrast of these images represents the piezoelectric field created by SAWs and the scale is the same for all three images.

6.4 Conclusions and perspectives

We have studied the effect surface acoustic waves (SAW) on the magnetic properties of microstructured Pt/Co/Pt squares with perpendicular magnetic anisotropy. We have observed that SAW can indeed induce large changes in the magnetic coercive field, up to 80% of the initial value. By using a thermal proximity scanning probe (SThM) we have shown that the changes in the magnetic properties are largely due to the SAW-induced heat dissipation.

Although certainly it was previously known that the propagation of SAWs could be associated to heat dissipation and increases of temperatures by coupling SAWs with different media, including polydimethylsiloxane (PDMS) [201] or liquids [202], a quantitative determination of the specific contribution of SAWs to the changes in temperature was missing.

One key aspect of our investigation has been provided by time-resolved AFM experiments, which show that even short SAW pulses can generate noticeable increases of temperature. Additionally, we also demonstrate that the heat generated by SAWs is a directional and fast mechanism to increase locally the temperature. This observation is important, as it opens up interesting perspectives in the remote control of magnetic nanodevices or in heat-assisted magnetic reversal in nanomagnets. Along this line, a particularly appealing prospect is to explore the possibility to create periodic gradients of temperature using, for instance, standing SAWs.

On the other hand, we should stress that our initial objective was to modify dynamically the PMA states via the coupling between spin precession (near H_c) and the dynamic magnetoelastic anisotropy caused by SAW (see appendix C). Although we have shown that the observed changes in the magnetic properties are largely driven by thermal effects, we cannot dismiss a certain minor contribution from changes in the magnetoelastic anisotropy induced by strain in SAWs. These effects, if present, could be an active mechanism in our results, but are difficult to distinguish from thermal effects. In order to shed more light on this issue, future experiments should be designed to asses the specific contribution of the changes in magnetoelastic anisotropy induced by SAW.

Chapter 7

Summary and perspectives

In the following, we summarize the most relevant outcomes and perspectives of the research described in Thesis.

Chapter 3: Magneto-optical activity intrinsic to polarons

We have determined the intrinsic contribution to the magneto-optical activity of self-trapped polarons in $La_{2/3}Ca_{1/3}MnO_3$ manganites. Our study has revealed a large magneto-optical response in the visible, almost two orders of magnitude larger than the background response of the material and comparable to photonic- or plasmonic-mediated magneto-optical enhancement. Additionally, we have identified the photoinduced electronic transitions responsible for the intrinsic magneto-optical activity of self-trapped polarons. This finding opens new perspectives to explore other pathways to obtain large magnetoelectric effects, using magneto-optics instead of magnetic properties. Along this line, an important challenge is to achieve high-quality manganite films on piezoelectric substrates, able to preserve the emergence of self-trapped polarons in a remarkable narrow range of temperatures around the ferromagnetic transition. On the other hand, ultrafast characterization of the optical response of self-trapped polarons is desirable to get more insights into their physics.

Chapter 4: Cation-specific contributions to the magnetism of Ce-doped YIG

We have analyzed the incorporation of Cerium into Yittrium Iron Garnet (YIG) and the consequences of this doping on the magnetic and electronic properties of YIG. Summarizing, our results show that Ce-doping triggers a selective charge transfer from Ce to the Fe tetrahedral sites in the YIG structure. This, in turn, causes a disruption of the electronic and magnetic properties of the parent compound, reducing the exchange coupling between the Ce and Fe magnetic moments and causing atypical magnetic behaviour. Our findings represent an important step forward for the comprehension of the physical processes that determine the optical properties of YIG-based compounds. This is especially relevant, taking into account that these materials are nowadays present in commercial devices in optical communication technologies.

Beyond optical applications, these findings may be relevant for other fields in which, e.g., spin waves are exploited. This is an important aspect, as YIG is nowadays one of the most researched compounds for spintronics. More specifically, site-specific doping in the YIG structure –as done in our study about Ce-doping– may reveal itself as an important toolkit for engineering the dynamic magnetic properties based on the demanding of potential applications.

Chapter 5: In-situ imaging of electric field-induced ferroelastic domain motion in $SrTiO_3$

We have used optical and magneto-optical imaging to analyze the spatial distributions of ferroelastic twin domains in $SrTiO_3$ crystals under the application of in-situ applied electric fields. Our work has enabled us to identify the sign of the anisotropy of the low-temperature dielectric behavior of $SrTiO_3$. Interestingly, the theoretical frame that we have developed to describe this anisotropy indicates the essential role of the emergence of an antiferroelectric lattice instability of the Ti ions that couples to polar and antiferrodistortive lattice modes. Our observations are very relevant for applications where understanding and controlling the distribution of all types of ferroelastic domains is essential for nanotechnology design. However, more research is needed in order to clarify the origin of the hysteretic behaviour of the dielectric response of $SrTiO_3$ at low-temperature. Recent results point to a polarity emerging at the twin domain walls; yet, one particularly challenging aspect is to determine if, eventually, an alternative polarity can emerge inside the ferroelastic domains.

Chapter 6: Directional heat dissipation generated by surface acoustic waves in $Co/Pt/LiNbO_3$ heterostructures

We have used magneto-optical microscopy to access the magnetic properties of the individual piezoelectric/magnetic microstructured magnetoelectric devices. Specifically, we have studied the effect surface acoustic waves (SAW) propagating on a piezoelectric ($LiNbO_3$) on the magnetic properties of microstructured Pt/Co/Pt squares with perpendicular magnetic anisotropy. Our results show that SAW can induce large changes in the magnetic coercive field, up to 80% of the initial value. By using a thermal proximity scanning probe we have shown that the changes in the magnetic properties are largely due to an intrinsic SAW induced heat dissipation. This observation is important, as it opens up interesting perspectives in the remote control of magnetic nanodevices or in heat-assisted magnetic reversal in nanomagnets. Along this line, a particularly appealing prospect is to explore the possibility to create periodic gradients of temperature using, for instance, standing SAWs. A part from that, further research is needed in order to understand how to modify dynamically the PMA states via the coupling between the magnetization of the microstructures and the magnetoelastic anisotropy induced by SAW (see appendix C).

Appendix A

Micromagnetic simulations of CoFeB domain pattern on tetragonal $SrTiO_3$

We simulated the imprinting of ferroelastic domains into a CoFeB film using micromagnetic solver MuMax3. In the simulations, the width of the ferroelastic $\{a_1, a_2\}$ twins is set to 2 μm. Strain transfer from these domains to the CoFeB film is implemented by an abrupt 90 degrees rotation of uniaxial magnetic anisotropy (K_u) at the domain boundaries as shown in the figure A.1. As input parameters for CoFeB we used a saturation magnetization of $M_s = 1.2 \cdot 10^6$ A/m, an exchange constant of $A = 2.1 \cdot 10^{-11}$ J/m, a magnetic damping parameter of $\alpha = 0.01$, and $K_u = 4.7 \cdot 10^4$ erg/cm^3 for $SrTiO_3$ at 10 K.

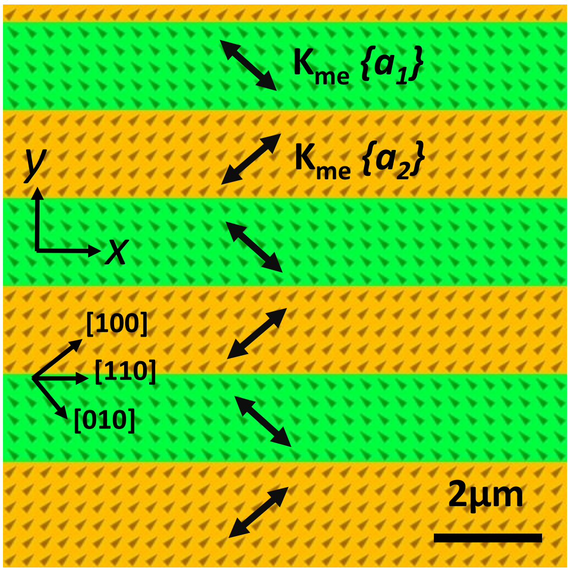

FIGURE A.1: Imposed regions of twins induced magnetoelastic anisotropy on CoFeB.

Appendix B

Co/Pt growth conditions

In order to grow Pt/Co/Pt thin films with PMA, an accurate control of the thickness is needed. We have grown Pt and Co on Si substrates by d.c. magnetron sputtering, with an Ar pressure of 0.005 mbar for Pt and 0.02 mbar for Co, at different sputtering powers during certain growth times. Thus, measuring the thickness by x-ray reflectometry, growth rates of Pt and Co have been computed (figure B.1). As can be appreciated, the growth rates increase linearly with the sputtering power. Since typically the critical Co thickness to induce PMA is below 2nm (see figure 6.3), the sputtering power has been settled to 5 W in order to get low enough growth rates, such as 0.2 Å/s, to control the Co thickness below the nanometer scale.

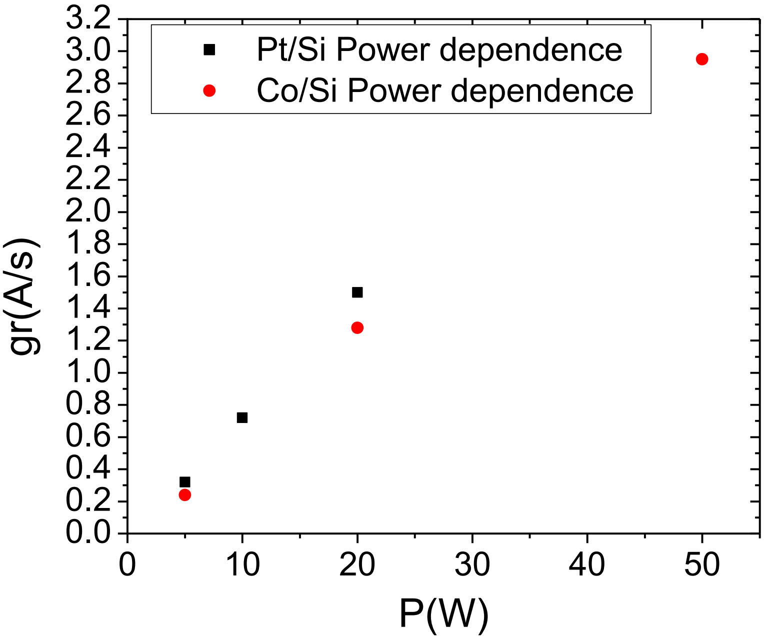

FIGURE B.1: Growth rates (g_r Å/s) for Pt (black squares) and Co (red squares) as a function of different sputtering powers.

Appendix C

Assited magnetization reversal mediated by SAWs magnetoelastic anisotropy in PMA films

SAW magnetoelastic effects probed by micromagnetic simulations

We have explored qualitatively the scenario where the assisted magnetization reversal is mediated by the coupling between spin precession and the dynamic change of the magnetoelastic anisotropy produced by SAWs. This mechanism has been tested modeling a ferromagnetic microstructure with PMA by micromagnetic simulations. Since SAWs are propagative strain transversal waves, the ferromagnetic film suffers time periods with tensile and compressive strain. Therefore, we have modeled [203, 204] the SAW induced magnetoelastic anisotropy (K_{me}) as the following:

$$\begin{aligned} K_{me}^{x} &= K_{me}\cos(2\pi f t) \\ K_{me}^{z} &= K_{me}\sin(2\pi f t) \end{aligned} \tag{C.1}$$

An oscillating K_{me} at the SAW frequency (f) in the x and z directions at 90 degrees out-of-phase respectively (figure C.1 a). We have taken $K_{me} \sim 1 \cdot 10^3$ J/cm^3 from experimental studies on Ni films [73] with $M_s = 450$ A/m, an exchange stiffness of $A = 10 \cdot 10^{-12}$ J/m and a damping of $\alpha = 0.03$. We have defined 2x2 μm structures of 1 nm thickness with an out-of-plane uniaxial anisotropy ($K_u = 140 \cdot 10^3$ J/cm^3) yielding the hysteresis response shown in the figure C.1 (b). The tiny size of the simulated magnetic structure, has been chosen to be smaller or comparable to the SAW's wavelength in order to assume an homogeneous strain over the structure exerted by the SAWs.

Large effects on the magnetization state are expected for SAW modulations similar to the spin precession frequency. We have simulated the magnetic evolution during $\sim$ 15 ns at SAW frequencies from 400 MHz to 1.6 GHz. Since the spin precession depends on the magnetic field, these evolutions have been studied at two different fields, at $\sim$ 5% (-0.039 T) and at $\sim$ 20% (-0.032 T) below the coercive field (H_c=0.041 T). Before start the time evolution at each SAW frequency, the magnetic state of the magnetic structures has been resettled via relaxing the magnetization state from saturation to the studied field. Figure C.1 (c) shows time evolutions at -0.039 T ($\sim$ 5% before H_c) at different SAWs frequencies, at slower (0.4 - 0.6 GHz) and at faster modulations (from 1.2 to 1.6 GHz) the out-of-plane magnetization (m_z) oscillates due to SAW around its natural state. Between 0.8 and 1 GHz, the m_z oscillates with a large amplitude and reverses its sign. Moreover, it can be observed that the m_z oscillation increases near the resonance between SAW and the spin precession. Similar behavior has been found at -0.032 T ($\sim$ 20% before H_c), nevertheless, m_z has been reversed for a higher and narrower range of frequencies around 1.2 GHz, as it expected, at -0.032 T, the precession is higher in frequency. Summarizing, we have shown that the coupling between a modulation of the magnetoelastic anisotropy caused by SAW and the magnetization dynamics in a PMA material could result in an assisted magnetization switching well below the coercive field.

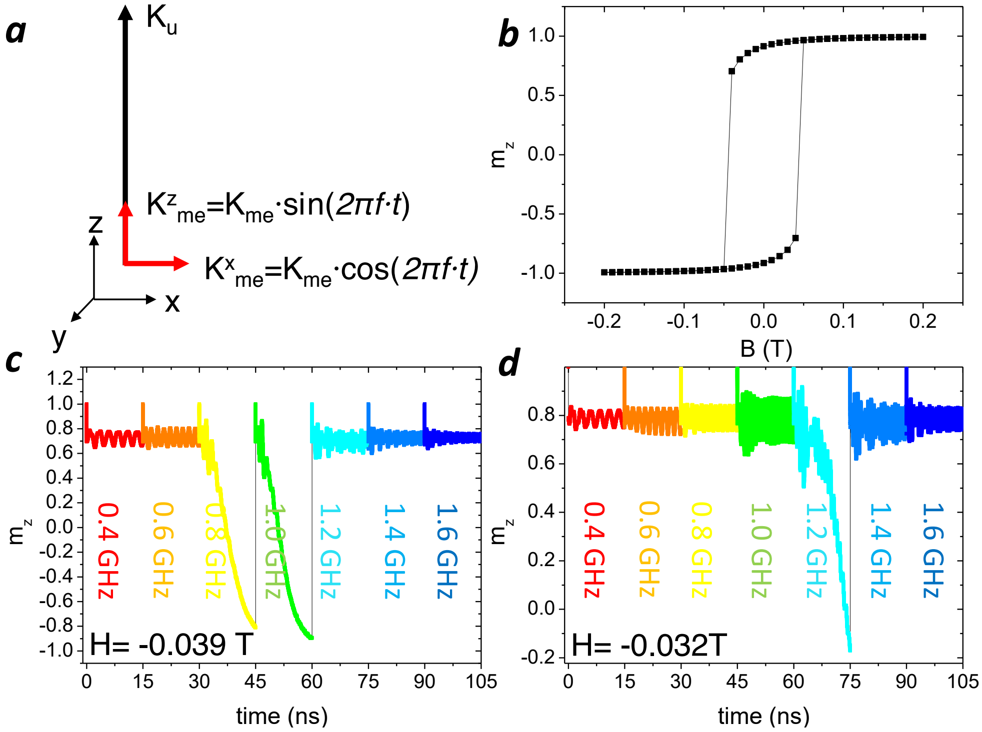

FIGURE C.1: (a) Scheme of used anisotropies in the micromagnetic simulations, K_u indicates the PMA of the Ni film and $K^{x,z}_{me}$ the components of SAW induced magnetoelastic anisotropy. (b) Out-of-plane hysteresis response. (c) and (d) Time evolutions of the magnetization at SAW frequencies from 0.4 to 1.6 GHz at H=-0.039 T and H=-0.032 T respectively.

SAW magnetoelastic effects probed by photoemission electron microscopy (PEEM)

In order to see possible dynamical changes on the magnetic domain pattern of our Pt/Co/Pt microstructured ultrathin films as a function of the SAW frequency, we have measured stroboscopically the magnetic contrast by XMCD in a photoemission electron microscopy (PEEM) at Alba synchrotron (CIRCE beamline [200]). Such an experiment provide a direct probe to the magnetoelastic effect disentangled from the thermal effects. Details of the stroboscopic measurements can be found in reference [73]. Since PEEM is an electron microscope working at very low electron energies, the images are strongly influenced by any potential variation on the surface. SAWs are a periodic displacement of the piezoelectric surface, with an associated surface potential wave as shown in the scheme of figure C.2. For these reasons, PEEM images are sensitive to the periodic piezoelectric field created by SAWs. Figure C.3 (a) shows two XAS images taken stroboscopically at two opposite SAW phases, +90° and -90°, for a SAW signal of $f_{\text{SAW}} = 499.654$ MHz and with a periodic wavelength of $\lambda_{\text{SAW}} \sim 8$ μm which can be appreciated on top of the Pt/Co/Pt squares of 4x4 μm. Thus, stroboscopic PEEM images shows a direct visualization of the SAW wave and allows the determination of strain wave position and propagation direction schematically depicted in C.3 (a) by the orientation of the magnetoelastic K_{me} in each region respectively.

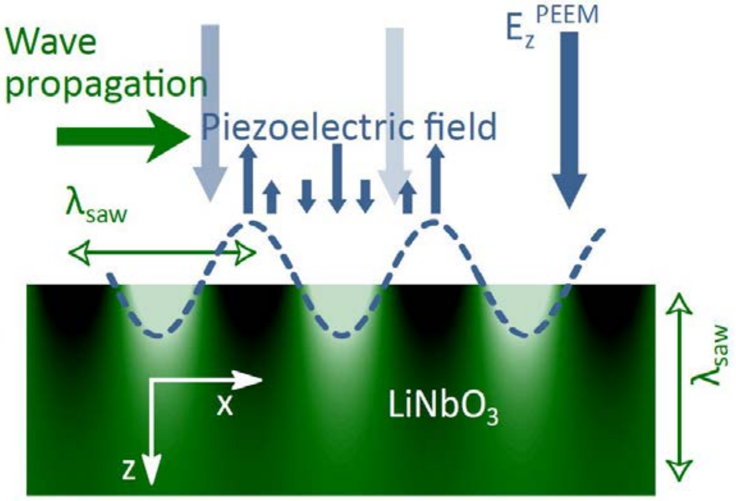

FIGURE C.2: SAWs piezoelectric field scheme. Extracted from [73].

Next, we have taken XMCD images at the same two opposite SAW phases (+90°, -90°) in order to resolve the magnetic domain pattern as a function of regions under compressive and tensile SAW induced strains. After saturating the Pt/Co/Pt microstructures with negative field out of the plane, we have applied a small positive field below H_c. Thus, the microstructures started to switch from their boarders sides reaching a metastable magnetic state. Figure C.3 (b) shows a XMCD sequence of alternating the SAWs phases (+90°, -90°, +90°). Tiny changes on the magnetization-domain configuration can be observed as a function of the SAW phase (indicated by arrows). Our experiments indicate that in certain regions, the magnetic domains feels, the strain induced by SAW. The observed changes might be explained with the previous micromagnetic simulations where the m_z oscillates without being reversed for a SAW frequency below or above the simulated reversal magnetization at resonance.

These stroboscopic experiments show that the magnetic domain states of our Pt/Co/Pt ultrathin films with PMA can be dynamically modified at the SAW's frequency. However, these effects are very small and we cannot attribute them to the observed coercive reduction under SAW shown in the main text.

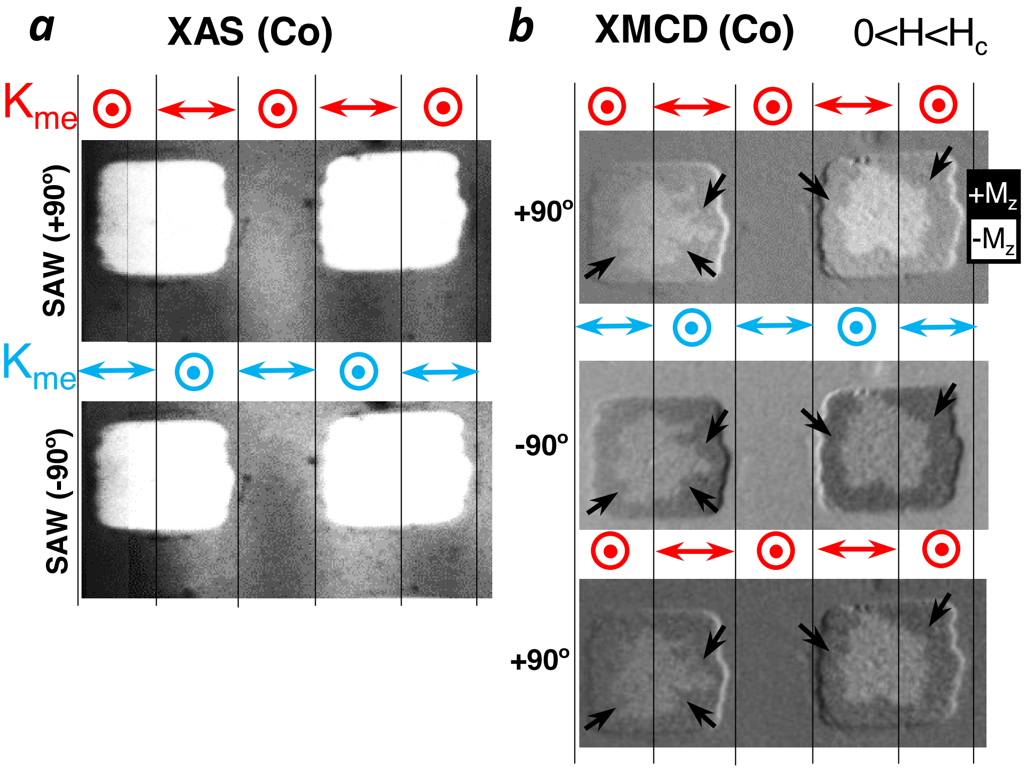

FIGURE C.3: (a) Stroboscopic XAS images at the Co L$_3$ edge with SAW opposite phases (+90, -90). (b) Stroboscopic XMCD images for a sequence of +90°, -90, +90° SAW phases. The arrows indicates magnetic regions that exhibit small changes at the SAW frequency.

As a conclusion, of experimental results from Chapter 6, we have seen a reduction of the coercive field under SAW and such a change depends on the SAW amplitude. However, the frequency dependence of the assisted magnetization changes can not be extracted from our experiments because each SAW harmonic, even with the same applied power, propagates with different power (as shown in S_{21} spectra in the main text). Moreover, as we have shown with the micromagnetic simulations, the SAW frequency and the applied magnetic field (the magnetization state of the microestructures) are crucial ingredients of the SAW induced strain effects on the PMA microestructures. Therefore, the magnetoelastic coupling might be an active mechanism present in the reduction of the coercive field, as shown by the stroboscopic XMCD data. However, from our experiments, we can not quantify the magnetoelastic effect with respect to the heating effect and, thus, we consider that both effects are present in the reduction of the coercive field created by the SAWs.

Appendix D

SThM tip calibration

SThM uses the resistance changes of a Pt AFM-like tip as a probe of temperature. At first order, electrical resistance of the tip resistive element at a temperature T_{Tip}, can be written as following,

$$R(T_{Tip}) = R(T_{RT})[1 + \alpha(T_{Tip} - T_{RT})], \tag{D.1}$$

where $R(T_{RT})$ is the resistance at room temperature and α is the temperature coefficient of its electrical resistivity. In order to measure precisely the tip's resistance, it has been integrated in a Wheatstone bridge, schematically depicted in figure D.1. An ac voltage source has been used in order to improve the signal to noise ratio and to remove possible electric couplings caused by the SAW's rf power source, filtering the output voltage (V_{BA}) with a Lock-in amplifier.

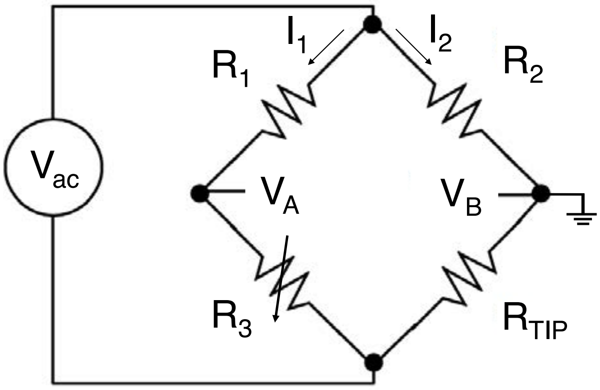

FIGURE D.1: Wheatstone bridge scheme to determine the SThM tip's resistance. The input is an ac voltage source V_{ac} and the output V_{BA} amplitude is obtained by Lock-in filtering.

Solving the electrical circuit, the output voltage V_{BA} is given by:

$$V_{BA} = V_{ac}\left(\frac{R_{Tip}}{R_2 + R_{Tip}} - \frac{R_3}{R_1 + R_3}\right). \tag{D.2}$$

Since the R_{Tip} is proportional to the temperature, the best measurement sensitivity is got when the output varies largely for smaller resistance changes. To reach this condition, we have settled $R_1 = R_2$ and R_3 has been replaced by a potentiometer. Varying

R_3 until null the output $V_{BA} = 0$ V at RT, the resistance of the tip is equal to R_3 and therefore, small variations of R_{Tip} will affect largely V_{BA}. We have used a commercial SThM tip that changes its resistance one ohm per Kelvin ($\alpha = 1\ \Omega/\mathrm{K}$), thus, the output change per degree, using $R_1 = 2600\ \Omega$ and $R_3 = 340\ \Omega$, is $V_{BA} = 3.006 \cdot 10^{-4} \cdot V_{ac}$. Moreover, the signal has been amplified with a gain of 200 using an AD8429 amplifier with a feedback resistor of $30\ \Omega$. Then, for $V_{ac} = 2$ V, the output signal per degree is $V_{BA} = 0.120$ V/K. In order to check it, we have measured at different controlled temperatures using a Peltier cell obtaining a good agreement with the predicted output sensitivity.

We have checked the calibration for each experiment using a control test before and after each set of measurements. Figure D.2 shows the SThM measurement for a well controlled increment of temperature (using a Peltier cell and a thermocouple) and the SAW induced increment at 773 MHz at 25 dBm. Thus, the SAW heat at 773 MHz (25 dBm) has been used also as a control before and after each set of SThM measurements.

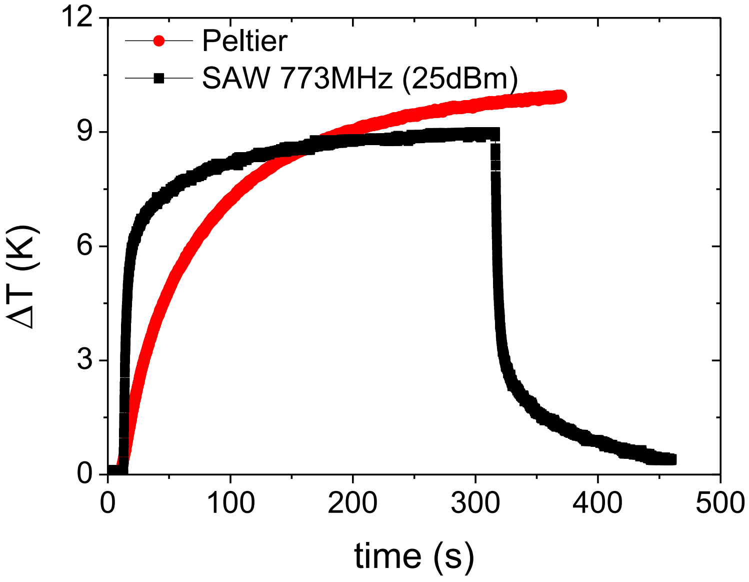

FIGURE D.2: Temperature increment measured for a well controlled heating source (Peltier Cell) settled at $\Delta T = 10$ K and for SAW at 773 MHz (25 dBm).

Bibliography

[1] J. Mannhart and D. G. Schlom. "Oxide Interfaces—An Opportunity for Electronics". In: *Science* 327.5973 (2010), pp. 1607–1611. ISSN: 0036-8075. DOI: `10.1126/science.1181862`. eprint: `http://science.sciencemag.org/content/327/5973/1607.full.pdf`. URL: `http://science.sciencemag.org/content/327/5973/1607`.

[2] D.G. Schlom and L.N. Pfeiffer. "Oxide electronics: Upward mobility rocks!" In: *Nature Materials* 9 (2010), pp. 881–883. DOI: `10.1038/nmat2888`.

[3] D.G. Schlom and J. Mannhart. "Oxide electronics: Interface takes charge over Si". In: *Nature Materials* 10 (2011), pp. 168–169. DOI: `10.1038/nmat2965`.

[4] C. N. R. Rao and G. V. Subba Rao. *Transition metal oxides : crystal chemistry, phase transition, and related aspects*. U.S. Department of Commerce, National Bureau of Standards., 1974.

[5] Masatoshi Imada, Atsushi Fujimori, and Yoshinori Tokura. "Metal-insulator transitions". In: *Rev. Mod. Phys.* 70 (4 1998), pp. 1039–1263. DOI: `10.1103/RevModPhys.70.1039`. URL: `https://link.aps.org/doi/10.1103/RevModPhys.70.1039`.

[6] Hermann Arthur Jahn and Edward Teller. "Stability of polyatomic molecules in degenerate electronic states. I. Orbital degeneracy". In: *Proceedings of the Royal Society of London A: Mathematical, Physical and Engineering Sciences*. Vol. 161. 905. The Royal Society. 1937, pp. 220–235.

[7] JH Van Vleck. "The Jahn-Teller Effect and Crystalline Stark Splitting for Clusters of the Form XY6". In: *The Journal of Chemical Physics* 7.1 (1939), pp. 72–84.

[8] Stephen Blundell. *Magnetism in Condensed Matter*. Oxford University Press, 2001.

[9] Michael D Kaplan and Benjamin G Vekhter. *Cooperative Phenomena in Jahn-Teller Crystals*. Springer Science and Business Media, 2012.

[10] Richard Phillips Feynman. "Slow electrons in a polar crystal". In: *Physical Review* 97.3 (1955), p. 660.

[11] VI Mel'Nikov and EI Rashba. "Bound Polaron and Phonon States". In: *ZhETF Pisma Redaktsiiu* 10 (1969), p. 95.

[12] Alexandre S Alexandrov and Nevill Francis Mott. *Polarons & bipolarons*. World Scientific Singapore, 1995.

[13] Soma Mukhopadhyay Ashok Chatterjee. *Polarons and Bipolarons: An Introduction*. Chapman & Hall Pure and Applied Mathematics.

[14] Lide M. Rodriguez-Martinez and J. Paul Attfield. "Cation disorder and the metal-insulator transition temperature in manganese oxide perovskites". In: *Phys. Rev. B* 58 (5 1998), pp. 2426–2429. DOI: `10.1103/PhysRevB.58.2426`. URL: `http://link.aps.org/doi/10.1103/PhysRevB.58.2426`.

[15] Yuya Shoji and Tetsuya Mizumoto. "Magneto-optical non-reciprocal devices in silicon photonics". In: *Science and Technology of Advanced Materials* 15.1 (2014), p. 014602.

[16] Manabu Gomi, H Furuyama, and M Abe. "Strong magneto-optical enhancement in highly Ce-substituted iron garnet films prepared by sputtering". In: *Journal of applied physics* 70.11 (1991), pp. 7065–7067.

[17] M Chandra Sekhar et al. "Giant Faraday rotation in Bi x Ce 3-x Fe 5 O 12 epitaxial garnet films". In: *Optics express* 20.9 (2012), pp. 9624–9639.

[18] Mehmet C Onbasli et al. "Optical and magneto-optical behavior of Cerium Yttrium Iron Garnet thin films at wavelengths of 200–1770 nm". In: *Scientific reports* 6 (2016).

[19] Lei Bi et al. "On-chip optical isolation in monolithically integrated non-reciprocal optical resonators". In: *Nature Photonics* 5.12 (2011), pp. 758–762.

[20] Taichi Goto, Mehmet C Onbaşlı, and CA Ross. "Magneto-optical properties of cerium substituted yttrium iron garnet films with reduced thermal budget for monolithic photonic integrated circuits". In: *Optics express* 20.27 (2012), pp. 28507–28517.

[21] Xiao Liang et al. "First principles calculation on the magnetic, optical properties and oxygen vacancy effect of CexY3- xFe5O12". In: *Applied Physics Letters* 106.5 (2015), p. 052401.

[22] You Xu, Jie Hui Yang, and Xi Juan Zhang. "Quantum theory of the strong magneto-optical effect of Ce-substituted yttrium iron garnet". In: *Physical Review B* 50.18 (1994), p. 13428.

[23] K Alex Müller, W Berlinger, and E Tosatti. "Indication for a novel phase in the quantum paraelectric regime of SrTiO 3". In: *Zeitschrift für Physik B Condensed Matter* 84.2 (1991), pp. 277–283.

[24] E. K. H. Salje et al. "Domains within Domains and Walls within Walls: Evidence for Polar Domains in Cryogenic $\mathrm{SrTiO_3}$". In: *Phys. Rev. Lett.* 111 (24 2013), p. 247603. DOI: `10.1103/PhysRevLett.111.247603`. URL: `https://link.aps.org/doi/10.1103/PhysRevLett.111.247603`.

[25] Xiao Lin et al. "Fermi surface of the most dilute superconductor". In: *Physical Review X* 3.2 (2013), p. 021002.

[26] J. Hemberger et al. “Electric-field-dependent dielectric constant and nonlinear susceptibility in $SrTiO_3$”. In: *Phys. Rev. B* 52 (18 1995), pp. 13159–13162. DOI: `10.1103/PhysRevB.52.13159`. URL: `https://link.aps.org/doi/10.1103/PhysRevB.52.13159`.

[27] Gervasi Herranz et al. “Engineering two-dimensional superconductivity and Rashba spin–orbit coupling in LaAlO3/SrTiO3 quantum wells by selective orbital occupancy”. In: *Nature communications* 6 (2015).

[28] AF Santander-Syro et al. “Two-dimensional electron gas with universal subbands at the surface of SrTiO3”. In: *Nature* 469.7329 (2011), pp. 189–193.

[29] A. D. Caviglia et al. “Tunable Rashba Spin-Orbit Interaction at Oxide Interfaces”. In: *Phys. Rev. Lett.* 104 (12 2010), p. 126803. DOI: `10.1103/PhysRevLett.104.126803`. URL: `https://link.aps.org/doi/10.1103/PhysRevLett.104.126803`.

[30] AF Santander-Syro et al. “Giant spin splitting of the two-dimensional electron gas at the surface of SrTiO3”. In: *Nature materials* 13.12 (2014), pp. 1085–1090.

[31] Jochen Mannhart and DG Schlom. “Oxide interfaces—an opportunity for electronics”. In: *Science* 327.5973 (2010), pp. 1607–1611.

[32] Cheng Cen et al. “Oxide nanoelectronics on demand”. In: *Science* 323.5917 (2009), pp. 1026–1030.

[33] Alexandre Fête et al. “Large modulation of the Shubnikov–de Haas oscillations by the Rashba interaction at the LaAlO3/SrTiO3 interface”. In: *New Journal of Physics* 16.11 (2014), p. 112002.

[34] A Ohtomo and HY Hwang. “A high-mobility electron gas at the LaAlO3/SrTiO3 heterointerface”. In: *Nature* 427.6973 (2004), pp. 423–426.

[35] YZ Chen et al. “A high-mobility two-dimensional electron gas at the heteroepitaxial spinel/perovskite complex oxide interface of {\ gamma}-Al2O3/SrTiO3”. In: *Nature Communications* 4.1371 (2013).

[36] Beena Kalisky et al. “Locally enhanced conductivity due to the tetragonal domain structure in LaAlO3/SrTiO3 heterointerfaces”. In: *Nature materials* 12.12 (2013), pp. 1091–1095.

[37] Maayan Honig et al. “Local electrostatic imaging of striped domain order in LaAlO3/SrTiO3”. In: *Nature materials* 12.12 (2013), pp. 1112–1118.

[38] Yiftach Frenkel et al. “Anisotropic transport at the LaAlO3/SrTiO3 interface explained by microscopic imaging of channel-flow over SrTiO3 domains”. In: *ACS applied materials & interfaces* 8.19 (2016), pp. 12514–12519.

[39] Tuomas H. E. Lahtinen, Jussi O. Tuomi, and Sebastiaan van Dijken. "Pattern Transfer and Electric-Field-Induced Magnetic Domain Formation in Multiferroic Heterostructures". In: *Advanced Materials* 23.28 (2011), pp. 3187–3191. ISSN: 1521-4095. DOI: 10.1002/adma.201100426. URL: http://dx.doi.org/10.1002/adma.201100426.

[40] Tuomas H. E. Lahtinen et al. "Alternating domains with uniaxial and biaxial magnetic anisotropy in epitaxial Fe films on BaTiO3". In: *Applied Physics Letters* 101.26 (2012), p. 262405. DOI: 10.1063/1.4773482. eprint: http://dx.doi.org/10.1063/1.4773482. URL: http://dx.doi.org/10.1063/1.4773482.

[41] Tuomas H. E. Lahtinen and Sebastiaan van Dijken. "Temperature control of local magnetic anisotropy in multiferroic CoFe/BaTiO3". In: *Applied Physics Letters* 102.11 (2013), p. 112406. DOI: 10.1063/1.4795529. eprint: http://dx.doi.org/10.1063/1.4795529. URL: http://dx.doi.org/10.1063/1.4795529.

[42] Ben Van de Wiele et al. "Electric field driven magnetic domain wall motion in ferromagnetic-ferroelectric heterostructures". In: *Applied Physics Letters* 104.1 (2014), p. 012401. DOI: 10.1063/1.4860963. eprint: http://dx.doi.org/10.1063/1.4860963. URL: http://dx.doi.org/10.1063/1.4860963.

[43] Kévin J. A. Franke et al. "Size Dependence of Domain Pattern Transfer in Multiferroic Heterostructures". In: *Phys. Rev. Lett.* 112 (1 2014), p. 017201. DOI: 10.1103/PhysRevLett.112.017201. URL: https://link.aps.org/doi/10.1103/PhysRevLett.112.017201.

[44] Diego López González et al. "Electric-field-driven domain wall dynamics in perpendicularly magnetized multilayers". In: *AIP Advances* 7.3 (2017), p. 035119. DOI: 10.1063/1.4979267. eprint: http://dx.doi.org/10.1063/1.4979267. URL: http://dx.doi.org/10.1063/1.4979267.

[45] Diego López González et al. "Influence of magnetic field and ferromagnetic film thickness on domain pattern transfer in multiferroic heterostructures". In: *Journal of Magnetism and Magnetic Materials* 441 (2017), pp. 404 –408. ISSN: 0304-8853. DOI: https://doi.org/10.1016/j.jmmm.2017.06.004. URL: http://www.sciencedirect.com/science/article/pii/S0304885317309563.

[46] Diego López González et al. "Reconfigurable magnetic logic based on the energetics of pinned domain walls". In: *Applied Physics Letters* 108.3 (2016), p. 032402. DOI: 10.1063/1.4940119. eprint: http://dx.doi.org/10.1063/1.4940119. URL: http://dx.doi.org/10.1063/1.4940119.

[47] T.H.E. Lahtinen, K.J.A. Franke, and S. van Dijken. "Electric-field control of magnetic domain wall motion and local magnetization reversal". In: *Scientific Reports* 2 (2012), p. 258. DOI: 10.1038/srep00258.

[48] Arianna Casiraghi et al. “Influence of elastically pinned magnetic domain walls on magnetization reversal in multiferroic heterostructures”. In: *Phys. Rev. B* 92 (5 2015), p. 054406. DOI: `10.1103/PhysRevB.92.054406`. URL: `https://link.aps.org/doi/10.1103/PhysRevB.92.054406`.

[49] J.H. Haeni et al. “Room-temperature ferroelectricity in strained $SrTiO_3$”. In: *Nature* 430 (2004), pp. 758–761. DOI: `10.1038/nature02773`.

[50] P. Zubko et al. “Strain-Gradient-Induced Polarization in $SrTiO_3$ Single Crystals”. In: *Phys. Rev. Lett.* 99 (16 2007), p. 167601. DOI: `10.1103/PhysRevLett.99.167601`. URL: `https://link.aps.org/doi/10.1103/PhysRevLett.99.167601`.

[51] M. Itoh et al. “Ferroelectricity Induced by Oxygen Isotope Exchange in Strontium Titanate Perovskite”. In: *Phys. Rev. Lett.* 82 (17 1999), pp. 3540–3543. DOI: `10.1103/PhysRevLett.82.3540`. URL: `https://link.aps.org/doi/10.1103/PhysRevLett.82.3540`.

[52] Daniel E. Grupp and Allen M. Goldman. “Giant Piezoelectric Effect in Strontium Titanate at Cryogenic Temperatures”. In: *Science* 276.5311 (1997), pp. 392–394. ISSN: 0036-8075. DOI: `10.1126/science.276.5311.392`. URL: `http://science.sciencemag.org/content/276/5311/392`.

[53] J. F. Scott, E. K. H. Salje, and M. A. Carpenter. “Domain Wall Damping and Elastic Softening in $SrTiO_3$: Evidence for Polar Twin Walls”. In: *Phys. Rev. Lett.* 109 (18 2012), p. 187601. DOI: `10.1103/PhysRevLett.109.187601`. URL: `https://link.aps.org/doi/10.1103/PhysRevLett.109.187601`.

[54] E. K. H. Salje and J. F. Scott. “Ferroelectric Bloch-line switching: A paradigm for memory devices?” In: *Applied Physics Letters* 105.25 (2014), p. 252904. DOI: `10.1063/1.4905001`. eprint: `http://dx.doi.org/10.1063/1.4905001`. URL: `http://dx.doi.org/10.1063/1.4905001`.

[55] H. J. Harsan Ma et al. “Local Electrical Imaging of Tetragonal Domains and Field-Induced Ferroelectric Twin Walls in Conducting $SrTiO_3$”. In: *Phys. Rev. Lett.* 116 (25 2016), p. 257601. DOI: `10.1103/PhysRevLett.116.257601`. URL: `https://link.aps.org/doi/10.1103/PhysRevLett.116.257601`.

[56] J. Fontcuberta et al. “Polar domain walls trigger magnetoelectric coupling”. In: *Scientific Reports* 5 (2015). DOI: `10.1038/srep13784`. URL: `https://www.nature.com/articles/srep13784`.

[57] Evgeny Y Tsymbal. “Spintronics: Electric toggling of magnets”. In: *Nature materials* 11.1 (2012), pp. 12–13.

[58] Manuel Bibes, Agnès Barthélémy, et al. “Towards a magnetoelectric memory”. In: *Nat. Mater* 7 (2008), pp. 425–426.

[59] Ondrej Vlasin et al. “Interface Magnetoelectric Coupling in Co/Pb (Zr, Ti) O3”. In: *ACS applied materials & interfaces* 8.11 (2016), pp. 7553–7563.

[60] Carlos AF Vaz et al. "Magnetoelectric coupling effects in multiferroic complex oxide composite structures". In: *Advanced Materials* 22.26-27 (2010), pp. 2900–2918.

[61] JF Scott. "Applications of magnetoelectrics". In: *Journal of Materials Chemistry* 22.11 (2012), pp. 4567–4574.

[62] James F Scott. "Room-temperature multiferroic magnetoelectrics". In: *NPG Asia Materials* 5.11 (2013), e72.

[63] Chengliang Lu et al. "Multiferroic oxide thin films and heterostructures". In: *Applied physics reviews* 2.2 (2015), p. 021304.

[64] Morgan Trassin. "Low energy consumption spintronics using multiferroic heterostructures". In: *Journal of Physics: Condensed Matter* 28.3 (2015), p. 033001.

[65] Jing Ma et al. "Recent progress in multiferroic magnetoelectric composites: from bulk to thin films". In: *Advanced Materials* 23.9 (2011), pp. 1062–1087.

[66] Carlos AF Vaz. "Electric field control of magnetism in multiferroic heterostructures". In: *Journal of Physics: Condensed Matter* 24.33 (2012), p. 333201.

[67] Carlos Antonio Fernandes Vaz and Urs Staub. "Artificial multiferroic heterostructures". In: *Journal of Materials Chemistry C* 1.41 (2013), pp. 6731–6742.

[68] Vincent Garcia, Manuel Bibes, and Agnès Barthélémy. "Artificial multiferroic heterostructures for an electric control of magnetic properties". In: *Comptes Rendus Physique* 16.2 (2015), pp. 168–181.

[69] Chun-Gang Duan, Sitaram S Jaswal, and Evgeny Y Tsymbal. "Predicted magnetoelectric effect in Fe/BaTiO 3 multilayers: ferroelectric control of magnetism". In: *Physical Review Letters* 97.4 (2006), p. 047201.

[70] James M Rondinelli, Massimiliano Stengel, and Nicola A Spaldin. "Carrier-mediated magnetoelectricity in complex oxide heterostructures". In: *Nature Nanotechnology* 3.1 (2008), pp. 46–50.

[71] FW Voltmer, RM White, and CW Turner. "Magnetostrictive generation of surface elastic waves". In: *Applied Physics Letters* 15.5 (1969), pp. 153–154.

[72] Colin Campbell. *Surface acoustic wave devices for mobile and wireless communications*. Academic press, 1998.

[73] M. Foerster et al. "Simultaneous imaging of strain waves and induced magnetization dynamics at the nanometer scale". In: *ArXiv e-prints* (2016). arXiv: `1611.02847 [cond-mat.mes-hall]`.

[74] M. Weiler et al. "Elastically Driven Ferromagnetic Resonance in Nickel Thin Films". In: *Phys. Rev. Lett.* 106 (11 2011), p. 117601. DOI: `10.1103/PhysRevLett.106.117601`. URL: `https://link.aps.org/doi/10.1103/PhysRevLett.106.117601`.

[75] M. Weiler et al. "Spin Pumping with Coherent Elastic Waves". In: *Phys. Rev. Lett.* 108 (17 2012), p. 176601. DOI: `10.1103/PhysRevLett.108.176601`. URL: `https://link.aps.org/doi/10.1103/PhysRevLett.108.176601`.

[76] S. Ikeda et al. "A perpendicular-anisotropy CoFeB-MgO magnetic tunnel junction". In: *Nature Materials* 9 (2010), pp. 721–724. DOI: `10.1038/nmat2804`.

[77] J. J. Nowak et al. "Demonstration of Ultralow Bit Error Rates for Spin-Torque Magnetic Random-Access Memory With Perpendicular Magnetic Anisotropy". In: *IEEE Magnetics Letters* 2 (2011), pp. 3000204–3000204. ISSN: 1949-307X. DOI: `10.1109/LMAG.2011.2155625`.

[78] A. D. Kent and D.C. Worledge. "A new spin on magnetic memories". In: *Nature Nanotechnology* 10 (2015), pp. 187–191. DOI: `10.1038/nnano.2015.24`.

[79] A.K Zvezdin and V.A Kotov. *Modern Magnetooptics and Magnetooptical Materials*. CRC Press, 1997.

[80] Jeffrey McCord. "Progress in magnetic domain observation by advanced magneto-optical microscopy". In: *Journal of Physics D: Applied Physics* 48.33 (2015), p. 333001. URL: `http://stacks.iop.org/0022-3727/48/i=33/a=333001`.

[81] M. Fox. *Optical properties of solids*. Oxford University press, 2007.

[82] D. B. Tanner. *Optical effects in solids*. Department of Physics, University of Florida, USA, 2013. URL: `https://www.phys.ufl.edu/~tanner/notes.pdf`.

[83] A F Drake. "Polarisation modulation-the measurement of linear and circular dichroism". In: *Journal of Physics E: Scientific Instruments* 19.3 (1986), p. 170. URL: `http://stacks.iop.org/0022-3735/19/i=3/a=002`.

[84] Ashish Arora, Sandip Ghosh, and Vasam Sugunakar. "A mirror based polar magneto-optical Kerr effect spectroscopy arrangement". In: *Review of Scientific Instruments* 82.12 (2011), p. 123903. DOI: `10.1063/1.3669782`. eprint: `http://dx.doi.org/10.1063/1.3669782`. URL: `http://dx.doi.org/10.1063/1.3669782`.

[85] K. W. Hipps and G. A. Crosby. "Applications of the photoelastic modulator to polarization spectroscopy". In: *The Journal of Physical Chemistry* 83.5 (1979), pp. 555–562. DOI: `10.1021/j100468a001`. eprint: `http://dx.doi.org/10.1021/j100468a001`. URL: `http://dx.doi.org/10.1021/j100468a001`.

[86] K. Postava et al. "Transverse magneto-optical Kerr effect measured using phase modulation". In: *Journal of the European Optical Society - Rapid publications* 1.0 (2006). ISSN: 1990-2573. URL: `http://www.jeos.org/index.php/jeos_rp/article/view/06017`.

[87] Ondrej Vlasin. “Spectroscopy and confocal imaging of complex ferroic systems”. PhD thesis. Departament de Física, Universitat Autònoma de Barcelona., 2014. ISBN: 978-84-490-4357-4.

[88] Joachim Stöhr and Hans Christoph Siegmann. *Magnetism: From Fundamentals to Nanoscale Dynamics*. Springer-Verlag Berlin Heidelberg, 2006. DOI: `10.1007/978-3-540-30283-4`. URL: `http://www.springer.com/us/book/9783540302827`.

[89] Victor Antonov, Bruce Harmon, and Alexander Yaresko. *Electronic Structure and Magneto-Optical Properties of Solids*. Springer Netherlands, 2004. ISBN: 978-1-4020-1905-0. DOI: `10.1007/1-4020-1906-8`. URL: `https://link.springer.com/book/10.1007%2F1-4020-1906-8`.

[90] B. T. Thole et al. “X-ray circular dichroism as a probe of orbital magnetization”. In: *Phys. Rev. Lett.* 68 (12 1992), pp. 1943–1946. DOI: `10.1103/PhysRevLett.68.1943`. URL: `http://link.aps.org/doi/10.1103/PhysRevLett.68.1943`.

[91] Paolo Carra et al. “X-ray circular dichroism and local magnetic fields”. In: *Phys. Rev. Lett.* 70 (5 1993), pp. 694–697. DOI: `10.1103/PhysRevLett.70.694`. URL: `http://link.aps.org/doi/10.1103/PhysRevLett.70.694`.

[92] S Macke and E Goering. “Magnetic reflectometry of heterostructures”. In: *Journal of Physics: Condensed Matter* 26.36 (2014), p. 363201. URL: `http://stacks.iop.org/0953-8984/26/i=36/a=363201`.

[93] Milton Ohring. *Materials science of thin films, 2nd edition*. Elsevier, 2001. ISBN: 9780080491783.

[94] Ignasi Fina. *Ferroelectricity and magnetoelectric coupling in magnetic ferroelectrics and artificial multiferroic heterostructures*. Universitat de Barcelona, Barcelona, Spain, 2012.

[95] JF Scott et al. “Switching kinetics of lead zirconate titanate submicron thin-film memories”. In: *Journal of applied physics* 64.2 (1988), pp. 787–792.

[96] Manabu Gomi, Kensuke Satoh, and Masanori Abe. “Giant Faraday rotation of Ce-substituted YIG films epitaxially grown by RF sputtering”. In: *Japanese journal of applied physics* 27.8A (1988), p. L1536.

[97] LD Landau. “On the motion of electrons in a crystal lattice”. In: *Phys. Z. Sowjetunion* 3 (1933), pp. 664–665.

[98] Jozef T Devreese. “Optical properties of few and many Fröhlich polarons from 3D to 0D”. In: *Polarons in Advanced Materials*. Springer, 2007, pp. 3–61.

[99] A M Stoneham et al. “Trapping, self-trapping and the polaron family”. In: *Journal of Physics: Condensed Matter* 19.25 (2007), p. 255208. URL: `http://stacks.iop.org/0953-8984/19/i=25/a=255208`.

[100] T Holstein. "Studies of polaron motion: Part I. The molecular-crystal model". In: *Annals of Physics* 8.3 (1959), pp. 325 –342. ISSN: 0003-4916. DOI: `http://dx.doi.org/10.1016/0003-4916(59)90002-8`. URL: `http://www.sciencedirect.com/science/article/pii/0003491659900028`.

[101] T. Holstein. "Studies of polaron motion: Part II. The "small" polaron". In: *Annals of Physics* 8.3 (1959), pp. 343 –389. ISSN: 0003-4916. DOI: `http://dx.doi.org/10.1016/0003-4916(59)90003-X`. URL: `http://www.sciencedirect.com/science/article/pii/000349165990003X`.

[102] G. B. Arnold and T. Holstein. "Faraday Rotation of Small Polarons". In: *Phys. Rev. Lett.* 33 (26 1974), pp. 1547–1549. DOI: `10.1103/PhysRevLett.33.1547`. URL: `https://link.aps.org/doi/10.1103/PhysRevLett.33.1547`.

[103] F. M. Peeters and J. T. Devreese. "Magneto-optical absorption of polarons". In: *Phys. Rev. B* 34 (10 1986), pp. 7246–7259. DOI: `10.1103/PhysRevB.34.7246`. URL: `https://link.aps.org/doi/10.1103/PhysRevB.34.7246`.

[104] J. M. D. Coey, M. Viret, and S. von Molnár. "Mixed-valence manganites". In: *Advances in Physics* 48.2 (1999), pp. 167–293. DOI: `10.1080/000187399243455`. eprint: `http://dx.doi.org/10.1080/000187399243455`. URL: `http://dx.doi.org/10.1080/000187399243455`.

[105] Y Tokura. "Critical features of colossal magnetoresistive manganites". In: *Reports on Progress in Physics* 69.3 (2006), p. 797. URL: `http://stacks.iop.org/0034-4885/69/i=3/a=R06`.

[106] AJ Millis. "Lattice effects in magnetoresistive manganese perovskites". In: *Nature* 392.6672 (1998), pp. 147–150.

[107] J L García-Muñoz et al. "Bandwidth narrowing in bulk $La_{2/3}A_{1/3}MnO_3$ magnetoresistive oxides". In: *Journal of Physics: Condensed Matter* 8.50 (1996), p. L787. URL: `http://stacks.iop.org/0953-8984/8/i=50/a=003`.

[108] J. M. Caicedo, J. Fontcuberta, and G. Herranz. "Magnetopolaron-induced optical response in transition metal oxides". In: *Phys. Rev. B* 89 (4 2014), p. 045121. DOI: `10.1103/PhysRevB.89.045121`. URL: `http://link.aps.org/doi/10.1103/PhysRevB.89.045121`.

[109] J. Fontcuberta et al. "Colossal Magnetoresistance of Ferromagnetic Manganites: Structural Tuning and Mechanisms". In: *Phys. Rev. Lett.* 76 (7 1996), pp. 1122–1125. DOI: `10.1103/PhysRevLett.76.1122`. URL: `http://link.aps.org/doi/10.1103/PhysRevLett.76.1122`.

[110] Jose Manuel Caicedo Roque. "Magneto-Optical spectroscopy of complex systems. Magnetic oxides and photonic crystals". PhD thesis. 2012. ISBN: 9788449033452. URL: `http://hdl.handle.net/10803/96793`.

[111] D. Hrabovský et al. “Jahn-Teller contribution to the magneto-optical effect in thin-film ferromagnetic manganites”. In: *Phys. Rev. B* 79 (5 2009), p. 052401. DOI: `10.1103/PhysRevB.79.052401`. URL: `http://link.aps.org/doi/10.1103/PhysRevB.79.052401`.

[112] J. M. Caicedo et al. “Strong magnetorefractive and quadratic magneto-optical effects in $(\mathrm{Pr}_{0.4}\mathrm{La}_{0.6})_{0.7}\mathrm{Ca}_{0.3}\mathrm{MnO}_3$”. In: *Phys. Rev. B* 82 (14 2010), p. 140410. DOI: `10.1103/PhysRevB.82.140410`. URL: `http://link.aps.org/doi/10.1103/PhysRevB.82.140410`.

[113] J M Caicedo et al. “Large magnetorefractive effect in magnetite”. In: *New Journal of Physics* 12.10 (2010), p. 103023. URL: `http://stacks.iop.org/1367-2630/12/i=10/a=103023`.

[114] M. Quijada et al. “Optical conductivity of manganites: Crossover from Jahn-Teller small polaron to coherent transport in the ferromagnetic state”. In: *Phys. Rev. B* 58 (24 1998), pp. 16093–16102. DOI: `10.1103/PhysRevB.58.16093`. URL: `http://link.aps.org/doi/10.1103/PhysRevB.58.16093`.

[115] J. H. Jung et al. “Determination of electronic band structures of CaMnO_3 and LaMnO_3 using optical-conductivity analyses”. In: *Phys. Rev. B* 55 (23 1997), pp. 15489–15493. DOI: `10.1103/PhysRevB.55.15489`. URL: `http://link.aps.org/doi/10.1103/PhysRevB.55.15489`.

[116] Y. Okimoto et al. “Anomalous Variation of Optical Spectra with Spin Polarization in Double-Exchange Ferromagnet: $\mathrm{La}_{1-x}\mathrm{Sr}_x\mathrm{MnO}_3$”. In: *Phys. Rev. Lett.* 75 (1 1995), pp. 109–112. DOI: `10.1103/PhysRevLett.75.109`. URL: `http://link.aps.org/doi/10.1103/PhysRevLett.75.109`.

[117] S. G. Kaplan et al. “Optical Evidence for the Dynamic Jahn-Teller Effect in $\mathrm{Nd}_{0.7}\mathrm{Sr}_{0.3}\mathrm{MnO}_3$”. In: *Phys. Rev. Lett.* 77 (10 1996), pp. 2081–2084. DOI: `10.1103/PhysRevLett.77.2081`. URL: `http://link.aps.org/doi/10.1103/PhysRevLett.77.2081`.

[118] J. H. Jung et al. “Midgap states of $\mathrm{La}_{1-x}\mathrm{Ca}_x\mathrm{MnO}_3$: Doping-dependent optical-conductivity studies”. In: *Phys. Rev. B* 57 (18 1998), R11043–R11046. DOI: `10.1103/PhysRevB.57.R11043`. URL: `http://link.aps.org/doi/10.1103/PhysRevB.57.R11043`.

[119] A. S. Moskvin et al. “Interplay of $p-d$ and $d-d$ charge transfer transitions in rare-earth perovskite manganites”. In: *Phys. Rev. B* 82 (3 2010), p. 035106. DOI: `10.1103/PhysRevB.82.035106`. URL: `http://link.aps.org/doi/10.1103/PhysRevB.82.035106`.

[120] I. C. Infante et al. “Elastic and orbital effects on thickness-dependent properties of manganite thin films”. In: *Phys. Rev. B* 76 (22 2007), p. 224415. DOI: `10.1103/PhysRevB.76.224415`. URL: `https://link.aps.org/doi/10.1103/PhysRevB.76.224415`.

[121] S. Estradé et al. "Cationic and charge segregation in La2/3Ca1/3MnO3 thin films grown on (001) and (110) SrTiO3". In: *Applied Physics Letters* 93.11 (2008), p. 112505. DOI: `10.1063/1.2981574`. eprint: `http://dx.doi.org/10.1063/1.2981574`. URL: `http://dx.doi.org/10.1063/1.2981574`.

[122] M. Rubio-Roy et al. "Magneto-Optical Enhancement by Plasmon Excitations in Nanoparticle/Metal Structures". In: *Langmuir* 28.24 (2012). PMID: 22594822, pp. 9010–9020. DOI: `10.1021/la301239x`. eprint: `http://dx.doi.org/10.1021/la301239x`. URL: `http://dx.doi.org/10.1021/la301239x`.

[123] Juan F. Galisteo-López et al. "Self-Assembled Photonic Structures". In: *Advanced Materials* 23.1 (2011), pp. 30–69. ISSN: 1521-4095. DOI: `10.1002/adma.201000356`. URL: `http://dx.doi.org/10.1002/adma.201000356`.

[124] E. Yablonovitch. "Photonics: One-way road for light". In: *Nature* 461 (2009), pp. 744–745. DOI: `10.1038/461744a`.

[125] V.V. Temnov et al. "Active magneto-plasmonics in hybrid metal-ferromagnet structures". In: *Nature Photonics* 4 (2010), pp. 107–111. DOI: `10.1038/nphoton.2009.265`.

[126] N. Maccaferri et al. "Ultrasensitive and label-free molecular-level detection enabled by light phase control in magnetoplasmonic nanoantennas". In: *Nature Communications* 6 (Feb. 2015), p. 6150. DOI: `10.1038/ncomms7150`.

[127] F. Rivadulla et al. "Suppression of Ferromagnetic Double Exchange by Vibronic Phase Segregation". In: *Phys. Rev. Lett.* 96 (1 2006), p. 016402. DOI: `10.1103/PhysRevLett.96.016402`. URL: `https://link.aps.org/doi/10.1103/PhysRevLett.96.016402`.

[128] J. M. D. Coey, M. Viret, and S. von Molnár. "Mixed-valence manganites". In: *Advances in Physics* 48.2 (1999), pp. 167–293. DOI: `10.1080/000187399243455`. eprint: `http://dx.doi.org/10.1080/000187399243455`. URL: `http://dx.doi.org/10.1080/000187399243455`.

[129] Haiming Yu et al. "Magnetic thin-film insulator with ultra-low spin wave damping for coherent nanomagnonics". In: *Scientific reports* 4 (2014), p. 6848.

[130] Y Kajiwara et al. "Transmission of electrical signals by spin-wave interconversion in a magnetic insulator". In: *Nature* 464.7286 (2010), pp. 262–266.

[131] Hidekazu Kurebayashi et al. "Controlled enhancement of spin-current emission by three-magnon splitting". In: *Nature materials* 10.9 (2011), pp. 660–664.

[132] Akihiro Kirihara et al. "Spin-current-driven thermoelectric coating". In: *Nature materials* 11.8 (2012), pp. 686–689.

[133] Mathias Weiler et al. "Experimental test of the spin mixing interface conductivity concept". In: *Physical review letters* 111.17 (2013), p. 176601.

[134] Maximilian Schmid et al. “Transverse spin Seebeck effect versus anomalous and planar Nernst effects in permalloy thin films”. In: *Physical review letters* 111.18 (2013), p. 187201.

[135] C Leycuras et al. “Magnetic and magneto-optical properties of a cerium YIG single crystal”. In: *IEEE Transactions on magnetics* 21.5 (1985), pp. 1660–1662.

[136] Andrii V Chumak et al. “All-linear time reversal by a dynamic artificial crystal”. In: *Nature communications* 1 (2010), p. 141.

[137] Daoxin Dai, Jared Bauters, and John E Bowers. “Passive technologies for future large-scale photonic integrated circuits on silicon: polarization handling, light non-reciprocity and loss reduction”. In: *Light: Science & Applications* 1.3 (2012), e1.

[138] FDM Haldane and S Raghu. “Possible realization of directional optical waveguides in photonic crystals with broken time-reversal symmetry”. In: *Physical review letters* 100.1 (2008), p. 013904.

[139] Gerald F. Dionne. *Magnetic Oxides*. Springer US, 2004. ISBN: 978-1-4419-0053-1. DOI: `10.1007/978-1-4419-0054-8`.

[140] Martin Bolduc et al. “Magnetism and magnetooptical effects in Ce–Fe oxides”. In: *IEEE transactions on magnetics* 42.10 (2006), pp. 3093–3095.

[141] M Gomi et al. “Sputter deposition of Ce-substituted iron garnet films with giant magneto-optical effect”. In: *IEEE Translation Journal on Magnetics in Japan* 5.4 (1990), pp. 294–299.

[142] Andreas Kehlberger et al. “Enhanced Magneto-optic Kerr Effect and Magnetic Properties of $\mathrm{CeY_2Fe_5O_{12}}$ Epitaxial Thin Films”. In: *Phys. Rev. Applied* 4 (1 2015), p. 014008. DOI: `10.1103/PhysRevApplied.4.014008`. URL: `https://link.aps.org/doi/10.1103/PhysRevApplied.4.014008`.

[143] J Walowski et al. “Intrinsic and non-local Gilbert damping in polycrystalline nickel studied by Ti: sapphire laser fs spectroscopy”. In: *Journal of Physics D: Applied Physics* 41.16 (2008), p. 164016.

[144] Michael Farle. “Ferromagnetic resonance of ultrathin metallic layers”. In: *Reports on Progress in Physics* 61.7 (1998), p. 755. URL: `http://stacks.iop.org/0034-4885/61/i=7/a=001`.

[145] RL Streever and PJ Caplan. “Nuclear-Magnetic-Resonance Studies of Fe 57 in Rare-Earth Iron Garnets”. In: *Physical Review B* 4.9 (1971), p. 2881.

[146] M Deb et al. “Magneto-optical Faraday spectroscopy of completely bismuth-substituted Bi 3 Fe 5 O 12 garnet thin films”. In: *Journal of Physics D: Applied Physics* 45.45 (2012), p. 455001. URL: `http://stacks.iop.org/0022-3727/45/i=45/a=455001`.

[147] R. M. Bozorth. *Ferromagnetism*. Aug. 1993, p. 992.

[148] Alessandro Barla et al. “Design and performance of BOREAS, the beamline for resonant X-ray absorption and scattering experiments at the ALBA synchrotron light source”. In: *Journal of Synchrotron Radiation* 23.6 (Nov. 1, 2016). cited By 0, pp. 1507–1517. DOI: `10.1107/S1600577516013461`. URL: `http://scripts.iucr.org/cgi-bin/paper?S1600577516013461`. published.

[149] Eli Stavitski and Frank MF De Groot. “The CTM4XAS program for EELS and XAS spectral shape analysis of transition metal L edges”. In: *Micron* 41.7 (2010), pp. 687–694.

[150] Charles L Melcher et al. “Cerium oxidation state in LSO: Ce scintillators”. In: *IEEE transactions on nuclear science* 52.5 (2005), pp. 1809–1812.

[151] E Pellegrain et al. “Characterization of Nanocrystalline γ-Fe2O3 with Synchrotron Radiation Techniques”. In: *physica status solidi (b)* 215.1 (1999), pp. 797–801.

[152] V Hari Babu et al. “Epitaxial growth and magnetic properties of ultrathin iron oxide films on BaTiO3 (001)”. In: *Journal of Applied Physics* 114.11 (2013), p. 113901.

[153] SW Yu et al. “Atomic origin of 3d94 f 1 configuration in La3+ solids”. In: *Journal of Physics: Condensed Matter* 27.40 (2015), p. 405501.

[154] Xiaofeng Guo et al. “Cerium substitution in yttrium iron garnet: valence state, structure, and energetics”. In: *Chemistry of Materials* 26.2 (2013), pp. 1133–1143.

[155] BT Thole et al. “X-ray circular dichroism as a probe of orbital magnetization”. In: *Physical Review Letters* 68.12 (1992), p. 1943.

[156] Paolo Carra et al. “X-ray circular dichroism and local magnetic fields”. In: *Physical Review Letters* 70.5 (1993), p. 694.

[157] CT Chen et al. “Experimental confirmation of the X-ray magnetic circular dichroism sum rules for iron and cobalt”. In: *Physical review letters* 75.1 (1995), p. 152.

[158] DJ Huang et al. “Spin and Orbital Magnetic Moments of F e 3 O 4”. In: *Physical review letters* 93.7 (2004), p. 077204.

[159] Cinthia Piamonteze, Piter Miedema, and Frank MF De Groot. “Accuracy of the spin sum rule in XMCD for the transition-metal L edges from manganese to copper”. In: *Physical Review B* 80.18 (2009), p. 184410.

[160] T Okane et al. “Magnetic behavior near the boundary of 4 f delocalization in ferromagnetic CeRu 2 Ge 2 and paramagnetic CeRu 2 Si 2 observed by Ce M 4, 5 XAS and XMCD”. In: *Physical Review B* 86.12 (2012), p. 125138.

[161] Gerrit van der Laan and BT Thole. “X-ray-absorption sum rules in jj-coupled operators and ground-state moments of actinide ions”. In: *Physical Review B* 53.21 (1996), p. 14458.

[162] P Novák et al. “Evidence for Magnetic Interactions between Distant Cations in Yittrium Iron Garnet”. In: *Physical review letters* 75.3 (1995), p. 545.

[163] J Geshev, ADC Viegas, and Joao Edgar Schmidt. “Negative remanent magnetization of fine particles with competing cubic and uniaxial anisotropies”. In: *Journal of applied physics* 84.3 (1998), pp. 1488–1492.

[164] J Geshev et al. “Dependence of the magnetization and remanence of single-domain particles on the second cubic anisotropy constant”. In: *Journal of Applied Physics* 90.12 (2001), pp. 6243–6250.

[165] MA Gilleo. “Ferromagnetic insulators: garnets”. In: *Handbook of Ferromagnetic Materials* 2 (1980), pp. 1–53.

[166] JB Goodenough. *In Magnetism and the Chemical Bond; Cotton, FA; Olah, GA; Prigogine, I., Eds.; Interscience monographs Chemistry*. 1963.

[167] Thomas Wolfram and Sinasi Ellialtioglu. *Electronic and optical properties of d-band perovskites*. Cambridge University Press, 2006.

[168] RA Cowley. “The phase transition of strontium titanate”. In: *Philosophical Transactions of the Royal Society of London A: Mathematical, Physical and Engineering Sciences* 354.1720 (1996), pp. 2799–2814.

[169] Farrel W Lytle. “X-Ray Diffractometry of Low-Temperature Phase Transformations in Strontium Titanate”. In: *Journal of Applied Physics* 35.7 (1964), pp. 2212–2215.

[170] Qun Hui et al. “Total scattering and reverse Monte Carlo study of the 105 K displacive phase transition in strontium titanate”. In: *Journal of Physics: Condensed Matter* 17.5 (2005), S111.

[171] A. V. Kityk et al. “Low-frequency superelasticity and nonlinear elastic behavior of $\mathrm{SrTiO_3}$ crystals”. In: *Phys. Rev. B* 61 (2 2000), pp. 946–956. DOI: `10.1103/PhysRevB.61.946`. URL: `https://link.aps.org/doi/10.1103/PhysRevB.61.946`.

[172] J. C. Slonczewski and H. Thomas. “Interaction of Elastic Strain with the Structural Transition of Strontium Titanate”. In: *Phys. Rev. B* 1 (9 1970), pp. 3599–3608. DOI: `10.1103/PhysRevB.1.3599`. URL: `https://link.aps.org/doi/10.1103/PhysRevB.1.3599`.

[173] K Alex Müller and H Burkard. “SrTiO3: An intrinsic quantum paraelectric below 4 K”. In: *Physical Review B* 19.7 (1979), p. 3593.

[174] Eric Courtens. “Birefringence of SrTiO3 Produced by the 105 K Structural Phase Transition”. In: *Physical Review Letters* 29.20 (1972), p. 1380.

[175] V. K. Vlasko-Vlasov et al. “Direct Magneto-Optical Observation of a Structural Phase Transition in Thin Films of Manganites”. In: *Phys. Rev. Lett.* 84 (10 2000), pp. 2239–2242. DOI: `10.1103/PhysRevLett.84.2239`. URL: `https://link.aps.org/doi/10.1103/PhysRevLett.84.2239`.

[176] Robert Loetzsch, Ingo Uschmann, and Eckhard Förster. “Spatially resolved twin domain distribution and lattice parameter variations in the near-surface region of SrTiO single crystals.” In: *Applied Physics A: Materials Science and Processing* 106.3 (2012), pp. 563 –566. ISSN: 09478396.

[177] Z. Erlich et al. “Optical Study of Tetragonal Domains in LaAlO3/SrTiO3”. In: *Journal of Superconductivity and Novel Magnetism* 28.3 (2015), p. 1017. DOI: `10.1007/s10948-014-2714-x`. URL: `http://dx.doi.org/10.1007/s10948-014-2714-x`.

[178] R. Loetzsch et al. “The cubic to tetragonal phase transition in SrTiO3 single crystals near its surface under internal and external strains”. In: *Applied Physics Letters* 96.7 (2010), p. 071901. DOI: `10.1063/1.3324695`. eprint: `http://dx.doi.org/10.1063/1.3324695`. URL: `http://dx.doi.org/10.1063/1.3324695`.

[179] Bernard Dennis Cullity and Chad D Graham. *Introduction to magnetic materials*. John Wiley & Sons, 2011.

[180] Dexin Wang et al. “Magnetostriction effect of amorphous CoFeB thin films and application in spin-dependent tunnel junctions”. In: *Journal of Applied Physics* 97.10 (2005), p. 10C906. DOI: `10.1063/1.1848355`. eprint: `http://dx.doi.org/10.1063/1.1848355`. URL: `http://dx.doi.org/10.1063/1.1848355`.

[181] Sen Zhang et al. “Giant electrical modulation of magnetization in Co40Fe40B20/Pb (Mg1/3Nb2/3) 0.7 Ti0. 3O3 (011) heterostructure”. In: *Scientific reports* 4 (2014), p. 3727.

[182] Arne Vansteenkiste et al. “The design and verification of MuMax3”. In: *AIP Advances* 4.10 (2014), p. 107133. DOI: `10.1063/1.4899186`. eprint: `http://dx.doi.org/10.1063/1.4899186`. URL: `http://dx.doi.org/10.1063/1.4899186`.

[183] Massimiliano Stengel. “Unified ab initio formulation of flexoelectricity and strain-gradient elasticity”. In: *Phys. Rev. B* 93 (24 2016), p. 245107. DOI: `10.1103/PhysRevB.93.245107`. URL: `https://link.aps.org/doi/10.1103/PhysRevB.93.245107`.

[184] M. Yazdi-Rizi et al. “Anisotropy of infrared-active phonon modes in the monodomain state of tetragonal $SrTiO_3$ (110)”. In: *Phys. Rev. B* 95 (2 2017), p. 024105. DOI: `10.1103/PhysRevB.95.024105`. URL: `https://link.aps.org/doi/10.1103/PhysRevB.95.024105`.

[185] Hiromoto Uwe and Tunetaro Sakudo. “Stress-induced ferroelectricity and soft phonon modes in $SrTiO_3$”. In: *Phys. Rev. B* 13 (1 1976), pp. 271–286. DOI: `10.1103/PhysRevB.13.271`. URL: `https://link.aps.org/doi/10.1103/PhysRevB.13.271`.

[186] Na Sai and David Vanderbilt. “First-principles study of ferroelectric and antiferrodistortive instabilities in tetragonal $\mathrm{SrTiO_3}$”. In: *Phys. Rev. B* 62 (21 2000), pp. 13942–13950. DOI: 10.1103/PhysRevB.62.13942. URL: https://link.aps.org/doi/10.1103/PhysRevB.62.13942.

[187] J Hemberger et al. “Quantum paraelectric and induced ferroelectric states in SrTiO3”. In: *Journal of Physics: Condensed Matter* 8.25 (1996), p. 4673. URL: http://stacks.iop.org/0953-8984/8/i=25/a=021.

[188] H. W. Jang et al. “Ferroelectricity in Strain-Free SrTiO3 Thin Films”. In: *Phys. Rev. Lett.* 104 (19 2010), p. 197601. DOI: 10.1103/PhysRevLett.104.197601. URL: https://link.aps.org/doi/10.1103/PhysRevLett.104.197601.

[189] P. F. Carcia. “Perpendicular magnetic anisotropy in Pd/Co and Pt/Co thin film layered structures”. In: *Journal of Applied Physics* 63.10 (1988), pp. 5066–5073. DOI: 10.1063/1.340404. URL: http://dx.doi.org/10.1063/1.340404.

[190] N. Nakajima et al. “Perpendicular Magnetic Anisotropy Caused by Interfacial Hybridization via Enhanced Orbital Moment in Co/Pt Multilayers: Magnetic Circular X-Ray Dichroism Study”. In: *Phys. Rev. Lett.* 81 (23 1998), pp. 5229–5232. DOI: 10.1103/PhysRevLett.81.5229. URL: https://link.aps.org/doi/10.1103/PhysRevLett.81.5229.

[191] D. Weller et al. “Orbital magnetic moments of Co in multilayers with perpendicular magnetic anisotropy”. In: *Phys. Rev. B* 49 (18 1994), pp. 12888–12896. DOI: 10.1103/PhysRevB.49.12888. URL: https://link.aps.org/doi/10.1103/PhysRevB.49.12888.

[192] D. Weller et al. “Magnetic and magneto-optical properties of cobalt-platinum alloys with perpendicular magnetic anisotropy”. In: *Applied Physics Letters* 61.22 (1992), pp. 2726–2728. DOI: 10.1063/1.108074. URL: http://dx.doi.org/10.1063/1.108074.

[193] J. B. González-Díaz et al. “Cobalt dependence of the magneto-optical response in magnetoplasmonic nanodisks”. In: *Applied Physics Letters* 97.4 (2010), p. 043114. DOI: 10.1063/1.3474617. URL: http://dx.doi.org/10.1063/1.3474617.

[194] M. Kisielewski et al. “Magnetic anisotropy and magnetization reversal processes in Pt/Co/Pt films”. In: *Journal of Magnetism and Magnetic Materials* 260.1 (2003), pp. 231 –243. DOI: http://dx.doi.org/10.1016/S0304-8853(02)01333-1. URL: http://www.sciencedirect.com/science/article/pii/S0304885302013331.

[195] L. Thevenard et al. "Precessional magnetization switching by a surface acoustic wave". In: *Phys. Rev. B* 93 (13 2016), p. 134430. DOI: 10.1103/PhysRevB.93.134430. URL: https://link.aps.org/doi/10.1103/PhysRevB.93.134430.

[196] T. Koyama et al. "Dependence of Curie temperature on Pt layer thickness in Co/Pt system". In: *Applied Physics Letters* 106.13 (2015), p. 132409. DOI: 10.1063/1.4916824. eprint: http://dx.doi.org/10.1063/1.4916824. URL: http://dx.doi.org/10.1063/1.4916824.

[197] Vineeth Mohanan Parakkat, K. R. Ganesh, and P. S. Anil Kumar. "Tailoring Curie temperature and magnetic anisotropy in ultrathin Pt/Co/Pt films". In: *AIP Advances* 6.5 (2016), p. 056118. DOI: 10.1063/1.4944343. eprint: http://dx.doi.org/10.1063/1.4944343. URL: http://dx.doi.org/10.1063/1.4944343.

[198] Séverine Gomès, Ali Assy, and Pierre-Olivier Chapuis. "Scanning thermal microscopy: A review". In: *physica status solidi (a)* 212.3 (2015), pp. 477–494. ISSN: 1862-6319. DOI: 10.1002/pssa.201400360. URL: http://dx.doi.org/10.1002/pssa.201400360.

[199] Clemens CW Ruppel and Tor A Fjeldly. *Advances in surface acoustic wave technology, systems and applications*. Vol. 2. World scientific, 2001.

[200] Lucia Aballe et al. "The ALBA spectroscopic LEEM-PEEM experimental station: layout and performance". In: *Journal of Synchrotron Radiation* 22.3 (2015), pp. 745–752. DOI: 10.1107/S1600577515003537. URL: https://doi.org/10.1107/S1600577515003537.

[201] B.H. Ha et al. "Acoustothermal heating of polydimethylsiloxane microfluidic system". In: *Scientific Reports* 5 (July 2015), p. 11851. DOI: 10.1038/srep11851.

[202] Richie J. Shilton et al. "Rapid and Controllable Digital Microfluidic Heating by Surface Acoustic Waves". In: *Advanced Functional Materials* 25.37 (2015), pp. 5895–5901. ISSN: 1616-3028. DOI: 10.1002/adfm.201501130. URL: http://dx.doi.org/10.1002/adfm.201501130.

[203] Bertram Alexander Auld. *Acoustic fields and waves in solids*. 1973.

[204] MF Lewis. "On Rayleigh waves and related propagating acoustic waves". In: *Rayleigh-Wave Theory and Application*. Springer, 1985, pp. 37–58.